Distribution Agreement

In presenting this thesis or dissertation as a partial fulfillment of the requirements for an advanced degree from Emory University, I hereby grant to Emory University and its agents the non-exclusive license to archive, make accessible, and display my thesis or dissertation in whole or in part in all forms of media, now or hereafter known, including display on the world wide web. I understand that I may select some access restrictions as part of the online submission of this thesis or dissertation. I retain all ownership rights to the copyright of the thesis or dissertation. I also retain the right to use in future works (such as articles or books) all or part of this thesis or dissertation.

Signature:

_____   _____

  Alessandro Barone   Date

Patient-Specific Modeling in Cardiac Electrophysiology:

Parameter Estimation and Personalization

By

Alessandro Barone

Doctor of Philosophy

Mathematics

_____

Alessandro Veneziani, Ph.D.

Advisor

_____

James Nagy, Ph.D.

Committee Member

_____

Lars Ruthotto, Ph.D.

Committee Member

_____

Flavio Fenton, Ph.D.

Committee Member

Accepted:

_____

Lisa A. Tedesco, Ph.D.

Dean of the James T. Laney School of Graduate Studies

_____

Date

Patient-Specific Modeling in Cardiac Electrophysiology:

Parameter Estimation and Personalization

By

Alessandro Barone

B.A. in Mathematical Engineering, Politecnico di Milano, 2012

M.Sc. in Mathematical Engineering, Politecnico di Milano, 2014

Advisor: Alessandro Veneziani, Ph.D.

An abstract of

A dissertation submitted to the Faculty of the

James T. Laney School of Graduate Studies of Emory University

in partial fulfillment of the requirements for the degree of

Doctor of Philosophy

in Mathematics

2019

Abstract

Patient-Specific Modeling in Cardiac Electrophysiology:

Parameter Estimation and Personalization

By Alessandro Barone

Computational modeling in cardiac electrophysiology (EP) has long played a central role in the study of physio-pathological dynamics of electrical propagation. One of the most significant challenges to face is the translation process of numerical (*in silico*) investigations to clinical practice. In silico simulations can potentially impact the quality of cardiac arrhythmia therapy, reducing the risk of *in vivo* testing. However, the clinical use of virtual experiments is hindered by the need of customization of mathematical models to *patient-specific* data. The personalization process involves the fine tuning of many model parameters, that cannot be measured directly, via *accurate* and *efficient data assimilation* techniques. This work is particularly focused on the estimation of cardiac conductivities, crucial parameters of the Bidomain and Monodomain models – currently the most used mathematical descriptions of cardiac electrical behavior. This Thesis addresses the challenge described above yielding four main contributions. (1) We perform an extensive and thorough synthetic and *experimental validation* of the deterministic *variational* data assimilation method proposed by Yang and Veneziani in 2015 to retrieve conductivities from potential recordings. The results demonstrate that the procedure provides accurate space-dependent conductivity estimates that reproduce most of the observed dynamics. (2) The *Proper Generalized Decomposition* (PGD) reduced-order model technique is investigated for the first time in EP to improve the efficiency of the variational technique. Relying on the off-line/on-line paradigm and without the need of any preliminary knowledge of the high-fidelity solution, we show in 2D and 3D settings that the strategy enables nearly real-time estimation preserving reasonable accuracy. (3) With the goal of assessing the robustness of the results, we propose a *statistical* formulation of the estimation problem for Monodomain conductivities. Exploiting the computational convenience of the on-line PGD solution, the methodology allows a reliable quantification of the uncertainty of two-dimensional estimates. (4) Using a virtual personalized heart model efficiently reconstructed from high resolution MRI images and ECG data via a *physics-based* reduced-order model approach, we perform a preliminary study of the induction of ventricular electrical anomalies with respect to different conduction properties in view of optimizing arrhythmia treatments in silico.

Patient-Specific Modeling in Cardiac Electrophysiology:

Parameter Estimation and Personalization

By

Alessandro Barone

B.A. in Mathematical Engineering, Politecnico di Milano, 2012

M.Sc. in Mathematical Engineering, Politecnico di Milano, 2014

Advisor: Alessandro Veneziani, Ph.D.

A dissertation submitted to the Faculty of the

James T. Laney School of Graduate Studies of Emory University

in partial fulfillment of the requirements for the degree of

Doctor of Philosophy

in Mathematics

2019

Acknowledgments

I vividly remember when I left Italy on January 1st 2015 to start this amazing journey in the US. The enthusiasm, the energy and the curiosity about all the adventures waiting for me, but honestly also the worry for the challenges I was about to face. Surely the beginning wasn't easy at all, but well, I must say that the last five years have been full of incredible people and unforgettable experiences that will always have a special place in my heart. There are a lot of people I am grateful to and helped me become who I am now.

I begin by expressing my gratitude to my advisor Alessandro Veneziani. Thank you for always supporting me, for your enthusiasm that you instilled in me, for the freedom you granted me in developing and improving my research skills. Your passion has been a great source of motivation and inspiration for me. I am and will always be grateful for trusting me, everything you taught me made me a better researcher and, most importantly, a better person. I will always laugh when recalling the day of my Master thesis defense in Milan when, in front of my parents, you said "Quando vieni ti spezzo le ossa!". Well, instead you made me shape and fortify them.

I would like to thank Alessio Gizzi, the hours-long conversations we had were so enlightening and full of insightful advices that greatly contributed to shape this work. Your stimulating challenges and deep knowledge of cardiac electrophysiology modeling greatly strengthened my professional profile.

I thank Flavio Fenton and his collaborators for the precious contribution and comments throughout these years.

I also thank Jim Nagy and Lars Ruthotto for generously offering their time and helpful suggestions for reviewing this Thesis. I acknowledge the NSF Project DMS 1412963 and the XSEDE Consortium, Grant TG-ASC160069 for supporting my research.

I would have had a much harder time in these five years without an amazing group of friends. I will not name everyone because it would take too many pages, so please don't feel sad if I don't mention you. A special thank goes to my dearest friends, Sofia and Massi. I can't imagine how all of this would have been without you. I won't never forget that day, a few days after arriving at Emory, when I was so sad and homesick and I first stepped into

the office and saw the gifts you prepared for me on my desk. That moment filled my heart and made me see crystal clear what true friendship really means.

A huge thank you goes to my friends Samy, Vicman and Big Larry, the laughter, the funny moments and conversations made the PhD much lighter and easier to deal with.

Thank you Manuela for being such a nice friend and for bringing the taste of Abruzzo during these years.

And also thanks to all my other PhD and Latino friends, for all the time we spent together and for letting me appreciate different cultures.

I was very lucky to share these years with my wonderful friends of SalsAtlanta. You have been like a family to me and thanks to you I grew as a person discovering new passions and sides of myself I wasn't aware of and learning how to make everyday life more joyful and cheerful.

Finally, Mamma, Papà, Pierluigi, Teddy, non importa la lontananza o quanto grandi siano le difficoltà, io so che non sarò mai solo e non posso esprimere pienamente quanto ciò mi rende sereno e tranquillo. Il vostro amore incondizionato è il cardine della mia ricerca.

Nonno, questa tesi è per te, per essere sempre al mio fianco.

Contents

List of Figures

List of Tables

Chapter 1

Introduction

Electrical malfunctions of the heart are among the most common cardiovascular diseases, the leading cause of death worldwide [1]. Irregular cardiac rhythms, named *cardiac arrhythmias*, can potentially be life-threatening: in particular, arrhythmias occurring in the ventricles (the heart's lower chambers) can degenerate into *ventricular fibrillation*, which is an erratic, disorganized firing of impulses from the ventricles prohibiting the heart to pump blood thus leading to collapse and cardiac death. Depending on the kind and severity of rhythm disorder, the treatment of arrhythmia includes drug therapies, the implantation of artificial pacemakers and catheter ablation. Taking anti-arrhythmic drugs is a palliative remedy only controlling abnormal heart rhythm. Moreover, several side effects may occur such as allergic reactions, chest pain, dizziness and fainting.

Cardiac Resynchronization Therapy (CRT) is one of the procedures to implant a pacemaker (an example is shown in Fig. 1.1) in the chest to help restore normal heart beat. Three wires (leads) connected to the device monitor heart rate to detect irregularities and emit tiny pulses of electricity at certain intervals to resynchronize the heart. CRT has shown a significant improvement in symptoms, overall quality of life and mortality rate [2,3]. However, insufficient personalization affects the effectiveness of the therapy. In fact, around 30% of patients do not respond to this invasive treatment [4] mainly because of lack of *patient-specific* tuning of pacing intervals between the electrical stimulations. Furthermore, leads placement in the heart depends on the cardiac anatomy of the individual.

The goal of *catheter ablation* is stopping arrhythmias by scarring the portion of tissue
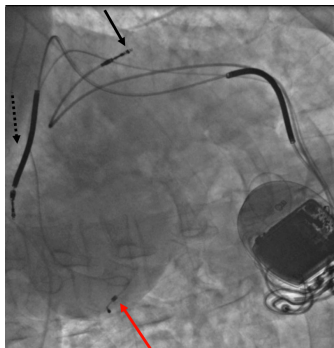
Figure 1.1: Example of a CRT device with three leads: a right atrial lead (solid black arrow), a right ventricular lead (dashed black arrow), and a coronary sinus lead (red arrow) enabling pacing of the left ventricle. The device delivers stimuli to the heart through the leads following a certain pacing protocol so to correct the rhythm disorder. From Wikimedia Commons, Author: Gregory Marcus, MD.

that triggers or sustains abnormal electrical signals. Supported by a computerized, three-dimensional mapping system, the electrophysiologist uses flexible catheters inserted through a vein and guides them into the heart chambers. Then, the catheters deliver thermal energy destroying the tissue causing rhythm disturbance. Ablation is less invasive than CRT and has high success rate (around 90% for ventricular arrhythmias). However, an accurate detection of the ablation area is crucial for an optimal individualized therapy but still quite challenging to pursue in clinical setting. In addition, recurrence of irregular rhythm occurs in at least 20 to 40% of the patients [5, 6]. In general, the impact of individual, patient-specific factors is largely neglected in current treatments of arrhythmias. Advances in *personalized electrophysiology* (EP) are needed for better therapy planning, intervention guidance and outcome prediction.

Mathematical and numerical modeling in cardiac EP is a mature field of applied and computational mathematics, supported by an abundant and comprehensive literature [7–10] (to mention a few). Numerical simulations in electrocardiology are progressively becoming part of medical research and clinical practice: application to atrial or ventricular arrhythmias [11, 12], improvement of drug therapies [13], CRT [14, 15], catheter ablation [16–18] have been explored. Multi-scale mathematical frameworks have been developed to simulate the cardiac electrical function at the whole-organ scale [19–21]. The increasing interest in computational EP is motivated by the convenience of *in silico* over *in vivo* testing. In

fact, in silico experiments (i.e., numerical simulations of possible scenarios) allow to investigate the pathology as well as the outcome of potential therapies *before* their actual clinical implementation, reducing the risk of invasive tests. Furthermore, virtual testing is an extremely useful resource to design new devices at limited planning costs, as the effectiveness of different configurations can be predicted before production.

To be of clinical utility, two conditions must be fulfilled:

- EP models must be *accurately personalized* so to reflect a given patient's physiology.

- Parameter estimation in EP must be *efficient* enough to be compatible with clinical time frames.

The personalization issue involves the fine tuning of the many parameters (e.g., cardiac tissue conductivities) featured by the relevant equations on patient-specific data. While tremendous research effort has been devoted to this problem [22–28], a *robust and precise quantification* of the parameters that govern the equations associated to EP models still remains an open challenge, in particular in an experimental setting. A *reliable estimation* of these quantities and *validation* against real data are crucial in view of using computational models to study and evaluate patient-specific EP in silico, with the potential of optimizing medical procedures, such as choosing optimal electrode locations and pacing protocol for CRT or detecting ideal ablation areas.

As for the efficiency issue, developing patient-specific EP models requires immense computational effort limiting the use of mathematical electrocardiology in clinical setting. In fact, parameter estimation procedures are computationally intensive as many queries of forward solvers (usually involving partial differential equation (PDE)) with different model parameters are needed. To capture all the clinically significant features, fine spatial and temporal resolutions of discretized EP equations are required resulting in heavy computations. A reasonable trade-off between efficiency and complexity is difficult to achieve from a modeling perspective as well. The more physiologically detailed the model, the larger the number of equations and parameters. As for hardware solutions, the increasing availability of high performance computing resources enables more detailed simulations in the view of clinical applications [29–32]. The use of graphics processing units (GPUs) has

also been of interest in EP modeling [33–36], yet parallel implementations are not straight-forward. Strategies coping with the issue of alleviating computational complexity from a software viewpoint involve mathematical *model reduction* techniques based on the definition of a surrogate for the forward problem which is more affordable to solve. While some approaches have been investigated with promising results [37–41], particular properties of EP models such as nonlinearity and wave-front propagation dynamics make the application of reduced-order modeling in this field problematic. To sum up, an *accurate* and *efficient* personalization is both necessary and challenging to integrate computational EP in the diagnosis, prognosis and treatments of cardiac arrhythmias.

1.1 Contribution and Thesis Outline

The objective of this Thesis is to contribute to the translation process of computational cardiac EP to bedside by developing precise and fast parameter estimation procedures with the goal of better informing clinical decision making. This can be done by means of *data assimilation* techniques incorporating experimental data into mathematical models and by exploring alternative *model order reduction* approaches aiming to reduce computational complexity. The quantification of *cardiac conductivity*, a critical parameter in EP modeling [42], is the primary concern of this Thesis. We face the estimation problem from four different perspectives, each one of them privileging either *accuracy* or *efficiency* or looking for a reasonable compromise.

The first approach considers the *variational data assimilation* procedure presented in [26], which intends to assimilate data by solving a suitable constrained optimization problem which consists of the minimization of a functional measuring the misfit between available patient-specific data and computed solution, using as a constraint the EP model. In this part of the Thesis, the estimation is pursued by matching the model behavior with the observed electrical wave propagation. Our contribution is the synthetic validation considering several realistic experimental settings and, in particular, an extensive and accurate validation against *in vitro* measurements. To the best of our knowledge, this is the first time that such a detailed verification of the reliability of a methodology for cardiac conductivity

estimation using real data is carried out. We will verify that this procedure is accurate at the expense of heavy computations. We will resort to parallel computing to contain computational burden.

The second strategy consists of adopting a *Proper Generalized Decomposition* (PGD) technique [43–45] for the reduction of the costs associated with the misfit calculation. This method relies on a classical off-line-on-line paradigm, where an appropriate basis functions set is constructed by solving the equations in the parameter space. A special separation-of-variable technique is used to perform this step efficiently. Then, when one needs to compute the solution for a different set of parameters (on-line stage), like in the inverse problem for conductivity estimation, the evaluation follows promptly by the solution of an algebraic problem. While PGD was already applied in many contexts [46–48], this work represents the first contribution in cardiac EP. We will see that, with a careful implementation, significant speed up can be achieved keeping an adequate estimation and reproduction of the physics.

The third method tackles the inversion from a *statistical* viewpoint [49,50] with the goal of providing a quantification of the uncertainty. The solution of the inverse problem is a probability distribution that can be used to obtain not only point but also spread estimates. This additional information may be helpful to the users for a more comprehensive assessment of the quality and the robustness of the estimation. This strategy entails more expensive and sometimes unaffordable calculations than deterministic ones. To limit computational complexity, some attempts in literature were done using simplified equations [51, 52]. This part of the chapter serves as the first application of statistical techniques with more accurate EP models. We will combine it with the PGD method for fast exploration of the solution distribution in the parameter space.

Finally, the fourth procedure focuses on a *physics-based* reduced-order modeling approach considering a simplified description of the electrical dynamics. Following a consolidated framework [21, 53, 54], a realistic heart model will be reconstructed from medical images and individualized EP state will be estimated from electrocardiogram (ECG) data at near real-time. In this part of the Thesis, the focus is more on efficiency, whereas we do not expect to accurately reproduce the observed electrical dynamics, but only match some ECG features informative of the physiological conditions of the patient. Based on

this personalization, we will then study the induction of cardiac arrhythmias in view of contributing to a better ablation therapy planning.

The Thesis is organized as follows. We start in **Chapter 2** presenting the mathematical background relevant for this work. First, we quickly describe the anatomy and electrophysiology of the heart. We then review the models used in computational cardiac EP for describing electrical excitation, both at cellular and tissue level.

In **Chapter 3**, we first recall the inverse problem of the estimation of cardiac conductivities introduced in [26]. After presenting the numerical approximation, we test the variational data assimilation procedure in several synthetic settings to investigate the sensitivity with respect many practical issues, such as the level noise in the data and the amount of information. We then perform an extensive and accurate validation against experimental measurements using canine right ventricles.

In **Chapter 4**, we present the PGD method for mitigating the computational burden of the forward solve and in turn of the inverse problem. After a description in a general setting, we apply the technique to an EP model. We then analyze its reliability in capturing the physics of the system and we apply it to the optimization problem in a synthetic setting to gain computational efficiency. We continue by formulating the problem in a Bayesian framework with the goal of providing a quantification of the uncertainty related to the estimates. Finally, we present some numerical results with synthetic data.

Chapter 5 deals with the problem of personalization by using a simplified EP model promoting fast calculation. First, we describe the reconstruction of a virtual heart from clinical images as well as the personalization strategy. We then simulate ventricular tachycardia to allow in silico experiments of ablation procedures.

Concluding remarks and suggestions for future research directions will be addressed in **Chapter 6**.

List of abbreviations For the sake of readability, we add a list of the abbreviations used in this Thesis. AP (Action Potential), APD (Action Potential Duration), AV (Atrio-Ventricular), BEM (Boundary Element Method), BDF (Backward Differentiation Formulas), BICP (Bidomain Inverse Conductivity Problem), BPM (Beats Per Minute), BZ (Bor-

der Zone), CL (Cycle Length), CM (Conditional Mean), CMR (Cardiovascular Magnetic Resonance), CRT (Cardiac Resynchronization Therapy), CV (Conduction Velocity), DI (Diastolic Interval), DO (Discretize-then-Optimize), DOF (Degrees of Freedom), EA (Electrical Axis), ECG (Electrocardiogram), ECS (Extra-Cellular Space), EP (Electro-Physiology), FEM (Finite Element Method), FK (Fenton-Karma), ICP (Inverse Conductivity Problem), ICS (Intra-Cellular Space), KKT (Karush-Kuhn-Tucker), LA (Left Atrium), LAT (Local Activation Time), LBM (Lattice-Boltzmann Method), LV (Left Ventricle), MAP (Maximum A Posteriori), MCMC (Markov Chain Monte Carlo), MH (Metropolis Hastings), MI (Myocardial Infarction), MICP (Monodomain Inverse Conductivity Problem), MM (Minimal Model), MRI (Magnetic Resonance Image) MS (Mitchell-Schaeffer), OD (Optimize-then-Discretize), ODE (Ordinary Differential Equation), PDE (Partial Differential Equation), PGD (Proper Generalized Decomposition), POD (Proper Orthogonal Decomposition), PPDF (Posterior Probability Distribution Function), RA (Right Atria), RC (Restitution Curve), RM (Rogers-McCulloch), RV (Right Ventricle), SA (Sino-Atrial), SVD (Singular Value Decomposition), VA (Ventricular Arrhythmia), VT (Ventricular Tachycardia).

Disclosure The work presented here led to some publications, some already published or to appear, others submitted or in preparation. Some Chapters are strictly related to these papers. We mention this circumstance at the beginning of each of those Chapters. However, we preferred here to organize the stream of the research in a more structured presentation for the sake of readability.

Chapter 2

Mathematical Models in Cardiac Electrophysiology

In this Chapter, we present the mathematical models of cardiac excitation used in this Thesis. We first provide a short overview of the anatomy and the electrophysiology of the heart, both at microscopic and macroscopic scales (Section 2.1). Then, we review the mathematical formulation of the electrical activity at cellular level which in turn allows us to describe the potential propagation at tissue level (Section 2.2). In particular, we will consider the Bidomain, Monodomain and graph-based models to test our proposed methodologies.

2.1 Anatomy and Electrophysiology of the Heart

This Section has the purpose of briefly illustrating the anatomy and the electrical activity of the heart. In Section 2.1.1, we describe the main components of the heart muscle and its fundamental role in sustaining proper function of the body. We provide an overview of the electrical activity at cellular level in Section 2.1.2 and of electrical conductive system of the heart in Section 2.1.3.
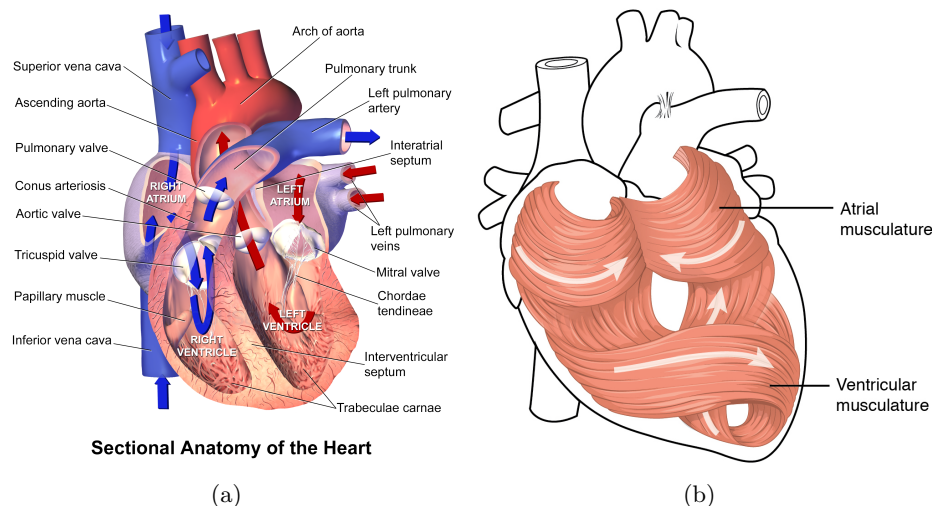
Figure 2.1: (a) Sectional anatomy of a healthy human heart (anterior view) showing the four chambers, the major vessels, the valves and the path of blood flow. The red arrows show the direction in which oxygenated blood flows from the lungs to the rest of the body. The blue arrows show the direction in which deoxygenated blood flows from the body to the lungs. From Wikimedia Commons, source: Blausen Medical Communications, Inc. (b) Heart musculature. This involved pattern allows the heart to contract more effectively than a simple linear pattern would. From Wikimedia Commons, source: Anatomy & Physiology, Connexions Web site. http://cnx.org/content/col11496/1.6/, Jun 19, 2013.

2.1.1 Macroscopic description

The heart is situated between the lungs in the middle of the chest, slightly to the left of the sternum, and is supported inside a double-layered membrane called the *pericardium*. The inner layer of the pericardium is attached to the heart muscle, whereas the outer layer anchors it to the surrounding walls. The space between the two layers, the *pericardial cavity*, contains a supply of lubricating serous fluid and it lets the heart move as it beats.

The heart muscle is called *myocardium* and it includes the muscle between the outer surface, the *epicardium*, and the inner layer, the *endocardium*. The lower tip of the heart is called *apex* and the posterior part is known as the *base*. The heart is divided by a wall of muscle, the *septum*, into left and right halves and it has four major chambers. The upper thinner walled chambers are called the *left atrium* (LA) and the *right atrium* (RA), and the lower, larger, thicker walled chambers are called the *left ventricle* (LV) and the *right ventricle* (RV). A detailed cross-section of a human heart is shown in Fig. 2.1(a).

Cardiac *myocytes* are the major constituent of heart muscle. In human ventricular

tissue, myocytes can be approximated by a cylinder with a length of 80 to 100 μm and a diameter of 10 to 20 μm [7]. Myocytes are bounded by a lipid membrane, the *sarcolemma*, and coupled to other cells by *gap junction* channels enabling the conduction of the electrical signal. Myocytes are arranged in *fibers* and layers of fibers, called *sheets*, constitute the myocardium. The sheets feature on average four layers and are surrounded by a matrix of collagenous connective tissue. This results in a complex muscle pattern (illustrated in Fig. 2.1(b)), as the fibers swirl and spiral around the chambers of the heart. They wrap around the atria in figure 8 pattern [55, 56]. Deeper layers also form a figure 8 around the two ventricles and proceed toward the apex. More superficial layers surround both ventricles. The fibers turn clockwise from the apex to the base at the epicardium, have circular geometry in the myocardium, and go counterclockwise close to the endocardium [57, 58].

The right and the left side of the heart work in unison producing a rhythmical heartbeat. This coordinate contraction provides a continuous circulation of blood to meet the hematologic requirements of all cells of the body. Fig. 2.1(a) depicts a complete blood circulation throughout the heart. The RA receives deoxygenated blood from the body through veins called superior and inferior cava. From the RA, the blood travels to the RV. Once the RV is full, it pumps the blood into the pulmonary artery which leads to the lungs, where the blood picks up oxygen and offloads carbon dioxide. Newly oxygenated blood travels to the LA via the pulmonary vein. Then, the LA contracts pushing blood into the LV. The LV is responsible for pumping this oxygenated blood out to the body via the aorta. The aorta is the largest blood vessel in the body and carries blood up towards the head, the arms and the thorax, before arching over and traveling down the vertebral column to carry blood towards the other abdominal organs and the legs. The LV is the largest and thickest chamber of the heart since it has to pump blood further around the body and against higher pressure, compared with the RV. The period during which the atria and the ventricles relax and fill with blood is called *diastole*; the period of contraction during which blood is pushed out of the heart is called *systole* [7].

The heart has four valves that help ensure that blood only flows in one direction. The *tricuspid* valve on the right and the *mitral* valve on the left regulate blood flow through each

respective atrium and ventricle pair. The *papillary muscles* in both the ventricles attach to the cusps of the tricuspid and mitral valves via tendinous cords and contract to prevent inversion or prolapse of these valves during contraction. The *pulmonary* valve lies between the RV and the pulmonary artery and the *aortic* valve separates the LV and the aorta.

2.1.2   Electrophysiology of cardiac myocytes

The sarcolemma encapsulates the cardiac muscle cell, separating the inner volume known as the *intracellular space* (ICS) to the volume outside, called the *extracellular space* (ECS). The sarcolemma is a semipermeable membrane, i.e., it features small pores that allow only specific ions of a certain size and/or charge to pass through [7]. Since these pores regulate the ion flow across the membrane, they are often referred to as *ion channels*. The movement of ions through the ion channels causes a potential difference between the ICS and ECS defined as *transmembrane potential u* (or *membrane potential*):

$$u = u_i - u_e,$$

where u_i is the potential in the intracellular space, the *intracellular potential*, and u_e the potential in the extracellular space, the *extracellular potential*.

The ions that play a key role in cardiac electrophysiology are Na^+, K^+ and Ca^{2+}. Under resting conditions, the concentration of these ions in the ICS and ECS is substantially different. These concentration gradients provide the potential energy to drive the formation of the transmembrane potential. The voltage at which there is no net flow of a particular ion type across the membrane is called *Nernst potential*. The Nernst potential E_x for an ion x can be calculated from the *Nernst equation* [7]

$$E_x = \frac{RT}{z_x F} \log_e \left(\frac{[x]_e}{[x]_i} \right),$$

where R is the universal gas constant; T the absolute temperature; z_x the valence of the ion; F the Faraday's constant; $[x]_i$ and $[x]_e$ the intracellular and the extracellular concentrations of the ion x. The concentrations at equilibrium give the Nernst potentials of $E_{Na} = 70$ mV,

$E_K = -88$ mV and $E_{Ca} = 128$ mV at body temperature (37° C) [7,59].

The electrical excitation triggered by the ion fluxes through the ion channels is called *Action Potential* (AP). The standard model used to understand the cardiac AP is that of the ventricular myocyte. It is composed of 5 phases (0-4)[1], beginning and ending with phase 4 this numeration (an illustration is given in Fig. 2.2).

- **Phase 4: The resting phase**. In absence of a stimulus, the cell membrane is in a polarized state due to a constant outward leak of K^+ through the ion channels. The resting transmembrane potential is around -85 mV [60] which is close to E_K, reflecting the high permeability of the membrane to K^+. Na^+ and Ca^{2+} channels are closed in this state.

- **Phase 0: Depolarization**. If a sufficiently large stimulus, e.g., a synaptic input or electrical pacing, is applied to the cardiac cell, the transmembrane potential rises above a critical value known as *threshold potential*. At this point, enough Na^+ channels have opened to generate a self-sustaining inward Na^+ current. Ca^{2+} channels open when the transmembrane potential is greater than -40 mV causing a small but steady inward flow of Ca^{2+}. The sharp increase of the AP towards zero is called *depolarization*. The peak of the transmembrane potential is between 40 mV and 50 mV, which is close to E_{Na}, since the cell membrane is highly permeable to Na^+.

- **Phase 1: Early repolarization**. Na^+ channels close at most after 1 or 2 ms because, simultaneous with activation, a second, slightly slower conformational change in the channel molecule occurs causing inactivation. The transmembrane potential rapidly decreases towards zero (*repolarization*) due to the steady outward current of K^+.

- **Phase 2: The plateau phase**. Ca^{2+} channels are still open and the inward Ca^{2+} current hold the transmembrane potential in a depolarized state. There is a near balance (*"plateau"*) of charge moving into and out of the cell.

- **Phase 3: Repolarization**. Ca^{2+} channels are gradually inactivated and the persistent flow of K^+ causes the cell to repolarize returning to the resting state. The cell

---

[1]This numeration is commonly used in literature [7].
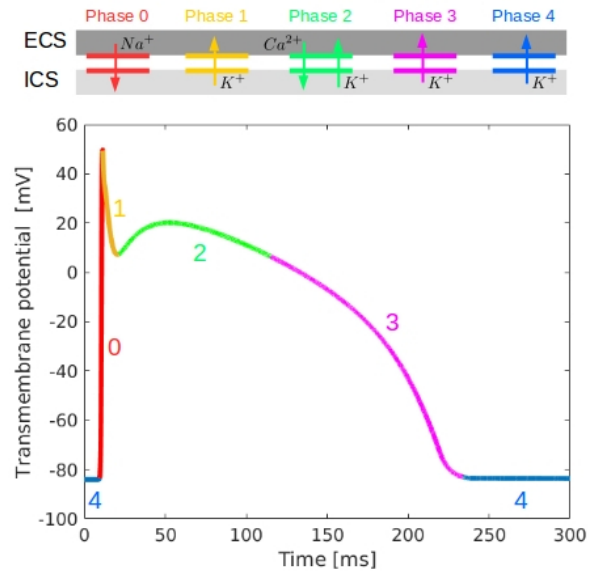
Figure 2.2: Typical action potential of a ventricular myocyte. From resting state of phase 4, the AP begins in phase 0 with the voltage becoming more positive due to the inward Na^+ current causing a sharp upstroke. This is followed by a rapid repolarization of the cell in phase 1. Then, in phase 2, the transmembrane potential remains almost constant due to a near balance between inward Ca^{2+} and outward K^+ currents. The AP terminates in phase 3 returning to resting conditions due to K^+ leaving the cell and causing a decrease in the transmembrane pontential.

is prepared for a new cycle of depolarization.

The time interval in which u is greater than a certain threshold (usually anywhere from 70% to 90% recovery from the peak voltage to the resting potential) is commonly denoted as *Action Potential Duration* (APD) (see Fig. 2.3(a)). Assuming to apply a sequence of stimuli with a period called pacing *cycle length* (CL), the time interval in which the cell rests is called diastolic interval (DI) and it is given by $DI = CL - APD$. It has been observed experimentally that, if the cell is paced with a series a stimuli with decreasingly low CL, this causes a shortening of the APD. This dependence of APD on CL is typically characterized as *restitution* of APD. An example of Restitution Curve (RC) is provided by Fig. 2.3(b). The use of the restitution curve plays a central role in determining the parameter of the ionic models described in Section 2.2.1 so to accurately simulate the observed dynamics of the system.

Electrical impulses can be initiated by a special type of cardiac cell, the *pacemaker cells*. Cardiac pacemaker cells have *natural automacity*, meaning they generate regular
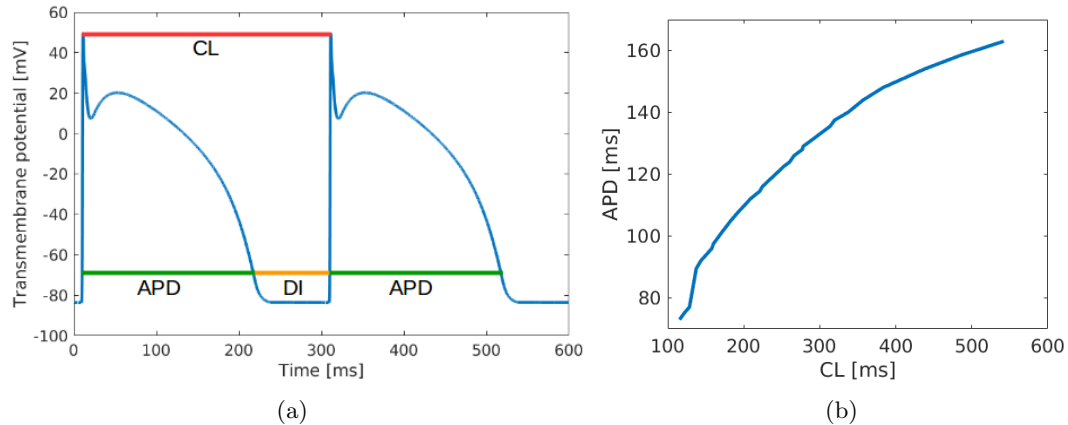
Figure 2.3: (a) APD stands for action potential duration; CL is the pacing cycle length; the diastolic interval DI is DI = CL - APD (b) Example of *restitution curve*, functional relationship between APD and CL. Fast pacing (low CL) shortens the APD.

and spontaneous APs. They are mostly found in the *sinoatrial (SA) node*, but also in the *atrioventricular (AV) node* and the *Purkinje fibers* (see Section 2.1.3 for more details). The particular AP generated by pacemaker cells (see Fig. 2.4) is very different to that in non-pacemaker cells, such as ventricular myocyte, as pacemaker cells do not have extended periods of time when they are quiescent.

2.1.3 Electrophysiology of the heart

To pump blood throughout the body, the muscles of the heart must contract coordinately. The mechanical activity is regulated by electrical impulses propagated by the electrical conduction system of the heart, shown in Fig. 2.4.

Spontaneous electrical stimulation begins at the SA node located in the RA. Propagating through the atria, the signal reaches the AV node. The AV node consists of similar pacemaker cells as found in the SA node. However, these cells intrinsically generate stimuli at a slower rate, so they turn to be placed by the excitation coming from the SA node [7]. Conduction at the AV node is much slower giving time for the atria to contract and push blood into the ventricles before the AP reaches them and make them contract. From the AV node, the electrical propagation stimulates the *bundle of His* which runs down the right side of the septum. After a short distance, this common bundle splits into right and left
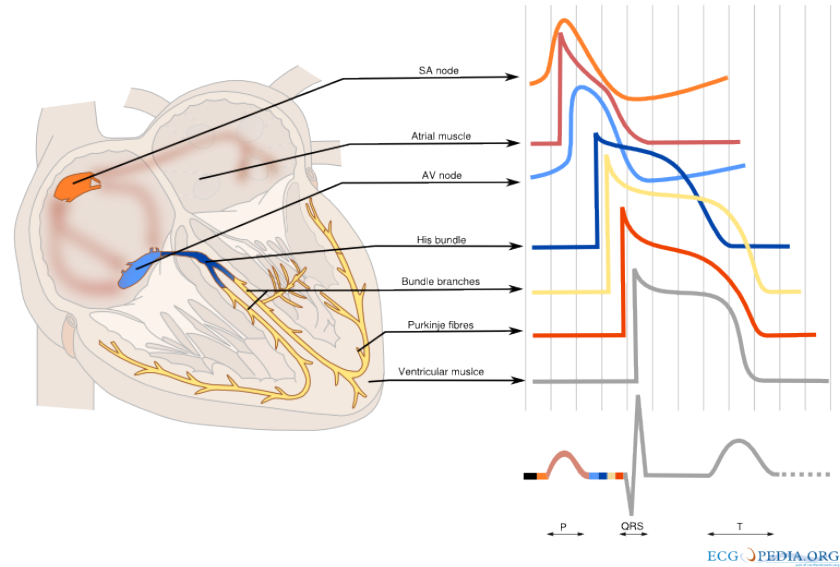
Figure 2.4: Electrical conduction system of the heart, AP waveform of different cardiac cells and idealized ECG signal. The AP generated in the SA node by pacemaker cells is propagated through the right atrium to the AV node, along the Bundle of His and through bundle branches and Purknje fibers for each side of the heart to cause contraction. This process allows blood to be pumped throughout the body. There are important physiological differences between pacemaker cells and those that simply conduct it, such as ventricular myocytes. The main differences lie in the type of ion channels and the mechanism by which they are activated resulting in different configuration of the AP waveform. AP activity within the heart can be recorded to produce an electrocardiogram (ECG). This is a series of upward and downward spikes (labelled P, Q, R, S and T) that represent the depolarization and repolarization of the AP in the atria and ventricles. The ECG representation is divided in portions with different colors corresponding to the AP of the type of cells that define the pattern of the signal. From Wikimedia Commons, source: CardioNetworks.

bundle branches, continuing to subdivide into a complex network of fibers called *Purkinje fibers*. The signal is carried along these fibers in the endocardial surface of both ventricles and within the ventricular myocardium. The fast conduction through the bundle branches and the Purkinje fibers cause the entire endocardium to be excited almost simultaneously. These electrical signals are generated rhythmically, which in turn results in the coordinated rhythmic contraction and relaxation of the heart.

The cardiac electrical activity can be monitored on the body surface with *electrocardiography*, a non-invasive medical process that produces an *electrocardiogram* (ECG). In the conventional 12-lead ECG, a complete picture of heart's electrical activity is portrayed by recording information over a period of time from 12 different perspectives. These 12 views

are gathered by placing electrodes on the chest, wrists and ankles that detect the small electrical changes due to depolarization followed by repolarization during heartbeat. Each lead represents the potential difference between different electrode groups. Fig. 2.4 depicts a normal idealized ECG signal. The *P wave* reflects the depolarization of the atria, from the SA node to the AV node, which usually takes less than 80 ms. Conduction disturbances in the atria or AV node will cause this wave to be longer. The rapid depolarization of the ventricles is represented by the *QRS complex*. It has a much larger amplitude than the P wave because of the large muscle mass of the ventricles compared to the atria. Atrial repolarization also occurs but it is masked by the QRS complex. The duration of the QRS complex is 60 to 100 ms. Any defects in conduction within the Purkinje system or other parts of the ventricles will be reflected in a prolonged QRS complex. The *T wave* corresponds to the repolarization of the ventricles, and generally takes longer to complete than the depolarization. ECG features will be used in Chapter 5 in a patient-specific framework.

This orderly pattern of depolarization gives rise to the characteristic ECG tracing. To the trained clinician, an ECG conveys a large amount of information about the structure of the heart and the function of its electrical conduction system. Any deviation from the normal tracing is potentially pathological and therefore of clinical significance. For example, an irregular QRS complex without P waves is the hallmark of atrial fibrillation; however, other findings can be present as well, such as a bundle branch block that alters the shape of the QRS complexes.

2.2 Modeling Electrical Activity

In this Section, we review the mathematical models used to represent the cardiac excitation at cellular level (Section 2.2.1) and at tissue level (Section 2.2.2). The models described here play a central role in this Thesis.

2.2.1 Cell modeling

The action potential (AP), the change in the transmembrane potential over time, is the result of electrochemical gradients driving the flow of ions across the membrane. This po-
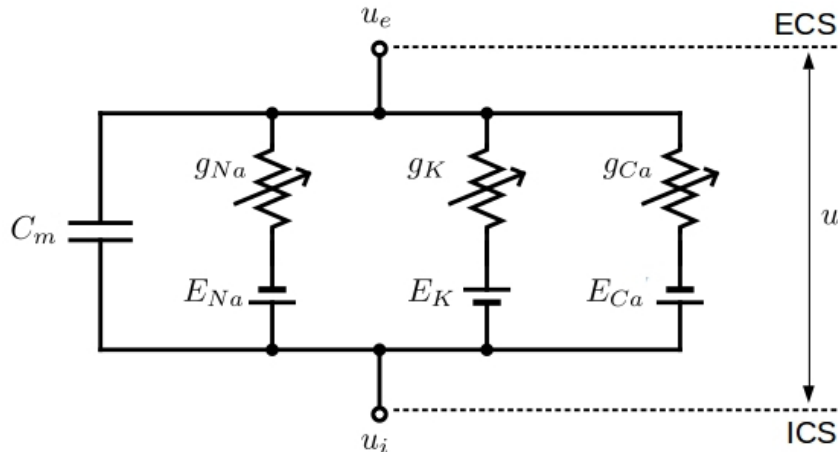
Figure 2.5: Electric circuit modeling the flow of current across the cell membrane. A capacitor with capacitance C_m is used to model the charge storage capacity of the cell membrane, variable resistors are used to model the various types of ion channels embedded in membrane, and batteries are used to represent the electrochemical potentials established by differing intra- and extracellular ion concentrations. The current flow through a given ion channel x depends on the conductance of the channel g_x, and the difference between u and the Nerst potential E_x governs the direction of the current flow.

tential variation can be described using an equivalent electric circuit based on the Hodgkin-Huxley model of the squid giant axon [61]. The electrical activity of the cell membrane can be modeled with a capacitor in parallel with a sequence of resistors representing the ion channels in the membrane, as shown in Fig. 2.5.

For the current flow I_x through the channel of a given ion x, its direction is determined by the difference between the transmembrane potential u and the Nernst potential E_x, that is the equilibrium situation for the ion x. If u is equal to E_x, then the inward and outward flows of ion x are equal. If u is higher or lower than E_x, then there will be a net flow of x one way or the other across the membrane with the ionic current proportional to the difference between u and E_x

$$I_x = g_x(u - E_x),$$

where g_x is the *conductance* of the channel for the ion x (note that the conductance is the inverse of the resistance, so $g_x = 1/R_x$ if R_x is the resistance). Generally, the conductances are described using non-linear functions because of the complex dependencies on the opening and closing of the associated channels, transmembrane potential and concentrations of ions. With the conductances arranged in parallel, the total current I_{ion} flowing through the ion

channels is given by $I_{ion} = \sum_x I_x$. I_{ion} is placed in parallel with the current flowing through the capacitance C_m of the cell membrane yielding the following expression for the total current I_m through the cell membrane over time t

$$I_m = C_m \partial_t u + I_{ion} \tag{2.1}$$

where ∂_t denotes the partial derivative with respect to time. The AP from a single isolated cell (meaning $I_m = 0$) can be reconstructed by solving the ordinary differential equation (ODE)

$$\partial_t u = -\frac{I_{ion} + I_{app}}{C_m} \tag{2.2}$$

where I_{app} represents an external stimulus that may be required to reach its threshold potential.

A broad range of ionic models have been developed to simulate the transmembrane currents I_{ion} and other cellular ionic processes generating cardiac AP. These models differ on the cell types (SA node, AV node, atrial, ventricular, Purkinje fibers models having different AP waveforms, see Fig. 2.4), and on the level of details and complexity used to describe the mechanism of the problem (either *biophysically-based* or *simplified phenomenological* models). *Biophysically-based* models represents the electrical activity of the cell by accurately modeling sub-cellular features such as specialized compartments and ion transfers through channels, pumps and exchangers. Some of the better known models are the Beeler-Reuter model of mammalian ventricular cell [62], Luo-Rudy II model of guinea pig ventricular cells [59], Courtemanche-Ramirez-Nattel (CRN) model of human atrial cells [63], Ten Tusscher-Noble-Noble-Panfilov of human ventricular cells [64]. A more comprehensive summary can be found at [7, 65, 66]. These models can be extremely realistic, but they feature high level of complexity, hence their numerical solutions in large-scale problems are often computationally demanding. As an alternative, *simplified phenomenological* ionic models have been proposed to provide an AP at a minimal computational cost. Typically, these models were formulated from biophysically-detailed ones considering only the most contributing sub-cellular processes to the AP. In spite of their computational affordability,

these approaches still preserve a reasonable level of accuracy. In this work, we will consider only simplified phenomenological models.

A general form of this class of models reads

$$\begin{cases} I_{ion} = \sum_{i=1}^{M} I_{x_i}(u, \mathbf{w}) \\ \mathrm{d}_t \mathbf{w} = \mathbf{g}(u, \mathbf{w}) \end{cases} \tag{2.3}$$

where M is the number of ion species; I_{x_i} the ionic current associated with the ion species x_i; $\mathbf{w}$ the vector of J gating variables $\{w_j\}_{j=1}^{J}$ that prescribe the dynamics of the various currents that make up I_{ion}; d_t represents the total derivative with respect to time. The dynamics of the transmembrane potential u is governed by equation (2.2). The gating variable w_j describes the probability that the j-th gate will be open to allow the flow of ions under different conditions, thus it operates in the range [0,1]. The general form of the conductance formulation for the ion x_i is given by

$$g_{x_i} = \bar{g}_{x_i} w_j$$

where $\bar{g}_{x_i}$ is the maximal conductance of the cell membrane to ion x_i. The time dependence of the gating variable w_j is typically described by an ODE

$$\mathrm{d}_t w_j = \alpha_{w_j}(1 - w_j) - \beta_{w_j} w_j \tag{2.4}$$

where α_{w_j} and β_{w_j} are known as *rate constants* and are in general voltage-dependent. When $w_j = 0$, the j-th gate is completely shut and no current associated with ion species x_i will flow. When $w_j = 1$, the j-th gate is completely open and current will flow based on the maximal conductance and the difference between the transmembrane and reversal potentials. Equation (2.4) can be reshaped as

$$\mathrm{d}_t w_j = \frac{w_{j,\infty} - w_j}{\tau_{w_j}} \tag{2.5}$$

where

$$w_{j,\infty} = \frac{\alpha_{w_j}}{\alpha_{w_j} + \beta_{w_j}}$$

$$\tau_{w_j} = \frac{1}{\alpha_{w_j} + \beta_{w_j}} \,.$$

Here, $w_{j,\infty}$ represents the steady-state behavior of the gate and τ_{w_j} the time constant associated with the activation or inactivation processes. In this description, the present state of the gate is expressed as a deviation from the steady state and the time constants dictates how long it will take for the gate to return to a steady-state in the absence of further perturbations. In other words, given an initial state, equation (2.5) describes an exponential approach to $w_{j,\infty}$ as time approaches infinity.

The simplest of phenomenological models is a polynomial that uses just one variable, therefore it can be solved easily and used in large-scale simulations. However, this model does not attempt to represent repolarization as it only tracks the depolarization phase. Thus, it is unsuitable to simulate reentry, an electrophysiologic mechanism occurring during repolarization responsible for the majority of clinically important arrhythmias. We will focus on models that can reproduce a full AP. In particular, we introduce four possible ionic models, the Rogers-McCulloch (RM) model [67], the Mitchell-Schaeffer (MS) model [68], the Fenton-Karma (FK) model [69], and the Minimal model (MM) [70].

The specific description of the time evolution of $\mathbf{w}$ and the associated nonlinear reaction function $I_{ion}(u, \mathbf{w})$ are provided according to the level of complexity inherent the specific model. In fact, RM, MS, FK and MM models are characterized by two, two, three and four variables respectively, with associated 1, 2, 3, and 3 ionic currents and 6, 5, 12, and 28 constitutive parameters.

The study and parametric characterization of ionic models relies on both local- and global-in-space/time features. The space and time course of the membrane voltage following an electrical stimulation, i.e. an elicited AP excitation wave, has been historically linked to specific measurable subfeatures of the AP wave, i.e. the APD and the Conduction Velocity (CV) (see [65] for details). In what follows, we will specifically use the restitution curve (RC), describing the dependence of APD on the pacing cycle length CL to adopt a convenient set of modeling parameters qualitatively reproducing the observed behavior.

State-of-the-art fitting genetic algorithms [71] may provide an accurate estimation of those parameters, but they are not the focus of the present Thesis. We empirically identify a good-enough approximation of AP shape and restitution curves. Such a choice allows us to prove the reliability of our estimation procedure also in presence of poor fitting power or high experimental error. We refer to Section 3.3.1 for more details about the calibration process. The model parameters are reported in Table 2.1.

The Rogers-McCulloch Model   The RM model derives from the FitzHugh-Nagumo (FHN) one [72, 73], which uses a cubic polynomial to describe the excitation and includes a gating variable so depolarization and repolarization can be captured. The FHN model yields only a coarse approximation of a typical cardiac AP, particularly in the plateau and repolarization phases. A better approximation is given by the RM model [74] which reads (only one gating variable $\mathbf{w} = [v]$)

$$\mathrm{d}_t v = \eta_2 (u/u_p - \eta_3 v) \tag{2.6}$$

where $I_{ion}(u, \mathbf{w})$ only consists of one term

$$I_{ion}(u, \mathbf{w}) = Gu(1 - u/u_{th})(1 - u/u_p) + \eta_1 uv \tag{2.7}$$

where u is in unit of mV. When u is greater than the threshold u_{th}, the upstroke of AP starts and drives the transmembrane potential to the plateau voltage u_p, otherwise the transmembrane potential tends to the resting potential $u = 0$. By the cubic description of I_{ion} the model captures the most relevant features of an AP, therefore it can be adopted with adjusted model parameters for patient-specific simulations, when the goal is more like a qualitative study. RM will be the model of choice to validate our estimation procedure in a 2D synthetic setting (Chapter 3, Section 3.2.1) and to test the performance of PGD and its application to Bayesian inversion in Chapter 4.

The Mitchell-Schaeffer Model   The MS model is a FitzHugh-Nagumo-like phenomeno-logical model [66] that qualitatively reproduces cardiac AP dynamics and restitution fea-

tures. Thanks to its simplicity, the model is numerically efficient. In addition, it is possible to carry out a comprehensive sensitivity analysis on its parameters; last but not least, it is possible to derive from the reaction-diffusion model an explicit formula for the restitution curve [68].

The MS reaction kinetics reads ($\mathbf{w} = [v]$):

$$\mathrm{d}_t v = (1-v)/\tau_{open} - (v/\tau_{close} + (1-v)/\tau_{open})H(u - u_{gate}) \tag{2.8}$$

where $I_{ion}(u, \mathbf{w})$ is given by the sum of two currents, inward and outward, respectively:

$$J_{in} = vu^2(1-u)/\tau_{in}, \qquad J_{out} = u/\tau_{out}, \tag{2.9}$$

with u dimensionless and $u \in [0,1]$; $H(\cdot)$ is the standard Heaviside step function. We will focus on MS model in Chapter 3 (Section 3.3) to perform experimental validation and its computational efficiency will be exploit in numerical simulation for clinical applications (Chapter 5).

The Fenton-Karma Model The FK model is a generalization of the original two-variable Karma model [75] able to properly approximate time course, restitution properties and spiral wave dynamics of the cardiac AP excitation wave [69, 76]. Although the model does not reproduce realistic AP shapes (in particular the spike-and-dome behavior of myocardial cells), it is complex enough to exhibit many of the characteristics of cardiac cells, but also simple enough that much of its behavior can be understood analytically.

Model equations are ($\mathbf{w} = [v, w]$)

$$\begin{aligned} \mathrm{d}_t v &= H(u_c - u)(1-v)/\tau_v^-(u) - H(u - u_c)v/\tau_v^+ \\ \mathrm{d}_t w &= H(u_c - u)(1-w)/\tau_w^- - H(u - u_c)w/\tau_w^+ \end{aligned} \tag{2.10}$$

where $I_{ion}(u, \mathbf{w})$ is given by the sum of three currents, fast inward J_{fi}, slow outward J_{so},

and slow inward J_{si}, respectively:

$$J_{fi} = -vH(u - u_c)(1 - u)(u - u_c)/\tau_d$$

$$J_{so} = uH(u_c - u)/\tau_o + H(u - u_c)/\tau_r \qquad (2.11)$$

$$J_{si} = -w(1 + \tanh(k(u - u_c^{si})))/2\tau_{si},$$

and the voltage-dependent time constant is

$$\tau_v^-(u) = H(u - u_v)\tau_{v1}^- + H(u_v - u)\tau_{v2}^-, \qquad (2.12)$$

with u dimensionless and $u \in [0, 1]$. The sigmoid function $1 + \tanh(k(u - u_c^{si})$ provides a smooth approximation of the Heaviside step function. We will carry out a comparison between FK and MS models for the experimental validation in terms of accuracy of the reconstruction of the optical mapping data in Chapter 3 (Section 3.3).

The Minimal Model   The MM model is based on the FK one with the addition of a fourth variable to adjust the inward current to reproduce the spike-and-dome morphology for myocardial cells. It provides a description of the human and animal ventricular cells reproducing in detail experimentally measured characteristics of action potentials. These characteristics are both at cell and tissue-level including: action potential amplitude and morphology, upstroke conduction velocity (CV) of the excitation wave, APD and CV restitution curves, spatio-temporal alternans and spiral waves as dynamics fundamental features of cardiac arrhythmias [70]. Moreover, it can be fitted to reproduce the dynamics of other - more complex - physiological models, yet it is computationally more efficient. For $\mathbf{w} = [v, w, s]$, it reads

$$d_t v = (1 - H(u - \theta_v))(v_\infty - v)/\tau_v^- - H(u - \theta_v)v/\tau_v^+$$

$$d_t w = (1 - H(u - \theta_w))(w_\infty - w)/\tau_w^- - H(u - \theta_w)w/\tau_w^+ \qquad (2.13)$$

$$d_t s = ((1 + \tanh(k_s(u - u_s)))/2 - s)/\tau_s$$

where the three currents are given by

$$J_{fi} = -vH(u - \theta_v)(u - \theta_v)(u_u - u)/\tau_{fi}$$

$$J_{si} = -H(u - \theta_w)ws/\tau_{si} \qquad (2.14)$$

$$J_{so} = (u - u_o)(1 - H(u - \theta_w))/\tau_o + H(u - \theta_w)/\tau_{so}$$

and the voltage-dependent time constants are

$$\tau_v^- = (1 - H(u - \theta_v^-))\tau_{v1}^- + H(u - \theta_v^-)\tau_{v2}^-$$

$$\tau_w^- = \tau_{w1}^- + (\tau_{w2}^- - \tau_{w1}^-)(1 + \tanh(k_w^-(u - u_w^-)))/2$$

$$\tau_{so}^- = \tau_{so1}^- + (\tau_{so2}^- - \tau_{so1}^-)(1 + \tanh(k_{so}(u - u_{so})))/2$$

$$\tau_s = (1 - H(u - \theta_w))\tau_{s1} + H(u - \theta_w)\tau_{s2} \qquad (2.15)$$

$$\tau_o = (1 - H(u - \theta_o))\tau_{o1} + H(u - \theta_o)\tau_{o2}$$

$$v_\infty = 1 - H(u - \theta_v^-)$$

$$w_\infty = (1 - H(u - \theta_o))(1 - u/\tau_{w\infty}) + H(u - \theta_o)w_\infty^*.$$

with u dimensionless and $u \in [0, 1.5]$. u can be expressed in unit of mV by the following scaling $u_{mV} = 85.7u - 84$. MM model will be used to perform synthetic validation in Chapter 3 in a 3D setting (Section 3.2.2) and in the case of more realistic physical properties and 2D geometry of canine tissue (Section 3.2.4).

2.2.2 Tissue modeling

When constructing mathematical models for electrical activity in the tissue, one possible approach would be to describe the domain as a set of separate cells, and couple them together using mathematical formulations for the known coupling mechanisms. However, using this strategy would be feasible only for very small samples of tissue because of the prohibitively large number of cells. Hence, we consider a continuous approximations of the tissue, in the sense that a quantity is defined as the average over a small but multicellular volume. In this way, we avoid the difficulties of modeling the discrete nature of the tissue. Following this approach, the tissue is represented by two domains, the *intracellular* and the *extracellular*

RM parameters					
G	u_{th}	u_p	η_1	η_2	η_3
1.5 Ω^{-1}cm^{-2}	13 mV	100 mV	4.4 Ω^{-1}cm^{-2}	0.012	1

MS parameters				
τ_{in}	τ_{out}	τ_{close}	τ_{open}	u_{gate}
0.3	10	69	220	0.13

FK parameters											
u_c	τ_d	τ_o	τ_r	k	u_c^{si}	τ_{si}	τ_v^+	τ_w^-	τ_w^+	τ_{v1}^-	τ_{v2}^-
0.13	0.1724	12.5	130	10	0.85	127	1.62	80	1020	38.2	38.2

MM parameters									
u_o	u_u	θ_v	θ_w	θ_v^-	θ_o	τ_{v1}^-	τ_{w2}^-	k_w^-	u_w^-
0	1.58	0.3	0.015	0.015	0.006	60	20	65	0.03
τ_w^+	τ_{fi}	τ_{o1}	τ_{o2}	k_{so}	u_{so}	τ_{s1}	τ_{s2}	k_s	u_s
280	0.11	6	6	2	0.65	2.7342	3	2.0994	0.9087
	τ_{si}	τ_{v2}^-	τ_v^+	τ_{w1}^-	τ_{so1}	τ_{so2}	$\tau_{w\infty}$	w_∞^*	
	2.8723	1150	1.4506	70	43	0.2	0.07	0.94	

Table 2.1: Ionic models parameters tuned to qualitatively reproduce the time course of the AP signal and the restitution curves. More details about the tuning process are provided in Section 3.3.1. Time is in unit of ms.

ones, so that the effects of the potential difference across the membrane can be included. Both domains are assumed to be continuous, and they both fill the complete volume of the heart muscle. The justification for viewing the intracellular space as continuous is that the muscle cells are connected via so-called *gap junctions*. These are small channels embedded in the cell membrane, which form direct contact between the internals of two neighboring cells. Because of the gap junctions, substances such as ions or small molecules may pass directly from one cell to another, without entering the space between the two cells (the extracellular domain).

The Bidomain Model   This continuum (volume-averaged) approach to describe the tissue leads to the *Bidomain Model*, considered as the most physiologically founded description of cardiac excitation at tissue level. It was first proposed in [77] and then applied to cardiac tissue in [78, 79]. Similarly to what has been done in Section 2.1.2, we define the electrical potentials u_i and u_e in the intracellular and extracellular spaces respectively which at each point must be viewed as quantities averaged over a small volume. An important consequence of these definitions is that every point in the heart muscle is assumed to be

in both the intracellular and the extracellular domains, and consequently is assigned both an intracellular and an extracellular potential. Moreover, we can define the transmembrane potential u at every point in the tissue as $u = u_i - u_e$. Other assumptions are [7]

- there is no direct current flow between the intracellular and extracellular domains;

- the current flows between the extracellular and extramyocardial (for example the torso) spaces through the boundary of the cardiac domain;

- the quasi-static assumption [80] is adopted, i.e., any change over time of electric and magnetic fields generated inside the body are omitted.

Therefore, the current densities in the two domains are given by

$$
\begin{aligned}
\mathbf{J}_i &= -\boldsymbol{\sigma}_i \nabla u_i \\
\mathbf{J}_e &= -\boldsymbol{\sigma}_e \nabla u_e
\end{aligned}
\tag{2.16}
$$

where $\mathbf{J}_i$ is the intracellular and $\mathbf{J}_e$ the extracellular current densities; $\boldsymbol{\sigma}_i$ and $\boldsymbol{\sigma}_e$ the conductivity tensors in the two domains, in general function of the local spatial coordinates; ∇ the spatial gradient operator. Any current that leaves one of the intra- and extracellular spaces must across the membrane and flow into the other domain. This means the change of current density in each domain should be equal in magnitude and opposite in sign. Furthermore, by the conservation of current densities, the change of current density in each domain should be equal to the current I_m flowing across the membrane. These relations are expressed as

$$
-\nabla \cdot (\boldsymbol{\sigma}_e \nabla u_e) = \nabla \cdot (\boldsymbol{\sigma}_i \nabla u_i) = \beta I_m
\tag{2.17}
$$

where β is the surface-to-volume ratio of the cell membrane; $\nabla\cdot$ the divergence operator. The current flow across the membrane I_m can be described as in equation (2.1)

$$
I_m = C_m \partial_t u + I_{ion}
\tag{2.18}
$$

where the term I_{ion} would be given by a coupled ionic model. Combining the equations (2.17) and (2.18), we obtain the Bidomain model in the symmetric form as

$$
\begin{cases}
\beta C_m \partial_t u = \nabla \cdot (\boldsymbol{\sigma}_i \nabla u_i) - \beta I_{ion}(u, \mathbf{w}) \\
-\beta C_m \partial_t u = \nabla \cdot (\boldsymbol{\sigma}_e \nabla u_e) + \beta I_{ion}(u, \mathbf{w}) \quad \text{in } Q \\
\mathrm{d}_t \mathbf{w} = \mathbf{g}(u, \mathbf{w})
\end{cases}
\tag{2.19}
$$

completed by the following boundary and initial conditions

$$
\begin{cases}
\boldsymbol{\sigma}_i \nabla u_i \cdot \mathbf{n} = 0, \quad \boldsymbol{\sigma}_e \nabla u_e \cdot \mathbf{n} = 0 \qquad \text{on } \partial Q \\
u(\mathbf{x}, 0) = u_0(\mathbf{x}), \quad \mathbf{w}(\mathbf{x}, 0) = \mathbf{w}_0(\mathbf{x}) \quad \text{in } \Omega \,.
\end{cases}
\tag{2.20}
$$

Here, $Q = \Omega \times [0, T]$; $\partial Q = \partial \Omega \times [0, T]$; $\Omega \subset \mathbb{R}^d$ ($d = 2$ or 3) is a bounded domain; $[0, T]$ a fixed time interval; $\mathbf{x}$ the spatial coordinates; $\mathbf{n}$ the outward unit normal vector on the boundary $\partial \Omega$. The boundary conditions $(2.20)_1$ are of Neumann-type, usually adopted in the present context [7]. In physical terms, they try to mimic an insulated tissue. From a mathematical point of view, it is well known that Neumann-type conditions minimize the sensitivity of arbitrary data on the simulation results [81], though they yield an approximation of the complex phenomenology. It is possible for an external stimulus current to be applied to either domain (I_{si} and I_{se}) so that

$$
\nabla \cdot (\boldsymbol{\sigma}_i \nabla u_i) = \beta I_m - I_{si}
$$

$$
-\nabla \cdot (\boldsymbol{\sigma}_e \nabla u_e) = \beta I_m + I_{se} \,.
$$

The resulting Bidomain model reshaped in a parabolic-elliptic form [7] in terms of the transmembrane potential u and extracellular potential u_e reads

$$
\begin{cases}
\beta C_m \partial_t u = \nabla \cdot (\boldsymbol{\sigma}_i \nabla u) + \nabla \cdot (\boldsymbol{\sigma}_i \nabla u_e) - \beta I_{ion}(u, \mathbf{w}) + I_{si} & \text{in } Q \\
-\nabla \cdot (\boldsymbol{\sigma}_i \nabla u) - \nabla \cdot \big((\boldsymbol{\sigma}_i + \boldsymbol{\sigma}_e)\nabla u_e\big) = I_{si} - I_{se} & \text{in } Q \\
\mathrm{d}_t \mathbf{w} = \mathbf{g}(u, \mathbf{w}) & \text{in } Q
\end{cases}
\tag{2.21}
$$

with boundary and initial conditions

$$
\begin{cases}
\boldsymbol{\sigma}_i \nabla u \cdot \mathbf{n} + \boldsymbol{\sigma}_i \nabla u_e \cdot \mathbf{n} = 0, \quad \boldsymbol{\sigma}_e \nabla u_e \cdot \mathbf{n} = 0 \quad \text{on } \partial Q \\
u(\mathbf{x}, 0) = u_0(\mathbf{x}), \quad \mathbf{w}(\mathbf{x}, 0) = \mathbf{w}_0(\mathbf{x}) \qquad \text{in } \Omega .
\end{cases}
\tag{2.22}
$$

u is uniquely defined, while u_i and u_e are determined up to the same additive time-dependent constant. This common constant is related to the choice of the reference potential and it is usually selected so that u_e has zero average on Ω, i.e., $\int_\Omega u_e(\mathbf{x}) \, d\mathbf{x} = 0$. By applying the divergence theorem to the elliptic equation $(2.21)_2$, we require the compatibility condition for the Bidomain system to be solvable: $\int_\Omega (I_{si} - I_{se}) \, d\mathbf{x} = 0$. An extensive well-posedness analysis for the system of the macroscopic Bidomain model coupled with a microscopic cellular model can be found in [82, 83].

A relevant issue for the purpose of this Thesis is the representation of the conductivity tensor in the context of a complex orthotropic three-dimensional tissue. We refer to the cardiac fibers principal directions [7, 84]. In detail, let $(\mathbf{a_l}, \mathbf{a_t}, \mathbf{a_n})$ be the orthonormal unit vectors related to the structure of the myocardium with $\mathbf{a_l}$ the longitudinal fiber direction, $\mathbf{a_t}$ and $\mathbf{a_n}$ the orthogonal directions to the fiber in the sheet and orthogonal to the sheet, respectively. Accordingly, we can decompose the conductivity tensors as:

$$
\boldsymbol{\sigma}_j(\mathbf{x}) = \sigma_{jl}(\mathbf{x}) \mathbf{a_l} \mathbf{a_l}^T + \sigma_{jt}(\mathbf{x}) \mathbf{a_t} \mathbf{a_t}^T + \sigma_{jn}(\mathbf{x}) \mathbf{a_n} \mathbf{a_n}^T,
$$

where $j = i, e$ and $\sigma_{jl}, \sigma_{jt}, \sigma_{jn}$ denote the longitudinal-, tangential- and normal-to-the-fiber conductivities, respectively.

In the following, we assume that the tissue can be conveniently described as a transverse isotropic material (i.e. $\sigma_{jt}(\mathbf{x}) = \sigma_{jn}(\mathbf{x})$) and the tensor simplifies to

$$
\boldsymbol{\sigma}_j(\mathbf{x}) = \sigma_{jt}(\mathbf{x}) \mathbf{I} + (\sigma_{jl}(\mathbf{x}) - \sigma_{jt}(\mathbf{x})) \mathbf{a_l} \mathbf{a_l}^T,
\tag{2.23}
$$

where $\mathbf{I}$ is the $d \times d$ identity tensor.

An accurate patient-specific description of the fiber structure and the conductivity tensors is crucial in clinical applications. The fiber orientation can be obtained *in vitro* using

histology [57] or imaging technique like diffusion tensor MRI [85–87]. These procedures are effective *ex vivo*, but tracking the fiber direction in moving heart is highly complex and the imaging techniques usually take long acquisition time, which makes a precise representation of the myocardium fiber quite challenging. Some *in vivo* real-time techniques to map myofiber orientation have been analyzed [88], but further investigation is still needed in this direction. Numerically, simplified models are used by mapping an analytical map on idealized geometries to real left ventricles [89, 90]. In this Thesis, we will focus on the estimation of cardiac conductivities assuming the fiber orientation known a priori.

The Bidomain model yields the most complete description of electrical potential in the cardiac tissue. However, it is computationally demanding because of the involvement of different time and space scales. In fact, a normal heartbeat can last on the order of one second, while the AP dynamics varies abruptly in few milliseconds (see Phase 0 in Fig. 2.2). Moreover, potential gradients are localized in a small area of few millimeters square, whereas simulations for clinical applications involve portions of cardiac tissue with sizes of the order of centimeters. Thus, spatial discretization has to be on the order of a tenth of millimeter. Therefore, Bidomain simulations with realistic 3D models may feature discrete problems with more than $O(10^7)$ that need to be solved for thousands of time steps.

Another drawback of the Bidomain model emerges in its numerical discretization. In fact, $(2.19)_{1,2}$ can be written in matrix form as

$$
\beta C_m \begin{bmatrix} 1 & -1 \\ -1 & 1 \end{bmatrix} \frac{\partial}{\partial t} \begin{bmatrix} u_i \\ u_e \end{bmatrix} = \begin{bmatrix} \nabla \cdot (\boldsymbol{\sigma}_i \nabla u_i) \\ \nabla \cdot (\boldsymbol{\sigma}_e \nabla u_e) \end{bmatrix} - \beta \begin{bmatrix} I_{ion}(u, \mathbf{w}) \\ -I_{ion}(u, \mathbf{w}) \end{bmatrix}.
$$

The vector of time derivatives is multiplied by a singular matrix, thus the Bidomain system is said to be *degenerate*. This leads a severe ill conditioning of the matrix associated with the fully discrete approximation and so its numerical solution requires significant computational effort.

The Monodomain Model   To reduce the computational complexity related to the Bidomain solution, a simplified *Monodomain Model* has been proposed [91, 92]. It relies on the assumption that the anisotropy of the intracellular and extracellular spaces is the same, i.e.,

the conductivity in the extracellular space is proportional to the intracellular conductivity

$$\boldsymbol{\sigma}_e = \lambda \boldsymbol{\sigma}_i \tag{2.24}$$

where λ is a scalar, representing the ratio between the conductivity of the intra- and extracellular spaces. Substituting equation (2.24) into equation $(2.21)_{1,2}$, we replace the two equations of the Bidomain model with a single parabolic reaction-diffusion PDE for the transmembrane potential u

$$\beta C_m \partial_t u = \nabla \cdot \Big(\frac{\lambda}{1+\lambda} \boldsymbol{\sigma}_i \nabla u \Big) - \beta I_{ion}(u, \mathbf{w}) + I_{app}.$$

If we introduce an effective conductivity $\boldsymbol{\sigma} = \lambda/(1+\lambda)\boldsymbol{\sigma}_i$ and $I_{app} = \lambda/(\lambda+1)I_{si} + 1/(\lambda+1)I_{se}$, we obtain the Monodomain model of cardiac excitation as

$$\begin{cases} \beta C_m \partial_t u = \nabla \cdot (\boldsymbol{\sigma} \nabla u) - \beta I_{ion}(u, \mathbf{w}) + I_{app} & \text{in } Q \\ \mathrm{d}_t \mathbf{w} = \mathbf{g}(u, \mathbf{w}) & \text{in } Q \end{cases} \tag{2.25}$$

completed by the boundary and initial conditions

$$\begin{cases} \boldsymbol{\sigma} \nabla u \cdot \mathbf{n} = 0 & \text{on } \partial Q \\ u(\mathbf{x}, 0) = u_0(\mathbf{x}), \quad \mathbf{w}(\mathbf{x}, 0) = \mathbf{w}_0(\mathbf{x}) & \text{in } \Omega. \end{cases} \tag{2.26}$$

The conductivity tensor $\boldsymbol{\sigma}$ is decomposed with respect to the cardiac fibers principal directions as done in equation (2.23). The Monodomain equation $(2.25)_1$ can be reshaped as

$$\partial_t u = \nabla \cdot (\mathbf{D} \nabla u) - \frac{I_{ion}(u, \mathbf{w})}{C_m} + \tilde{I}_{app} \tag{2.27}$$

where $\mathbf{D} = \boldsymbol{\sigma}/(\beta C_m)$ and $\tilde{I}_{app} = I_{app}/(\beta C_m)$.

The Monodomain model is a significant simplification of the original Bidomain equations, with advantages both for mathematical analysis and computation [93], and it has been intensively used in clinical applications. If there is no injection of current into the extracellular space, descriptions of AP propagation provided by Monodomain and Bidomain

models are close to each other even under the condition of unequal anisotropy ratio in the extracellular and intracellular spaces [91]. Moreover, the Monodomain model may serve as a powerful auxiliary tool to efficiently solve the Bidomain system [90, 94, 95].

However, the Bidomain assumption of separation of intracellular and extracellular spaces is necessary to accommodate the injection of current into the extracellular space during external stimulation and defibrillation [96–98]. During defibrillation, the unequal anisotropy of the intracellular and extracellular spaces plays an important role in generating virtual electrodes that are essential for successful defibrillation [99, 100].

The Eikonal and Graph-based models A further reduction of the computational complexity of the simulation of the excitation phase has been achieved by solving simplified kinematic models, *eikonal* and *graph-based models*, describing the motion of the excitation wavefront, instead of the time dependent voltage propagation. These models are based on the assumption that the speed of propagation varies more slowly and over much larger spatial scales than the transmembrane potential. The wavefront motion can be described by the *activation time* in the point $\mathbf{x}$ defined as the time at which the wavefront passes through the point $\mathbf{x}$. A governing equation for the activation time is an eikonal equation [66, 101], a static non-linear PDE explicitly derived from the previous models. On the other hand, graph-based models [102, 103] represent the cardiac tissue as a connected graph consisting of spatial nodes connected by edges. Every edge in the graph is assigned a cost, based on the time it takes the activation wavefront to traverse the corresponding path between two points in the tissue. Activation is initiated at one or several nodes, corresponding to the point or points where the tissue is initially stimulated. From there, the activation travels from node to node along the edges of the graph. At each node, an estimate of its activation time can be obtained by finding the accumulated cost of all edges traversed in order to reach it along a specific path. Typically, a very large number of paths can be taken between two nodes in the graph, so in order to obtain the best estimate of the activation time, the path with the lowest cost needs to be found.

Since these models only simulate the time at which the excitation wavefront reaches a given point, they lead to much faster computations, considering also that a coarse spatial

resolution is sufficient in these simulations. However, one important limitation of eikonal and graph-based models is that they only describe the time of depolarization disregarding the state of repolarization and refractoriness of cardiac cells. Those phenomena are very important for the simulation of arrhythmias. Some improvements have been proposed to include periodic arrhythmia [104] and capture the main characteristics of cardiac electrophysiology propagation (anisotropy, refractory period, repolarization, restitution curve) [52,105]. However, the Bidomain and Monodomain models are still considered the most appropriate and sophisticated approaches to study complex pathological conditions such as arrhythmias.

We will extensively use these models throughout this Thesis. In particular, in Chapter 3, the Bidomain model will be considered to perform synthetic validation and numerical sensitivity analysis of the estimation procedure (Section 3.2.1,3.2.2). Then, we will successfully use the Monodomain model as a surrogate to the Bidomain problem in Section 3.2.3. Due to its computational efficiency and accuracy in reconstructing Bidomain potential, the Monodomain equations will be then the model of choice to validate our parameter estimation method with optical mapping data in Section 3.3. We will continue focusing on the Monodomain problem to investigate a reduced-order modeling technique in Chapter 4. Last but not least, the Monodomain formulation will be used in Chapter 5 for simulating ventricular tachycardia, together with a parameter personalization performed with a graph-based model.

Chapter 3

The Inverse Conductivity Problem and its Validation

As mentioned in Chapter 1, one of the problems in using mathematical models for electro-physiology in clinics is the patient-specific customization. Specifically, in this Chapter we are concerned with the estimation of the cardiac conductivities (i.e., the Bidomain tensors $\boldsymbol{\sigma}_i$ and $\boldsymbol{\sigma}_e$ in (2.21), and the Monodomain one $\boldsymbol{\sigma}$ in (2.25)) for a specific individual. Far from being trivial, this problem has been addressed in pioneering works considering experimental quantification [106] or other techniques [107–109]. These strategies led to different ranges of possible values (see Table 3.1) with no common agreement on what the actual values are or should be used for simulations [110].

Direct computational methods based on multiscale arguments have been explored to obtain an estimate of cardiac conductivities [112–114], however they depend on empirical

Param $\downarrow$ Ref $\rightarrow$	Clerc [107]	Roberts [108]	Roberts [109]
σ_{il}	1.70	2.80	3.40
σ_{el}	6.20	2.20	1.20
σ_{it}	0.19	0.26	0.60
σ_{et}	2.40	1.30	0.80
σ_{il}/σ_{it}	8.95	10.77	5.67
σ_{el}/σ_{et}	2.58	1.69	1.50
σ_{il}/σ_{el}	0.27	1.27	2.83
σ_{it}/σ_{et}	0.08	0.20	0.75

Table 3.1: Conductivity values for the Bidomain model proposed in [111] ([mS/cm]).

values. More recently, *variational data assimilation* approaches [26, 111, 115] have been proposed to convert possible transmembrane and extra-cellular potential measures into an estimation of the conductivities. The mismatch between available data in specific measurement sites and the computed solution is minimized by the choice of the conductivity tensors, under the constraint of the Bidomain equations. These strategies can lead to viable procedures also in clinics, as potential on the heart muscle may be measured in vivo too. However, the variational procedure proposed in [111, 115], based on classical least-square approach, is computationally intensive and requires analysis, refinement and validation. On the other hand, the methodology presented in [26] following a derivative-based approach was proven to be more accurate and robust. The procedure was however tested only *in silico* and considering uniform conductivities.

The objective of this Chapter is to extend and throughly validate the approach in [26] for solving the estimation problem, called *Inverse Conductivity Problem* (ICP), using experimental data. In view of the validation with real data, there is however the need of understanding some practical sensitivity aspects of the method. As a theory of *identifiability* is missing (i.e., the proof that the map linking the conductivities to the measures is injective), we need to assess the numerical sensitivity of the algorithm to different experimental designs on both simplified and real geometries. In this Chapter, we test the accuracy of the conductivity estimate in a number of in silico realistic test cases to inform the experimental procedure for the validation. This task is achieved in the first part of the Chapter referring to the Bidomain model and the conductivity tensors are assumed uniform in space, i.e., the tissue is homogeneous. The design of future experiments aiming to validate this approach, especially on human heart, will strongly rely on these results. For the purpose of reducing the computational time of parameter estimation, we extend the methodology to consider the Monodomain model and experimentally explore the possibility of using the Monodomain formulation as a *predictor* of the conductivities estimates for the Bidomain equations. This means that we solve the ICP for the Monodomain model and check how the solution is informative for the Bidomain conductivities. We will see that estimated Monodomain conductivity constitutes a good surrogate to Bidomain tensors estimates.

Because of the intrinsic heterogeneity of the cardiac tissue, the assumption of uniform

conductivities is quite unrealistic. Moreover, in clinically relevant applications, discontinuities in the conductivity fields are expected because of the presence of scars or slow conducting areas perturbing the normal electrical propagation. Therefore, in the second part of the Chapter, we consider the more realistic case of spatial dependent conductivity tensors, i.e., the tissue is heterogeneous. First, we assess the accuracy of the methodology for the estimation of Monodomain conductivity in a pathological tissue featuring a scar. Finally, we perform an extensive experimental validation on real canine data.

The Chapter is organized as follows. In Section 3.1, we introduce the ICP and the variational formulation using both Bidomain and Monodomain models. We then present the numerical approximation. Section 3.2 analyzes several synthetic settings for a verification of the procedure in view of real validation. Finally, in Section 3.3, we test the problem with experimental data of canine ventricles, showing that our numerical solution does actually provide a reliable estimation of the conductivities also in an experimental setting.

The content of this Chapter is reflected by the two papers [116] and [117]. Although the content is already published in those two papers, in this Chapter we decided to synthesize the self-standing presentation there, to make the reading more fluent.

3.1 The Inverse Conductivity Problem

In this Section, the theoretical framework and the numerical approximation of the ICP for conductivity estimation is presented. We describe the problem using the Bidomain model following [26] and we extend it to include the Monodomain formulation as well as spatial-dependent conductivities.

3.1.1 The variational formulation of the ICP

For the sake of generality, we postulate that the conductivity tensors belong to the admissible functional space

$$C_{ad} = \{\boldsymbol{\sigma} \in \mathbf{H}^1(\Omega) : \boldsymbol{\sigma}(\mathbf{x}) \in [\tilde{m}, \tilde{M}]^{2d}, \forall \mathbf{x} \in \Omega\} \tag{3.1}$$

where $\mathbf{H}^1(\Omega) \equiv (H^1(\Omega))^{2d}$ and $\tilde{m}$ and $\tilde{M}$ are positive constants. Notice that, for the solution of the forward problem, it would suffice assuming the conductivities as bounded functions ($L^\infty(\Omega)$) of the space variables (e.g., piecewise constant). The same admissible space works for the inverse problem when using a regularization based on the values of the conductivities and not on their (space) derivatives, as done in [26]. However, here we need additional regularization terms, so we restrict our admissible space to $\mathcal{C}_{ad}$.

Assuming the tissue axially isotropic, the conductivity tensors can be represented as in equation (2.23). In general, the conductivities are spatial dependent, meaning the tissue is heterogeneous. In case of homogeneous tissue, the tensors can be characterized by the conductivity parameters $\boldsymbol{\sigma} = (\sigma_{il}, \sigma_{el}, \sigma_{it}, \sigma_{et})$ for the Bidomain equations, and $\boldsymbol{\sigma} = (\sigma_{ml}, \sigma_{mt})$ for the Monodomain model.

The *Bidomain Inverse Conductivity Problem* (BICP) [26] aims to find the conductivity tensors that minimize the mismatch between available potential measures and the corresponding solution of the Bidomain system. This means that we find the tensors $\{\boldsymbol{\sigma}_i, \boldsymbol{\sigma}_e\} \in C_{ad}$ minimizing the misfit functional

$$\mathcal{J}(\boldsymbol{\sigma}_i, \boldsymbol{\sigma}_e) = \frac{1}{2} \int_0^T \int_{\Omega_{obs}} \left[(u(\boldsymbol{\sigma}_i, \boldsymbol{\sigma}_e) - u_{meas})^2 + (u_e(\boldsymbol{\sigma}_i, \boldsymbol{\sigma}_e) - u_{e,meas})^2 \right] d\mathbf{x} dt + \mathcal{R}(\boldsymbol{\sigma}_i, \boldsymbol{\sigma}_e)$$

(3.2)

subject to the Bidomain equations completed by an appropriate ionic model (2.21). Here, u_{meas} and $u_{e,meas}$ denote the experimental data measured on the observation domain $\Omega_{obs} \subset \Omega$. They can be generated in a synthetic setting, and, more interestingly, obtained *in vitro* using voltage optical mapping [97, 118, 119] or *in vivo* by back-mapping body surface potentials [120, 121] possibly by potential reconstruction from electrocardiogram phase analysis of standard gated SPECT [122]. $\mathcal{R}$ denotes a Tikhonov-like regularization term that reads

$$\mathcal{R}(\boldsymbol{\sigma}_i, \boldsymbol{\sigma}_e) = \frac{\alpha_1}{2} \left(\|\boldsymbol{\sigma}_i - \boldsymbol{\sigma}_{i,mean}\|^2 + \|\boldsymbol{\sigma}_e - \boldsymbol{\sigma}_{e,mean}\|^2 \right) + \frac{\alpha_2}{2} \left(\|\nabla \boldsymbol{\sigma}_i\|^2 + \|\nabla \boldsymbol{\sigma}_e\|^2 \right) \quad (3.3)$$

where α_1, α_2 are regularization coefficients weighting the impact of the regularization on the minimization procedure; $\boldsymbol{\sigma}_{\cdot,mean}$ an average of available conductivity values from the

literature; $\|\cdot\|$ the L^2-norm. The term weighting $\|\nabla\boldsymbol{\sigma}.\|^2$ controls the smoothness of the conductivity field in case of heterogeneous tissue, i.e., conductivities are spatial dependent.

This is a minimization problem constrained by a system of partial differential equations (PDEs), that can be approached in different ways [123–125]. We purse here an approach based on the Lagrange multipliers. For the sake of generality, we consider the abstract problem: minimize the functional $\mathcal{J}(\sigma) = \mathcal{J}(u(\sigma), \sigma)$ under the constraint $F(u, \sigma) = 0$. Following the common terminology, we call u the *state variable* and σ the *control variable*. To find the minimum, we totally differentiate this functional with respect to the control variable. By a direct application of the chain rule in the differentiation, we can include the constraint in the minimization process. However, in the present problem the constraint is implicitly stated as a set of partial differential equations and its explicit introduction in the minimization process may be troublesome. Therefore, we introduce the Lagrangian functional $\mathcal{L}(u, \sigma, \lambda) = \mathcal{J}(u, \sigma) - \lambda^* F(u, \sigma)$ where λ is the *adjoint variable* or *Lagrange multiplier*. The star $*$ reminds that the term $\lambda^* F(u, \sigma)$ is in general a *duality* between the functional space of multipliers and the one of state variables - reducing to a classical product for classical function minimization problems. Following this approach, the BICP Lagrangian functional reads

$$
\begin{aligned}
\mathcal{L}(u, u_e, &\mathbf{w}, \boldsymbol{\sigma}_i, \boldsymbol{\sigma}_e, p, q, \mathbf{r}) = \mathcal{J}(\boldsymbol{\sigma}_i, \boldsymbol{\sigma}_e) \\
&- \int_0^T \int_\Omega q\Big(\beta C_m \partial_t u - \nabla \cdot (\boldsymbol{\sigma}_i \nabla u) - \nabla \cdot (\boldsymbol{\sigma}_i \nabla u_e) + \beta I_{ion}(u, \mathbf{w}) - I_{si}\Big)\, d\mathbf{x}dt \\
&- \int_0^T \int_\Omega p\Big(-\nabla \cdot (\boldsymbol{\sigma}_i \nabla u) - \nabla \cdot ((\boldsymbol{\sigma}_i + \boldsymbol{\sigma}_e)\nabla u_e) - I_{si} + I_{se}\Big)\, d\mathbf{x}dt \\
&- \int_0^T \int_\Omega \mathbf{r} \cdot \Big(\mathrm{d}_t \mathbf{w} - \mathbf{g}(u, \mathbf{w})\Big)\, d\mathbf{x}dt
\end{aligned}
\tag{3.4}
$$

where $q(\mathbf{x}, t)$, $p(\mathbf{x}, t)$ and $\mathbf{r}(\mathbf{x}, t)$ are the Lagrange multipliers. We denote $V = H^1(\Omega)$, $H = L^2(\Omega)$, $U = V/\mathbb{R}$. The quotient space is used because the solution u_e is determined up to an additive constant (see Section 2.2.2). Then, $(u, q) \in (L^2(0, T; V))^2$, $(u_e, p) \in (L^2(0, T; U))^2$, $(\mathbf{w}, \mathbf{r}) \in (L^2(0, T; H))^{2g}$, where g is the number of gating variables of the ionic model; $(I_{si}, I_{se}) \in (L^2(0, T; V^*))^2$, where V^* denotes the dual space of V. According to this approach [123], the solution is obtained by finding the critical points of the functional

with respect to the state variables, the Lagrange multipliers and the control variables. This leads to the so called Karush-Kuhn-Tucker (KKT) system. In particular, it is promptly verified that the (Gateaux) differentials with respect to the Lagrange multipliers gives the constraint equations $F(u, \sigma) = 0$, i.e. the Bidomain problem (2.21) (with the appropriate ionic model). Setting the partial derivatives $\partial_u \mathcal{L}$, $\partial_{u_e} \mathcal{L}$ and $\partial_\mathbf{w} \mathcal{L}$ equal to zero, we construct the *adjoint equations*

$$
\begin{cases}
-\beta C_m \partial_t q = \nabla \cdot (\boldsymbol{\sigma}_i \nabla q) + \nabla \cdot (\boldsymbol{\sigma}_i \nabla p) - \partial_u \mathbf{g} \cdot \mathbf{r} - \beta \partial_u I_{ion}(u, \mathbf{w}) q \\
\qquad \qquad + (u - u_{meas}) \chi_{\Omega_{obs}} & \text{in } Q \\[2mm]
-\nabla \cdot (\boldsymbol{\sigma}_i \nabla q) - \nabla \cdot ((\boldsymbol{\sigma}_i + \boldsymbol{\sigma}_e) \nabla p) = (u_e - u_{e,meas}) \chi_{\Omega_{obs}} & \text{in } Q \\[2mm]
\mathrm{d}_t \mathbf{r} = \partial_\mathbf{w} \mathbf{g} \cdot \mathbf{r} + \beta \partial_\mathbf{w} I_{ion}(u, \mathbf{w}) q & \text{in } Q \\[2mm]
(\boldsymbol{\sigma}_i \nabla p + \boldsymbol{\sigma}_i \nabla q) \cdot \mathbf{n} = 0, \quad \boldsymbol{\sigma}_e \nabla p \cdot \mathbf{n} = 0 & \text{on } \partial Q \\[2mm]
q(\mathbf{x}, T) = 0, \quad \mathbf{r}(\mathbf{x}, T) = \mathbf{0} & \text{in } \Omega
\end{cases}
\tag{3.5}
$$

where $\chi_{\Omega_{obs}}$ is the indicator function of the observation domain Ω_{obs}. Notice that this problem is backward in time. Finally, we obtain [26] the so called *optimality conditions*

$$
\begin{aligned}
\frac{\mathcal{D}\mathcal{J}}{\mathcal{D}\sigma_{ik}} &= \frac{\partial \mathcal{L}}{\partial \sigma_{ik}} = -\int_0^T \mathbf{a_k} \mathbf{a_k}^T \nabla(u + u_e) \cdot \nabla(p + q)\, dt + \frac{\partial \mathcal{R}}{\partial \sigma_{ik}} = 0 \\
\frac{\mathcal{D}\mathcal{J}}{\mathcal{D}\sigma_{ek}} &= \frac{\partial \mathcal{L}}{\partial \sigma_{ek}} = -\int_0^T \mathbf{a_k} \mathbf{a_k}^T \nabla u_e \cdot \nabla p\, dt + \frac{\partial \mathcal{R}}{\partial \sigma_{ek}} = 0
\end{aligned}
\tag{3.6}
$$

where $\mathbf{a_k}$ represents the fiber direction and k stands for l, t.

In practice, the solution of the KKT system given by (2.21,3.5,3.6) (completed by the appropriate ionic model) is hard to obtain monolithically, and an iterative approach is usually pursued. This means that, for a given guess of the control variables $\{\boldsymbol{\sigma}_i^{(0)}, \boldsymbol{\sigma}_e^{(0)}\}$ and setting $k = 0$, we solve

  (i) the Bidomain system with the current guess for the conductivities (notice that the problem is independent of the Lagrange multiplier), so to compute the state variables $u^{(k)}$, $u_e^{(k)}$, $\mathbf{w}^{(k)}$;

  (ii) the adjoint problem with the current guess for the conductivities and the state vari-

ables to obtain the Lagrange multipliers $p^{(k)}$, $q^{(k)}$ and $\mathbf{r}^{(k)}$;

(iii) the optimality conditions with $u^{(k)}, u_e^{(k)}, \mathbf{w}^{(k)}, p^{(k)}, q^{(k)}$ and $\mathbf{r}^{(k)}$ to obtain the new approximation $\{\boldsymbol{\sigma}_i^{(k+1)}, \boldsymbol{\sigma}_e^{(k+1)}\}$, and set $k = k + 1$.

These iterations end when a convergence test (on the residual of the optimality conditions in our case) is fulfilled.

In general, the rigorous theoretical analysis of parameter estimation problems is generally quite difficult and not always conclusive. A theoretical analysis of a control problem in electrocardiology for the optimal placement of pace-making stimuli has been successfully developed [126–128]. Works addressing general functional settings and results are available [129, 130]. For this particular problem, the existence of a minimizer of the misfit functional is proved in [26] with the phenomenological Rogers-McCulloch ionic model that completes the Bidomain system. Uniqueness is still an open problem, though.

Following a similar variational approach, it is possible to introduce the *Monodomain Inverse Conductivity Problem* (MICP) and the misfit functional reads

$$\mathcal{J}(\boldsymbol{\sigma}) = \frac{1}{2} \int_0^T \int_{\Omega_{obs}} (u(\boldsymbol{\sigma}) - u_{meas})^2 \, d\mathbf{x} dt + \mathcal{R}(\boldsymbol{\sigma}) \tag{3.7}$$

subject to the Monodomain equations completed by an appropriate ionic model (2.25) with

$$\mathcal{R}(\boldsymbol{\sigma}) = \frac{\alpha_1}{2} \|\boldsymbol{\sigma} - \boldsymbol{\sigma}_{mean}\|^2 + \frac{\alpha_2}{2} \|\nabla \boldsymbol{\sigma}\|^2 . \tag{3.8}$$

For easiness of reading, we do not report the lagrangian functional and the adjoint equations to solve, based on exactly the same considerations done for the BICP. The optimality conditions for MICP are

$$\frac{\mathcal{D}\mathcal{J}}{\mathcal{D}\sigma_k} = \frac{\partial \mathcal{L}}{\partial \sigma_k} = - \int_0^T \mathbf{a_k} \mathbf{a_k}^T \nabla u \cdot \nabla q \, dt + \frac{\partial \mathcal{R}}{\partial \sigma_k}, \quad \text{with} \quad k = l, t. \tag{3.9}$$

3.1.2 Numerical approximation

The numerical solution of the Bidomain problem is the subject of an abundant literature, as specific mathematical features of the problem make it challenging [89,90,131–134]. Following

a quite consolidated strategy [90], we decouple the PDEs system and the ODEs ionic model. A semi-implicit time discretization based on backward differentiation formulas (BDF) is used. Let Δt be the time step, hereafter we use superscript l for those variables at time $t = l\Delta t$. We denote by T the final time and let $L = T/\Delta t$, $t^l = l\Delta t$.

The Bidomain system after time discretization reads

$$
\begin{cases}
\beta C_m \dfrac{\bar{\alpha}_0}{\Delta t} u^{l+1} = \nabla \cdot (\boldsymbol{\sigma}_i \nabla u^{l+1}) + \nabla \cdot (\boldsymbol{\sigma}_i \nabla u_e^{l+1}) - \beta I_{ion}(\tilde{u}^{l+1}, \mathbf{w}^{l+1}) + I_{si}^{l+1} \\
\qquad\qquad + \beta C_m \sum_{i=1}^{s} \dfrac{\bar{\alpha}_i}{\Delta t} u^{l+1-i} & \text{in } \Omega \\
-\nabla \cdot (\boldsymbol{\sigma}_i \nabla u^{l+1}) - \nabla \cdot ((\boldsymbol{\sigma}_i + \boldsymbol{\sigma}_e) \nabla u_e^{l+1}) = I_{si}^{l+1} - I_{se}^{l+1} & \text{in } \Omega \\
\dfrac{\bar{\alpha}_0}{\Delta t} \mathbf{w}^{l+1} = \sum_{i=1}^{s} \dfrac{\bar{\alpha}_i}{\Delta t} \mathbf{w}^{l+1-i} + \mathbf{g}(\tilde{u}^{l+1}, \mathbf{w}^{l+1}) & \text{in } \Omega \\
(\boldsymbol{\sigma}_i \nabla u^{l+1} + \boldsymbol{\sigma}_i \nabla u_e^{l+1}) \cdot \mathbf{n} = 0, \quad \boldsymbol{\sigma}_e \nabla u_e^{l+1} \cdot \mathbf{n} = 0 & \text{on } \partial\Omega
\end{cases}
\tag{3.10}
$$

with given initial condition on u^0 and $\mathbf{w}^0$. Here $\bar{\alpha}_i$'s are the coefficients of the second order BDF ($\bar{\alpha}_0 = 3/2, \bar{\alpha}_1 = 2, \bar{\alpha}_2 = -1/2$). The term $\tilde{u}^{l+1}$ in the nonlinear functions $I_{ion}(u, \mathbf{w})$ and $\mathbf{g}(u, \mathbf{w})$ is a second order time extrapolation of u^{l+1}, i.e., $\tilde{u}^{l+1} = 2u^l - u^{l-1}$ and in particular $\tilde{u}^1 = u^0$.

Similarly, the adjoint equations after time discretization read

$$
\begin{cases}
\beta C_m \dfrac{\alpha_0}{\Delta t} q^l = \nabla \cdot (\boldsymbol{\sigma}_i \nabla p^l) + \nabla \cdot (\boldsymbol{\sigma}_i \nabla q^l) + \beta \partial_u I_{ion}(u^l, \mathbf{w}^l) \tilde{q}^l + \partial_u \mathbf{g}^l \cdot \mathbf{r}^l \\
\qquad\qquad + \beta C_m \sum_{i=1}^{s} \dfrac{\alpha_i}{\Delta t} q^{l+i} + (u^l - u_{meas}^l) \chi_{\Omega_{obs}} & \text{in } \Omega \\
-\nabla \cdot (\boldsymbol{\sigma}_i \nabla q^l) - \nabla \cdot (\boldsymbol{\sigma}_i + \boldsymbol{\sigma}_e) \nabla p^l) = (u_e^l - u_{e,meas}^l) \chi_{\Omega_{obs}} & \text{in } \Omega \\
\dfrac{\alpha_0}{\Delta t} \mathbf{r}^{l+1} = \sum_{i=1}^{s} \dfrac{\alpha_i}{\Delta t} \mathbf{r}^{l+1-i} + \beta \partial_{\mathbf{w}} I_{ion}^l \tilde{q}^l + \partial_{\mathbf{w}} \mathbf{g} \cdot \mathbf{r}^l & \text{in } \Omega \\
(\boldsymbol{\sigma}_i \nabla p^l \cdot + \boldsymbol{\sigma}_i \nabla q^l) \cdot \mathbf{n} = 0, \quad \boldsymbol{\sigma}_e \nabla p^l \cdot \mathbf{n} = 0 & \text{on } \partial\Omega
\end{cases}
\tag{3.11}
$$

with the final condition $q^L = 0$ and $\mathbf{r}^L = \mathbf{0}$. $\tilde{q}^l$ is the second order time extrapolation of q^l, i.e., $\tilde{q}^l = 2q^{l+1} - q^{l+2}$ and in particular $\tilde{q}^{L-1} = q^L$.

As for the space discretization, we consider the finite element method (FEM). Let space $H_h^1 = \left\{ \mathrm{span}\{\phi_j\}_{j=1}^M \subset H^1 \right\}$ be the finite-dimensional subspace of H^1 of piecewise linear functions with dimension M, where $\{\phi_j\}_{j=1}^M$ are the generic (Lagrange) basis functions of

this space. The approximated finite element solutions read

$$u_h(\mathbf{x}, t) = \sum_{j=1}^{M} u_j(t)\phi_j(\mathbf{x}), \ u_{e,h}(\mathbf{x}, t) = \sum_{j=1}^{M} u_{e,j}(t)\phi_j(\mathbf{x}).$$

For the BICP, we assume uniform conductivity tensors. Let us denote by $\mathbf{M}$ the mass matrix with entries $[\mathbf{M}]_{jk} = \int_\Omega \phi_k \phi_j \, d\mathbf{x}$, and by $\mathbf{S}_\tau$ the stiffness matrices with entries $[\mathbf{S}_\tau]_{jk} = \int_\Omega \boldsymbol{\sigma}_\tau \nabla \phi_k \cdot \nabla \phi_j d\mathbf{x}$, where τ stands for i, e.

For $\mathbf{u} = [u_j]$ and $\mathbf{u}_e = [u_{e,j}]$, after discretization in time and then in space, the associated algebraic Bidomain system reads

$$\begin{bmatrix} \mathbf{A} & \mathbf{S}_i \\ \mathbf{S}_i & \mathbf{S}_i + \mathbf{S}_e \end{bmatrix} \begin{bmatrix} \mathbf{u}^{l+1} \\ \mathbf{u}_e^{l+1} \end{bmatrix} = \begin{bmatrix} \mathbf{b}_1^{l+1} \\ \mathbf{b}_2^{l+1} \end{bmatrix} \tag{3.12}$$

where $\mathbf{A} = \beta C_m \frac{\bar{\alpha}_0}{\Delta t} \mathbf{M} + \mathbf{S}_i$ and the right hand side writes

$$\mathbf{b}_1^{l+1} = \left[\langle I_{si}^{l+1} - \beta I_{ion}(\tilde{u}^{l+1}, \mathbf{w}^{l+1}), \phi_j \rangle_{L^2} \right] + \beta C_m \mathbf{M} \sum_{i=1}^{s} \frac{\bar{\alpha}_i}{\Delta t} \mathbf{u}^{l+1-i},$$

$$\mathbf{b}_2^{l+1} = \left[\langle I_{si}^{l+1} - I_{se}^{l+1}, \phi_j \rangle_{L^2} \right].$$

Similarly, the algebraic form of the adjoint equations reads

$$\begin{bmatrix} \mathbf{A} & \mathbf{S}_i \\ \mathbf{S}_i & \mathbf{S}_i + \mathbf{S}_e \end{bmatrix} \begin{bmatrix} \mathbf{q}^l \\ \mathbf{p}^l \end{bmatrix} = \begin{bmatrix} \mathbf{d}_1^l \\ \mathbf{d}_2^l \end{bmatrix} \tag{3.13}$$

and the right hand side

$$\mathbf{d}_1^l = \left[\langle q_*^l + (u^l - u_{meas}^l)\chi_{\Omega_{obs}}, \phi_j \rangle_{L^2} \right] + \beta C_m \mathbf{M} \sum_{i=1}^{s} \frac{\bar{\alpha}_i}{\Delta t} \mathbf{q}^{l+i},$$

$$\mathbf{d}_2^l = \left[\langle (u_e^l - u_{e,meas}^l)\chi_{\Omega_{obs}}, \phi_j \rangle_{L^2} \right]$$

where $q_*^l = -\beta \partial_u I_{ion}^l \tilde{q}^l - \partial_u \mathbf{g}^l \cdot \mathbf{r}^l$.

Since $\mathbf{u}_e$ is unique up to a constant, the kernel of the algebraic matrix in (3.12) is

span$\{\mathbf{0},\mathbf{1}\}^T$. The singular system (3.12) is solved by the GMRES method[2] (tol=10^{-8}), which is a reliable strategy for elliptic problems with homogeneous Neumann boundary conditions [135]. The reactive dominating term presented after time discretization is stabilized by using a mass lumping technique which intends to alleviate the numerical instabilities caused by dominating reactive terms following time discretization. It consists of the approximation of the mass matrix using a diagonal (lumped) matrix. The diagonal entries are the sums of the elements of each row of the mass matrix. More details can be found in [136]. Then, we force the average of $\mathbf{u}_e$ to be zero at each time iteration. As already pointed out, the efficient solution and preconditioning of the Bidomain equations have been investigated in many papers [10,89,90,134]. In this work, we resort to a standard ILU right preconditioner [137] (with level of fill 1) without entering in further detail. The numerical solution of the Monodomain model is obtained with CG method.

The computation of the optimality conditions (3.6) in the case of uniform conductivities only involves matrix vector multiplications of stiffness matrices and state and adjoint solutions. On the contrary, the case of heterogeneous tissue requires more attention. We only consider spatial dependent conductivity tensors in the MICP, so we refer to the optimality conditions (3.9). Recalling (2.23), the Monodomain conductivity tensor $\boldsymbol{\sigma}(\mathbf{x})$ is characterized by the fields $\sigma_l(\mathbf{x})$ and $\sigma_t(\mathbf{x})$. The mesh for the approximation of the conductivity fields is coarser than the one describing the potential propagation. In fact, while the excitation wave initiates at a cellular level due to the ion fluxes through the cell membrane, the conduction varies at a larger scale. Thus, it is sufficient to discretize the conductivity fields on macro areas of the tissue to capture possible heterogeneities. Furthermore, this choice also represents a convenient trade-off between effectiveness of the estimation and computational costs since it limits the number of parameters to estimate allowing the use of standard optimization algorithms. $\sigma_l(\mathbf{x})$ and $\sigma_t(\mathbf{x})$ are approximated with P1 finite elements on the coarse mesh, i.e., $\sigma_{k,h}(\mathbf{x}) = \sum_{i=1}^{N} \sigma_k^i \varphi_i(\mathbf{x})$, where $k = l, t$, N is the number of DOFs of the

---

[2]CG method could be used here since the matrix in (3.12) is symmetric semi-definite (one eigenvalue is zero). However, GMRES is extensively used for solving the Bidomain system within LifeV, the software considered for the majority of the simulations (see end of the Section). For instance, highly optimization of the libraries implementing GMRES in LifeV was performed in [90] to solve a non-symmetric system derived from an alternative Bidomain formulation. GMRES and CG methods for the Bidomain system generally yield comparable performances in this software. Therefore, we stick with the former for the sake of implementation.

coarse mesh and $\{\varphi_j\}_{j=1}^N$ are the generic (Lagrange) basis functions of the finite-dimensional subspace of H^1 of piecewise linear functions with dimension N. Moreover

$$\frac{\mathcal{DJ}}{\mathcal{D}\sigma_{k,h}(\mathbf{x})} = \sum_{l=1}^N \frac{\mathcal{DJ}}{\mathcal{D}\sigma_k^l}\varphi_l(\mathbf{x})$$

and $\mathcal{DJ}/\mathcal{D}\sigma_k^l$, $\forall l = 1, \cdots, N$, can be determined as

$$\Big\langle \sum_{l=1}^N \frac{\mathcal{DJ}}{\mathcal{D}\sigma_k^l}\varphi_l(\mathbf{x}), \varphi_j(\mathbf{x}) \Big\rangle = -\int_0^T \int_\Omega \mathbf{a_k}\mathbf{a_k}^T \nabla u \cdot \nabla q \varphi_j(\mathbf{x})\, d\mathbf{x}dt + \int_\Omega \frac{\partial \mathcal{R}}{\partial \sigma_k}\varphi_j(\mathbf{x})\, d\mathbf{x}.$$

By definition of $\langle \cdot, \cdot \rangle$,

$$\Big\langle \sum_{l=1}^N \frac{\mathcal{DJ}}{\mathcal{D}\sigma_k^l}\varphi_l(\mathbf{x}), \varphi_j(\mathbf{x}) \Big\rangle = \int_\Omega \sum_{l=1}^N \frac{\mathcal{DJ}}{\mathcal{D}\sigma_k^l}\varphi_l(\mathbf{x}) \cdot \varphi_j(\mathbf{x})\, d\mathbf{x},$$

accordingly, we have

$$\frac{\mathcal{DJ}}{\mathcal{D}\sigma_{k,h}(\mathbf{x})} = \mathbf{M}_{coarse}\frac{\mathcal{DJ}}{\mathcal{D}\sigma_k}, \quad \frac{\mathcal{DJ}}{\mathcal{D}\sigma_k} = \Big[\frac{\mathcal{DJ}}{\mathcal{D}\sigma_k^l}\Big], \; l = 1, \ldots, N$$

where $\mathbf{M}_{coarse}$ is the mass matrix related to the coarse mesh with entries $[\mathbf{M}_{coarse}]_{jl} = \int_\Omega \varphi_l(\mathbf{x})\varphi_j(\mathbf{x})\, d\mathbf{x}$. Therefore, $\frac{\mathcal{DJ}}{\mathcal{D}\sigma_k}$ can be computed as the solution of the linear system

$$\mathbf{M}_{coarse}\frac{\mathcal{DJ}}{\mathcal{D}\sigma_k} = \mathbf{f},$$

where

$$\mathbf{f} = [f_j], \quad f_j = -\int_0^T \int_\Omega \mathbf{a_k}\mathbf{a_k}^T \nabla u \cdot \nabla q \varphi_j(\mathbf{x})\, d\mathbf{x}dt + \int_\Omega \frac{\partial \mathcal{R}}{\partial \sigma_k}\varphi_j(\mathbf{x})\, d\mathbf{x}$$

for $j = 1, \ldots, N$. We compute f_j as follows. At time $t = l\Delta t$, we have that

$$-\int_\Omega \mathbf{a_k}\mathbf{a_k}^T \nabla u \cdot \nabla q \varphi_j(\mathbf{x})\, d\mathbf{x} + \int_\Omega \frac{\partial \mathcal{R}}{\partial \sigma_k}\varphi_j(\mathbf{x})\, d\mathbf{x} =$$

$$-\int_\Omega \mathbf{a_k}\mathbf{a_k}^T \sum_{s=1}^M u_s(t)\nabla\phi_s(\mathbf{x}) \cdot \sum_{v=1}^M q_v(t)\nabla\phi_v(\mathbf{x})\varphi_j(\mathbf{x})\, d\mathbf{x} + \int_\Omega \frac{\partial \mathcal{R}}{\partial \sigma_k}\varphi_j(\mathbf{x})\, d\mathbf{x} = \qquad (3.14)$$

$$-\mathbf{q}^T\mathbf{S}_k^j\mathbf{u} + \int_\Omega \frac{\partial \mathcal{R}}{\partial \sigma_k}\varphi_j(\mathbf{x})\, d\mathbf{x},$$

where

$$[\mathbf{S}_k^j]_{sv} = \int_\Omega \mathbf{a_k} \mathbf{a_k}^T \nabla \phi_v(\mathbf{x}) \cdot \nabla \phi_s(\mathbf{x}) \varphi_j(\mathbf{x}) \, d\mathbf{x}, \quad k = l, t.$$

Finally, we sum up all the contributions for each time step to get f_j. The time dependence is included in the coefficients $u_s(t)$ and $q_v(t)$ characterizing the unsteady state and adjoint solutions.

The update of the conductivities in the algorithm for the solving the KKT system (2.21,3.5,3.6) is performed by the BFGS method with Armijo line search [138]. Different stopping criteria were tested for BFGS, either

$$\frac{\left\|\nabla \mathcal{J}(\boldsymbol{\sigma}^k)\right\|}{\left\|\nabla \mathcal{J}(\boldsymbol{\sigma}^0)\right\|} < 10^{-6} \text{ or } \frac{\left\|\mathcal{J}^k - \mathcal{J}^{k-1}\right\|}{\left\|\mathcal{J}^0\right\|} < 10^{-6} \text{ or } \frac{\left\|\boldsymbol{\sigma}^k - \boldsymbol{\sigma}^{k-1}\right\|}{\left\|\boldsymbol{\sigma}^{k-1}\right\|} < 10^{-6}.$$

Notice that the Lagrangian multipliers approach is applied to the continuous problem. This is the so-called *Optimize-then-Discretize* (OD) approach and it computes the solution over the entire time interval. The drawback of this approach is the presence of the backward-in-time adjoint problems, so the iterations required a sequence of forward/backward time iterations that generally result to be computationally demanding. An alternative approach is to first discretize (in time, in particular) and then to perform the optimization process on the sequence of pseudo-stationary time discrete problems. This sort of *Discretize-then-Optimize* approach is computationally more efficient, yet it computes a sequence of estimates at each time step, eventually to be averaged and, in general, sub-optimal for the original problem [124]. Hybrid strategies consist of introducing macro subdivisions in time by means of *check points*, so to work with forward/backward in time problems over smaller intervals [26]. In this Thesis, we stick to the original OD approach.

Several numerical simulations have been performed considering both uniform and spatial dependent conductivities in synthetic and experimental settings. In particular, in Section 3.2.1 and 3.2.2, we present numerical results in 2D and 3D settings, respectively, using the BICP with homogeneous tissue. In the latter case, simulations run both on simplified (yet realistic for in vitro experiments) and real left ventricle geometries reconstructed from SPECT images, as a proof of concept in view of clinical applications. The role of the solution

of the MICP as a predictor of the Bidomain estimate is explored in Section 3.2.3. Then, we analyze the performance of the estimation procedure in case of heterogeneous tissue and set up the numerical discretization in view of experimental validation in Section 3.2.4. Finally, an extensive real validation is presented in Section 3.3.

From the implementation viewpoint, the simulations discussed in Section 3.2.1 have been performed in the Freefem++ environment [139], whereas, in the rest of the chapter, we focused on LifeV [140, 141], an object oriented C++ parallel finite element library based on the Trilinos project [142] developed by different groups worldwide. The change of software was due to the fact that LifeV is more suitable for parallel computing and more efficient than Freefem++. Therefore, with the increasing computational complexity of the 3D simulations and the heterogeneous tissue tests, LifeV was the preferred software. While using many Trilinos packages, the rest of the LifeV code was implemented from scratch.

We also used different hardwares according to the computation time of the simulations. In particular, the 2D simulations in Section 3.2.1 were performed on a laptop with processor Intel Core i5-3337U 1.8 GHz, whereas 3D simulations in Section 3.2.2 and 3.2.3 were carried out using 8 cores on a high performance cluster named Cheetah, equipped with Xeon L5420 2.5 GHz CPUs. Because of heavier computational cost, the synthetic tests in Section 3.2.4 with spatial dependent conductivities were performed using 16 cores on Cheetah and the experimental validation in Section 3.3 was carried out on Stampede II high performance cluster of the XSEDE consortium using 96 cores on SKX nodes (Intel Xeon Platinum 8160 Skylake 2.1GHz nominal).

3.2   Synthetic Validation

In this Section, we perform a synthetic validation of the variational data assimilation approach with the Bidomain equations considering different geometries and potential experimental and realistic settings. In particular, in this first set of simulations, we investigate the numerical sensitivity of our methodology to the number and the location of the probing sites that make up Ω_{obs}. Another critical parameter to analyze is the amount of measurement data of u_e necessary to ensure a good accuracy of the estimation. In fact, as

already pointed out in [26], extracellular potential data are necessary for reliable estimates. However, measuring extracellular potential in experiments is much more troublesome than transmembrane voltage. We consider the number of observation points for transmembrane and extracellular potentials independently. We also analyze the performance of the methodology using different stimuli conditions. Moreover, the dependence of the reliability of the estimation to the number of snapshots u_{meas} and $u_{e,meas}$ used to perform the inversion need to be studied. This can be investigated by testing the inversion over different time intervals $[0, T]$. It is reasonable to expect that the larger the T, the more accurate the estimates are. Finally, a preliminary synthetic testing useful for real validation is presented.

3.2.1   Sensitivity analysis in 2D

We present 2D test cases aiming to investigate the numerical sensitivity of the algorithm under different experimental settings, characterized by the number and the location of the measurement sites and the stimuli conditions. We solved the BICP using Rogers-McCulloch model (2.6) with $u_0(\mathbf{x}) = 0$ mV, $\mathbf{w}_0(\mathbf{x}) = 0$, $\beta = 1000$ cm^{-1} and $C_m = 1$ μF/cm^2. The domain was a square $\Omega = [0, 1] \times [0, 1] \subset \mathbb{R}^2$ of size 1 cm^2. A constant fiber angle was chosen as $\theta = -48°$. Four stimuli of $I_{si} = I_{se} = 10^5 \mu A$/cm^3 were applied in the domain at the center of each quarter of the square for a duration of 1 ms. The cardiac tissue is assumed homogeneous and synthetic data was generated with the conductivity parameters $\boldsymbol{\sigma}_{exact} = (\sigma_{il}, \sigma_{el}, \sigma_{it}, \sigma_{et}) = (2.8, 2.2, 0.26, 1.3)$ mS/cm from Table 3.1. The space discretization method for generating the synthetic data was given by *quadratic* finite elements on a 250×250 grid, the simulation time step was $\Delta t = 0.005$ ms, and synthetic data was recorded every $dt_{snap} = 1$ ms until reaching $T = 25$ ms. This means we have 25 snapshots of u_{meas} and $u_{e,meas}$ to perform the estimation. The numerical discretization for the inversion was carried out using *linear* finite elements on a 50×50 grid and $\Delta t = 0.05$ ms. In such a way, we prevent any *inverse crime* since the space for solving the inverse problem is different from the one generating the data. Moreover, the synthetic data is perturbed at each time step by adding Gaussian noise with zero mean and standard deviation equal to $p \max |u|$, where p is the percentage of noise, and the maximum is taken in both space and time. We set the regularization coefficient $\alpha_1 = 0$. The terms $\|\nabla \boldsymbol{\sigma}.\|^2$ equal zero because

(a) $t = 2$ ms   (b) $t = 15$ ms
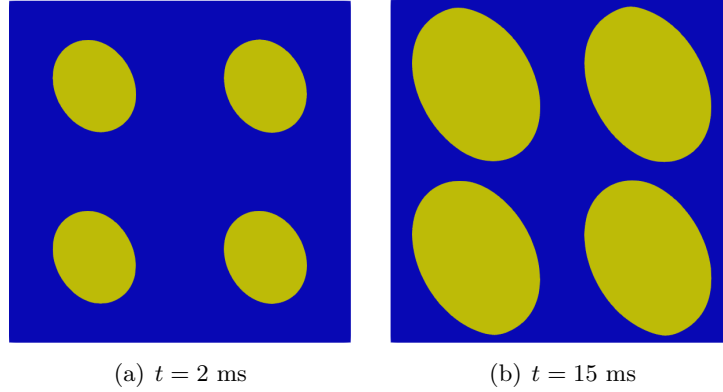
Figure 3.1: Propagation of the transmemebrane potential with four stimuli generated by the Bidomain model (contour line $u_{meas} = 50$ mV).

of the tissue homogeneity assumption, i.e., the tensors are uniform in space. The synthetic measure of transmembrane potential is shown in Fig. 3.1. In all the following tests, the initial guess for BFGS was $\boldsymbol{\sigma}_0 = (1, 1, 1, 1)$ mS/cm.

TEST 1 - Equally spaced measurement sites   The positions of the sites were assumed to be known a prior and equally spaced on a cartesian grid. First of all, we analyze the sensitivity and the accuracy of the estimates varying the percentage of noise p in the synthetic data up to 15%. The number of sites is equal to 36, arranged into an array over the tissue domain consisting of 6×6 sites with spacing of 1.667 mm. Results are shown in Table 3.2. The method estimates accurately the true values of the conductivities, even when the measurements are highly noisy. Notice that, in this specific case, the value σ_{et} is generally the slowest to converge. Keeping the same level of noise, we compare the estimates varying the number of sites. We test 4,9,16,25 equally spaced observation points respectively for both u and u_e. Results for $p = 5\%$ are listed in Table 3.3. The dashes identify test cases when convergence fails. Using 16 sites or more yields reliable estimates.

We also test the performance of the method when the sites are not equally spaced, yet they are localized nearby the stimuli. Clustering the observation points in the areas where most of the dynamics occurs might improve the accuracy of the estimation procedure. We keep the total number of sites equal to 36 and vary the percentage of noise p up to 15%. From Table 3.4, we notice however that the different position of the sites does not significantly

% noise	0	5	10	15
σ_{il}	2.80	2.81	2.82	2.82
σ_{el}	2.23	2.22	2.23	2.23
σ_{it}	0.22	0.22	0.22	0.22
σ_{et}	1.24	1.20	1.20	1.18

Table 3.2: Equally spaced measurement sites, # u sites = # u_e sites = 36.

# sites	≤ 9	16	25
σ_{il}	-	2.93	2.80
σ_{el}	-	2.32	2.25
σ_{it}	-	0.23	0.22
σ_{et}	-	1.30	1.24

Table 3.3: Equally spaced measurement sites, 5% noise.

% noise	0	5	10	15
σ_{il}	2.89	2.88	2.88	-
σ_{el}	2.24	2.24	2.23	-
σ_{it}	0.22	0.22	0.22	-
σ_{et}	1.24	1.24	1.23	-

Table 3.4: Unevenly spaced measurement sites, #u sites = #u_e sites = 36.

# sites	13	14	15	16	17	18	19	20	23	25
σ_{il}	2.68	-	-	2.69	2.80	0.88	3.11	3.21	2.78	-
σ_{el}	2.16	-	-	1.94	2.08	3.56	2.05	1.94	2.00	-
σ_{it}	0.19	-	-	0.20	0.19	2.72	0.20	0.20	0.20	-
σ_{et}	1.17	-	-	1.24	1.26	0.86	1.32	1.42	1.27	-

Table 3.5: One stimulus applied in the center of Ω, u, u_e random sites localized in the subdomain $[0.3, 0.7]\,\mathrm{cm} \times [0.3, 0.7]$ cm, 5% noise.

Numerical sensitivity results in 2D setting, conductivities measured in mS/cm. $\boldsymbol{\sigma}_{exact} = (2.8, 2.2, 0.26, 1.3)$ mS/cm.
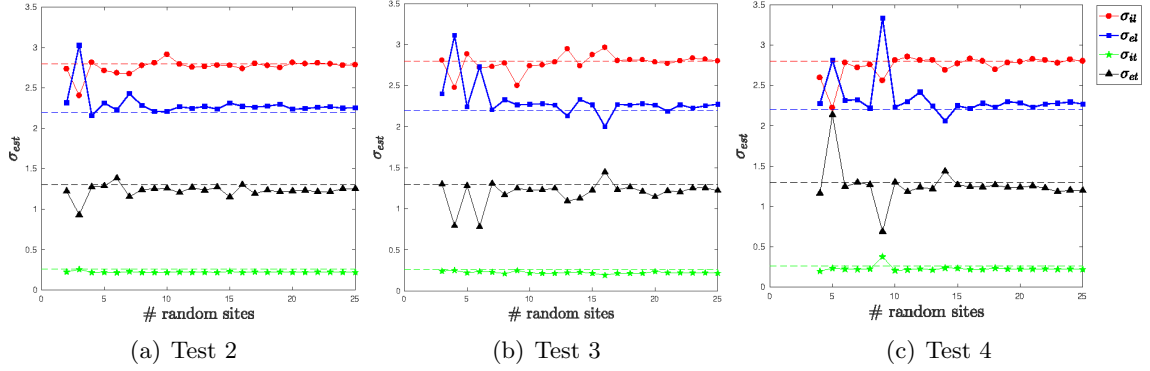
Figure 3.2: Estimated conductivities ([mS/cm]) obtained in the 2D tests vs. number of random sites (up to 25). The dashed lines represent the exact values. (a) Randomly spaced sites for u_e measurements and equally spaced for u measurements (#u sites = 25). (b) Randomly spaced sites for u and u_e measurements. (c) Randomly spaced sites for u and u_e measurements in a subdomain.

improve the accuracy of the estimates. Actually, in case of highly noisy data ($p = 15\%$), the optimization algorithm fails to converge. Therefore, in view of designing an experiment for measuring cardiac excitation, recording data at equally spaced observation sites over the whole domain seems to be a good choice.

TEST 2 - Randomly spaced measurement sites (u_e only)   Recording extracellular potential data is troublesome in practice. Therefore, we need to investigate the performance of the optimization algorithm in case of lack of u_e measurements. We vary the number of u_e measurement sites from 2 to 25 while keeping 25 equally spaced sites for u. The locations of u_e sites are the realization of independently and identically distributed (i.i.d.) uniform random variables defined over the tissue. It is indeed important to evaluate the reliability of our method in presence of uncertainty on the location of sites since, in experimental setting, we might not exactly know where the measurement sites are located on the tissue. For each number of u_e sites, the estimated conductivities shown in Fig. 3.2(a) are the sample mean of the estimated values of multiple runs of the inverse problem with different realizations of the uniform random variables. We notice that at least 10 u_e probing sites are required to guarantee reasonable accuracy.

(a) $|\sigma_{il} - \sigma_{il,true}|$

(b) $|\sigma_{it} - \sigma_{it,true}|$

(c) $|\sigma_{el} - \sigma_{el,true}|$

(d) $|\sigma_{et} - \sigma_{et,true}|$
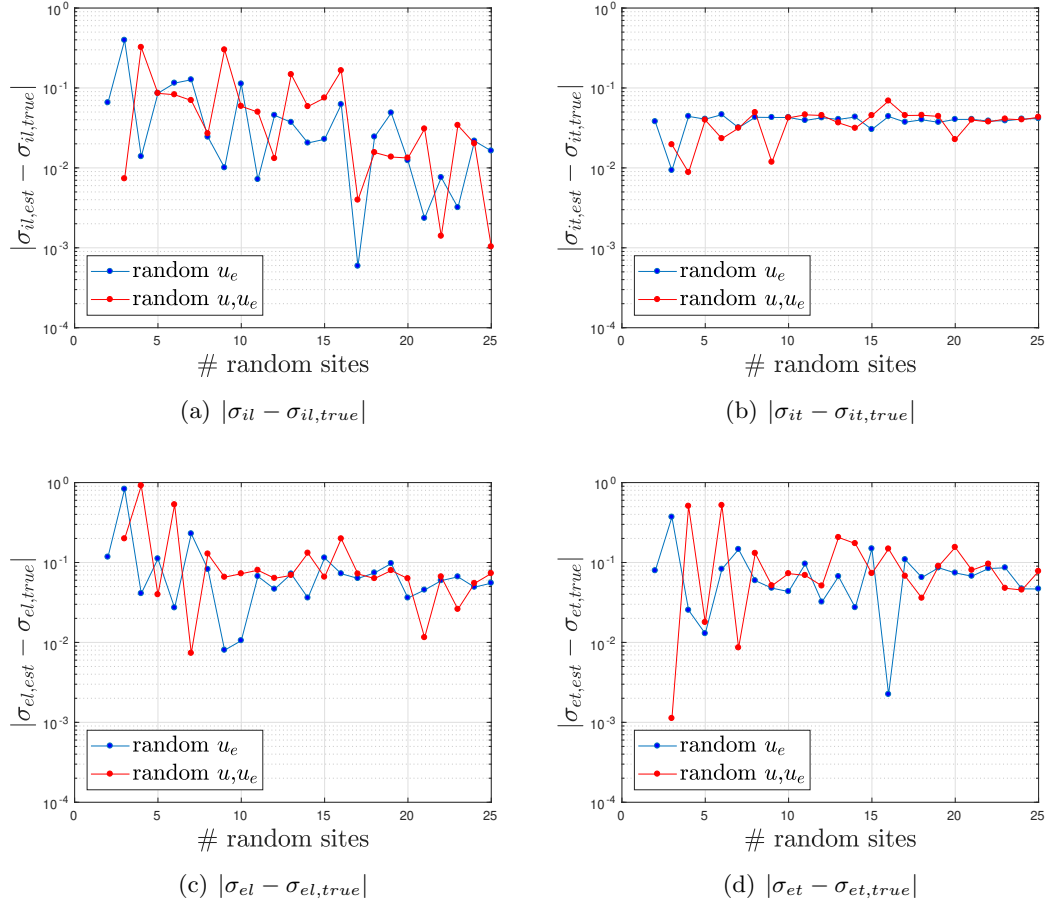
Figure 3.3: Comparison of the estimation error for Test 2 (blue line) and 3 (red line) in the 2D case.

TEST 3 - Randomly spaced measurement sites (u and u_e) Here, we introduce uncertainty over the measurement sites also for u, still assuming they are i.i.d. distributed over the domain Ω. The sample means of the estimated parameters for different number of sites are provided in Fig. 3.2(b). Fig. 3.3 shows a comparison between the error $|\boldsymbol{\sigma} - \boldsymbol{\sigma}_{true}|$ of Test 2 and 3. Introducing uncertainty in the location of measurement sites for both transmembrane and extracellular potentials does not prevent a reasonable estimation of the conductivities. It actually helps the optimization algorithm to reach convergence even when we use few random sites. Indeed, when we selected the site position *a priori*, we got reasonable results only using 16 equally spaced sites or more. This robustness of the method in presence of noise and uncertainty induced by random sites is a very desirable feature in view of the validation with in vitro experiments. Indeed, the experimental data as well as

(a) Samples mean (b) Standard deviation
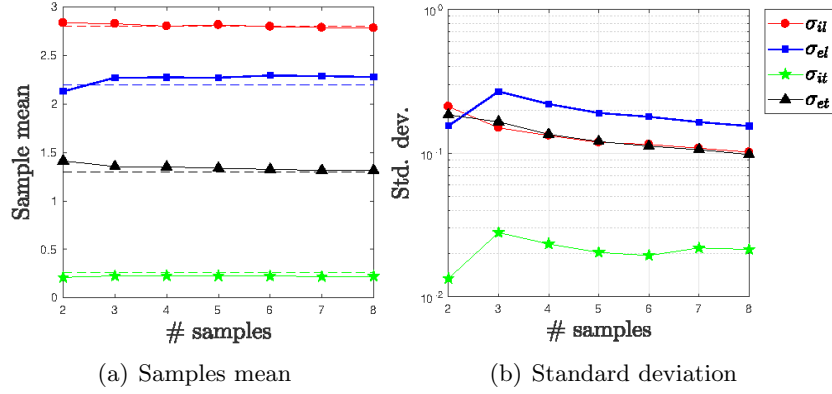
Figure 3.4: Sample mean and standard deviation ([mS/cm]) for Test 3, # random sites = 5. # samples stands for the number of inverse problems used to compute the sample mean of the estimates.

the position of the sites on the tissue are usually affected by noise and these results suggest that the method can work properly anyway.

We also analyze the convergence of the sample mean of the estimates with respect to the number of inverse problems. Each inversion corresponds to a different realization of the random variables describing the location of the probing sites. Fig. 3.4 shows the behavior of the sample mean and the standard deviation of the estimates as the number of realizations increases for the case of 5 random sites. We considered a maximum of 8 realizations. As expected, the larger is the number of samples, the better the sample mean matches the exact values featuring a lower standard deviation. This does not apply to σ_{it} that, however, features a small standard deviation even with a small number of samples.

TEST 4 - Clustered and randomly spaced measurement sites (u and u_e)   In this test, we assume u and u_e sites i.i.d. randomly distributed on a subset of the domain. More specifically, the sites were localized only in the bottom left quarter of Ω around the location of just one of the four stimuli (see Fig. 3.5(a)). As shown in Fig. 3.2(c), the algorithm provides good results even in this case.

TEST 5 - Clustered and randomly spaced measurement sites (u and u_e) with only one stimulus   The results of the Test 4 may suggest that the wavefront propagation triggered by only one pacing stimulus could be informative enough to detect the right

Figure 3.5: (a) Random sites are localized in the area delimited by the red square. (b)-(c) Propagation of the AP in the case of one stimulus in the center of the domain at $t = 2$ ms and $t = 15$ ms, respectively (contour line $u_{meas} = 50$ mV).

conductivity parameters. Therefore, we tested an experimental setting consisting of pacing the tissue only in one point, for instance at its center, instead of stimulating in four different areas as done so far. So, the purpose is investigating whether or not the propagation dynamics obtained with one stimulus carries enough information to guarantee an accurate estimation (see Fig. 3.5(b),3.5(c)). This could be extremely beneficial for the feasibility of the experiments since applying four simultaneous stimuli is challenging in practice.

As assumed before, u and u_e measurements sites are taken to be randomly distributed following an uniform distribution. The difference here is that they are localized just in the subdomain $[0.3, 0.7]$ cm $\times [0.3, 0.7]$ cm where most of the dynamics occurs. By looking at Table 3.5, we notice that the estimated parameters are inaccurate. For less than 12 sites, no reasonable estimate is obtained. We conclude that multiple stimuli are required to obtain a reliable estimation of the conductivities, as data triggered by only one stimulus are not informative enough.

The optimization procedure does not provide better estimations even when we apply a sequence of four stimuli in the center of the slab. The propagation dynamics triggered by multiple stimuli applied in different areas of the tissue seems to be critical to obtain a more accurate estimation of the conductivities. However, let us recall that the inversion is performed in the time interval [0,25] ms. Accuracy might be improved by considering a larger time interval, for instance [0,60] ms, thus including more snapshots in the inversion. In this way, we have more information about the dynamics of the system which can help

(a) $t = 2$ ms   (b) $t = 15$ ms

Figure 3.6: Propagation of the AP with five stimuli applied on the top surface of the slab (contour line $u_{meas} = -20$ mV).

to obtain more precise results. In fact, for the case of 20 probing sites, the estimates are (2.81,2.22,0.24,1.26) mS/cm which, comparing to the corresponding results in Table 3.5, are in better agreement with the exact values.

3.2.2   Sensitivity analysis in 3D

We present a series of test cases performed on a 3D slab $\Omega = [0,5] \times [0,5] \times [0,0.5] \subset \mathbb{R}^3$ measured in cm^3 with 24272 mesh nodes. We coupled the Bidomain model with Minimal ionic model (2.13) in the canine version with $u_0(\mathbf{x}) = -84$ mV and $\mathbf{w}_0(\mathbf{x}) = [1,1,0]$. In each simulation, five stimuli of $I_{app} = 10^5 \mu A/\text{cm}^3$ were applied with four at the corners and one at the center of the top surface of the domain ($z = 0.5$ cm) for a duration of 1 ms (Fig. 3.6). A constant fiber angle was chosen as $\theta = -48°$, as done in [26]. Synthetic data were generated with uniform conductivity parameters $\boldsymbol{\sigma}_{exact} = (3.4, 1.2, 0.6, 0.8)$ mS/cm from Table 3.1 and the initial guess for the optimization procedure $\boldsymbol{\sigma}_0 = (4,3,2,1)$ mS/cm. Simulations were ran with $T = 30$ ms, $\Delta t = 0.05$ ms, $t_{snap} = 1$ ms and 5% noise. As done for 2D tests, we set the regularization parameter α_1 equal to 0. In order to limit computational costs, here the data are generated on the same mesh used for solving the inverse problem and not finer meshes, and successively mitigated by the addition of noise to mitigate the impact of the coincidence of the solvers for the direct and inverse solvers, leading to overoptimistic results. We will consider this aspect when discussing our results.

# u_e sites	4	9	16	25	36	49	64	81	100
σ_{il}	4.95	2.74	3.21	2.23	3.34	3.01	3.09	3.08	3.27
σ_{el}	0.93	1.26	1.27	1.16	1.19	1.21	1.26	1.16	1.23
σ_{it}	1.67	0.72	0.62	0.81	0.57	0.63	0.65	0.63	0.63
σ_{et}	0.63	0.74	0.79	0.85	0.86	0.81	0.83	0.78	0.82

Table 3.6: Estimated conductivities ([mS/cm]) with equally spaced measurement sites on a slab. $\boldsymbol{\sigma}_{exact} = (3.4, 1.2, 0.6, 0.8)$ mS/cm, 5% noise.

TEST 1 - Equally spaced measurement sites   Similarly to the 2D tests in Section 3.2.1, u and u_e measurement sites are equally spaced on the top surface of the slab. Firstly, we intend to check the sensitivity of the conductivity estimation to different number of sites. From Table 3.6, we notice that the optimization procedure provides accurate estimation with at least 36 measurements. As already done in Test 5 of the previous Section, a way to refine the estimates is performing the inversion on a larger time interval. Indeed, some portion of the domain might not be activated by the wave front propagation in the time range $[0, 30]$ ms considered in these simulations, so the sites falling in those areas do not contribute to the computation of the misfit. We tested the algorithm with $T = 60$ ms and 25 equally spaced sites. The estimates are $(3.36, 1.21, 0.54, 0.82)$ mS/cm and, by comparing with Table 3.6, they better match the exact values of the parameters. However, the higher accuracy comes along with heavier computational burden, so this strategy does not seem suitable in case of limited computational resources or measurement data. This approach will be used in 3.2.4 and 3.3 where accuracy is privileged over computational efficiency.

TEST 2 - Randomly spaced measurement sites (u_e)   As measuring u_e is generally problematic, we investigate the accuracy of the estimation with different number of u_e measurement sites following an uniform distribution on the top surface of the slab keeping the (high) number of u measurement sites constant. We consider 100 equally spaced sites for u measurements on the top surface of the mesh. We vary the total number of random sites for u_e measurements from 5 to 100. The sample mean of the estimated conductivities is shown in Fig. 3.7(a). In this specific case, the parameter σ_{il} is the most sensitive to the uncertainty on the location of u_e sites, but overall the estimates are reliable, especially from 40 sites on.
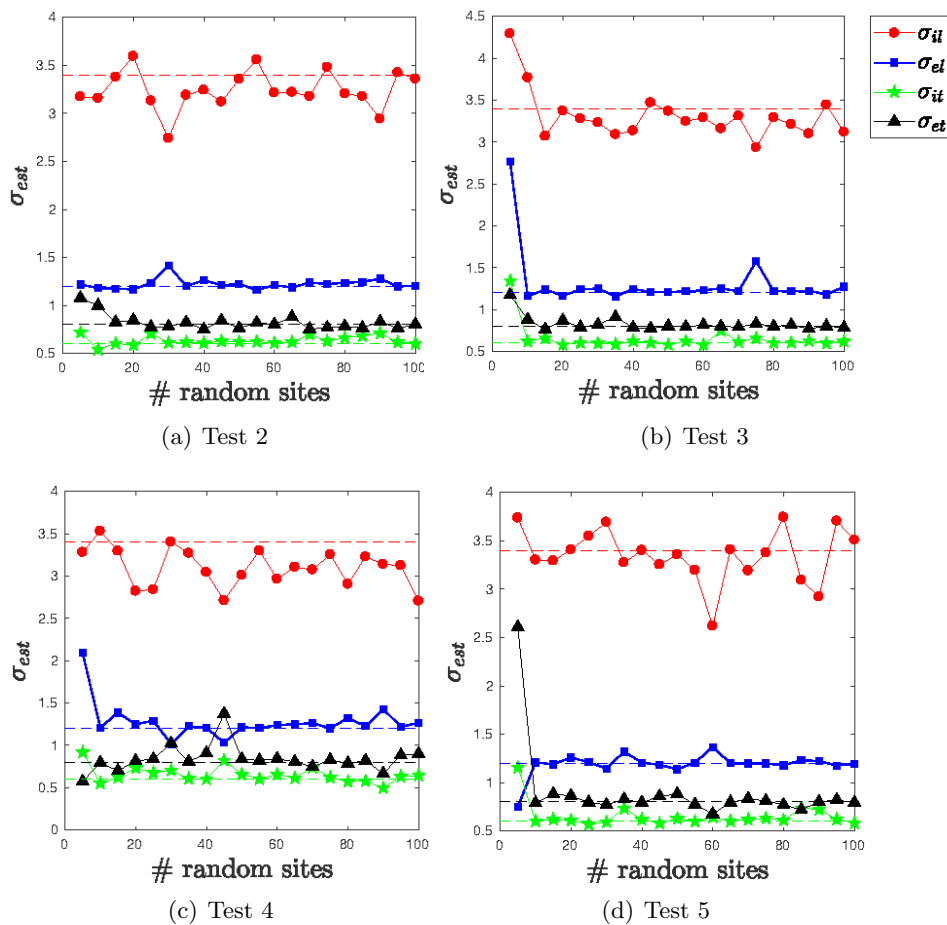
Figure 3.7: Estimated conductivities ([mS/cm]) obtained in the 3D tests vs. number of random sites (up to 100). (a) Random sites for u_e. (b) Random sites for u_e,u. (c) Clustered random sites for u_e,u, one stimulus. (d) Random sites for u_e,u, non-simultaneous stimuli.
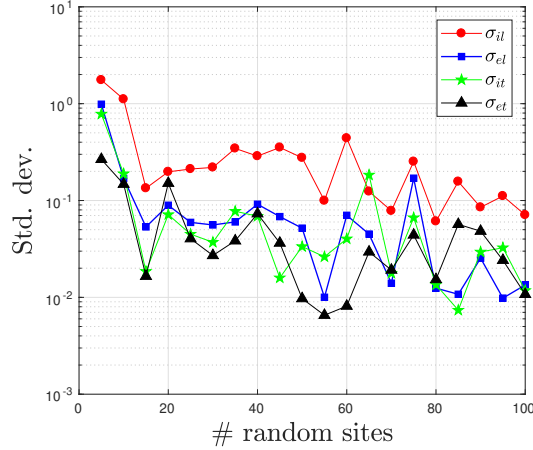
Figure 3.8: Standard deviation ([mS/cm]) of Test 3 (3D slab). A general decreasing trend of the standard deviation can be noticed for all the estimates.

TEST 3 - Randomly spaced measurement sites (u and u_e) As done in Test 4 of Section 3.2.1, we assume also the u measurement sites to follow an uniform distribution on the top surface of the slab. Fig. 3.7(b) show the results from 5 to 100 sites. The optimization algorithm still provides accurate estimates even with a relatively low number of estimates. This confirms the consistency of our method with the solution of the problem, however we speculate that the coincidence of the discrete solvers for the forward and inverse problems may lead to overoptimistic results (in spite of the random noise added to the data). Finally, it is reasonable to expect that the standard deviation decreases as more random sites are used. This is confirmed by Fig. 3.8 implying that the estimates are more robust as more sites are considered in the inverse problem.

TEST 4 - Clustered and randomly spaced measurement sites (u and u_e) with one stimulus Similarly to Test 6 in Section 3.2.1, we analyze the performance of the estimation procedure when only one stimulus is applied in the center of the top surface of the slab. The location of u and u_e sites follow a uniform distribution over the subset $[1, 4]\,\text{cm} \times [1, 4]\,\text{cm}$ of the top surface. The estimations are shown in Fig. 3.7(c) from different number of random sites. The overall result is less accurate than Test 2 and 3, especially for the parameter σ_{il}. Again, this test confirms the consistency of the numerical solution with the exact one, probably made overaccurate for the coincidence of the solvers for the forward

and inverse problems. This is apparent when noting that the results are in this case more accurate than the ones obtained for the analogous in 2D (Test 5 in the previous Section).

TEST 5 - Randomly spaced measurement sites (u and u_e), non-simultaneous stimuli   This test is similar to Test 3 with the difference that the five stimuli are applied at different times. Starting from the stimulus in the center of the top surface, each stimulus is applied every 2 ms. Indeed, in real experimental setting, stimulating the tissue with multiple impulses at the same time is challenging. Estimations in Fig. 3.7(d) show that the optimization procedure is reliable. This confirms the previous results obtained in the 2D setting suggesting that applying multiple stimuli in different areas of the domain is the experimental design providing the most accurate results. Estimation errors of the different test cases are shown in Fig. 3.9.

A real ventricle simulation   To test the impact of real geometries on the performances of the method, we run simulations on a real left ventricular geometry reconstructed from SPECT images [90]. We solved the BICP on a mesh with 22470 degrees of freedom. Fig. 3.10 displays a realistic representation of the fiber structure used in the simulation. The fiber orientation was first obtained on an ellipsoid domain and then properly adopted the real domain, as already done in [90]. Our concern in these tests is focused on the interplay between the location of the stimuli and the sites. This study may give us better insights on how to set an experiments aimed for clinical applications. We analyze the accuracy of the estimation in two different experimental settings: in the first one, we apply four stimuli on the whole tissue, whereas in the second one we stimulate only the inner wall of the ventricle (see Fig. 3.10). In each experimental setting, the measurement sites are picked either on the whole tissue or only on the inner wall and their locations are assumed to be either equally or randomly spaced.

Tables 3.7 and 3.8 show that, for each experimental setting, the estimation procedure yields quite inaccurate results in case of equally spaced observation points. On the other hand, regardless where the tissue is stimulated, the best estimates are provided in case of randomly spaced sites placed on the whole tissue.
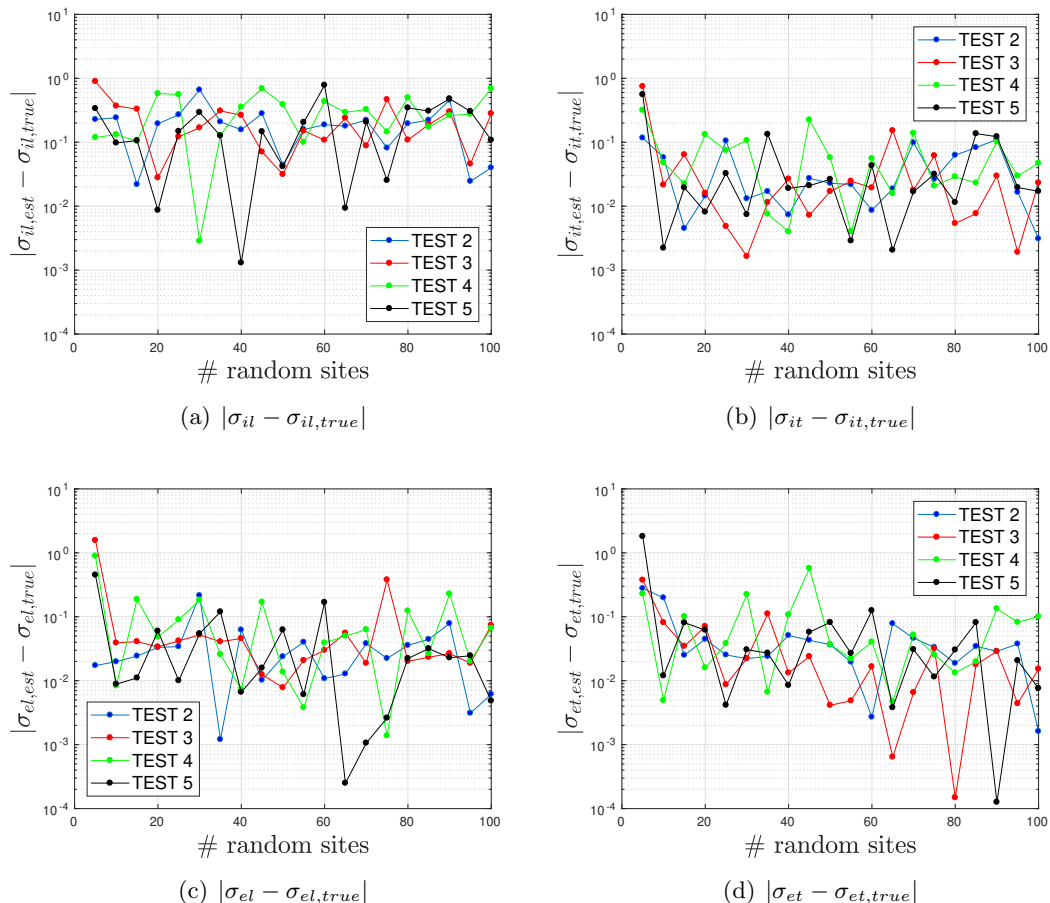
Figure 3.9: Comparison of the estimation error for different experimental settings in the 3D slab.
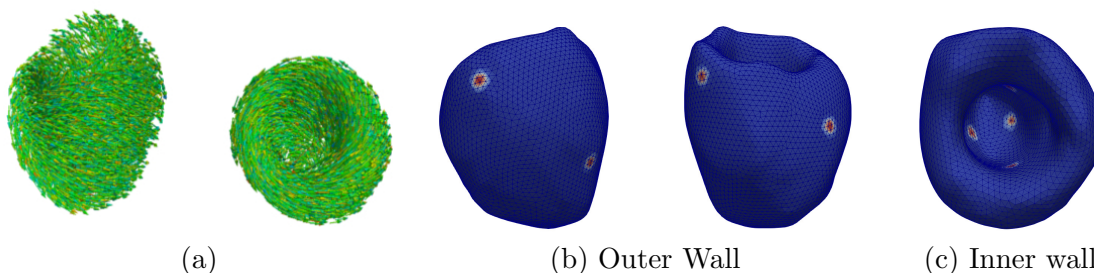
Figure 3.10: (a) Myocardial fiber orientation used in simulation from two different viewpoints. Image from [26]. (b-c) Location of the stimuli on the real left ventricle.

Sites	Equally spaced		Randomly spaced	
Location	whole tissue	inner wall	whole tissue	inner wall
σ_{il}	3.94	3.61	3.37	3.51
σ_{el}	1.71	2.30	1.13	1.10
σ_{it}	0.44	0.46	0.61	0.63
σ_{et}	0.61	0.25	0.85	0.94

Table 3.7: Estimates ([mS/cm]) in the case of four stimuli applied on the whole ventricle.

Sites	Equally spaced		Randomly spaced	
Location	whole tissue	inner wall	whole tissue	inner wall
σ_{il}	3.75	4.01	3.53	3.83
σ_{el}	1.38	1.46	1.29	1.76
σ_{it}	0.51	0.41	0.65	0.73
σ_{et}	0.79	0.46	0.77	0.70

Table 3.8: Estimates ([mS/cm]) in the case of four stimuli applied on the inner wall of the ventricle.

$\boldsymbol{\sigma}_{exact} = (3.4, 1.2, 0.6, 0.8)$ mS/cm, # sites $= 1000$, $T = 30$ ms, $\Delta t = 0.05$ ms, $t_{snap} = 1$ ms, $\boldsymbol{\sigma}_0 = (4, 3, 2, 1)$ mS/cm, 5%noise.

3.2.3 Surrogating the BICP with the MICP

Even with a substantial lack of physiological motivation in the assumption of proportionality between the two conductivity tensors, the Monodomain model is a popular and useful approximation of the Bidomain problem for the approximation of the transmembrane potential. It has been used for preconditioning the solution of the Bidomain problem [90, 94], or in an adaptive modeling framework [95]. In addition, as previously mentioned, an accurate quantification of the Bidomain conductivities relies on the availability of extracellular potential, yet difficult to measure in practice. Since the Monodomain equations (2.25) do not depend on the extracellular potential, an alternative approach might be using the MICP as a surrogate to the BICP. Another advantage of using MICP is that it can be a practical workaround for high computational cost related to BICP. In fact, MICP is much cheaper to solve than the BICP (we experience about 7 times faster when the two problems are solved on the same computer architecture). Also, reduced order models for MICP have been already studied [41], providing an even more efficient approach to the classical variational one used here.

In practice, we test here an approach to reconstruct the Monodomain conductivity

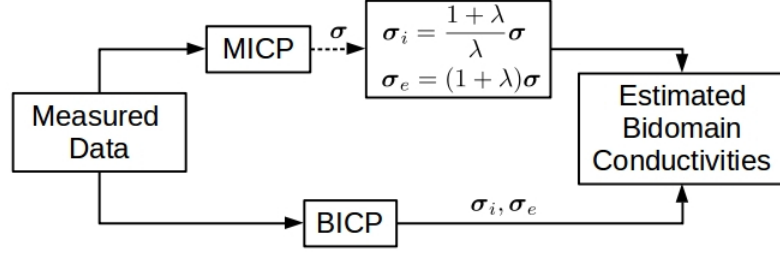Figure 3.11: Possible approaches for the BICP: at the bottom the original formulation of the BICP, at the top the surrogate approach solving the MICP and eventually extracting the conductivity tensors for the Bidomain model.

tensor $\boldsymbol{\sigma}$ with a twofold purpose. On the one hand, we use the estimated Monodomain conductivity to surrogate an estimate for the Bidomain tensors $\boldsymbol{\sigma}_e$ and $\boldsymbol{\sigma}_i$. Then, we test how close the approximation to the original data set (synthetically generated by a Bidomain solver) with the estimated tensor $\boldsymbol{\sigma}$ is. In other terms, *we use the estimated tensor of the Monodomain model as an effective parameter*, whose quantification is intended to fit the data. We combine in this way a physical model with a data-oriented approach. The scheme is illustrated in Fig. 3.11.

Data obtained under the assumption $\boldsymbol{\sigma}_e = \lambda \boldsymbol{\sigma}_i$ The Monodomain model is derived from the Bidomain model by assuming that $\boldsymbol{\sigma}_i$ and $\boldsymbol{\sigma}_e$ are proportional, i.e., $\boldsymbol{\sigma}_e = \lambda \boldsymbol{\sigma}_i$. By assuming such proportionality to hold and then using the potential u generated by the Bidomain model as synthetic data for our estimation procedure, we intend to analyze how close the estimated conductivity reconstructed by MICP is to the exact values of conductivities used by the Bidomain model. Notice that in this case even using the same mesh we do not have any inverse crime, as the data are generated by the Bidomain system and the conductivities are reconstructed by the Monodomain problem.

The synthetic measurements were generated on the slab mesh by the Bidomain model with $(\sigma_{il}, \sigma_{el}, \sigma_{it}, \sigma_{et}) = (3.45, 4.485, 0.575, 0.7475)$ mS/cm ($\lambda = 1.3$). Since $\boldsymbol{\sigma} = \frac{\lambda}{\lambda+1} \boldsymbol{\sigma}_i$, the exact Monodomain conductivity is $\boldsymbol{\sigma}_{exact} = (\sigma_l, \sigma_t) = (1.95, 0.325)$ mS/cm. Following Fig. 3.11 (top path), the test was performed with $\Delta t = 0.025$ ms, $\Delta t_{snap} = 0.5$ ms, 1% of noise. We referred to the Minimal model for canine ventricular cells. The estimation procedure starts from $\boldsymbol{\sigma}_0 = (1, 1)$ mS/cm. As assumed in some test cases in 3.2.2, we considered the
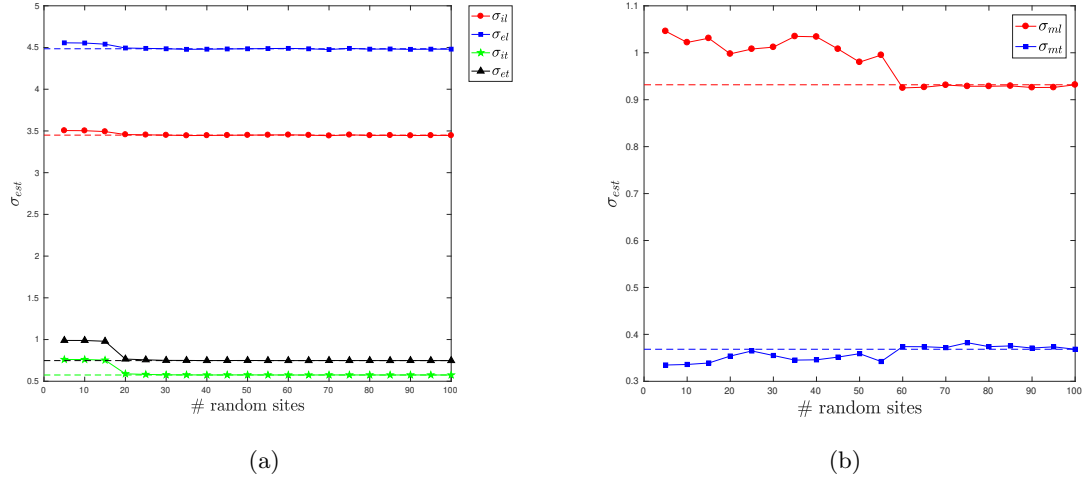
Figure 3.12: Estimation results ([mS/cm]) of MICP as surrogate of BICP vs. number of random sites (up to 100). (a) Estimated conductivities by the MICP and using the Bidomain solution u with $(\sigma_{il}, \sigma_{el}, \sigma_{it}, \sigma_{et}) = (3.45, 4.485, 0.575, 0.7475)$ mS/cm as synthetic data. The Monodomain assumption of proportionality $\boldsymbol{\sigma}_e = \lambda \boldsymbol{\sigma}_i$ holds ($\lambda = 1.3$) and the exact value for MICP to reconstruct is $\boldsymbol{\sigma}_{exact} = (1.95, 0.325)$ mS/cm. (b) Estimated conductivities by the MICP and using the Bidomain solution u with $(\sigma_{il}, \sigma_{el}, \sigma_{it}, \sigma_{et}) = (3.4, 1.2, 0.6, 0.8)$ mS/cm as synthetic data. Here $\boldsymbol{\sigma}_m$ denotes the Monodomain conductivity tensor.

# run	1	2	3	4	5	6	7	8	9	10
σ_l	3.00	1.80	1.77	1.96	1.81	1.94	1.77	1.82	1.83	1.80
σ_t	1.01	1.02	0.98	0.33	1.42	0.34	1.37	1.37	1.66	1.20

Table 3.9: Sensitivity of MICP to the initial guess $\boldsymbol{\sigma}_0 = (3, 1)$ mS/cm and location of the measurement sites. $\boldsymbol{\sigma}_{exact} = (1.95, 0.325)$ mS/cm.

position of u measurement sites to follow an i.i.d. uniform distribution defined over the top surface of the slab. For each number of sites, we ran the MICP 10 times with different realizations of the measurement locations and computed the average of the estimates as the final estimation result. Fig. 3.12(a) shows that the conductivity values estimated by the MICP are significantly accurate.

However, as expected, these results are sensitive to the initial guess $\boldsymbol{\sigma}_0$. As a matter of fact, we did not find a clear convergence pattern over 10 runs (see Table 3.9, 100 measurement sites) when testing with another initial guess $\boldsymbol{\sigma}_0 = (3, 1)$ mS/cm. A practical workaround for the identification of the conductivity can be to run using different initial guesses and identifying the presence of a pattern (as it happens for $\boldsymbol{\sigma}_0 = (1, 1)$ mS/cm).

Generic conductivities In this test, we no longer assume proportionality between the intracellular and extracellular conductivities. Our goal is to check whether an appropriate estimate of the Monodomain conductivity tensor $\boldsymbol{\sigma}$ based on our variational procedure can still lead to an accurate reconstruction of the potential propagation generated by the Bidomain solver. Notice that, in this case, we do not have an exact value for $\boldsymbol{\sigma}$ to compare our results. In fact, the ultimate goal here is to find a representative value for the tensor $\boldsymbol{\sigma}$ that, regardless to a precise physical explanation, could reproduce the potential data reliably. This will be extremely helpful while performing experimental validation.

We computed the Bidomain solution u with $(\sigma_{il}, \sigma_{el}, \sigma_{it}, \sigma_{et}) = (3.4, 1.2, 0.6, 0.8)$ mS/cm and solved the MICP. As usual, for each number of random sites, the final estimates are an average of 10 conductivity values reconstructed testing the estimation procedure with different realizations of the measurement position. We picked $\boldsymbol{\sigma}_0 = (1.2, 0.3)$ mS/cm as the initial guess for the optimization algorithm. By looking at Fig. 3.12(b), we notice that, from 60 measurement sites on, the estimates converge to the values $\boldsymbol{\sigma} = (0.93, 0.37)$ mS/cm.

Then, by using such estimated conductivity values in the forward Monodomain problem, we compared the Monodomain solution u with the Bidomain one. Fig. 3.13 shows that the reconstruction of the potential by the Monodomain solver gives an excellent matching with the Bidomain solution. Actually, we expected to retrieve the same AP weveform because Bidomain and Monodomain solvers are coupled with the same ionic model (Minimal model) which is responsible of the AP shape. However, it is remarkable that the reconstructed AP via the Monodomain model does not feature any shift in time with respect to the Bidomain AP, meaning the solution provided by the MICP reproduces the same wave propagation velocity of the Bidomain data.

As noticed in the previous test, the estimation depends on the initial guess $\boldsymbol{\sigma}_0$ as well as the location of the measurement sites. Table 3.10 shows that, for 100 sites, the reconstructed conductivities are consistent with the result obtained with $\boldsymbol{\sigma}_0 = (1.2, 0.3)$ mS/cm only for few runs of the optimization algorithm. Despite few runs in which the method provides parameters substantially different from $\boldsymbol{\sigma} = (0.93, 0.37)$ mS/cm, the estimation procedure reconstructs conductivities close to $\boldsymbol{\sigma}_0$ in the majority of the runs.

This dependence can be mitigated by introducing a Tikhonov-like regularization term,
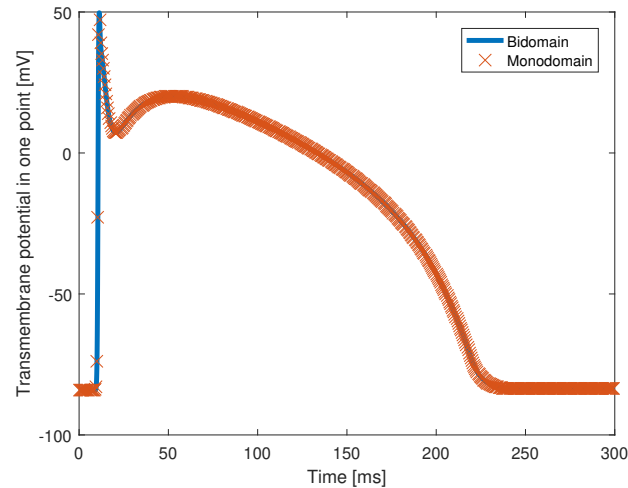
Figure 3.13: Comparison between the reconstructed Monodomain AP u and the Bidomain solution. The solution of the MICP reproduces the same wave propagation velocity of the Bidomain data.

	# run	1	2	3	4	5	6	7	8	9	10
(a)	σ_l	1.01	1.00	0.93	1.00	1.00	1.02	1.00	1.00	0.92	1.81
	σ_t	1.00	1.00	0.37	1.00	1.00	1.00	1.00	1.00	0.38	0.51
(b)	σ_l	1.11	2.01	0.93	1.31	2.00	2.03	2.01	2.01	2.01	2.01
	σ_t	1.66	1.00	0.37	1.21	1.00	1.04	1.00	1.00	1.00	1.00

Table 3.10: (a) $\boldsymbol{\sigma}_0 = (1, 1)$ mS/cm, (b) $\boldsymbol{\sigma}_0 = (2, 1)$ mS/cm. Sensitivity of MICP on the initial guess $\boldsymbol{\sigma}_0$ and location of the measurement sites. The rows represent the estimated conductivity values ([mS/cm]) for each run of MICP picking 100 random sites. Marked in red are the estimates consistent with $\boldsymbol{\sigma} = (0.93, 0.3)$ mS/cm obtained originally with $\boldsymbol{\sigma}_0 = (1.2, 0.3)$ mS/cm.

#	1	2	3	4	5	6	7	8	9	10
σ_l	1.74	1.76	1.74	1.33	1.75	1.16	1.75	0.93	0.93	1.76
σ_t	0.33	0.35	0.33	0.50	0.34	0.33	0.34	0.37	0.37	0.35
$\mathcal{J}$	0.040	0.038	0.033	0.031	0.034	0.004	0.043	0.001	0.001	0.363

Table 3.11: Estimates ([mS/cm]) of MICP using Tikhonov-like regularization ($\alpha = 10^{-4}, r = 0.25$) and $\boldsymbol{\sigma}_0 = (1,1)$ mS/cm ($\mathcal{J}(\boldsymbol{\sigma}_0) = 0.0611$). Marked in red are the estimates consistent with $\boldsymbol{\sigma} = (0.93, 0.37)$ mS/cm obtained with $\boldsymbol{\sigma}_0 = (1.2, 0.3)$ mS/cm.

for example $\mathcal{R}(\boldsymbol{\sigma})) = \alpha/2 \left\| \sigma_t/\sigma_l - r \right\|^2$, where r is a reasonably guessed ratio. From Table 3.11, we notice that the method does not stagnate close to the initial guess anymore, but it detects different local minima. Among them, $\boldsymbol{\sigma} = (0.93, 0.37)$ mS/cm, consistent with the results obtained in the previous test, provides the most accurate estimate since it features the lowest value of the misfit functional $\mathcal{J}$.

The results lead to two conclusions. Using MICP to surrogate the computation of the conductivities is beneficial for an estimate of the Bidomain tensors if the simplifying assumption behind the Monodomain problem is reasonably accurate. In fact, the estimate of $\boldsymbol{\sigma}$ is accurate enough to generate a good estimate of the Bidomain tensors. This approach is sensitive to the initial guess - as expected - and workarounds based on the introduction of Tikhonov-like regularization terms can be exploited. This aspect will deserve further investigation.

More in general, the solution of the MICP provides a tensor $\boldsymbol{\sigma}$ that allows an accurate reconstruction of the potential. In practice, if one is interested in having a nominal tensor (regardless of the physical explanation) to be used in the numerical simulations for the accurate computation of the transmembrane potential, this approach candidates as a viable solution joining reliability and computational efficiency.

What we have learned so far

1. The accuracy of the BICP depends on extracellular potential measurements which are troublesome to record experimentally. Therefore, simulations were performed in order to get more insights on the minimal number of recordings needed to ensure reasonable accuracy. Numerical results suggest that reliable estimates are obtained with at least 10 u_e sites.

2. Under the condition established in the previous point 1, the estimation procedure is robust in presence of uncertainty induced by random sites as well as lack of precise information about the position of observation points. This is an important feature especially in clinical applications where data is affected by noise.

3. An experimental setting featuring multiple stimulations for initiating the propagation seems to carry more information about the dynamics of the system than a one point pacing protocol, thus resulting in a more precise estimation. However, results are similar in case of data recorded on a larger time window.

4. The estimation of the Monodomain conductivity is a good surrogate of the Bidomain one. Moreover, using the Monodomain eliminates the problem of extracellular potential recording, thus it is more feasible in clinical settings.

3.2.4   Moving towards real validation

In view of real validation, we aim to investigate the performances of the estimation procedure in case of more realistic tissues featuring heterogeneity. In addition, an accurate identification of the proper numerical discretization necessary for experimental validation is performed. Henceforth, we restrict our attention to the Monodomain problem. This is due to the fact that, not only MICP can be regarded as a surrogate of the BICP as seen in the previous Section, but also its computational convenience with respect to the Bidomain system is crucial in clinical applications [93]. We refer to the reshaped Monodomain equation presented in (2.27) with dimensionless voltage u. For the sake of notation, the conductivity tensor $\mathbf{D} = \boldsymbol{\sigma}/(\beta C_m)$ is denoted by $\boldsymbol{\sigma}$ as usual, now measured in cm^2/ms.

The methodology is tested on 2D geometries since the optical mapping data used for experimental validation consist of voltage recordings on a 2D grid. We consider planar waves of cardiac excitation during regular pacing [119] for which the Bidomain and Monodomain formulations ensure the same level of accuracy. This propagation dynamics is generated by applying only one stimulus which, as previously discussed, is not the most suitable experimental design. However, since we collected a large amount of optical data, the inversion can be tested on a larger time interval. As seen in Test 1 of 3.2.2, this allows us to increase

the accuracy of the estimation at the expense of computational efficiency. We identified both hardware and software solutions to cope with the higher computational burden. On one hand, these simulations were carried out using more cores than the previous tests so to reduce computation time. On the other hand, the goal is to improve the initial guess of the optimization algorithm. As for any nonlinear iterative problems, the choice of the initial guess is critical both for the final solution (in absence of uniqueness of the solution) as well as the convergence speed. The choice needs to be clearly educated based on the problem at hand and the experience (or the available literature). Yet, this may be not optimal. For this reason, we investigate here two different techniques, hereafter denoted as *Standard* and *Refined*, respectively, for deciding an initial guess $\boldsymbol{\sigma}_0$. In the Standard scheme, we perform the optimization procedure globally on the time interval $[0, \mathrm{T}]$ as previously described in 3.1.2 with an initial guess suggested by the experience (trial and error). In the Refined approach, the arbitrary/trial and error initial guess $\boldsymbol{\sigma}_0$ is improved by adopting the following pre-processing strategy, relying on the time-independence of the conductivities. First, the full time span $[0, \mathrm{T}]$ is divided into shorter time intervals of length $\mathrm{dt_{opt}}$. Then, in each time slot, we perform the optimization using as initial guess the estimation obtained in the previous time interval. Obviously, in the first time interval $[0, \mathrm{dt_{opt}}]$, the optimization procedure starts from $\boldsymbol{\sigma}_0$. Once the last optimization step is performed, the final estimation is used as initial guess of our estimate in the full time interval $[0, \mathrm{T}]$. The overall Refined procedure is expected to be more convenient as the last estimate will converge more rapidly thanks to the new initial guess, that is supposed to be more informed.

Standard vs. refined schemes The computational domain is selected to be a square $[0, 6]\,\mathrm{cm} \times [0, 6]\,\mathrm{cm}$. The conductivity fields $\sigma_l(\mathbf{x})$ and $\sigma_t(\mathbf{x})$ are defined on a coarse mesh (# DOF = 109) whereas the membrane potential is discretized on a finer mesh (# DOF = 94721). For the easiness of the implementation, the meshes are chosen to be nested, i.e., the nodes of the coarse mesh are also nodes of the fine one. Synthetic measurements u_{meas} were generated every $dt_{snap} = 2\,\mathrm{ms}$ for a global duration of $T = 300\,\mathrm{ms}$. The angle of the cardiac fibers is $\theta = -43°$ with respect to the x-axis, such that no symmetry appears on the squared domain. The observation domain Ω_{obs}, where we collect u_{meas}, consists of

8000 equally distributed points on the domain, which is comparable with the number of observation points we can get in optical mapping recordings. To test the two optimization schemes proposed above, we assume uniform conductivity fields in the domain Ω. Synthetic data were generated with $\sigma_{l,exact}(\mathbf{x}) = \sigma_{t,exact}(\mathbf{x}) = 6 \cdot 10^{-3}$ cm^2/ms and Gaussian noise with zero mean and standard deviation equal to $p \max |u|$, where p is the percentage of noise, and the maximum is taken in both space and time, was added at each time step. A stimulus of intensity $I_{app} = 0.5$ ms^{-1} is applied at the midpoint of the left edge of the square for a duration of 2 ms. The initial guess is $\sigma_{l,0}(\mathbf{x}) = \sigma_{t,0}(\mathbf{x}) = 4 \cdot 10^{-3}$ cm^2/ms and the mean conductivity values in (3.8) were taken as $\sigma_{l,mean}(\mathbf{x}) = \sigma_{t,mean}(\mathbf{x}) = 5 \cdot 10^{-3}$ cm^2/ms (see e.g. [69, 76]). To investigate the effect on the solutions of the regularization parameters, we performed several estimations with different values of α_1 and α_2 in the range $[10^{-7}, 1]$. As well known, this is a critical step in the numerical solution of inverse problems. For large values, the regularization term (3.8) prevails over the misfit term enforcing the results to be close to the expected (yet, arbitrary) mean conductivity values $\sigma_{l,mean}(\mathbf{x})$ and $\sigma_{t,mean}(\mathbf{x})$. On the other hand, the regularization is critical for the convexity of the functional to minimize and, ultimately, for the convergence of the numerical solver, that may be impaired by exceedingly small values of the parameters. After some experiments, we chose the values $\alpha_1 = 10^{-5}$ and $\alpha_2 = 10^{-4}$. As $\alpha_1 \ll \alpha_2$ the arbitrary choice of $\sigma_{l,mean}(\mathbf{x})$ and $\sigma_{t,mean}(\mathbf{x})$ marginally affects the solution, while gradient regularization results pretty effective for the convergence. Strategies for an automatic tuning of these parameters still need to be pursued.

For the initial guess, Table 3.12 shows a comparison between the Standard and Refined algorithms. The Refined scheme outperforms the Standard approach, both in terms of accuracy and efficiency. As a matter of fact, the estimated conductivities using the Refined OD approach features lower L^2-norm of the error. The use of the informed initial improves convergence of the optimization procedure reducing computational cost. Therefore, we use the Refined OD scheme throughout the following numerical tests.

Presence of a Scar   We now focus on the estimation of conductivities in a pathological tissue. In the following test, the cardiac tissue is scarred, that means that a portion of the tissue has an abnormal value of the conductivities. Detection of anomalies based on a similar

	L^2 error $\sigma_l|\sigma_t$	Exec. time	# fwd|bwd
Standard OD	$4.4 \cdot 10^{-2}|8.0 \cdot 10^{-2}$	31.5 h	85|36
Refined OD	$4.6 \cdot 10^{-3}|2.5 \cdot 10^{-2}$	21.0 h	28|19

Table 3.12: Comparison between standard and refined OD optimization strategies ($dt_{opt} =$ 10 ms). The refined OD scheme provides a more accurate estimation and is computationally cheaper than the standard OD approach. # fwd denotes the number of solves of the state equations, and # bwd represents the number of solves of the adjoint equations.

variational approach to the one advocated here is considered in recent works [143–145]. The presence of a scar on real patients may trigger pathological patterns in the action potential propagation. Here, the scar is represented (Fig. 3.14(a)) as a circular region with radius 1.5 cm located at the center of the tissue featuring the anomalous values of conductivities [146].

As shown in Fig. 3.14(b), the optimization procedure is able to detect correctly both the location of the scar and the conductivity values. The initial guess in Fig. 3.14(c) features a discontinuity on the tissue and this is a reasonable choice since the presence of a scar can be visually detected by looking at the data. However, the algorithm has been also tested starting from uniform conductivities and it provides similar results. The error $|u - u_{meas}|$ with the respect the dynamics showed in Fig. 3.14(d) at different time steps is shown in Fig. 3.14(e). The downside of our methodology in this case is that the computational burden substantially increases due to significant growth of the number of optimization iterations. The estimation process requires 132 forward solves and 58 backward solves, that means a huge increment with respect to the uniform case. This reflects on higher computation time, as it increases from 20 hours of the uniform case to roughly 70 hours.

Canine tissue geometry In view of the validation with experimental data, we test the accuracy of the estimation procedure considering a realistic 2D geometry of a portion of a canine ventricular tissue [119]. First of all, we need to assess an accurate resolution for the fine mesh used for modeling the membrane potential u so that the *Conduction Velocity* (CV) of the real wavefront propagation can be accurately reproduced. It is well-known from the literature that coarse meshes lead to overestimation of the CV [147–149]. Therefore, the mesh must be fine enough to accurately catch the physics of the problem. A reasonable level of discretization can be identified by looking at the plateau point of the CV

σ_l

σ_t

(a)

(b)

(c)

t = 10 ms

t = 20 ms

t = 30 ms

(d)

0.0   0.1

(e)

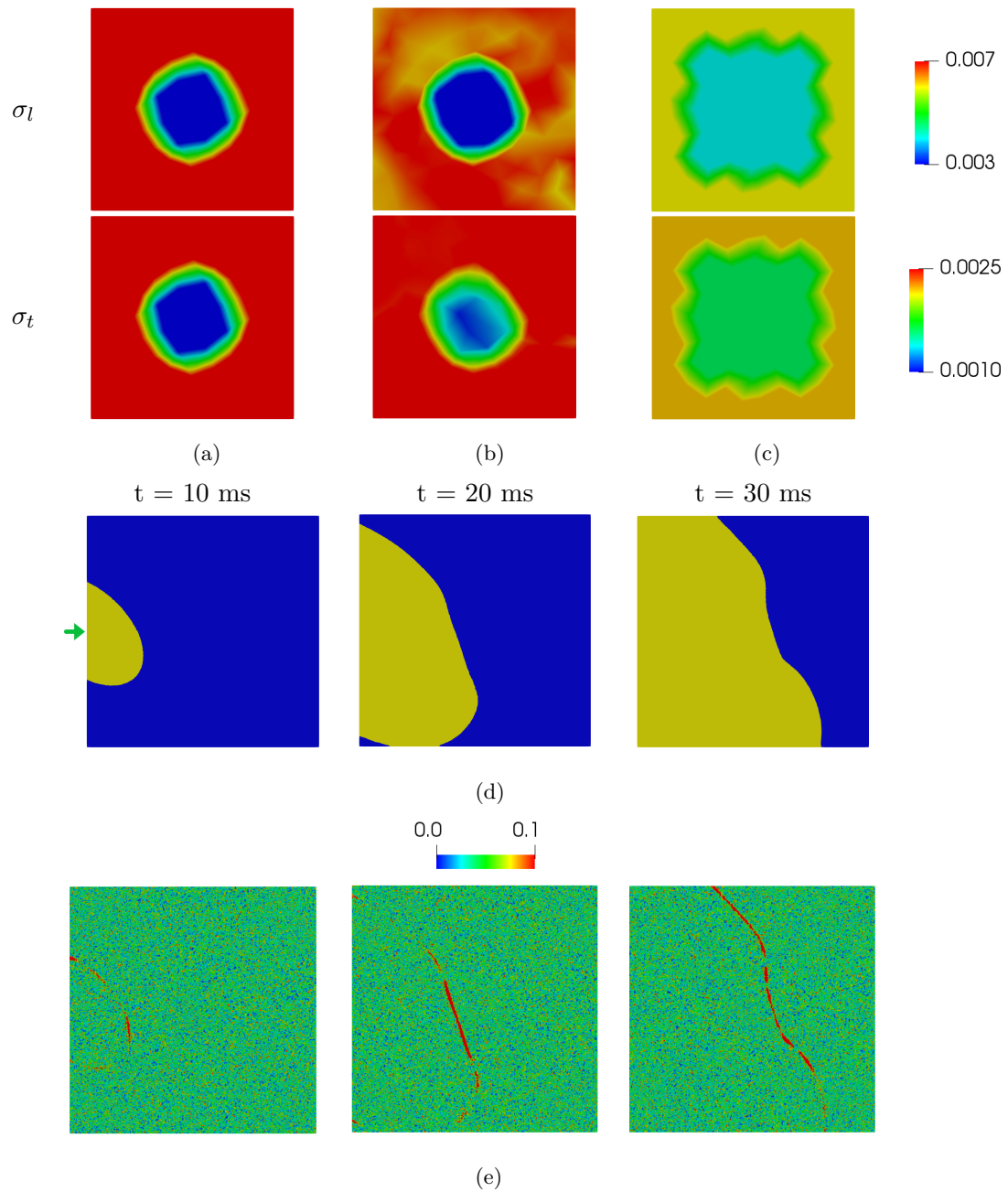Figure 3.14: (a) Pathological tissue with a circular scar in the center featuring lower conductivity ($[cm^2/ms]$); (b) Estimated conductivity fields; (c) Initial guess. (d) Synthetic AP propagation in presence of the scar. The wavefront slows down in the scar because of lower conductivity in that region. Green arrow indicates the site of stimulation. (e) $|u - u_{meas}|$ at different time steps (u is dimensionless).
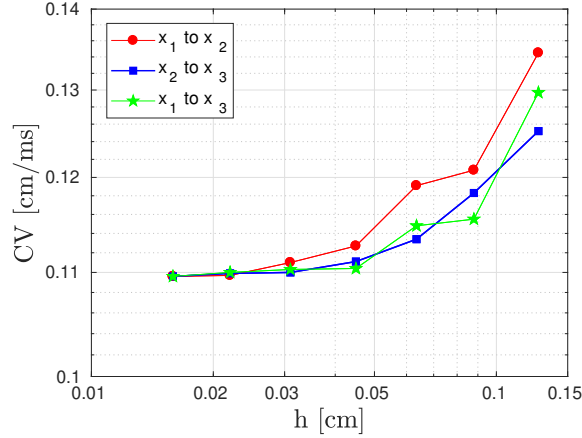
Figure 3.15: CV convergence plot at different resolutions h in three aligned points of the mesh. Any resolution $h < 0.03$ cm provides a reliable approximation of the physics of the system.

convergence plot. Such a plot is obtained by estimating the CV in some points of the mesh at different resolutions h, the maximum diameter of the mesh. Below a certain threshold on h, the CV remains constant meaning that the mesh is fine enough to reliably describe the dynamics of the system. Using fine meshes clearly increases the computational costs. This can be mitigated by resorting to non-conforming finite elements recently discussed in the literature [150].

From Fig. 3.15, we notice that for any $h < 0.03$ cm, the CV at three aligned points of the mesh remains constant, so we argue that $\bar{h} = 0.03$ cm is the minimum resolution of the mesh that guarantees an accurate approximation of the physics of the problem. Following this rationale, we chose $h = 0.028$ cm (corresponding to about 120k DOFs) which is a good trade-off between accuracy of the simulation and computational costs. The number of DOFs of the coarse mesh for the discretization of the conductivities is 99. Fig. 3.16(a) shows the cardiac fiber structure that was roughly approximated by looking at anatomy of the tissue. The stimulus is applied at the top of the domain for a duration of 2 ms. The potential propagation at different time steps for the case $\sigma_{l,exact}(\mathbf{x}) = 7 \cdot 10^{-3}$ cm^2/ms, $\sigma_{t,exact}(\mathbf{x}) = 2 \cdot 10^{-3}$ cm^2/ms is shown in Fig. 3.16(b). Gaussian noise with $p = 5\%$ was added to the synthetic data and $\sigma_{l,mean}(\mathbf{x}) = 6 \cdot 10^{-3}$ cm^2/ms, $\sigma_{t,mean}(\mathbf{x}) = 3 \cdot 10^{-3}$ cm^2/ms.

Several anisotropy ratios are chosen to test the estimation procedure as shown in Ta-
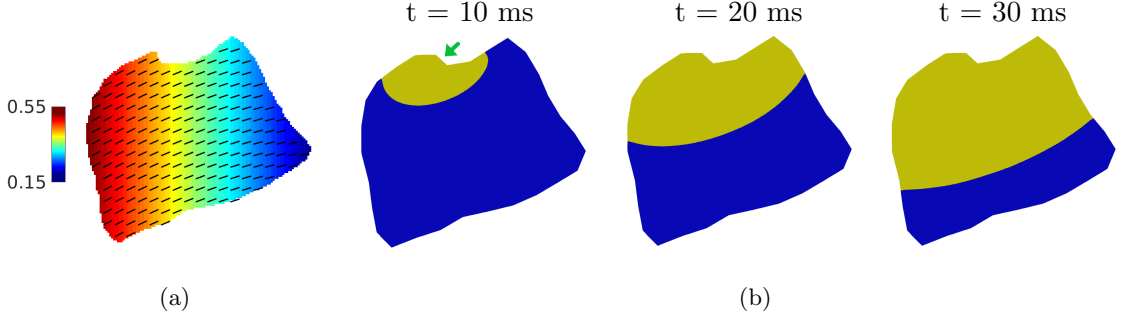
Figure 3.16: (a) Realistic geometry of a portion of a canine ventricular tissue and approximation of the fiber structure. The segments represent the local cardiac fiber direction and the colorbar indicates the value of the local fiber angle with respect to the x-axis. Unit is in radians. (b) Three snapshots of u_{meas} (contour line $u_{meas} = 0.75$). Green arrow indicates the site of stimulation where AP is triggered propagating towards the bottom.

$(\sigma_{l,exact}, \sigma_{t,exact})$	L2 error $\sigma_{l,est}\|\sigma_{t,est}$	mean	st.dev.
$(5.0, 2.0) \cdot 10^{-3}$	$3.6 \cdot 10^{-2}\|2.6 \cdot 10^{-2}$	$4.8 \cdot 10^{-3}\|2.0 \cdot 10^{-3}$	$3.1 \cdot 10^{-4}\|3.9 \cdot 10^{-5}$
$(6.0, 1.5) \cdot 10^{-3}$	$3.7 \cdot 10^{-2}\|2.3 \cdot 10^{-2}$	$5.8 \cdot 10^{-3}\|1.4 \cdot 10^{-3}$	$3.1 \cdot 10^{-4}\|4.3 \cdot 10^{-5}$
$(7.0, 2.0) \cdot 10^{-3}$	$4.6 \cdot 10^{-2}\|3.1 \cdot 10^{-2}$	$6.8 \cdot 10^{-3}\|2.1 \cdot 10^{-3}$	$8.7 \cdot 10^{-4}\|5.1 \cdot 10^{-5}$
$(10.0, 3.0) \cdot 10^{-3}$	$4.4 \cdot 10^{-2}\|3.2 \cdot 10^{-2}$	$9.8 \cdot 10^{-3}\|3.1 \cdot 10^{-3}$	$7.9 \cdot 10^{-4}\|4.4 \cdot 10^{-5}$

Table 3.13: L^2 relative error, mean and standard deviation of the estimated fields ($[\text{cm}^2/\text{ms}]$) in different cases for canine ventricular tissue geometry. The optimization procedure provides a reliable reconstruction of the true conductivity fields. In the last two cases featuring a faster CV, the accuracy of the estimation depends more significantly on the quality of the initial guess.

ble 3.13. In each case, the algorithm is able to accurately retrieve the true conductivity fields. When the CV is slow, meaning low conductivity, the method is robust with respect to the choice of $(\sigma_{l,0}, \sigma_{t,0})$. On the other hand, for the cases with faster CV, the initial guess has to be carefully selected to guarantee a reasonable accuracy. These simulations were more computationally demanding than the tests on the square domain (approximately 30 hours vs. 20 hours of the square case) because of the finer mesh resolution.

3.3 Experimental Validation

The purpose of this Section is to perform an extensive validation on *experimental data*. This is a fundamental step in assessing the actual reliability of the variational procedure in real problems. In Section 3.3.1, the experimental and numerical settings are described. An extensive comparison among numerical results from three different electrophysiological
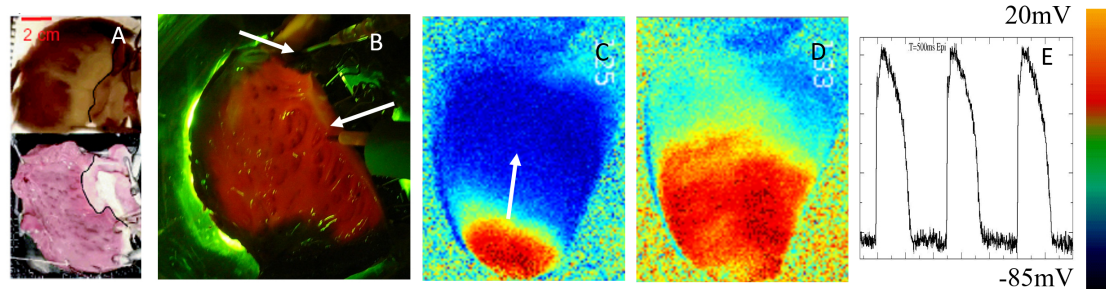
Figure 3.17: Example of experimental setting that drives our testing methodology. A) Canine right ventricle (RV) visualized from top and bottom with two optical mapping cameras. B) RV loaded with voltage dye and illuminated with green light, top arrow indicates perfusion that keeps the preparation alive, bottom arrow indicates stimulator to initiate voltage waves. C-D) Examples of a transmembrane wave voltage measured with optical mapping propagating from the apex to the base of a rabbit heart. E) optical mapping voltage signal from one pixel.

models and optical data is presented in Section 3.3.2 and 3.3.3.

3.3.1 Experimental and numerical settings

In this Section, we briefly illustrate the experimental protocol used to collect the experimental data and the calibration of the ionic models to deal with canine data.

Fluorescence optical data Fluorescence optical mapping recordings were obtained from canine right ventricle wedge preparations, according to the experimental protocols approved by the Institutional Animal Care and Use Committee of the Center for Animal Resources and Education at Cornell University. We refer to Fig. 3.17 and [97, 119] for details of the experimental setup. The imaging has a spatial resolution of $\sim 600\,\mu$m per pixel for a grid size of $\sim 7 \times 7\,\text{cm}^2$ and a temporal resolution of $2\,\text{ms}$. Data filtering and postprocessing were performed via a custom-built interactive Java program, in particular for removing signal drift and fluorescence noise, normalizing the signal on a pixel-by-pixel basis, averaging in time on a 7 frames length, and averaging in space with a two-dimensional weighted Gaussian function. The resulting analyzed data have been proved to retain tissue local heterogeneities, amenable for an extensive usage for modeling purposes [151–154]. For estimating space-dependent cardiac conductivities from action potential data obtained at different pacing Cycle Length (CL), we tuned the ionic model parameters to fit the restitution of APD (APD-

RC) introduced in Section 2.1.2. The experimental APD-RC was obtained by applying multiple electrical stimulations, e.g. 20, at constant pacing with period CL starting from high values (typically 1000 ms) and decreasing in 50 ms steps until reaching CL = 250 ms, after which CL was shortened in 10 ms ms decrements until capture was lost or ventricular fibrillation was induced. At each CL, pacing was applied for at least 1 min before recording to ensure that steady state was reached, then recordings were made for 5 s, or more, at each CL. APD was measured at 25% repolarization threshold ensuring a minimum level of basal noise. The RC is then obtained by plotting APD vs. CL. We recall that a list of acronyms and abbreviations can be found in Chapter 1.

Choice of the ionic models   As we refer to canine experimental data, we need to calibrate the ionic model accordingly. The Minimal model (MM) used in the synthetic validation does not fit at best the available experimental data, since the temporal resolution of the optical mapping camera used for data collection is not fine enough to catch the upstroke of the action potential. This results in a much smoother AP shape (see Fig. 3.18(a)). Therefore, although the MM model provides a realistic simulation of cellular electrical activity, we considered the Fenton-Karma (FK) (2.10) and Mitchell-Schaeffer (MS) models instead (2.8). Even though these models provide a much more simplified approximation of the physics of the problem, they are expected to provide a better reconstruction of the data at hand because of the AP shape similarity with optical data.

The model-based restitution curves were calculated performing one dimensional cable simulations and following a protocol similar to the experimental one. The ionic model parameters were manually tuned so to minimize the discrepancy between experimental and the modeled restitution curves. The AP shapes and restitution curves for the FK and MS ionic models are shown in Fig. 3.18(b), and 3.18(c), respectively. It is worth noting that, for the single case of experimental data we are considering, the MS model provides a better fit of the experimental RC than the FK one, especially at high CL, as well as a more accurate match of the AP shape. On the other hand, FK features a more realistic wavefront propagation at low CL, as we will see in the following tests. The 2D fine mesh for approximating u has the maximum diameter $h = 0.028$ cm, $T = 230$ ms, $dt_{snap} = 2$ ms
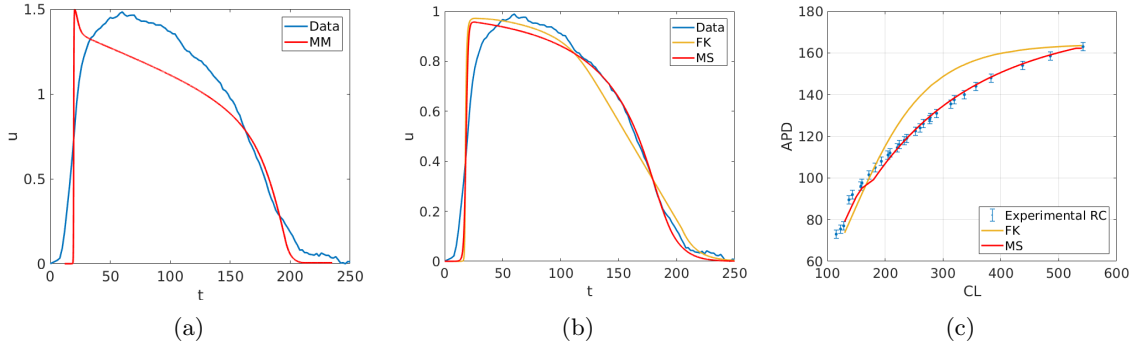
Figure 3.18: (a) AP shape modeled with the Minimal model. The AP features an upstroke that is missing in the experimental data. (b) Simulated AP shapes for FK and MS. Red curve represents the modeled AP and the blue the experimental one. MS provides a better match than FK especially in the repolarization phase. (c) Experimental APD restitution curve compared with the modeled ones obtained with MS and FK models.

and Tikhonov-like regularization term (3.8) is disabled ($\alpha_1 = \alpha_2 = 0$). The number of observation points varies among the tests we performed, but it is approximately 8000. It is worth stressing that, since we were given a large amount of data which was recorded before the research presented in this Thesis was performed, the sensitivity analysis presented in Section 3.2.1 and 3.2.2, in particular in the cases of lack of data, will be used to set up future experiments. As for computation time, depending on the ionic model and the values of CL, the following tests took on average between 2 and 5 hours, which is significantly less than the synthetic simulations. This is due to the higher number of cores involved in the computation as well as the highly optimized libraries and compilers available on the SKX nodes of Stampede II.

3.3.2 Validation at slow pacing rates

We estimated the conductivities from AP optical mapping measurements recorded at CL=540 ms. Three different resolutions $h_M = (1, 0.44, 0.25)$ cm are considered for the coarse mesh. The goal was determining the minimum resolution in order to capture enough heterogeneity in the conductivity fields and, in turns, to be able to provide an accurate reconstruction of the experimental data. For each resolution, conductivity fields are estimated using the FK model. The initial guess of the optimization algorithm was chosen so that the wavefront propagation is comparable to the experimental data.
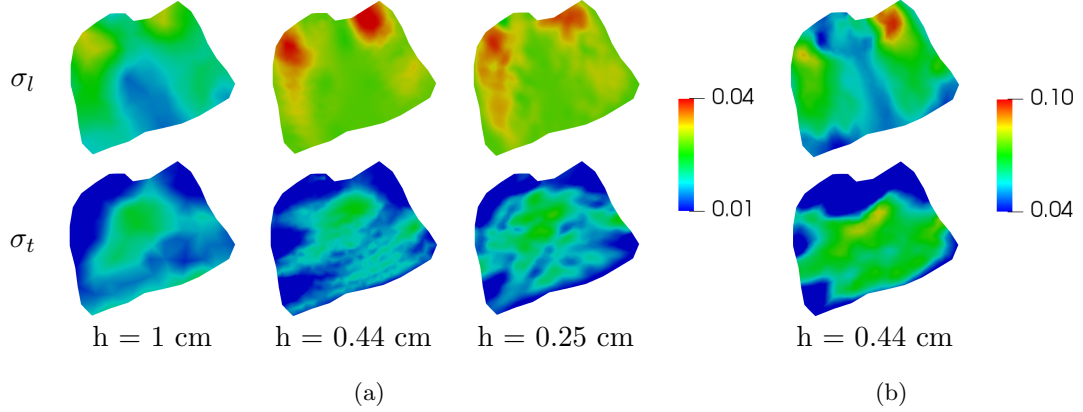
Figure 3.19: Estimated conductivity fields [(cm^2/ms)] at CL = 540 ms: (a) FK model with three levels of discretization of the coarse mesh; (b) MS model. While there is a huge difference between the estimations at $h = 1$ cm and $h = 0.44$ cm, the results at $h = 0.44$ and $h = 0.25$ cm are qualitatively similar. Therefore, we select the coarse mesh with $h = 0.44$ cm to perform experimental validation. Moreover, MS and FK models identify similar slow and fast conducting areas.

As shown in Fig. 3.19(a), the estimation highly depends on the mesh. In particular a significant discrepancy can be observed between the results obtained with $h_M = 1$ cm and $h_M < 1$ cm. The conductivity maps look qualitatively similar for $h_M = 0.44$ cm and $h_M = 0.25$ cm. Henceforth, we used the coarse mesh with $h_M = 0.44$ cm (# DOFs = 512) to limit computational costs. The conductivity fields obtained with the MS model shown in Fig. 3.19(b) are comparable – though varying over a wider range – to the ones retrieved with the FK one in Fig. 3.19(a), meaning that the two models are able to detect both fast and slow conducting regions. In addition, we tested the assumption of anisotropic conductivities by comparing the results with the reconstruction obtained assuming isotropic conductivities ($\sigma_l(\mathbf{x}) = \sigma_t(\mathbf{x})$) (displayed in Fig. 3.20).

Fig. 3.20 shows a comparison between the contours line at $u = 0.5$ of the experimental data and the modeled AP propagation using MS and FK models with anisotropic conductivity and FK model with isotropic conductivity at three snapshots. Regardless of the ionic model, the reconstruction of experimental data seems accurate both in shape of the wavefront and its velocity for $t = 16$ ms and $t = 20$ ms. As for $t = 12$ ms, the algorithm coupled with the FK model overestimates the conductivity in the region near the stimulation point leading to a higher CV. On the other hand, the MS outperforms FK providing a more
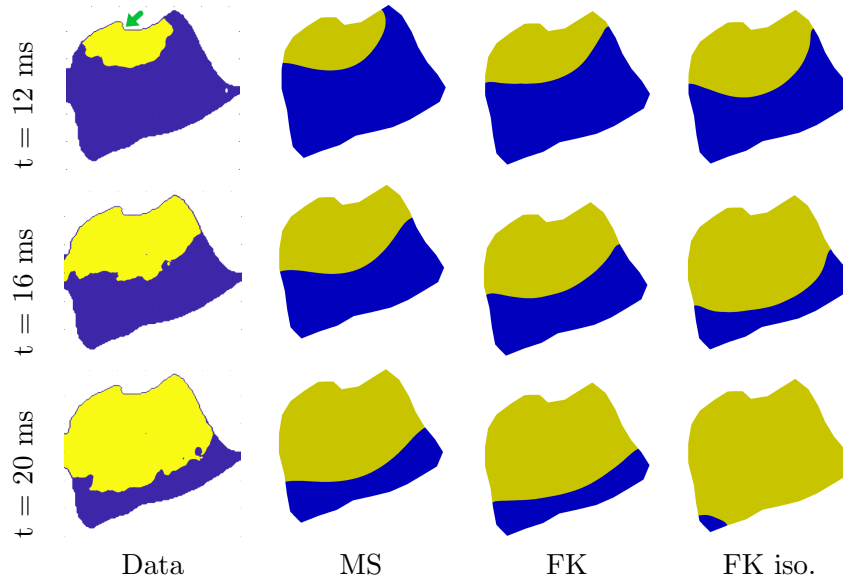
Figure 3.20: CL = 540 ms, comparison between experimental and modeled contour lines assuming anisotropic (MS and FK) and isotropic conductivity fields (FK iso.). Green arrow indicates the site of the stimulation. The lack of anisotropy in the conductivity leads to a poor reconstruction of the experimental data.

reasonable reconstruction of the wavefront propagation. Moreover, the estimation comes along with less computational effort since the MS model is much simpler and faster to solve than FK. Therefore, MS is preferable to FK both in terms of accuracy and reduction of the computational costs. However, for lower values of CL at which the dynamics of the system become more challenging to model, we may expect FK to perform better than MS since it provides a more accurate approximation of the physics of the problem.

Nevertheless, since the measurement errors are higher in proximity of the stimulation point and the data are more noisy, we will only focus on the modeled AP propagation sufficiently far away from the stimulation area in order to provide a fair comparison between the estimates. It is also noticeable that the assumption of anisotropic conductivities is crucial for the accurate reconstruction of the real data. As a matter of fact, assuming isotropic conductivity leads to poor reconstruction of the experimental data since the CV is overestimated at each snapshots. This might be due to the fact that the isotropic conductivity does not take into account the effect of the fibers on the propagation of the electrical signal which however seems to be crucial for an accurate reconstruction of the real AP. Henceforth, we consider anisotropic conductivities only.

3.3.3 The role of CL on the estimation

In the following numerical tests we investigate the interplay between the reliability of our estimation procedure and the value of CL. The conductivity fields are estimated using data collected at decreasing values of CL retrieved from the experimental APD restitution curve. For each value of CL, we consider two different strategies for initializing the optimization algorithm.

The first strategy is using the estimation of $\boldsymbol{\sigma}$ obtained at the previous CL as an initial guess for the next inverse problem. We call this a *dynamic* procedure, as it combines the experimental observations with a prior knowledge in order to initialize the optimization algorithm. The second approach, calles *static*, consists of using the same initial guess $\boldsymbol{\sigma}_0$ for all the parameter identifications performed at each value of CL. A uniform isotropic conductivity field of value 0.01 cm^2/ms (used to fit the experimental APD restitution curve) is chosen as initial guess.

The dynamic approach is expected to outperform the static one because the optimization algorithm starts from an initial guess already providing a reliable match of the data. Moreover, setting realistic initial condition $u_0(\mathbf{x})$ for the forward solver is crucial for an accurate simulation of the electrical propagation, especially at low CL. As a matter of fact, numerical experiments have shown that pacing of resting cardiac tissue ($u_0(\mathbf{x}) = 0$) at low CL does not trigger AP propagation. Therefore, $u_0(\mathbf{x})$ is set following a protocol similar to the experimental one. The tissue is electrically stimulated twice starting from high CL (typically 500 ms or higher) and decreasing in 50 ms decrements until reaching 300 ms, after which the CL is shortened in 20 ms decrements. Once the desired CL is reached, pacing is applied twice and the final state is stored and used as initial condition for the forward solve in the estimation process. By following this strategy, the system responds to stimuli even at low CL and electrical wave propagation is triggered.

Here, we report the results of the estimation for decreasing values of CL = [540, 440, 357, 320, 289, 266, 233] ms. The estimated conductivity fields for different CL values and strategies using the MS model are shown in Fig. 3.21. Looking at the misfit $\mathcal{J}$ with MS and the dynamic vs the static strategy (see Fig. 3.22), the former provides a more accurate
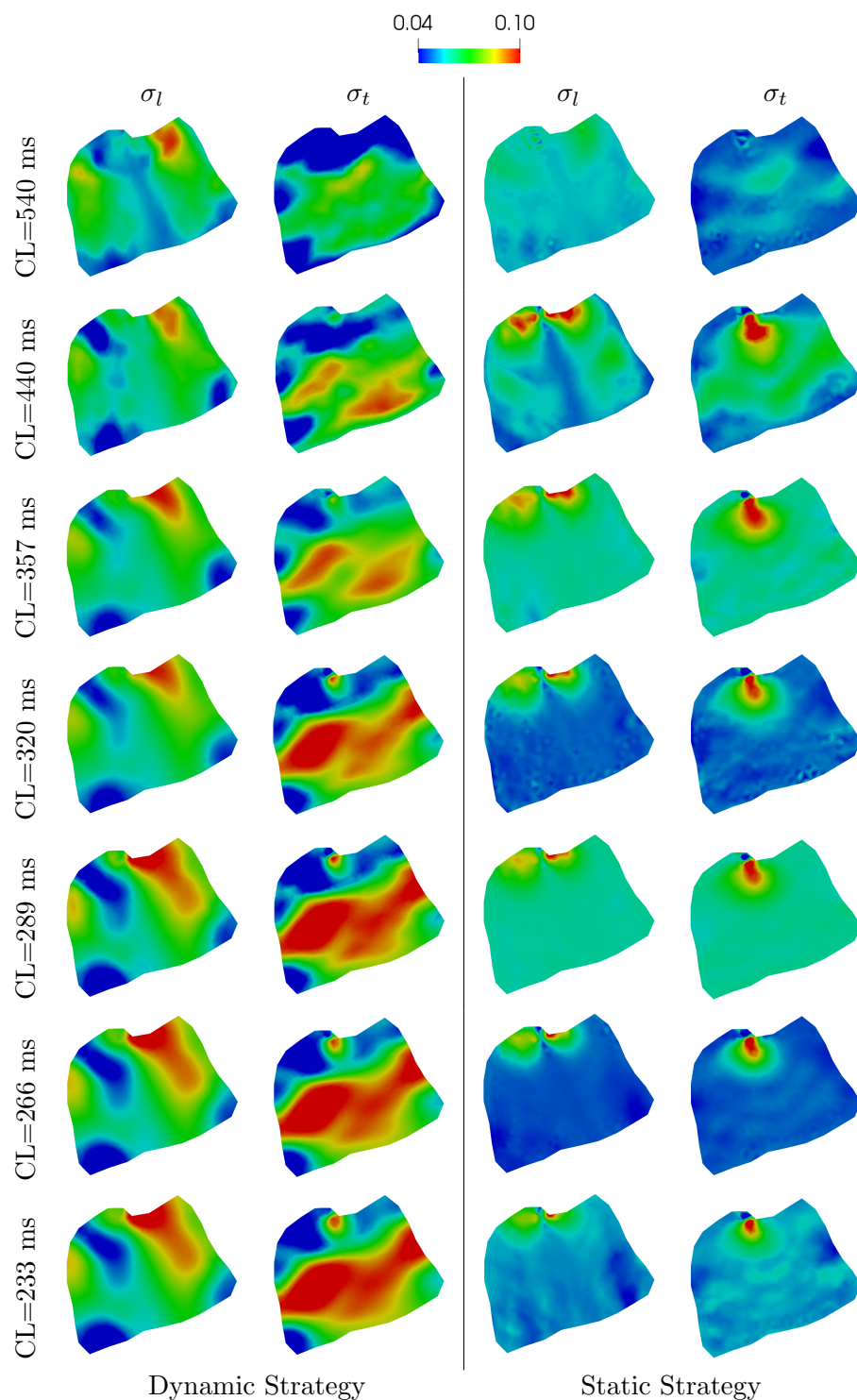
Figure 3.21: Dynamic vs Static strategy, estimated conductivity fields with MS model at different CL values. These results pinpoint how an educated selection of the initial guess is critical for the reliability of the estimation.
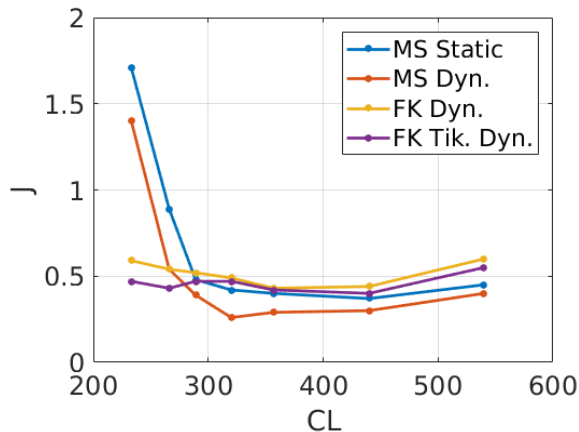
Figure 3.22: Value of misfit J for the different numerical settings tested. At fast pacing rates (low CL), both dynamic and static strategies with MS model (red and blue curve, respectively) lose accuracy as the misfit increases. By using the dynamic approach with FK model (orange curve), we can provide a better match of the experimental data. However, the reconstruction of the real AP propagation is still unsatisfactory (see Fig. 3.24). The dynamic technique with FK model and Tikhonov-like regularization is the best strategy both in terms of misfit and reconstruction of the data (see Fig. 3.24).

reconstruction of the experimental data and has therefore to be preferred.

However, both the strategies coupled with the MS model perform poorly as CL decreases resulting in an increase of the misfit. As MS aims to capture only the basic characteristics of the action potential, we get an overly simplified approximation of the dynamics, especially at low values of CL. Moreover, since it features only one gating variable, MS is not able to reliably reproduce the behavior of the system at fast pacing. This results in a underestimation of the conduction velocity. As noticed in Fig. 3.24, at low CL, the potential propagation is much slower than the real data at low CL. This is further highlighted by Fig. 3.25 which compares the experimental and modeled APs obtained with the two different procedures and ionic models in one point on the tissue in the time window [0,250] ms. The delay of the modeled AP is evident especially in the case CL = 233 ms when using MS model, regardless of the strategy. Moreover, the peak of the AP markedly decreases at low CL, in particular in the static procedure, contributing to the increase of the functional $\mathcal{J}$.

More realistic results can be obtained when using the FK model. At high CL, the estimation features slightly larger misfit than the dynamic strategy with MS model because of the better reconstruction of the AP shape provided by MS (see Fig. 3.22). However, the

strategy performs much better at low CL, in particular when CL < 300 ms, as the misfit functional remains stable. Despite of the improvement of the reconstruction, the results are still not fully satisfying since the conduction velocity is now overestimated leading to an increase of the conductivity, especially at low CL (see Fig. 3.26). This is highlighted in Fig. 3.25 too in which the AP simulated with FK at CL $= 233$ ms precedes the experimental data meaning that the wavefront propagation is faster. This disagrees with the physics of the system because it has been noticed in the experimental setting that the conduction velocity decreases as CL decreases. We argue that this can be caused by the high experimental errors nearby the stimulation point due both to the fluorescence noise and the lack of precise information about the location of the stimulator. Therefore, the estimation procedure might be more prone to lead to an inaccurate estimation of the conductivity fields, in particular in the region surrounding the site of the stimulation. To alleviate the negative impact of measurements errors on the reliability of the reconstruction, the strategy we followed was to identify with a trial-and-error process a reasonable estimation of the conductivity fields generating an AP propagation similar to the experimental one in proximity of the pacing point. The resulted conductivities are then enforced in the area by the stimulation point by enabling the Tikhonov-like regularization on mean conductivity values shown in (3.8). We considered the time window [0,8] ms in which the voltage wave is still close to the site of the stimulation. The contour line $u = 0.5$ of the experimental data at t$=8$ ms is shown in Fig. 3.23(a). Several conductivity fields and anisotropy ratios were tested and we finally impose $\sigma_{l,mean}(\mathbf{x}) = 9 \cdot 10^{-3}$ cm^2/ms, $\sigma_{t,mean}(\mathbf{x}) = 3 \cdot 10^{-3}$ cm^2/ms. Fig. 3.23(b) shows the modeled voltage wave at t$=8$ ms. The region in which the Tikhonov-like regularization is imposed is represented by the red region in Fig. 3.23(c). The shape of the area was chosen to be similar to the curvature of the wavefront of the experimental data. The weight α_1 of the Tikhonov-like regularization switches from $\alpha_1 = 10^{-2}$ in the red region to $\alpha_1 = 0$ elsewhere. In such a way, the estimates are enforced to be close to the prescribed mean value in the area by the site of the stimulation, whereas we disable the regularization in the rest of the domain so to let the estimation procedure detect the best match with the data.

This strategy yields a more accurate estimation, in particular at low CL, resulting in lower misfit value (see Fig. 3.22). Moreover, as it can be noticed in Fig. 3.24, the
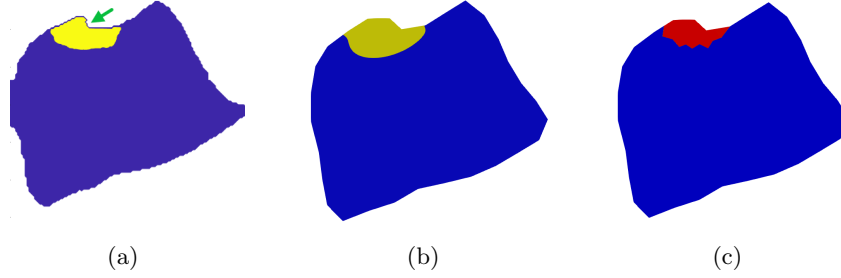
Figure 3.23: (a) Experimental AP at t=8 ms for CL=540 ms (contour line $u = 0.5$). The site of the stimulation is indicated by the green arrow; (b) Modeled AP propagation at t=8 ms for $\sigma_{l,mean}(\mathbf{x}) = 9 \cdot 10^{-3}$ cm^2/ms, $\sigma_{t,mean}(\mathbf{x}) = 3 \cdot 10^{-3}$ cm^2/ms (contour line $u = 0.5$); (c) The red area surrounding the site of the stimulation is the region in which the Tikhonov-like regularization on the mean conductivity fields is imposed and $\alpha_1 = 10^{-2}$, whereas $\alpha_1 = 0$ in the rest of the domain.

reconstruction of the data is more reliable in terms of the conduction velocity as well, since the modeled AP propagation is similar to the experimental one. It is also important noting from the shape of the contour line that the curvature of the wavefront varies along the tissue meaning that the procedure is able to detect the heterogeneity of the conductivity. Finally, the estimations of the conductivity fields reported in Fig. 3.26 are in agreement with the CV reduction at small CL as observed in the experiments.

3.4 Discussion

The results of our data-assimilation framework combining available measures with accurate models demonstrate the successful accomplishment of cardiac conductivities estimation. We performed here an extensive synthetic and experimental validation of the procedure with experimental data. We considered several scenarios to probe the accuracy and robustness of our procedure in a synthetic setting. This analysis is necessary to provide guidance on many practical issues for the design of future experiments. Then, we validated the procedure using fluorescence optical mapping recordings at different pacings. The results can be summarized as follows.

1. *Extracellular potential data is essential for accurate estimates.* However, as we recognize that the measure of the extracellular potential is much more complicated than the membrane voltage, we tried to reduce the number of the sites for u_e. We assess that the minimal number
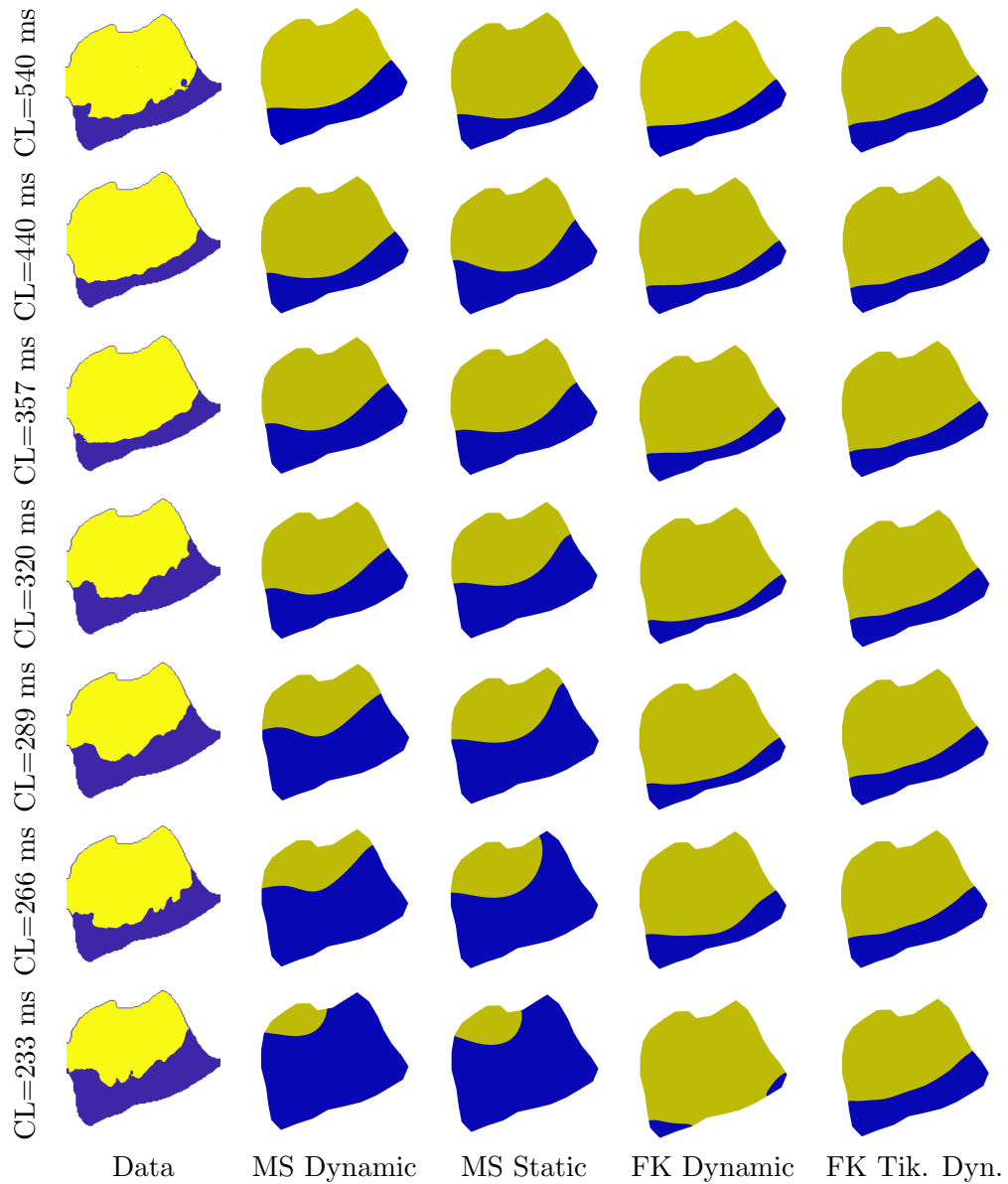
Figure 3.24: Comparison between experimental and modeled contour line $u = 0.5$ at $t = 20$ ms for different CL. At low CL, dynamic and static strategies with MS model underestimate the experimental CV, whereas dynamic approach with FK model simulates faster AP propagation. Enabling the Tikhonov-like regularization term allows us to provide a reasonable match of the experimental data at low CL.
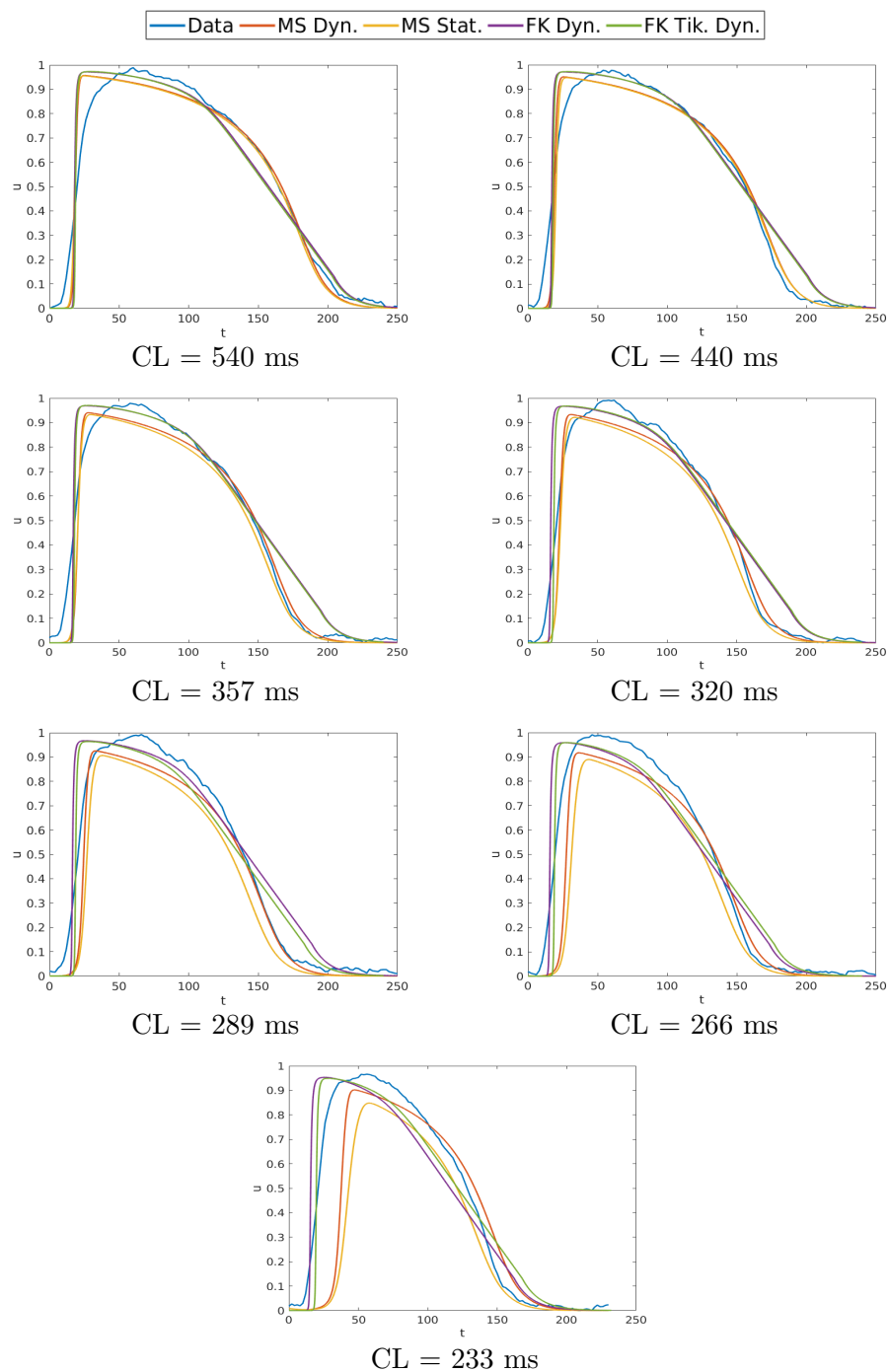
Figure 3.25: Comparison between experimental and modeled AP shapes using different strategies and ionic models. At low CL, the results obtained with MS model clearly diverge from the real data, both in terms of wavefront propagation and magnitude of the peak of the AP. FK model coupled with Tikhonov-like regularization in the dynamic framework gives the most reliable reconstruction of the experimental wavefront propagation.
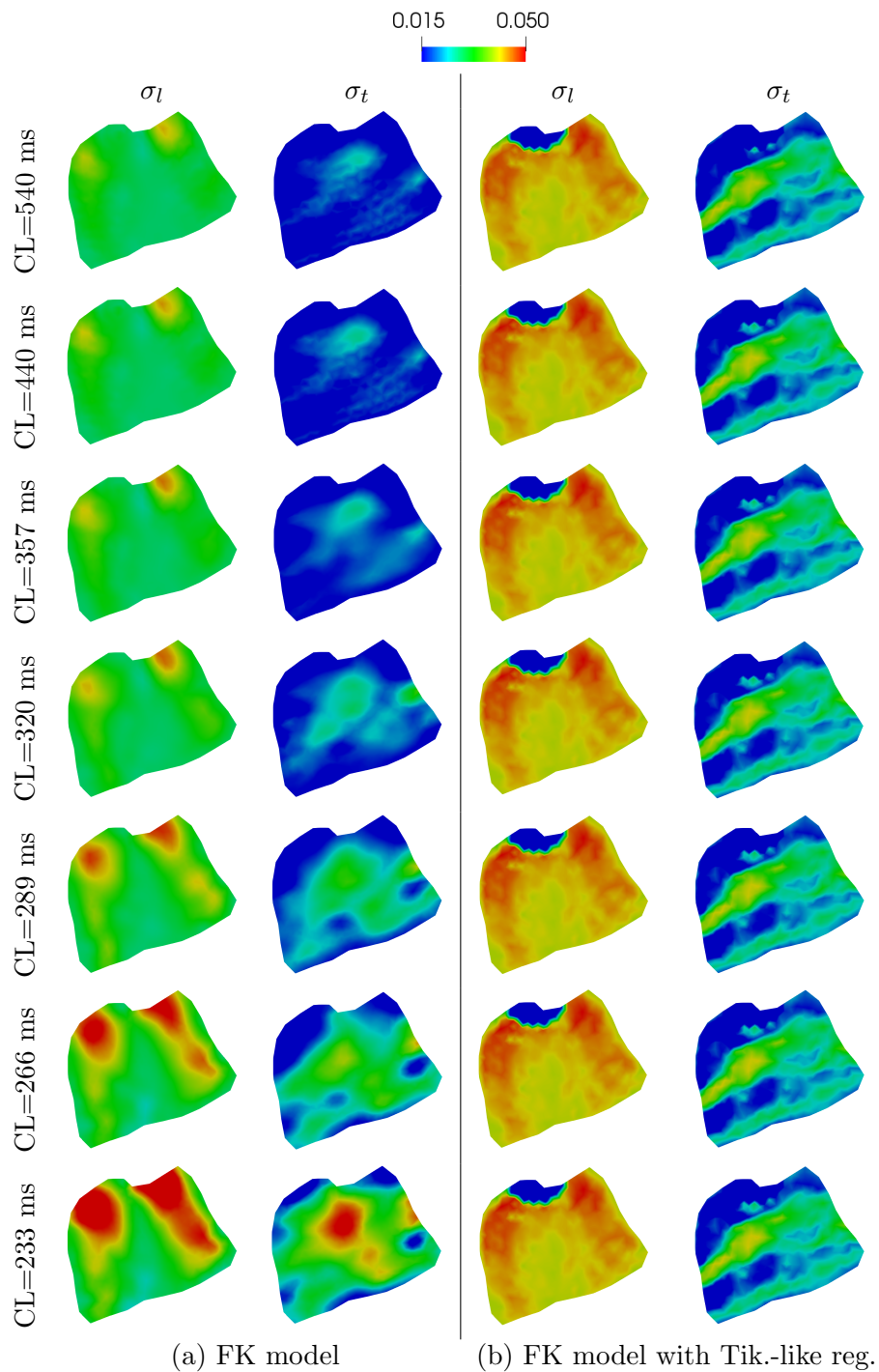
Figure 3.26: Dynamic Strategy: estimated conductivity fields with FK vs. FK with Tikhonov-like regularization. The conductivities estimated in (a) increase at low CL. This lacks physical foundation because it has been noticed in the experiments that the CV (and so the conductivity) decreases at low CL. On the other hand, the results obtained in (b) are more in line with the experimental expectation as the magnitude of the estimated fields does not increase at low CL.

of u_e sites required is around 10.

2. One of the most important conclusion is that *the exact location of the measurement sites has a marginal role on the quality of the estimation.* In fact, also with a random location of the sites (below a minimal number), we can get accurate estimations. In clinical settings, as the introduction of leads in the left ventricle is possible, it is not possible to precisely determine their position, yet these results suggest that this is not potentially detrimental to the estimate.

3. In general, we notice that *beyond a certain number of measure sites, adding more sites is not beneficial.*

4. In case of data recorded on a short time interval, *the presence of multiple simultaneous stimuli is critical to the quality of the estimate, while a single stimulus leads to a significantly poorer estimate.* However, in case of larger amount of data, the experimental setting with one stimulus leads to accurate estimation as well.

5. *The MICP does not require any extracellular measure and seems to be accurate enough for the transmembrane potential reconstruction.* This is an important aspect to consider for practical purposes. In fact, the results suggest that an accurate reconstruction of the transmembrane potential in patient-specific settings may be based on the solution of the MICP, being the conductivity tensor a nominal value assimilated from the data.

6. After a careful selection of the modeling and numerical setting, the method successfully reproduces most of the dynamics obtained from the experiments providing reasonable estimates of conductivity fields that are consistent with the data. The ionic models selected guarantee a relatively high reliability in spite of the low number of parameters they feature. However, their choice may be dictated by the CL pacing. While MS works properly over a wide range of CL pacing, at low frequency, FK performs better.

When modeling the electrophysiology and, specifically, setting up reliable parameter estimation procedures based on data, we have no silver bullet. The variety of options and modeling choices is huge and, generally, depends on the specific aims and regimes considered. The computational costs and the overall effectiveness of our estimation procedure are significantly affected by these choices, so the identification of the most convenient trade-offs is generally not easy. Also, it is worth mentioning that setting-up computationally efficient

methods is still an active research field, and the current scenario will likely change in the future [90, 91, 94, 150, 155–159] (to mention a few contributions).

A reliable and efficient estimation of cardiac conductivity for patient-specific modeling is turn for using optimization techniques in the therapy of cardiac disorders related to the potential propagation [126, 160–163]. Our ultimate goal, in fact, is the combination of data assimilation techniques and optimization procedures for improving the clinical activity. An extensive testing against experimental data is a fundamental step in this perspective to certify the credibility of the approach.

Chapter 4

Solution of the MICP Based on PGD-Model Reduction

Results from Chapter 3 pointed out that the variational procedure entails expensive computations and costs rapidly grow when the conductivity tensors feature discontinuities such as in presence of scars. These limitations may hinder its limitation to clinical problems featuring short time frames. We chose a hardware solution to deal with this issue exploiting the power of high performance clusters through parallel computing. However, parallelization is not always straightforward and, most importantly, long queue wait times on clusters (sometimes more than 48 hours) compromise the efforts for better performance and efficiency.

Reduced-order modeling techniques have been extensively investigated and developed in the engineering and mathematical literature (see e.g. [164–167]) as a valid alternative to improve the efficiency of rigorous identification procedures. In cardiac electrophysiology, several reduced-order models (ROMs) have been investigated [37, 39, 41, 168, 169] to replace the high-fidelity Bidomain/Monodomain models with educated and cheaper surrogates. They are constructed as a combination of basis functions generally built based on a previous knowledge of the solution for a predetermined set of values of the parameters (called snapshots). For instance, in the Proper Orthogonal Decomposition (POD) considered in [41], the snapshots are smartly selected based on the concept of *domain of influence* in the space of the conductivities, and the surrogate is constructed after a Singular Value

Decomposition (SVD) of the snapshot matrix. In this Chapter, we explore a ROM procedure that does not require any *a priori* knowledge of the solution. The Proper General Decomposition (PGD) is a a model reduction technique introduced by Chinesta et al. [43], specifically devised for parametrized differential problems to rapidly evaluate for different values of the parameters. Even though the PGD still relies on an off-line/on-line paradigm, this method does not require an initial computation of snapshots.

The idea is to treat the parameters of the problem as independent variables and to compute the solution over an extended domain, inclusive of the range the parameters are expected to belong to. As the actual numerical computation must be done on a highly dimensional domain, in the off-line stage, a special representation is introduced, where the basis functions representing the solution are factorized for each independent variable (including the parameters) or low-dimensional groups of variables. By advocating an iterative approach for computing the basis functions customized for the problem to solve, the PGD has been demonstrated to be an effective technique for computing an approximation of the differential equation in all the expected range of parameters in different fields of applications (see e.g. [48]). In the on-line phase, at this point, the solution is ready to be promptly evaluated for any value of the parameters as well as for any other independent variable. This is particularly effective in a variational parameter identification procedure, when the solution for different guesses of the parameters are tested in the iterative minimization process.

The rapid solution of the on-line phase makes affordable the introduction of Uncertainty Quantification techniques like the ones based on the application of Bayesian theory [49, 50]. These strategies can be used for the self-assessment of the quality and robustness of the parameter estimation. Unlike the deterministic variational approach considered so far, the solution of the inverse problem in a Bayesian framework is a probability distribution whose moments are informative of the reliability of the estimates. The downside is that this additional information implies more demanding calculations. Simplified physical models, such as the Eikonal model, have been used in literature [51, 52] to reduce computational complexity of statistical approaches at the expense of less accurate description of physiological and pathological dynamics. The PGD method enables for the first time the use of the more accurate Monodomain model in this context at reasonable costs.

In this Chapter, we explore the use of PGD to solve the Monodomain Inverse Conductivity Problem (MICP), both in the deterministic and statistical frameworks. After a short introduction to PGD in Section 4.1, we introduce the specific technical aspects of the application of PGD to the solution of the Monodomain problem in Section 4.2. Then, we assess the accuracy of the reduced model over a number of test cases. In particular, we start with simple 2D test problems yet on a morphology based previous studies on canine tissues. Then, we extend to 3D problems including a patient-specific left ventricle. In Section 4.3, we present and discuss the application of PGD to the solution of MICP. We then introduce the statistical formulation of the MICP in Section 4.4 presenting numerical results using the PGD reduction of the Monodomain model and we conclude with a final discussion in Section 4.5.

The content of the Sections 4.1-4.3 is reflected by the paper [170], whereas the work presented in 4.4 will be subject of a future publication.

4.1 PGD in a Nutshell

In this Section, we provide a short introduction to the PGD, to recall the basic ideas and introduce some notation and terminology. For a more complete introduction, the reader is referred to [43].

In what follows, $\Omega \subset \mathbb{R}^d$ is the physical space domain, where the dimension d here will be 2 or 3. We denote by V a Hilbert space, generally a subspace of the Sobolev space $H^1(\Omega)$. With $\boldsymbol{q} \in \mathbf{R}^\delta$ we denote a vector of parameters the problem we consider depends on. Let us focus for the moment on a generic parametrized elliptic problem in the weak form: find $u(\boldsymbol{x})$

$$a_{\boldsymbol{q}}(u, v) = F(v), \qquad \forall v \in V, \tag{4.1}$$

where $F : V \to \mathbb{R}$ is a linear continuous functional, and the form $a_{\boldsymbol{q}} : V \times V \to \mathbb{R}$ for any given admissible value of the parameters $\boldsymbol{q}$ is bilinear, continuous and coercive. More precisely, we assume that the parameter q_i for $i = 1, \ldots \delta$ ranges in an admissible interval $\mathcal{S}_i$, so that the admissible set for the parameters is the hyper-cube $\boldsymbol{\mathcal{S}} \equiv \mathcal{S}_1 \times \mathcal{S}_2 \ldots \times \mathcal{S}_\delta$. As our problem is actually the identification of the parameters, we regard the solution u as

a function of $\boldsymbol{x} \in \mathbb{R}^d$ and $\boldsymbol{q} \in \mathbb{R}^\delta$. Specifically, we assume that $u \in V \times L^2(\boldsymbol{S})$. The space $V \times L^2(\boldsymbol{S})$ will be denoted by W. The *extended* weak formulation, including the parameters as independent variables, is obtained by integrating (4.1) over $\boldsymbol{S}$ as

$$\mathcal{A}(w, v) \equiv \int_{\boldsymbol{S}} a_{\boldsymbol{q}}(u, v) d\boldsymbol{q}, \quad \mathcal{F}(v) \equiv \int_{\boldsymbol{S}} F(v) d\boldsymbol{q}.$$

The $d + \delta$-dimensional problem reads: find $u \in W$ s.t.

$$\mathcal{A}(u, v) = \mathcal{F}(v), \qquad \forall v \in W. \tag{4.2}$$

Notice that, with a little abuse of notation, we keep denoting the unknown and the test functions with the same symbols u, v, although now their dependence on the parameters $\boldsymbol{q}$ is explicitly outlined by their belonging to W.

As the number of dimensions of the problem is now increased, the numerical solution (e.g., with a generic Galerkin approach) may be problematic. We therefore proceed under the assumption of *separability*, that is typically postulated in unsteady problems to separate the space to the time dependence of the solution (semi-discretization). This means that the numerical solution is regarded as the linear combination of factors breaking up the dependence of the solution on the different independent variables into the product of low-dimensional sets of basis functions. Consequently, the numerical approximation of the problem takes the form

$$u_m(\boldsymbol{x}, \boldsymbol{q}) = \sum_{k=1}^m u_k^{\boldsymbol{x}}(\boldsymbol{x}) \prod_{l=1}^\delta u_k^l(q_l), \tag{4.3}$$

where the functions $u_k^{\boldsymbol{x}}(\boldsymbol{x}) \in V_h \subset V$ account for the $\boldsymbol{x}$-dependency of the solution and the functions $u_k^l(q_l) \in W^l \subset L^2(\mathcal{S}_l)$ for $l = 1, 2, \ldots \delta$ carry the dependence on the parameters. Correspondingly, the space W_m will denote the space of functions in the form (4.3), i.e.

$$W_m = \left\{ w_m(\boldsymbol{x}; \boldsymbol{q}) = \sum_{k=1}^m w_k^{\boldsymbol{x}}(\boldsymbol{x}) \prod_{l=1}^\delta w_k^l(q_l), \right.$$

$$\left. \text{with } w_k^{\boldsymbol{x}} \in V_h, \, w_k^l \in W^l \text{ (for any } l = 1, \ldots, \delta), \, \boldsymbol{x} \in \Omega, \, \boldsymbol{q} \in \boldsymbol{S} \right\}. \tag{4.4}$$

From now on, the dimension of V_h will be denoted by $N_h^{\boldsymbol{x}}$ and similarly $N^l \equiv \dim(W^l)$. Differently from a regular Galerkin approach, the basis functions are not selected a-priori (e.g., piecewise polynomials or Gaussian polynomials). Conversely, the computation of these functions is the result of a progressive construction customized on the problem to solve, performed in an iterative procedure that takes advantage of their factorized nature. In more details, the computation of the solution in this form is based on two steps: (i) a "greedy" weighted residual step to *enrich* the approximation $u_{m-1} \in W_{m-1}$ to $u_m \in W_m$ by adding the new contribution (or *mode*) $\delta_m u \equiv u_m^{\boldsymbol{x}}(\boldsymbol{x}) \prod_{l=1}^{\delta} u_m^l(q_l)$; (ii) a factorized computation of the mth term $\delta_m u$ based on a fixed-point iteration method called *Alternating-Direction Strategy* (ADS).

As for (i), we aim to find the new mode $\delta_m u$ by solving the weighted residual problem

$$\mathcal{A}(\delta_m u + u_{m-1}, v_m) = \mathcal{F}(v_m), \qquad \forall v_m \in W_m, \tag{4.5}$$

where $u_{m-1} \in W_{m-1}$ is the available approximation (at the beginning typically one sets $u_0 = 0$). The progressive addition of new terms stops when the solution does not change significantly. Technically, this leads to the (external) convergence criterion

$$\frac{\|u_m\|}{\|u_1\|} \leq \text{tol}_e, \tag{4.6}$$

where the tolerance is user-defined and the norm can be selected in different ways (e.g. $L^2(\Omega \times \boldsymbol{S})$). The rationale is that the new modes are adding a progressively less relevant contribution to the solution (as it happens, for instance, with the terms of a Sturm-Liouville Eigenfunction expansion), so that the left hand side of (4.6) does actually reduce when m increases.

As for (ii), we perform the computation of $\delta_m u$ in (4.5) by solving iteratively the component depending on each variable (or set of independent variables) independently, in a fixed-point frame (ADS). Introducing the fixed-point iterative index $j \geq 1$, let us assume to have a guess $\delta_{m,j-1} u = u_{m,j-1}^{\boldsymbol{x}}(\boldsymbol{x}) \prod_{l=1}^{\delta} u_{m,j-1}^l(q_l)$. We start computing the contribution

$u_{m,j}^{\boldsymbol{x}}(\boldsymbol{x})$ by solving the $d-$dimensional problem

$$\mathcal{A}(u_{m,j}^{\boldsymbol{x}} \prod_{l=1}^{\delta} u_{m,j-1}^l, v_m) = \mathcal{F}(v_m) - \mathcal{A}(u_{m-1}, v_m), \tag{4.7}$$

where $v_m = v_m^{\boldsymbol{x}} \prod_{l=1}^{\delta} u_{m,j-1}^l$ and the problem is solved for any $v_m^{\boldsymbol{x}} \in V_h$. Successively, we solve the dependence on the parameters q_r, $r = 1, 2, \ldots, \delta$ by solving the 1D problems

$$\mathcal{A}(u_{m,j}^{\boldsymbol{x}} u_{m,j}^r \prod_{l=1}^{r-1} u_{m,j}^l \prod_{l=r+1}^{\delta} u_{m,j-1}^l, v_m) = \mathcal{F}(v_m) - \mathcal{A}(u_{m-1}, v_m), \tag{4.8}$$

where this time $v_m = u_{m,j}^{\boldsymbol{x}} v_m^r \prod_{l=1}^{r-1} u_{m,j}^l \prod_{l=r+1}^{l} u_{m,j-1}^l$ and the computation runs for any $v_m^r \in W^r$. By solving this problem for $r = 1, 2, \ldots, \delta$, we complete the computation of $\delta_{m,j} u$.

Finally, by iterating this sequence of problems over j, the convergence to a stationary limit clearly leads to a fixed point that we select to be the $m - th$ contribution to the solution. A natural stopping criterion for the (internal) iterative loop reads therefore

$$\frac{\|\delta_{m,j} u - \delta_{m,j-1} u\|}{\|\delta_{m,j-1} u\|} \leq \mathrm{tol}_i. \tag{4.9}$$

Once this criterion is fulfilled, the computation of $\delta_m u$ is completed and $u_m = \delta_m u + u_{m-1}$ is available. All the steps involved in (4.7,4.8) can be written in an algebraic form that we do not report here for the sake of brevity. The PGD algorithm described here is summarized in Algorithm 1. Implementation details of this method in our specific problem are deferred to Section 4.2.2.

What is described in Algorithm 1 is actually what we define the *off-line* phase of the method, aiming at a reduction of the problem on a relatively small number of customized basis functions. The interest of the present paper in PGD is however motivated by the fact that after this phase, the solution is available not only on each space point but also over the entire admissible set of parameters $\boldsymbol{S}$. In the variational data assimilation procedure investigated in Chapter 3, we need to iteratively estimate the solution of our original problem for different values of the parameters, so to minimize the mismatch from the observations.

Algorithm 1 PGD algorithm

1: Define $\boldsymbol{\mathcal{S}}$;
2: Select a (finite element) basis function set for V_h;
3: Precompute all the components of $\mathcal{A}(\cdot, \cdot)$ independent of external iteration index k
4: Set the tolerances tol_e and tol_i;
5: Set the modal index $m \leftarrow 0$;
6: Set a maximum enrichment index m_{max}; set a maximum fixed point iterations j_{max};
7: Set the initial guess u_0;
8: **while** External loop criterion (4.6) is not fulfilled and $m \leq m_{max}$ **do**
9:     $m \leftarrow m + 1$;
10:     Set the fixed point index $j \leftarrow 0$;
11:     Set the initial guess $\delta_{m,0} u$;
12:     **while** Internal loop criterion (4.9) is not fulfilled and $j \leq j_{max}$ **do**
13:         $j \leftarrow j + 1$;
14:         Solve (4.7);
15:         **for all** $r = 1, \ldots, \delta$ **do**
16:             Solve (4.8);
17:         **end for**
18:     **end while**
19:     $u_m = u_{m-1} + u_m^{\boldsymbol{x},j} \prod_l u_m^{l,p}$;
20: **end while**

Once the PGD solution is available, the *on-line* cost of approximating u for different values of the parameters is trivially the cost of assembling the solution $u_m = \sum\limits_{k=1}^{m} u_k^{\boldsymbol{x}}(\boldsymbol{x}) \prod\limits_{l=1}^{\delta} u_k^l(q_l)$. The cost of this step is minimal, and this makes the PGD particularly interesting in our case. At this time we do not have theoretical results on the convergence of the loops involved in the off-line phase. The ultimate goal of this work is assessing the reliability of the off-line model reduction and verifying its computational competitiveness in solving our parameter estimation/data assimilation problem.

4.2   PGD Model Reduction of the Monodomain Problem

In this Section, we apply the PGD approach to obtain a surrogate of the Monodomain model (2.25), with the Monodomain equation reshaped as (2.27). We focus on the simple phenomenological Rogers-McCulloch (RM) model (2.6). As our goal is to assess a methodological procedure, so we defer the extension to more complex models such as Mitchell-Schaeffer (2.8) and Fenton-Karma (2.10) to future works. To avoid ambiguity and conflicts with the notation used in the previous Section, the gating variable v characterizing the

RM model is hereafter denoted as w. Moreover, the conductivity tensor $\mathbf{D} = \boldsymbol{\sigma}/(\beta C_m)$ is denoted by $\boldsymbol{\sigma}$ as usual.

4.2.1 Formulation of the reduced model

To solve the Monodomain system coupled with MS model adopting the PGD reduction, we preliminary perform a semi-discretization in time of the problem, as previously done in Section 3.1.2 for the numerical approximation of Bidomain/Monodomain models. This is not necessary, as the time variable could be considered as the other variables of the problem (space and conductivities). However, we preferred to eliminate the time dependence by a traditional finite difference discretization, so to rely on extensive evidence of the effectiveness of the approach. We recall that, with this approach, we decouple the PDE equation and the ODE ionic model. By defining a time step $\Delta t > 0$, the time interval $[0, T]$ is uniformly divided in N subintervals (t^n, t^{n+1}), with $t^0 = 0$, $t^N = T$ and $t^{n+1} = t^n + \Delta t = (n+1)\Delta t$, for any $n = 0, \ldots, N$. This strategy consists of a semi-implicit approach that automatically linearizes the problem at each time step. Thus, using a first order discretization in time in the Monodomain equations (2.25), at each time step t^{n+1}, for (u^n, w^n) available, we solve the problems (recall that RM model features a single gating variable)

$$\begin{cases} w^{n+1} = \Delta t g(u^n, w^{n+1}) + w^n \\ u^{n+1} - \Delta t \nabla \cdot (\boldsymbol{\sigma} \nabla u^{n+1}) = \Delta t I_{app}^{n+1} - \Delta t I_{ion}(u^n, w^{n+1}) + u^n \end{cases} \quad \text{in } \Omega, \qquad (4.10)$$

completed by the boundary conditions $(2.26)_2$.

The first (algebraic) equation explicitly reads

$$w^{n+1} = \frac{\eta_2 \Delta t}{(1 + \Delta t \eta_2 \eta_3) u_p} u^n + \frac{w^n}{1 + \Delta t \eta_2 \eta_3}. \qquad (4.11)$$

In the second (differential) equation, the ionic term reads

$$I_{ion}(u^n, w^{n+1}) = G u^n - G\left(\frac{1}{u_p} + \frac{1}{u_{th}}\right)(u^n)^2 + \frac{G}{u_p u_{th}}(u^n)^3 - \eta_1 u^n w^{n+1}, \qquad (4.12)$$

where the parameter values are listed in Table 2.1.

At each step, we apply the PGD model reduction to $(4.10)_2$. For $V = H^1(\Omega)$, the weak formulation for problem $(4.10)_2$ reads

$$a(u^{n+1}, v) = F(v) \quad \forall v \in V, \tag{4.13}$$

with

$$a(u^{n+1}, v) = \int_\Omega \Delta t\, \boldsymbol{\sigma} \nabla u^{n+1} \cdot \nabla v \, \mathrm{d}\Omega + \int_\Omega u^{n+1} v \, \mathrm{d}\Omega, \tag{4.14}$$

$$F(v) = \int_\Omega (\Delta t\, I_{app}^{n+1} - \Delta t\, I_{ion}(u^n, w^{n+1}) + u^n) v \, \mathrm{d}\Omega. \tag{4.15}$$

To apply the PGD approach, we introduce the space $W \equiv H^1(\Omega) \times L^2(\mathcal{S}_l) \times L^2(\mathcal{S}_t)$, where $\mathcal{S}_{l,t}$ are the admissible ranges for σ_l and σ_t, respectively. Then, the extended variational formulation reads like in (4.2) with

$$\mathcal{A}(u, v) = \int_{\mathcal{S}_l} \int_{\mathcal{S}_t} a(u, v) \, \mathrm{d}\sigma_l \, \mathrm{d}\sigma_t, \quad \mathcal{F}(v) = \int_{\mathcal{S}_l} \int_{\mathcal{S}_t} F(v) \, \mathrm{d}\sigma_l \, \mathrm{d}\sigma_t. \tag{4.16}$$

Again, we keep using the same symbols u and v even if now these functions are regarded as elements of W, to highlight their dependence on σ_l and σ_t.

To perform the model reduction, let W_m be the space

$$
W_m = \left\{ w_m(\boldsymbol{x}; \sigma_l, \sigma_t) = \sum_{k=1}^m w_k^{\boldsymbol{x}}(\boldsymbol{x}) w_k^{\sigma_l}(\sigma_l) w_k^{\sigma_t}(\sigma_t); \right.
$$
$$
\left. \text{with } w_k^{\boldsymbol{x}} \in V_h, \; w_k^{\sigma_l} \in W_h^{\sigma_l}, \; w_k^{\sigma_t} \in W_h^{\sigma_t}, \; \forall k = 1, \ldots, m \right\}, \tag{4.17}
$$

with V_h, $W_h^{\sigma_l}$ and $W_h^{\sigma_t}$ discrete subspaces of V, $L^2(\mathcal{S}_l)$ and $L^2(\mathcal{S}_t)$, respectively. The PGD solution is defined then as

$$u^{n+1}(\boldsymbol{x}; \sigma_l, \sigma_t) \approx \sum_{k=1}^m u_k^{n+1, \boldsymbol{x}}(\boldsymbol{x}) u_k^{n+1, \sigma_l}(\sigma_l) u_k^{n+1, \sigma_t}(\sigma_t). \tag{4.18}$$

The different contributions of the sum are computed up to the fulfillment of the criterion (4.6), while each additional term $u_k^{n+1, \boldsymbol{x}}(\boldsymbol{x}) u_k^{n+1, \sigma_l}(\sigma_l) u_k^{n+1, \sigma_t}(\sigma_t)$ is computed by the ADS strategy, breaking the solution into an iterative fixed-point solver, alternatively solving for

$\boldsymbol{x}$, σ_l and σ_t, as described in Section 4.1.

In the specific case of $(4.10)_2$, we can factorize the extended bilinear form and linear functional as follows. Let us write generically $u(\boldsymbol{x}, \sigma_l, \sigma_t) = u^{\boldsymbol{x}}(\boldsymbol{x})u^l(\sigma_l)u^t(\sigma_t)$ and $v(\boldsymbol{x}, \sigma_l, \sigma_t) = v^{\boldsymbol{x}}(\boldsymbol{x})v^l(\sigma_l)v^t(\sigma_t)$. Then, we can write

$$\mathcal{A}(u,v) = \sum_{j=1}^{10} a_j^{\boldsymbol{x}}(u^{\boldsymbol{x}}, v^{\boldsymbol{x}})a_j^l(u^l, v^l)a_j^t(u^t, v^t), \tag{4.19}$$

where the bilinear factors $a_j^{\boldsymbol{x}}, a_j^l, a_j^t$ are reported in Table 4.1. Notice that in the table $(\cdot, \cdot)$ stands for the regular L^2 product.

To factorize the linear functional $\mathcal{F}(v)$, we give a reduced order representation of the terms w^{n+1} and u^n as

$$u^n = \sum_{k=1}^{N_u} u_k^{n,\boldsymbol{x}} u_k^{n,\sigma_l} u_k^{n,\sigma_t}, \quad w^{n+1} = \sum_{k=1}^{N_w} w_k^{n+1,\boldsymbol{x}} w_k^{n+1,\sigma_l} w_k^{n+1,\sigma_t}. \tag{4.20}$$

Here, for the easiness of reading, we did not set the dimensions N_u and N_w as functions of the time index n, however, in general, they can change from one step to the other. Then, bearing in mind (4.11,4.12), it is possible to verify that

$$\mathcal{F}(v) = \sum_{j=1}^{N_F} F_j^{\boldsymbol{x}}(v^{\boldsymbol{x}})F_j^l(v^l)F_j^t(v^t), \tag{4.21}$$

where

$$\begin{aligned} N_F &= 1 + 2N_u + 2\binom{N_u}{1} + 3\binom{N_u}{2} + \binom{N_u}{3} + N_u N_w \\ &= 1 + 4N_u + \frac{3}{2}N_u(N_u - 1) + \frac{1}{6}N_u(N_u - 1)(N_u - 2) + N_u N_w. \end{aligned} \tag{4.22}$$

In fact, by direct computation, one function is required by I_{app} and N_u functions for the last component in (4.15). Then, regarding the ionic term I_{ion}, the linear term in u^n requires N_u functions, the quadratic one requires $\binom{N_u}{1} + \binom{N_u}{2}$ functions, the cubic one $\binom{N_u}{1} + 2\binom{N_u}{2} + \binom{N_u}{3}$ functions and the mixed multiplicative term uw in the RM model $N_u N_w$ functions. The functionals $F_j^{\boldsymbol{x}}, F_j^l, F_j^t$ are reported in the Table 4.2.

Exploiting these factorizations, the three ADS steps at the generic fixed point iteration

r read

$$
\begin{cases}
\displaystyle\sum_{j=1}^{10} \mathsf{a}_{\mathsf{j}}^{\boldsymbol{x}}(\mathsf{u}_{\mathsf{m,r}}^{\boldsymbol{x}}, \mathsf{v}^{\boldsymbol{x}}) a_j^l(u_{m,r-1}^l, u_{m,r-1}^l) a_j^t(u_{m,r-1}^t, u_{m,r-1}^t) = \\
\qquad \displaystyle\sum_{j=1}^{N_F} \mathsf{F}_{\mathsf{j}}^{\boldsymbol{x}}(\mathsf{v}^{\boldsymbol{x}}) F_j^l(u_{m,r-1}^l) F_j^t(u_{m,r-1}^t) - \sum_{j=1}^{10}\sum_{k=1}^{m-1} \mathsf{a}_{\mathsf{j}}^{\boldsymbol{x}}(\mathsf{u}_{\mathsf{k}}^{\boldsymbol{x}}, \mathsf{v}^{\boldsymbol{x}}) a_j^l(u_k^l, u_{m,r-1}^l) a_j^t(u_k^t, u_{m,r-1}^t) \\[2mm]
\displaystyle\sum_{j=1}^{10} a_j^{\boldsymbol{x}}(u_{m,r}^{\boldsymbol{x}}, u_{m,r}^{\boldsymbol{x}}) \mathsf{a}_{\mathsf{j}}^{\mathsf{l}}(\mathsf{u}_{\mathsf{m,r}}^{\mathsf{l}}, \mathsf{v}^{\mathsf{l}}) a_j^t(u_{m,r-1}^t, u_{m,r-1}^t) = \\
\qquad \displaystyle\sum_{j=1}^{N_F} F_j^{\boldsymbol{x}}(u_{m,r}^{\boldsymbol{x}}) \mathsf{F}_{\mathsf{j}}^{\mathsf{l}}(\mathsf{v}^{\mathsf{l}}) F_j^t(u_{m,r-1}^t) - \sum_{j=1}^{10}\sum_{k=1}^{m-1} a_j^{\boldsymbol{x}}(u_k^{\boldsymbol{x}}, u_{m,r}^{\boldsymbol{x}}) \mathsf{a}_{\mathsf{j}}^{\mathsf{l}}(\mathsf{u}_{\mathsf{k}}^{\mathsf{l}}, \mathsf{v}^{\mathsf{l}}) a_j^t(u_k^t, u_{m,r-1}^t) \\[2mm]
\displaystyle\sum_{j=1}^{10} a_j^{\boldsymbol{x}}(u_{m,r}^{\boldsymbol{x}}, u_{m,r}^{\boldsymbol{x}}) a_j^l(u_{m,r}^l, u_{m,r}^l) \mathsf{a}_{\mathsf{j}}^{\mathsf{t}}(\mathsf{u}_{\mathsf{m,r}}^{\mathsf{t}}, \mathsf{v}^{\mathsf{t}}) = \\
\qquad \displaystyle\sum_{j=1}^{N_F} F_j^{\boldsymbol{x}}(u_{m,r}^{\boldsymbol{x}}) F_j^l(u_{m,r}^l) \mathsf{F}_{\mathsf{j}}^{\mathsf{t}}(\mathsf{v}^{\mathsf{t}}) - \sum_{j=1}^{10}\sum_{k=1}^{m-1} a_j^{\boldsymbol{x}}(u_k^{\boldsymbol{x}}, u_{m,r}^{\boldsymbol{x}}) a_j^l(u_k^l, u_{m,r}^l) \mathsf{a}_{\mathsf{j}}^{\mathsf{t}}(\mathsf{u}_{\mathsf{k}}^{\mathsf{t}}, \mathsf{v}^{\mathsf{t}})
\end{cases}
$$

$$(4.23)$$

We outlined with a different font the factor being solved at each step. For easiness of reading, we do not report the factorization terms related to the case $d = 2$ as they can be computed in a similar fashion.

4.2.2   Implementation details

The spaces V_h, $W_h^{\sigma_l}$ and $W_h^{\sigma_t}$ are discretized using piecewise linear finite elements. At each time step, the initial guess at the beginning of the external loop is $u_0^{\boldsymbol{x}} = u_0^l = u_0^t = 0$, whereas the new $m - th$ contributions determined in the ADS iterations are initially set to $u_{m,0}^{\boldsymbol{x}} = u_{m,0}^l = u_{m,0}^t = 1$. As for the tolerance values tol_e and tol_i in Algorithm 1, we will focus on different values to investigate their impact on the performance of the PGD technique. The linear systems following the discretization of the three ADS steps in (4.23) are solved using CG method with a standard ILU right preconditioner [137]. While this strategy is appropriate to solve the first ADS step $(4.23)_1$ that may feature large linear systems originated from the discretization of the physical space, the remaining steps $(4.23)_{(2,3)}$ concern the parametric space, thus they may require the solution of smaller linear systems. Direct solvers are better suited in such cases as they may be more efficient depending on the software used. The optimization of this part of the implementation will be object of future work. Simulations were carried out in serial on a workstation equipped with Intel 6-Core i7-7800X CPU 3.50GHz and 64 GB of RAM. The code was implemented

Table 4.1: Factorization of the PGD increased bilinear form (4.16). Lines for $j = 1, \ldots, 9$ refer to the first term of (4.14), the last line, corresponding to $j = 10$, refers to the second component of (4.14).

j	$a_j^{\boldsymbol{x}}(u^{\boldsymbol{x}}, v^{\boldsymbol{x}})$	$a_j^{\sigma_l}(u^l, v^l)$	$a_j^{\sigma_t}(u^t, v^t)$
1	$\Delta t(\cos^2(\theta)\partial_x u^{\boldsymbol{x}}, \partial_x v^{\boldsymbol{x}})$	$(\sigma_l u^l, v^l)$	(u^t, v^t)
2	$\Delta t(\sin^2\theta\partial_x u^{\boldsymbol{x}}, \partial_x v^{\boldsymbol{x}})$	(u^l, v^l)	$(\sigma^t u^t, v^t)$
3	$\Delta t(\cos\theta\sin\theta\partial_y u^{\boldsymbol{x}}, \partial_x v^{\boldsymbol{x}})$	$(\sigma_l u^l, v^l)$	(u^t, v^t)
4	$-\Delta t(\cos\theta\sin\theta\partial_y u^{\boldsymbol{x}}, \partial_x v^{\boldsymbol{x}})$	(u^l, v^l)	$(\sigma^t u^t, v^t)$
5	$\Delta t(\cos\theta\sin\theta\partial_x u^{\boldsymbol{x}}, \partial_y v^{\boldsymbol{x}})$	$(\sigma_l u^l, v^l)$	(u^t, v^t)
6	$-\Delta t(\cos\theta\sin\theta\partial_x u^{\boldsymbol{x}}, \partial_y v^{\boldsymbol{x}})$	(u^l, v^l)	$(\sigma^t u^t, v^t)$
7	$\Delta t(\sin^2\theta\partial_y u^{\boldsymbol{x}}, \partial_y v^{\boldsymbol{x}})$	$(\sigma_l u^l, v^l)$	(u^t, v^t)
8	$\Delta t(\cos^2\theta\partial_y u^{\boldsymbol{x}}, \partial_y v^{\boldsymbol{x}})$	(u^l, v^l)	$(\sigma^t u^t, v^t)$
9	$\Delta t(\partial_z u^{\boldsymbol{x}}, \partial_z v^{\boldsymbol{x}})$	$(\sigma_l u^l, v^l)$	(u^t, v^t)
10	$(u^{\boldsymbol{x}}, v^{\boldsymbol{x}})$	(u^l, v^l)	(u^t, v^t)

Table 4.2: Factorization of the PGD increased linear functional (4.21). The first column indicates the number of components for any row. As for the indexes, $k, r, s = 1, \ldots, N_u$ and $j = 1, \ldots, N_w$.

	$F_j^{\boldsymbol{x}}(v^{\boldsymbol{x}})$	$F_j^l(v^l)$	$F_j^t(v^t)$	
1	$\Delta t(I_{app}^{n+1}, v^{\boldsymbol{x}})$	$(1, v^l)$	$(1, v^t)$	
N_u	$(u_k^{n,\boldsymbol{x}}, v^{\boldsymbol{x}})$	(u_k^{n,σ_l}, v^l)	(u_k^{n,σ_t}, v^t)	
N_u	$-\Delta t G(u_k^{n,\boldsymbol{x}}, v^{\boldsymbol{x}})$	$(u_k^{n,l}, v^l)$	$(u_k^{n,t}, v^t)$	
N_u	$\Delta t G(\frac{1}{V_p} + \frac{1}{V_{th}})((u_k^{n,\boldsymbol{x}})^2, v^{\boldsymbol{x}})$	$((u_k^{n,l})^2, v^l)$	$((u_k^{n,t})^2, v^t)$	
$\binom{N_u}{2}$	$2\Delta t G(\frac{1}{V_p} + \frac{1}{V_{th}})(u_k^{n,\boldsymbol{x}} u_r^{n,\boldsymbol{x}}, v^{\boldsymbol{x}})$	$(u_k^{n,l} u_r^{n,l}, v^l)$	$(u_k^{n,t} u_r^{n,t}, v^l)$	$r > k$
N_u	$-\Delta t \frac{G}{V_p V_{th}}((u_k^{n,\boldsymbol{x}})^3, v^{\boldsymbol{x}})$	$((u_k^{n,l})^3, v^l)$	$((u_k^{n,t})^3, v^t)$	
$2\binom{N_u}{2}$	$-3\Delta t \frac{G}{V_p V_{th}}, ((u_k^{n,\boldsymbol{x}})^2 u_j^{n,\boldsymbol{x}}, v^{\boldsymbol{x}})$	$((u_k^{n,l})^2 u_s^{n,l}, v^l)$	$((u_k^{n,t})^2 u_s^{n,t}, v^t)$	$s \neq k$
$\binom{N_u}{3}$	$-6\Delta t \frac{G}{V_p V_{th}}, (u_k^{n,\boldsymbol{x}} u_s^{n,\boldsymbol{x}} u_i^{n,\boldsymbol{x}}, v^{\boldsymbol{x}})$	$(u_k^{n,l} u_s^{n,l} u_i^{n,l}, v^l)$	$(u_k^{n,t} u_s^{n,t} u_i^{n,t}, v^t)$	$i > s > k$
$N_u N_w$	$\Delta t \eta_1(u_k^{n,\boldsymbol{x}} w_j^{n+1,\boldsymbol{x}}, v^{\boldsymbol{x}})$	$(u_k^{n,l} w_j^{n+1,l}, v^l)$	$(u_k^{n,t} w_j^{n+1,\sigma_t}, v^t)$	

in LifeV [140, 141], an object oriented C++ parallel finite element library based on the Trilinos project [142] developed by different groups worldwide.

4.2.3 Numerical results for the reduction of the forward problem

Here we investigate the performance of the PGD technique to reduce the Monodomain model in terms of accuracy of the solution and computational efficiency. We focus on the canine tissue geometry introduced in Section 3.2.4 in 2D and 3D settings and the real ventricle already considered in Section 3.2.2.

2D canine tissue geometry   We test the accuracy of the PGD technique applied to the Monodomain model using the 2D canine geometry. The tissue is assumed homogeneous, so the conductivity fields are identified by the two-dimensional vector $\boldsymbol{\sigma} = (\sigma_l, \sigma_t)$. The parameters belong to separate intervals $\sigma_l \in [m_l, M_l]$ and $\sigma_t \in [m_t, M_t]$, with $M_t < m_l$. In fact, it is observed that electrical conduction along the length of myocytes is faster than transverse direction [171, 172], thus σ_l should be greater than σ_t. Δ_l and Δ_t denote the interval lengths, i.e. $\Delta_l = M_l - m_l$ and $\Delta_t = M_t - m_t$. The cardiac fiber structure is shown in Fig. 3.16(a). One stimulus of $I_{app} = 250$ mV/ms is applied at the top of the domain for a duration of 2 ms. The space discretization method for u is given by linear finite elements on a 2D mesh with 22747 DOFs and the simulation time step is $\Delta t = 0.2$ ms until $T = 30$ ms. The conductivity parameters are assumed to belong to admissible space $\mathcal{C}_{ad} = [0.06, 0.09]\, \mathrm{cm}^2/\mathrm{ms} \times [0.01, 0.04]\, \mathrm{cm}^2/\mathrm{ms}$ ($\Delta_l = \Delta_t = 0.03$ cm^2/ms.) discretized with 250×250 DOFs. The bounds were manually tuned so to reproduce realistic wavefront propagation velocities observed in in vitro experiments (such as those in Section 3.3). u is measured in mV and we set $u_0(\boldsymbol{x}) = 0$ mV, $w_0(\boldsymbol{x}) = 0$.

In the following numerical tests, we investigate the interplay between the tolerance tol_e (associated to the number of modes) and the reliability of PGD. In fact, the lower the tolerance, the more accurate the PGD solution. However, this entails higher computational costs in the off-line phase as more modes are required to converge. We compare the full finite element (FE) Monodomain solution, the reference solution, with the PGD approximation varying tolerances, $\mathrm{tol}_e = (10^{-4}, 10^{-5}, 10^{-6})$, and conductivity values. The tolerance of the

2D canine tissue

Exe. time ↓ \tol$_e$ →	10^{-4}	10^{-5}	10^{-6}	FE
Off-line [h]	0.9	4.6	30.5	/
On-line [s]	0.1	0.15	0.2	15

3D canine tissue

Exe. time ↓ \tol$_e$ →	10^{-4}	10^{-5}	FE
Off-line [h]	8	41	/
On-line [s]	0.6	0.75	330

Real ventricle

Exe. time ↓ \tol$_e$ →	10^{-4}	10^{-5}	10^{-6}	FE
Off-line [h]	0.8	4.1	32	/
On-line [s]	0.1	0.15	0.2	60

Table 4.3: Off-line/on-line costs in terms of CPU time of the PGD approach for each test. After the off-line stage, whose complexity depends on the tolerance of the enrichment step, the evaluation of the PGD solution in the on-line phase is tremendously fast leading to a remarkable computational gain compared with the FE solution. The on-line execution times reported in the tables are approximated as they slightly vary according to the parameter values.

ADS fixed point iterations tol$_i$ is 10^{-2}.

Fig. 4.1(a) shows the number of modes at each time step. We notice that more modes are needed as the excitable wave travels through the tissue and the dynamics become more involved. Then they start decreasing at around t=22 ms as the wavefront propagation terminates. As expected, the number of modes needed for convergence increase with lower tolerance values. Consequently, it results in heavier computational burden of the off-line phase, as highlighted in Table 4.3. However, the computation of the PGD solution in the on-line phase is remarkably inexpensive. In this case, evaluating the PGD approximation at a given couple of parameters (σ_l, σ_t) only takes at most 0.2 s depending on the tolerance in contrast with 15 s of the corresponding FE solution, thus reducing the computation time of two orders of magnitude. The easy evaluation of the PGD solution is extremely helpful to set up a fast solver for the inverse problem, as we will see in Section 4.3.

In terms of accuracy, the quality of the PGD solution depends on the CV which, in this case, is mostly determined by the parameter σ_t. Fig. 4.1(b) displays the percentage L^2 relative error between FE and PGD solutions obtained with tol$_e$=10^{-4} for $\sigma_t = (0.01, 0.02, 0.03, 0.035, 0.04)$ cm^2/ms, ordered from lowest to highest CV ($\sigma_l = 0.09$ cm^2/ms). Regardless of the wavefront velocity, the discrepancy between FE and PGD ap-

proximation is minimal after the excitation terminates. On the other hand, during the potential propagation, we notice that the error increases at faster CVs, reaching almost 40% for $\sigma_t = 0.04$ cm^2/ms. The accuracy of the PGD solution improves for slow CV. For instance, for $\sigma_t = 0.01, 0.02$ cm^2/ms, the error is always below 10%. Therefore, we postulate that the PGD basis is informative enough to reproduce slow excitation waves, yet it needs further enrichment to accurately capture faster wavefront propagation. This is confirmed in Fig. 4.1(c) which compares the errors reducing the tolerance. We analyze three different anisotropy ratios $r = 2, 4$ and 6 – as typical for the cardiac tissue [7] – corresponding to $\boldsymbol{\sigma} = (0.07, 0.035)$ cm^2/ms, $(0.08, 0.02)$ cm^2/ms and $(0.084, 0.014)$ cm^2/ms, respectively. The case $r = 2$ features the highest CV as $\sigma_t = 0.035$ cm^2/ms, whereas the cases $r = 4, 6$ result in slower propagation. The approximation is overall inaccurate at the initial stages of the propagation because of the lack of regularity of the stimulus function I_{app} that abruptly goes to zero after 2 ms. Then, for the high CV case $r = 2$, the maximum of the error decreases from roughly 20% for tol$_e$=10^{-4} to approximately 10% and 3% for tol$_e$=$10^{-5}, 10^{-6}$, respectively. Therefore, enriching the PGD basis is necessary to ensure reasonable accuracy in case of high CV. For low CV cases $r = 4, 6$, the approximation slightly improves in case of richer PGD basis. However, setting tol$_e$=10^{-4} already guarantees a good approximation as the error is below 10%. In this particular numerical experiment, the accuracy of the PGD approximation does not seem to be sensitive on the value of the anisotropy ratio r. A comparison between FE and PGD transmembrane potentials varying tolerance values and anisotropy ratios tested is provided in Fig. 4.2. The snapshots are related to the time step featuring the highest error. For the high CV case $r = 2$ in (a), the PGD solution with tol$_e$=10^{-4} features a slower wavefront propagation than the FE one, thus CV is underestimated. In the other two tests, the propagation velocity is slightly overestimated for tol$_e$=10^{-4}, though the approximation is reasonably accurate. As already mentioned, lowering the tolerance improves the accuracy. This is evident by looking at the PGD solution for tol$_e$=10^{-6} that is qualitatively similar to the FE one. However, we remind that the off-line phase for constructing the PGD basis is more computationally demanding. Therefore, setting tol$_e$=10^{-5} seems to be the most convenient trade-off between accuracy and efficiency.
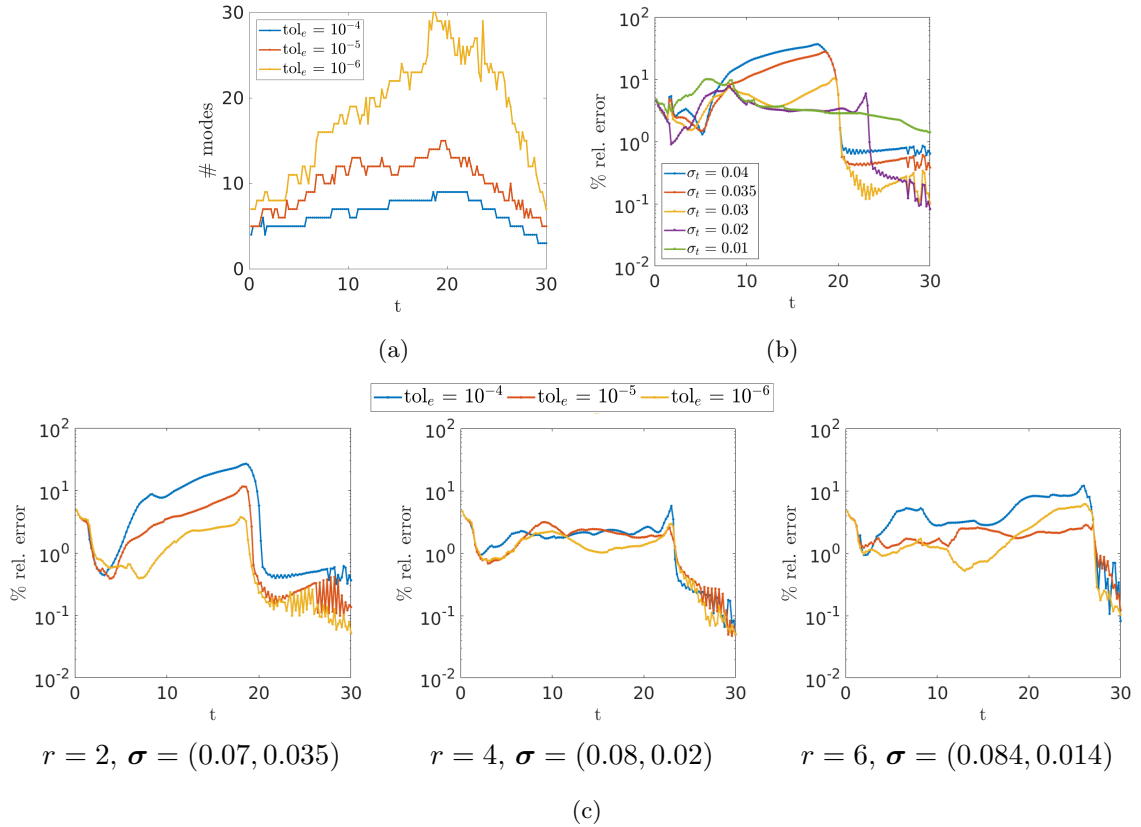
Figure 4.1: (a) PGD modes for different tolerances. The number of modes increases lowering the tolerances and resulting in heavier off-line phase (b) Percentage L^2 relative error between FE and PGD solutions for different conductivity values (ordered from high to slow CV and measured in [cm^2/ms]), tol$_e$=10^{-4}. The error drops as the CV decreases meaning that lower tolerance is needed for high CV cases. (c) Percentage L^2 relative error between FE and PGD solutions for different tolerances and anisotropy ratios. Error plots are displayed from high to slow CV. The approximation generally improves by enriching the PGD basis, especially in the case $r = 2$ for which the reduction of the error is more visible.
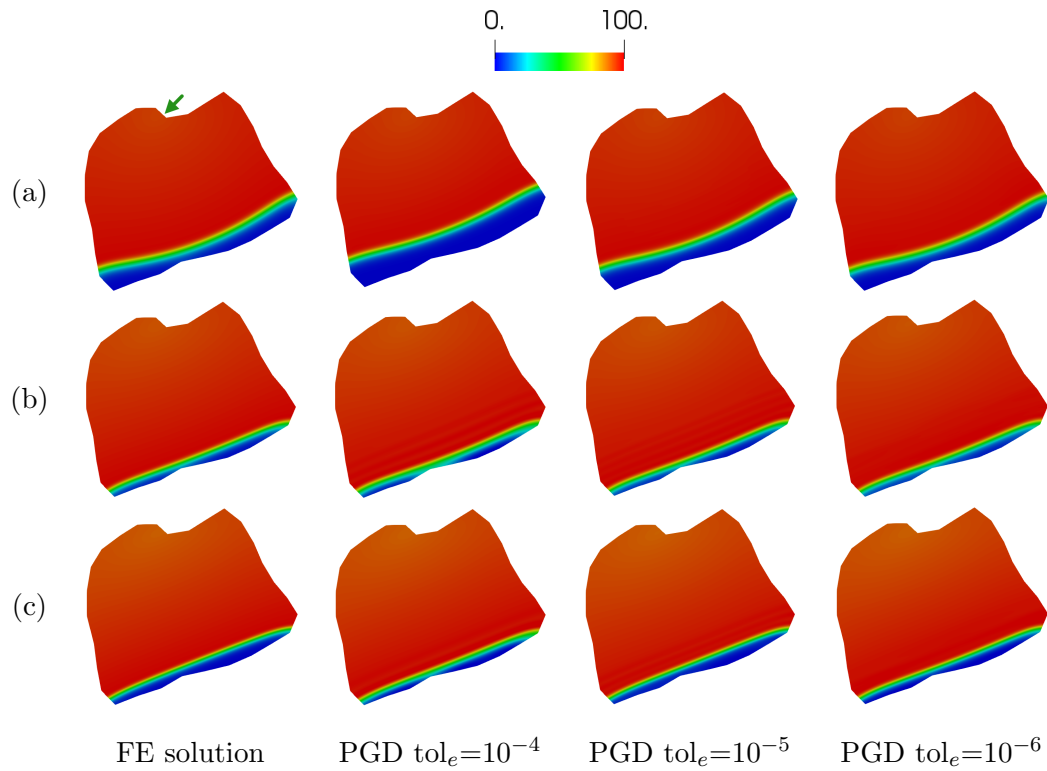
Figure 4.2: Comparison between FE and PGD solutions for different anisotropy ratios. The green arrow in row (a) indicates the stimulation site. (a) $r = 2$, $\boldsymbol{\sigma} = (0.07, 0.035)$ cm^2/ms, $t = 17$ ms. (b) $r = 4$, $\boldsymbol{\sigma} = (0.08, 0.02)$ cm^2/ms, $t = 22$ ms. (c) $r = 6$, $\boldsymbol{\sigma} = (0.084, 0.014)$ cm^2/ms, $t = 25$ ms. In the test $r = 2$, using tol$_e$=10^{-4} results in underestimating the CV of the FE solution, whereas the solution gets more accurate reducing the tolerance. In the other cases, the approximation is overall good even for tol$_e$=10^{-4}.

Since the choice $\mathrm{tol}_e{=}10^{-4}$ is the most promising in terms of computational efficiency, we explore possible ways to improve the quality of the resulting PGD approximation in case of high CV. In particular, three strategies are investigated: (a) refining the discretization of the admissible space $\mathcal{C}_{ad}$; (b) lowering the tolerance for the inner fixed point iterations tol_i; (c) narrowing the admissible interval for σ_t since the CV mostly depends on it. For strategy (a), $\mathcal{C}_{ad}$ is discretized with 500×500 DOFs instead of 250×250 of the previous tests. Regarding strategy (b), we test the accuracy of the PGD solution decreasing the tolerance tol_i from 10^{-2} to 10^{-4}. The percentage L^2 relative error of the approximation obtained with strategies (a) and (b) is reported in Fig. 4.3(a) for $\boldsymbol{\sigma} = (0.07, 0.035)$ cm^2/ms. Both the approaches perform poorly as they do not result in lower approximation error. In fact, adopting strategy (a), the error is similar to the previous test with coarser discretization of $\mathcal{C}_{ad}$. Following approach (b), the error slightly decreases in the initial stages of the wave propagation but then the error curve overlaps with the one of the previous numerical experiment. These methods not only do not improve the PGD approximation with $\mathrm{tol}_e{=}10^{-4}$, but they entail higher computational complexity: the finer discretization increases the costs of strategy (a), and approach (b) involves more iterations to reach convergence. On the other hand, method (c) successfully reduces the error. In Fig. 4.3(b), we analyze the performance of PGD with $\Delta_t = 0.01, 0.02$ cm^2/ms and compare it to the previous results obtained with $\Delta_t = 0.03$ cm^2/ms. Δ_l is fixed at 0.03 cm^2/ms. Narrower Δ_t yields an improvement of the PGD approximation, with $\Delta_t = 0.01$ cm^2/ms leading to the most accurate results. This is reasonable since restricting the admissible interval for σ_t implies less uncertainty on its value and fewer scenarios to predict. Therefore, the more knowledge and information we have on the parameter values, the better the approximation becomes. Moreover, it is also beneficial to efficiency as fewer modes are needed for convergence alleviating the computational demand of the off-line phase.

3D canine tissue geometry In the following experiments, the quality of the PGD approximation of the Monodomain model is assessed in a 3D framework. First, we consider a 3D canine tissue geometry obtained by extruding the 2D domain previously used along the z-axis. The resulting mesh is 0.5 cm thick and discretized with 136482 DOFs. The cardiac
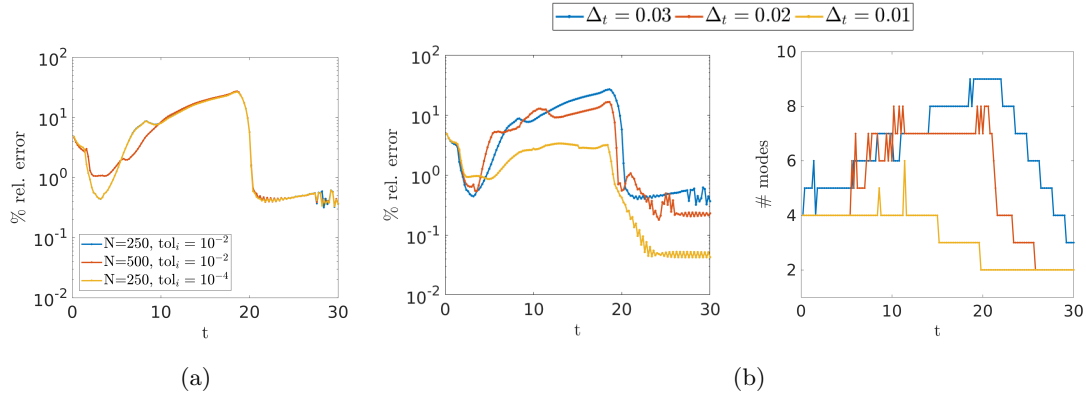
Figure 4.3: Possible improvements of PGD approximation with tol$_e$=10^{-4} in case of high CV ($\boldsymbol{\sigma} = (0.07, 0.035)$ cm^2/ms). (a) Percentage L^2 relative error for adopting two different strategies: increasing the number of DOFs for the discretization of $\mathcal{C}_{ad}$ vs. lowering the tolerances of the inner fixed point iteration section. These approaches are not effective as the error does not improve with respect to the previous tests. (b) Percentage L^2 relative error and number of modes when narrowing the admissible interval for σ_t (we keep $\Delta_l = 0.03$ cm^2/ms). Limiting the space where to seek the parameter σ_t results in lower error, especially for the case $\Delta_t = 0.01$ cm^2/ms (error reduced from roughly 20% to 3%), as well as fewer modes to reach convergence.

fiber structure on the top surface of the mesh is the same of the 2D case and then it is extruded along the z-axis as well. We consider the most general admissible space for the conductivity parameters $\mathcal{C}_{ad} = [0.06, 0.09]\,\mathrm{cm}^2/\mathrm{ms} \times [0.01, 0.04]\,\mathrm{cm}^2/\mathrm{ms}$, discretized with 250×250 DOFs. As done in the 2D tests, we analyze the anisotropy ratios $r = 2, 4$ and 6 corresponding to $\boldsymbol{\sigma} = (0.07, 0.035)$ cm^2/ms, $(0.08, 0.02)$ cm^2/ms and $(0.084, 0.014)$ cm^2/ms, respectively. Because of the finer resolution of the mesh, the off-line phase is more oner-ous than the 2D case: Table 4.3 shows that it takes 8 and 41 hours for tol$_e$=$10^{-4}, 10^{-5}$, respectively. The case tol$_e$=10^{-6} was not explored because it is computationally unafford-able. As for the on-line phase, adopting the PGD technique is extremely convenient since the evaluation of the reduced solution requires at most 0.7 s as opposed to 330 s for FE approximation.

As shown in Fig. 4.4, the errors varying tolerances and conductivity values are similar to the 2D ones reported in Fig. 4.1(c). For tol$_e$=10^{-4}, the case $r = 2$ corresponding to high CV features higher error than the other ones. Decreasing the tolerance to 10^{-5} qualitatively improves the solution. A comparison between FE and PGD transmembrane potentials for different tolerances and conductivities is carries out in Fig. 4.5. As already noted in the
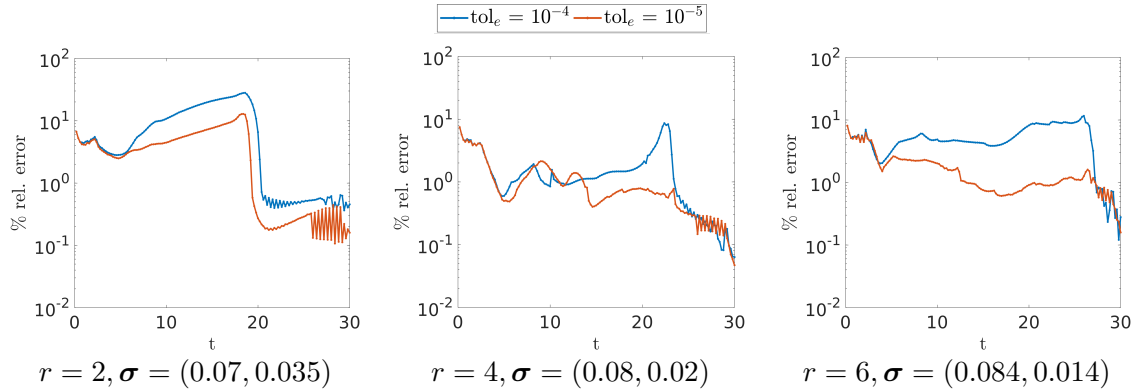
Figure 4.4: Percentage L^2 relative error for different tolerances and conductivity values ([cm^2/ms]) for the 3D canine geometry. Similarly to the 2D canine tests, there is a general improvement of the PGD approximation in case of reduction of the tolerance.

2D experiments, in the high CV case $r = 2$, the PGD solution obtained with tol$_e$=10^{-4} underestimates the CV yielding a poor approximation of the FE solution. In the cases $r = 2, 4$, although the CV is slightly overestimated, the PGD solution is closer to the FE one. Overall, the PGD approximation improves for tol$_e$=10^{-5} providing a better match of the wavefront propagation of the FE solution. Similarly the 2D case, the anisotropy ratio r does not have a significant impact on the accuracy of the PGD approach.

Real ventricle Here we test the performance of the PGD approach on the real left ventricular mesh introduced in Section 3.2.2. We recall that the mesh has 22470 DOFs and the fiber structure used is shown in Fig. 3.10. The conductivity values are the same as the previous tests. In this case, the resulting CVs are similar, whereas the influence of the anisotropy ratio r on the wavefront curvature is more evident. As the spatial discretization is coarser than the 3D canine geometry, we also included tol$_e$=10^{-6} in our analysis. As reported in Table 4.3, the off-line phase needs 0.8, 4.1 and 32 hours for tol$_e$=(10^{-4}, 10^{-5}, 10^{-6}), respectively. On the other hand, we underline that the on-line phase is extremely inexpensive as it requires at most 0.2 s as opposed to 60 s of the FE simulation.

The error between FE and PGD solution varying tolerances and conductivities is displayed in Fig. 4.6. Unlike the previous tests, the three anisotropy ratios tested show similar error for tol$_e$=10^{-4}, with a loss of accuracy for $r = 4, 6$ in comparison to the canine tissue tests. However, the approximation is overall reliable as the error is around 10%. The
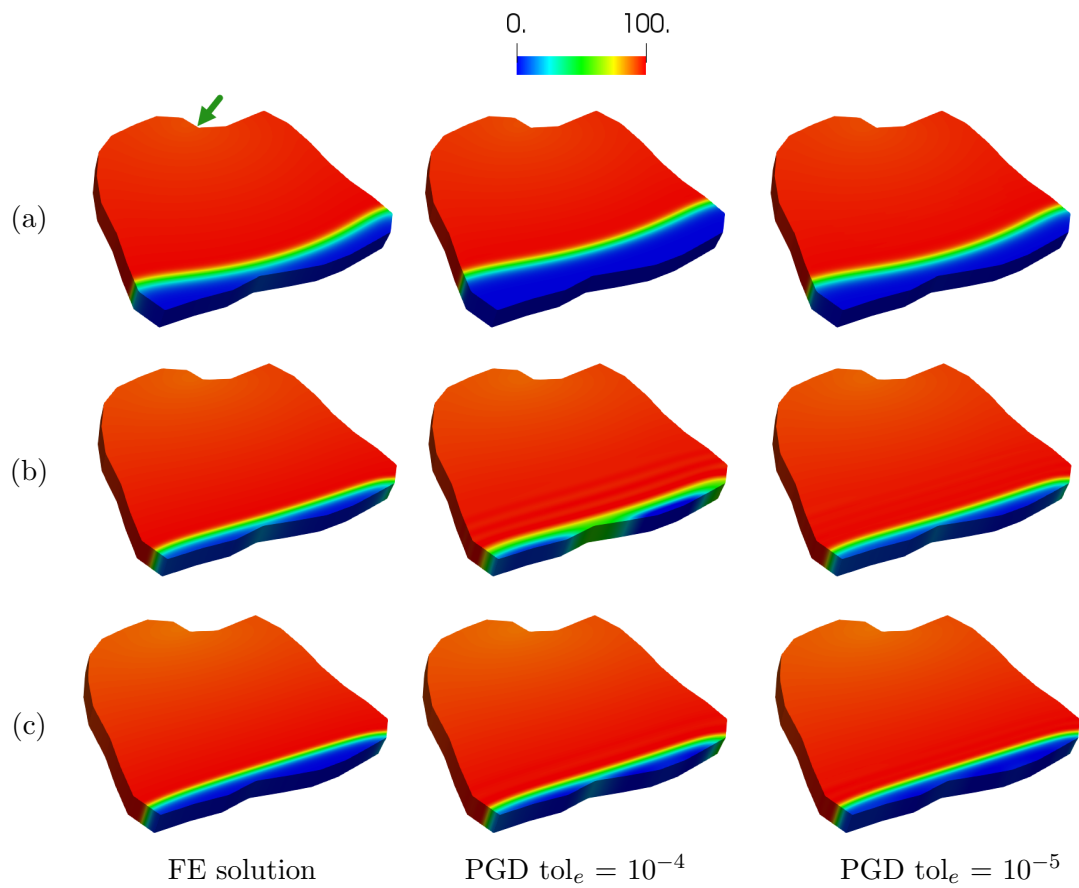
Figure 4.5: Comparison between FE and PGD solutions for different anisotropy ratios for canine geometry in 3D. The green arrow in row (a) indicates the stimulation site. (a) $r = 2$, $\boldsymbol{\sigma} = (0.07, 0.035)$ cm^2/ms, $t = 17$ ms. (b) $r = 4$, $\boldsymbol{\sigma} = (0.08, 0.02)$ cm^2/ms, $t = 22$ ms. (c) $r = 6$, $\boldsymbol{\sigma} = (0.084, 0.014)$ cm^2/ms, $t = 25$ ms. The discrepancy between FE and PGD solution is evident in row (a) for tol$_e$=10^{-4} as the CV is underestimated whereas the approximation is better in the other cases.
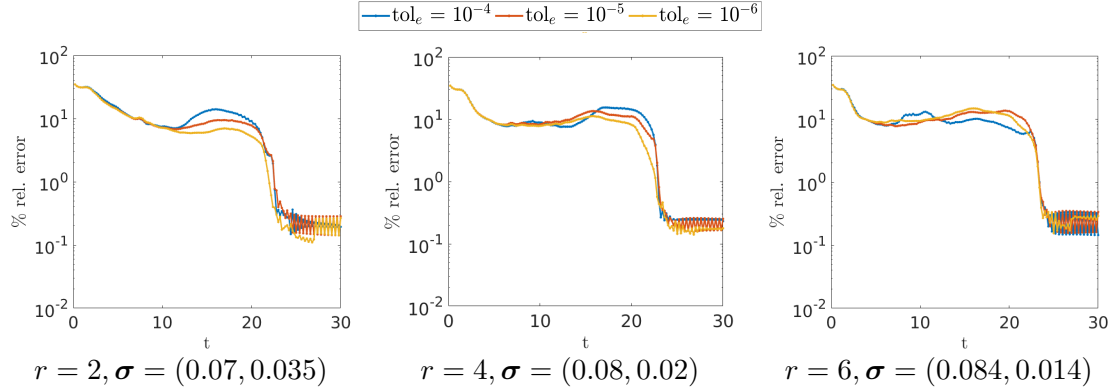
Figure 4.6: Percentage L^2 relative error for different tolerances and conductivity values ($[\text{cm}^2/\text{ms}]$) for the real ventricular geometry. The improvement of the PGD approach at lower tolerances is less evident in this case than the previous tests. The PGD solution is more sensitive to the anisotropy ratio r. In particular, for $r = 6$, the approximation worsens if more PGD modes are used.

negative impact of the discontinuity of I_{app} on the accuracy of the PGD technique is more evident in these experiments as the error at the initial stages of the simulation is around 30%. The reliability of the approximation does not benefit from lower tolerance values. Only the case $r = 2$ presents a reduction of the error, although less significant than the tests with canine geometry. For $r = 4$, the PGD solution with lower tolerance values is more accurate after $t = 15$ ms and the error drops only for few percentage points. Enriching the PGD basis does not improve the approximation in the case $r = 6$. On the contrary, the solution obtained with $\text{tol}_e = 10^{-4}$ better matches the FE one. Therefore, we speculate that in this particular test case the anisotropy ratio r plays a central role in the reliability of the PGD approach. Fig. 4.7 compares FE and PGD approximations. The improvement obtained with lower tolerance values is visible in row (a) as the PGD solution for $\text{tol}_e = 10^{-6}$ is more qualitatively similar to the FE simulation than the other ones. On the contrary, the cases $r = 4, 6$ do not profit from a richer PGD basis as the approximation for $\text{tol}_e = 10^{-4}$ looks closer to the FE solution.

4.3   Solving the PGD-MICP

In this section, we use the PGD transmembrane potential as a surrogate of the Monodomain solution to solve the MICP (3.7) for estimating cardiac conductivities. This means that

FE solution   PGD $\text{tol}_e = 10^{-4}$ PGD $\text{tol}_e = 10^{-5}$ PGD $\text{tol}_e = 10^{-6}$
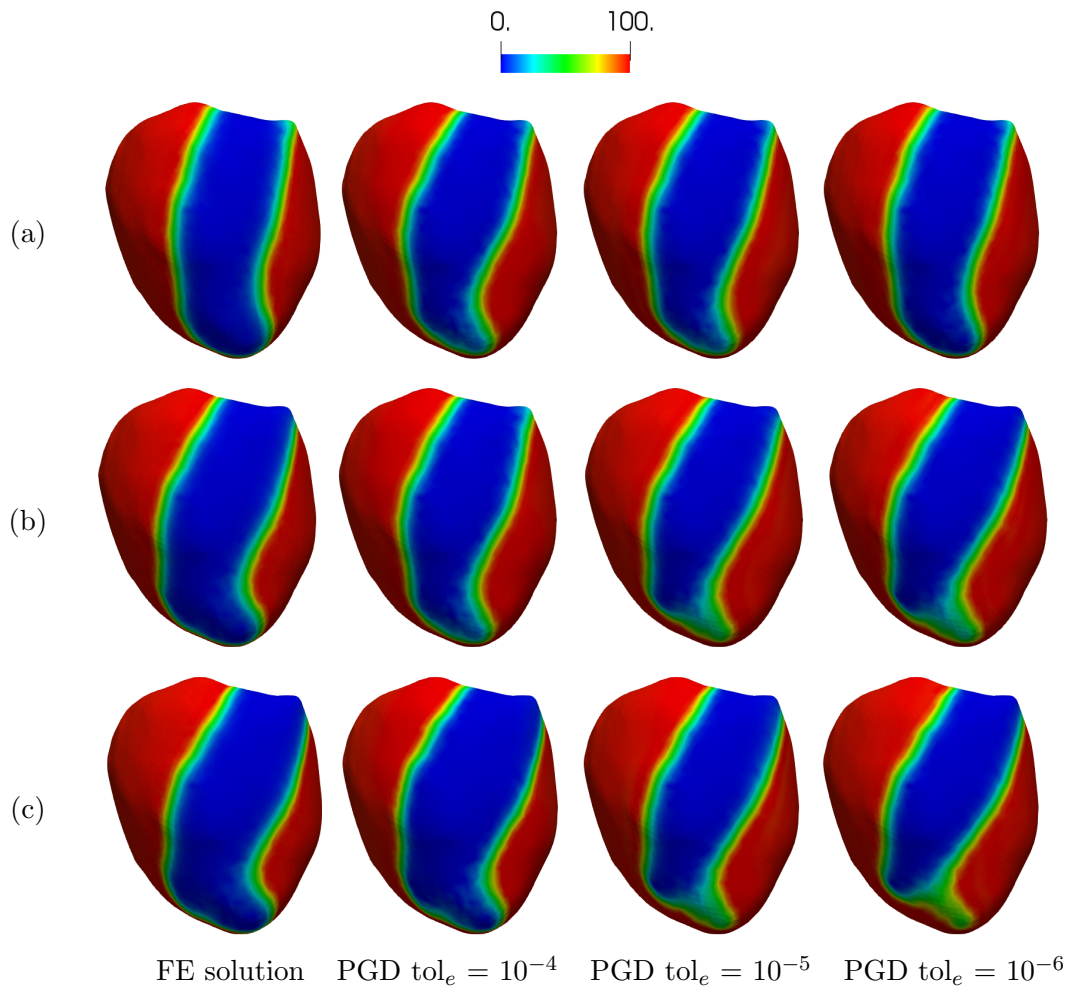
Figure 4.7: Comparison between FE and PGD solutions for different anisotropy ratios with the 3D ventricular geometry at $t = 20$ ms. The stimulation point is located at the inner wall of the ventricle, thus it is not visible from this visual perspective. (a) $r = 2$, $\boldsymbol{\sigma} = (0.07, 0.035)$ cm^2/ms. (b) $r = 4$, $\boldsymbol{\sigma} = (0.08, 0.02)$ cm^2/ms. (c) $r = 6$, $\boldsymbol{\sigma} = (0.084, 0.014)$ cm^2/ms. $r = 2$ is the only case in which more accuracy as the tolerance is reduced.

the misfit functional $\mathcal{J}$ is computed via the parametric PGD solution. The inversion is performed in a synthetic setting generating data in a finer spatial discretization and then adding at each time step Gaussian noise with zero mean and standard deviation equal to $p \max |u|$, where p is the percentage of noise, and the maximum is taken in both space and time. Synthetic measurements were recorded every $dt_{snap} = 2$ ms for a global duration of $T = 30$ ms, so 15 voltage recordings are used to calculate $\mathcal{J}$. The observation domain Ω_{obs} consists of 8000 equally distributed points on the domain, similarly to Section 3.2.4. Tikhonov regularization is not considered in these tests. The minimization of the misfit functional $\mathcal{J}$ is performed in MATLAB® using the sequential quadratic programming (SQP) algorithm [138], implemented by the `fmincon` routine. The search is constrained to the admissible parametric space $[m_l, M_l] \times [m_t, M_t]$. We set $\boldsymbol{\sigma}_0 = (0.06, 0.025)$ cm²/ms as initial guess. We evaluate the performance of the PGD method to solve the MICP varying tolerances and conductivity values – $r = 2, 4$ and 6 corresponding to $\boldsymbol{\sigma} = (0.07, 0.035)$ cm²/ms, $(0.08, 0.02)$ cm²/ms and $(0.084, 0.014)$ cm²/ms, respectively. Computing the PGD solution is even faster when solving the MICP because we only need to evaluate the misfit in a subset of observation points and for 15 time steps.

2D canine tissue geometry Considering the 2D canine mesh used in the previous section, we expect to get a more precise estimation for $r = 4$ since the PGD approximation is more accurate than the other conductivity couples (as already seen in Fig. 4.1(c)). The reliability of the estimation is assessed by looking in particular at the value of σ_t since it controls the CV.

Table 4.5 reports the results varying tolerances, conductivities and percentage of noise p. Regardless of the tolerance level and the value of p, the best estimates are obtained for $\boldsymbol{\sigma}_{exact} = (0.08, 0.02)$ cm²/ms, as expected. The recovery of the parameter σ_t is particularly precise, meaning that we can reliably reconstruct the true propagation dynamics with a comparable CV. On the other hand, more variability affects σ_l estimates. This is in accordance with the results of Section 4.2.3, where we noticed that the PGD solution depends more on the parameter σ_t, which controls the CV, and less sensitive to the value of σ_l. As for the other conductivity couples, the estimation obtained with the tol$_e$=10^{-4} is

less precise, especially for the high CV case $r = 2$, consistent with the fact that the PGD error is higher in this case, as shown in Fig. 4.1(c). An overall improvement of the results is visible with lower tolerance values. For $tol_e = 10^{-6}$, the estimates are accurate and robust with respect to the presence of noise in the data.

In view of better estimation in the case of high CV, we test the PGD approach to solve to MICP using narrower admissible ranges for σ_t with length $\Delta_t = 0.01$ and 0.02 cm^2/ms. We recall this strategy was used in the previous section to reduce the error of the PGD approximation (see Fig. 4.3). Table 4.6 shows more precise reconstruction using $\Delta_t = 0.01$ cm^2/ms both for $tol_e = 10^{-4}$ and 10^{-5}. This agrees with the results shown in Fig. 4.3 in which, for $\Delta_t = 0.01$ cm^2/ms, the PGD method is able to capture fast propagating excitable waves. Regarding $\Delta_t = 0.02$ cm^2/ms, a similar improvement is visible for $tol_e = 10^{-5}$, whereas this strategy is not as effective for $tol_e = 10^{-4}$.

As discussed previously, the great advantage of the PGD approximation is based on the extremely fast evaluation of the reduced solution in the on-line phase, making the inversion particularly inexpensive. In fact, solving the MICP using the PGD approximation of the transmembrane potential only takes at most 30 s in this test, according to Table 4.4. Furthermore, even in case of less accurate results such as the ones for $tol_e = 10^{-4}$, the PGD estimates may be helpful to speed up the solution of the MICP using the FE method. As a matter of fact, the PGD conductivities can be used as initial guess to accelerate convergence. This has been tested in the case of $\boldsymbol{\sigma}_{exact} = (0.07, 0.035)$ cm^2/ms and $tol_e = 10^{-4}$. Solving the MICP with FE approximation starting from the PGD estimates $\boldsymbol{\sigma}_0 = (0.0657, 0.0328)$ cm^2/ms requires 527 s to reach convergence with estimation $\boldsymbol{\sigma} = (0.07, 0.0349)$ cm^2/ms in contrast with 3293 s needed starting from $\boldsymbol{\sigma}_0 = (0.06, 0.025)$ cm^2/ms, which leads to a similar estimate $\boldsymbol{\sigma} = (0.0702, 0.0360)$ cm^2/ms.

3D canine tissue geometry   The MICP with PGD technique has been tested with the canine geometry in 3D as well. We recall we have not considered the case $tol_e = 10^{-6}$ because the off-line phase would be too expensive. As the PGD approximation of the transmembrane propagation in 3D yields similar results to the 2D case (as shown in Section 4.2.3), we expect results qualitatively comparable to the ones obtained in the 2D framework. This

tol$_e$ ↓ \test →	2D tissue	3D tissue	Real ventricle
10^{-4}	22	154	32
10^{-5}	25	180	36
10^{-6}	30	/	40

Table 4.4: Execution times [s] of reduced MICP based on the PGD approach for each test varying tolerance values of the enrichment step. Adopting the PGD technique allows quick estimates in less than a minute for the 2D tissue case and real ventricle or few minutes for the 3D tissue geometry. On the other hand, using FE approximation to solve MICP would require hours of computations. These are average values as times may vary depending on the realization of noise random variable and initial guess of the optimization procedure.

is confirmed in Table 4.7 as we notice better results for $\boldsymbol{\sigma}_{exact} = (0.08, 0.02)$ cm^2/ms with high precision for the parameter σ_t and a general improvement of the recovery decreasing the tolerance to 10^{-5}. We again highlight the huge computational saving related to the reduced MICP. In fact, despite the large number of DOFs of the 3D mesh (roughly 135K), the solution of the inverse problem only takes at most 180 s, as reported in Table 4.4.

Real ventricle Finally, we analyze the estimation in the real left ventricular test case. As previously discussed, the PGD approximation applied to this geometry is more sensitive to the anisotropy ratio r and features higher error (see Fig. 4.6), therefore the precision of the inversion may be affected. From Table 4.8, we note that using the PGD basis obtained with tol$_e$=10^{-4} leads to acceptable results only in the case $\boldsymbol{\sigma}_{exact} = (0.07, 0.035)$ cm^2/ms, whereas in the other tests the estimates, especially for σ_l, poorly represent the true values. The estimates become more accurate as the tolerance decreases. They reasonably match the exact conductivities in the case $\boldsymbol{\sigma}_{exact} = (0.07, 0.035)$ cm^2/ms and $\boldsymbol{\sigma}_{exact} = (0.08, 0.02)$ cm^2/ms, whereas the estimation of σ_l for $\boldsymbol{\sigma}_{exact} = (0.084, 0.014)$ cm^2/ms still lacks accuracy even for tol$_e$=10^{-6}. This agrees with the error pattern shown in Fig. 4.6, in which, for this particular parameter values, the discrepancy between FE and PGD solutions increases when reducing the tolerance. Table 4.4 shows that the convenience of solving the MICP with PGD approach is remarkable in these tests as well since results are obtained in at most 40 s.

$\text{tol}_e \downarrow \backslash\boldsymbol{\sigma}_{exact} \cdot 10^2 \rightarrow$	$r = 2$ (7.00,3.50)	$r = 4$ (8.00,2.00)	$r = 6$ (8.40,1.40)
10^{-4}	(6.57,3.28)	(8.11,1.93)	(8.98,1.29)
10^{-5}	(6.93,3.96)	(7.71,1.96)	(8.57,1.34)
10^{-6}	(6.90,3.56)	(7.80,1.96)	(8.22,1.35)

(Header above table: $p = 1\%$)

	(7.00,3.50)	(8.00,2.00)	(8.40,1.40)
10^{-4}	(6.56,3.27)	(7.91,1.93)	(8.97,1.31)
10^{-5}	(6.95,3.96)	(7.76,1.95)	(8.78,1.35)
10^{-6}	(6.83,3.56)	(7.84,1.97)	(8.31,1.35)

(Header above table: $p = 5\%$)

	(7.00,3.50)	(8.00,2.00)	(8.40,1.40)
10^{-4}	(6.55,3.24)	(8.05,1.93)	(8.98,1.30)
10^{-5}	(6.96,3.97)	(7.73,1.95)	(8.44,1.36)
10^{-6}	(6.82,3.56)	(7.91,1.96)	(8.26,1.35)

(Header above table: $p = 10\%$)

Table 4.5: The most accurate results are obtained for $\boldsymbol{\sigma} = (0.08, 0.02)$ as the PGD approximation is close to the FE solution. The estimates improve by reducing the tolerance in agreement with the error pattern seen in Fig. 4.1(c). Results are robust w.r.t the percentage of noise p.

$\Delta_t \downarrow \backslash p \rightarrow$	1%	5%	10%
0.03	(6.57,3.28)	(6.56,3.27)	(6.55,3.24)
0.02	(7.85,3.71)	(7.86,3.73)	(7.84,3.71)
0.01	(6.91,3.33)	(6.90,3.32)	(6.91,3.35)

(Header above table: $\text{tol}_e = 10^{-4}$)

$\Delta_t \downarrow \backslash p \rightarrow$	1%	5%	10%
0.03	(6.93,3.96)	(6.95,3.96)	(6.96,3.97)
0.02	(6.40,3.66)	(6.39,3.66)	(6.40,3.65)
0.01	(6.80,3.35)	(6.75,3.35)	(6.82,3.34)

(Header above table: $\text{tol}_e = 10^{-5}$)

Table 4.6: As an attempt to improve the estimation obtained for the high CV case $\boldsymbol{\sigma}_{exact} = (0.07, 0.035)$, we restrict the admissible domain Δ_t for σ_t. Improvement is visible for $\Delta_t = 0.01$ cm^2/ms whereas reducing the admissible interval to $\Delta_t = 0.02$ cm^2/ms is only effective for $\text{tol}_e=10^{-5}$. Results are robust w.r.t the percentage of noise p.

Estimation results of MICP using the PGD approximation as a surrogate of the Monodomain simulation for the 2D canine geometry. Conductivity values are magnified by a factor of 100 and measured in cm^2/ms.

$\text{tol}_e \downarrow \backslash \boldsymbol{\sigma}_{exact} \cdot 10^2 \rightarrow$	$p = 1\%$		
	$r = 2$	$r = 4$	$r = 6$
	(7.00,3.50)	(8.00,2.00)	(8.40,1.40)
10^{-4}	(6.78,3.21)	(8.07,1.98)	(8.98,1.32)
10^{-5}	(6.97,3.98)	(7.82,1.99)	(8.38,1.37)

	$p = 5\%$		
	(7.00,3.50)	(8.00,2.00)	(8.40,1.40)
10^{-4}	(6.90,3.20)	(8.11,1.97)	(8.96,1.31)
10^{-5}	(6.98,4.00)	(8.56,1.99)	(8.38,1.39)

	$p = 10\%$		
	(7.00,3.50)	(8.00,2.00)	(8.40,1.40)
10^{-4}	(6.81,3.25)	(8.13,1.96)	(9.00,1.32)
10^{-5}	(6.97,4.00)	(7.92,1.99)	(8.45,1.39)

Table 4.7: 3D canine geometry. Similarly to the 2D results, the case $r = 4$ features higher precision. The accuracy generally improves following a reduction of the tolerance.

$\text{tol}_e \downarrow \backslash \boldsymbol{\sigma}_{exact} \cdot 10^2 \rightarrow$	$p = 1\%$		
	$r = 2$	$r = 4$	$r = 6$
	(7.00,3.50)	(8.00,2.00)	(8.40,1.40)
10^{-4}	(6.53,3.46)	(8.98,1.56)	(7.10,1.22)
10^{-5}	(6.79,3.77)	(7.40,1.88)	(7.40,1.31)
10^{-6}	(6.75,3.62)	(7.57,2.06)	(7.70,1.45)

	$p = 5\%$		
	(7.00,3.50)	(8.00,2.00)	(8.40,1.40)
10^{-4}	(6.54,3.45)	(9.00,1.57)	(7.20,1.21)
10^{-5}	(6.81,3.78)	(7.36,1.88)	(7.46,1.20)
10^{-6}	(6.78,3.62)	(7.56,2.06)	(7.71,1.43)

	$p = 10\%$		
	(7.00,3.50)	(8.00,2.00)	(8.40,1.40)
10^{-4}	(6.55,3.45)	(8.90,1.56)	(7.21,1.21)
10^{-5}	(6.80,3.77)	(7.31,1.94)	(7.41,1.27)
10^{-6}	(6.79,3.60)	(7.58,2.06)	(7.69,1.46)

Table 4.8: Real ventricle. Estimation improves as tolerance reduces, expect for $\boldsymbol{\sigma}_{exact} = (0.084, 0.14)$ in which the results for σ_l are still inaccurate even for low tolerance.

Estimation results of MICP using PGD approximation as a surrogate of the Monodomain simulation in 3D setting. Conductivity values are magnified by a factor of 100 and measured in cm^2/ms.

4.4 PGD for MICP in a Bayesian Framework

Thus far, the problem of estimating cardiac conductivities was considered in a deterministic framework, i.e., we aimed to obtain a specific value for the conductivities, i.e., point estimates. In this section, we recast the inverse problem in the form of statistical *quest of information*. Besides providing point estimates, statistical inversion theory aims to assess the uncertainty about the variables based on the knowledge of the measurement process as well as the parameters of interest that are available prior to the measurement [49, 50, 173]. We adopt the Bayesian point of view [174]: any quantity that is not known exactly is regarded as a *random variable*. Even if we consider the conductivity an existing deterministic physical quantity that could, in principle, be measured, the lack of information about it justifies modeling it as a random variable. Thus, the randomness describes our degree of knowledge concerning its realization. The solution of the inverse problem is the *posterior probability distribution* that can be used to obtain estimates together with a systematic assessment of reliability and uncertainty of the unknown through the moments of the distribution. From the practical point of view, the adoption of a Bayesian perspective may be computationally demanding, as we will see. As a matter of fact, it requires many samples, i.e., evaluations of the solution for different values of the parameters. For this reason, in view of the encouraging results of the previous Section, the PGD can be an ideal frame to make the Bayesian perspective a viable one.

In Section 4.4.1, the formulation of the inverse problem in a Bayesian setting is presented. We then briefly introduce a class of algorithms, MCMC methods, used to explore the posterior distribution in Section 4.4.2. Lastly, in Section 4.4.4, the Bayesian estimation of conductivities is performed following the PGD approach.

4.4.1 Bayesian estimation

Let us first consider a Bayesian inverse problem in a general abstract setting. We denote random variables by capital letters and their realizations by lowercase letters. Different from the approach we have used so far that only produces point estimates, the final result of Bayesian estimation is the conditional distribution function of unknown variables on the

data, which is also called the *posterior probability density function* (PPDF). The PPDF can be computed by Bayes' formula:

$$p_{X|Y}(x|y) = \frac{p_{Y|X}(y|x)p_X(x)}{p_Y(y)} \qquad (4.24)$$

where X and Y denote the unknown random variable (scalar or vector) and the related data or measurements (vector), respectively. $p_{X|Y}(x|y)$ is the PPDF; $p_{Y|X}(y|x)$ is the *likelihood* function and the marginal distribution $p_X(x)$ is called the *prior* distribution. The likelihood function contains the forward model used in the classical deterministic inversion technique as well as information about the noise and other measurement and modeling uncertainties. The prior distribution reflects the knowledge of the unknowns, before the data Y is collected. As normalizing constant, $p_Y(y)$ is not needed in the exploration of the posterior space in (4.24). Therefore, the PPDF can be evaluated as follows:

$$p_{X|Y}(x|y) \propto p_{Y|X}(y|x)p_X(x). \qquad (4.25)$$

It is obvious that the physical quantities of interest are fixed instead of fluctuating. The rationale in modeling them as random variables is that uncertainty exists in our knowledge of these parameters since they are all derived from noisy data.

In view of formulating the MICP in a Bayesian setting, let us consider the Monodomain model reshaped in the form (2.27) (u measured in mV) coupled with the Rogers-McCulloch model (2.6). This model was chosen for its computational convenience and because it allows us to use the PGD approximation (see Section 4.2.3). Again, for the sake of notation, the conductivity tensor $\mathbf{D} = \boldsymbol{\sigma}/(\beta C_m)$ is denoted by $\boldsymbol{\sigma}$ as usual. The computation domain is assumed homogeneous, meaning the conductivity tensor can be identified by the vector of two parameters $\boldsymbol{\sigma} = (\sigma_l, \sigma_t)$. As in the case of classical inverse problems, the reconstruction of the unknown conductivity tensor is made possible by the measurement of the transmembrane potential at distinct points within $\Omega \times [0, T]$. Let U denote the directly observable random variable describing voltage and E the random vector of measurement noise. The components of the vector E are usually assumed as independent identically dis-

tributed (i.i.d.) Gaussian distributions with zero mean and variance ν^2 (standard deviation ν). With an abuse of notation, we still use the symbol $\boldsymbol{\sigma}$ to indicate the random conductivity tensor as well as its realization. $\boldsymbol{\sigma}$ and E are mutually independent. We omit subscripts in the probability density functions for the sake of notation. A realization of U, u_{meas}, is the actual observed voltage data, i.e., $u_{meas} = [u_{meas,1}^{(1)}, \ldots, u_{meas,N}^{(1)}, \ldots, u_{meas,1}^{(M)}, \ldots, u_{meas,N}^{(M)}]^T$, where

$$u_{meas,i}^{(j)} = u(\boldsymbol{\sigma}, \mathbf{x}_i, t_j) + e$$

where $i = 1, \ldots, N, j = 1, \ldots, M$ ($t_M = T$); N and M are the number of observation sites and available recordings, respectively; e is a scalar realization of the random measurement noise; u the transmembrane voltage.

The voltage dynamics can be described using the following relationship

$$U = F(\boldsymbol{\sigma}) + E \tag{4.26}$$

where F represents the solution of the Monodomain model (2.27) that computes the transmembrane potential with given conductivity values $\boldsymbol{\sigma}$. We assume that the numerical errors induced by F are much less in magnitude than the measurement errors which is reasonable for an appropriate choice of space and time discretization. If we select a value for $\boldsymbol{\sigma}$, the assumption of mutual independence between $\boldsymbol{\sigma}$ and E guarantees that the probability density of E, $p_{noise}(e)$, does not vary conditionally to $\boldsymbol{\sigma}$. Therefore, we deduce that U conditioned on $\boldsymbol{\sigma}$ is distributed like E, the probability density being translated by $F(\boldsymbol{\sigma})$, that is, the likelihood can be written as

$$p(U|\boldsymbol{\sigma}) = p_{noise}(E) = p_{noise}(U - F(\boldsymbol{\sigma})) = \frac{1}{(2\pi)^{n/2}\nu^n} \exp\left\{-\frac{(U - F(\boldsymbol{\sigma}))^T(U - F(\boldsymbol{\sigma}))}{2\nu^2}\right\} \tag{4.27}$$

where n is the total number of measurements. As for the prior distribution of the unknown conductivity, $p_{pr}(\boldsymbol{\sigma})$, the only information we have before collecting data is that $\boldsymbol{\sigma}$ belongs to an admissible space $\mathcal{C}_{ad} = [m_l, M_l] \times [m_t, M_t]$. Therefore, any possible conductivity value has equally probability. This is translated in modeling the conductivity tensor as a random variable following a uniform distribution, $\boldsymbol{\sigma} \in \mathcal{U}([m_l, M_l] \times [m_t, M_t])$. We also assume that

σ_l and σ_l are mutually independent, so $\sigma_l \sim \mathcal{U}(m_l, M_l)$ and $\sigma_t \sim \mathcal{U}(m_t, M_t)$.

With the above likelihood and prior distribution models, the PPDF can be evaluated as

$$p(\boldsymbol{\sigma}|U) \propto p(U|\boldsymbol{\sigma})p_{pr}(\boldsymbol{\sigma}) \propto \exp\left\{-\frac{(U - F(\boldsymbol{\sigma}))^T(U - F(\boldsymbol{\sigma}))}{2\nu^2}\right\}, \quad \boldsymbol{\sigma} \in \mathcal{C}_{ad}. \qquad (4.28)$$

Once the PPDF is known, a complete probabilistic specification of the unknowns under all uncertainties is enabled [175]. Various point estimators can be defined such as the *Maximum A Posteriori* (MAP) estimator

$$\boldsymbol{\sigma}_{MAP} = \arg\max_{\boldsymbol{\sigma}\in\mathcal{C}_{ad}} p(\boldsymbol{\sigma}|U) \qquad (4.29)$$

and the *Conditional Mean* (CM) estimator

$$\boldsymbol{\sigma}_{CM} = \mathbb{E}(\boldsymbol{\sigma}|U) = \int_{\mathcal{C}_{ad}} \boldsymbol{\sigma} p(\boldsymbol{\sigma}|U)\,d\boldsymbol{\sigma}. \qquad (4.30)$$

These estimates are the Bayesian counterpart of the deterministic solutions. More specifically, the computation of the MAP estimate is an optimization problem similar to the one we have solved so far while the CM estimate is obtained with numerical integration. Estimates of spread can be also computed, such as the *conditional covariance*

$$\Gamma(\boldsymbol{\sigma}|U) = \int_{\mathcal{C}_{ad}} (\boldsymbol{\sigma} - \mathbb{E}(\boldsymbol{\sigma}|U))(\boldsymbol{\sigma} - \mathbb{E}(\boldsymbol{\sigma}|U))^T p(\boldsymbol{\sigma}|U)\,d\boldsymbol{\sigma}. \qquad (4.31)$$

In our case, point estimates are vectors of two components and spread estimates are 2×2 matrices which can be summarized by the standard deviation of each component and their correlation coefficient.

4.4.2 Exploration by sampling

An analytical computation of point and spread estimates is generally unachievable. In the case that integration is over a low-dimensional space, estimates can be computed by means of common quadrature methods. A problem with these techniques is that they require a relatively good knowledge of the support of the probability distribution, which is usually

part of the information that we are actually looking for. This creates problems in our case, as we will discuss in Section 4.4.4. Moreover, in case we want to estimate a large number of parameters, the use of numerical quadrature rule is impractical. In fact, if the dimension r of the parameter space is large, then an $m-$point rule for each direction would require m^r integration points, exceeding the computational capacity of most computers.

An alternative strategy is resorting to sampling methods [176]. Let us assume one has an ensemble of independent samples from a target posterior distribution $p(x|y)$ ((4.28) in our case). We write $x^{(k)}, k = 1, \ldots, N_s \sim p(x|y)$, where N_s is the number of samples from the posterior distribution. Then, the mean of any function $f(x)$ of x can be approximated by the sample average

$$\mathbb{E}(f(x)|y) = \int f(x)p(x|y)\,dx \approx \frac{1}{N_s}\sum_{k=1}^{N_s} f(x^{(k)}). \tag{4.32}$$

The law of large numbers guarantees that the variance of the sample average behaves like $\propto N_s^{-1}$. For example, for the CM estimate, we would set $f(x) = x$ and for the posterior covariance $f(x) = (x - \mathbb{E}(x|y))(x - \mathbb{E}(x|y))^T$. The MAP estimate would be obtained as follows $x_{MAP} = \arg\max_{x^{(k)}} p(x^{(k)})$. Due to the slow polynomial convergence, a large ensemble of independent samples needs to be drawn from the distribution to ensure reliable results.

Moreover, the posterior probability that the $j - th$ component of x belongs to a certain interval $[a, b]$ can be obtained as

$$P(x_j \in [a, b]) \approx \frac{\# \text{ samples with } x_j \in [a, b]}{N_s}. \tag{4.33}$$

The key problem is how to draw samples from the posterior distribution. The most important methods for the generation of samples from an arbitrary probability distribution are the *Markov Chain Monte Carlo* (MCMC) methods. These algorithms generate samples $x^{(i)}$ while exploring the state space X (the primary unknowns) using a Markov chain mechanism [50, 177, 178]. The advantage of using MCMC is that one can draw samples even if it is only possible to evaluate the target distribution up to a normalizing constant. The

Metropolis-Hastings (MH) algorithm is the most basic form of all MCMC methods [177]. For a target distribution $p(x)$, the MH algorithm draws a candidate $x^{(*)}$ from a proposal distribution $q(x^{(*)}|x^{(i)})$ (easy to sample from) at each iteration, where $x^{(i)}$ is the sample at the previous iteration. The chain moves to the next state $x^{(*)}$ with an acceptance probability A defined as $A(x^{(*)}|x^{(i)}) = \min\left\{1, \frac{p(x^{(*)})q(x^{(i)}|x^{(*)})}{p(x^{(i)})q(x^{(*)}|x^{(i)})}\right\}$. The MH method is summarized in Algorithm 2. By its construction, the MH algorithm guarantees that the

---

Algorithm 2 MH algorithm

1: Define the proposal distribution $q(\cdot|\cdot)$ and set N_s;
2: Initialize $x^{(0)}$ and set $i \leftarrow 0$;
3: Compute $p(x^{(0)})$;
4: **while** $i < N_s$ **do**
5:      Sample $x^{(*)} \sim q(x^{(*)}|x^{(i)})$;
6:      Compute $p(x^{(*)})$;
7:      Compute the acceptance ratio $A = A(x^{(*)}|x^{(i)}) = \min\left\{1, \frac{p(x^{(*)})q(x^{(i)}|x^{(*)})}{p(x^{(i)})q(x^{(*)}|x^{(i)})}\right\}$;
8:      Sample $u \sim \mathcal{U}(0,1)$;
9:      **if** $u < A$ **then**
10:          Accept and set $x^{(i+1)} = x^{(*)}$, $p(x^{(i+1)}) = p(x^{(*)})$, $i \leftarrow i + 1$;
11:          Store $x^{(i)}$;
12:      **else**
13:          Reject;
14:      **end if**
15: **end while**

---

chain converges to the target distribution $p(x)$ for any proposal distribution [50]. However, careful design of the proposal will accelerate the convergence speed. In the case of symmetric proposal $q(x^{(*)}|x^{(i)}) = q(x^{(i)}|x^{(*)})$, the acceptance probability A simplifies to $A(x^{(*)}|x^{(i)}) = \min\left\{1, \frac{p(x^{(*)})}{p(x^{(i)})}\right\}$. From here, it is clear that moves going towards higher probability are accepted immediately and samples that take us to lower probabilities are sometimes accepted.

The Gibbs sampler is also a widely used MCMC algorithm. The approach followed in this method is to update a single component of X each time using the full conditional as the proposal distribution. More details can be found in [50, 179]. In this Thesis, we will use MH algorithm. We again underline that in statistical inversion one needs to draw many samples from the target distribution, so, in MH method, the evaluation of the posterior in step 6 of Algorithm 2, which involves a forward solve, must be efficient in order to limit

computational complexity. To this end, the PGD explored in the previous Sections can be a valid technique for fast Monodomain solutions.

4.4.3 Practical implementation of the MH algorithm

In this Section, we test the MH algorithm to explore the PPDF (4.28) with the purpose of providing point and spread estimates of the conductivity $\boldsymbol{\sigma}$ conditioned on the transmembrane potential data. Several practical issues need to be addressed. First, the evaluation of the likelihood function depends on the numerical approximation of the voltage dynamics. Referring to the 3D canine geometry considered in Section 4.2.3, it is clear that using full FE solution is computationally overwhelming as one single sample in MH algorithm would require 330 s. For this reason, we resort to the PGD approximation because of its extremely fast evaluation of the solution (in this case at most 0.2 s). Moreover, it is not simple to decide when the MCMC sample is large enough to cover the target distribution. Many samples are required to ensure a reasonable accuracy of the results since Monte Carlo integration has a slow rate of convergence. This is solved by looking at the results varying the number of samples N_s and picking the value for which we get steady estimates.

Other important and difficult issues affecting the quality of the sampling strategy are the following:

1. The choice of the proposal distribution $q(y|x)$ is crucial for performance of the MH method. A common choice in literature is using a symmetric random walk sampler [50, 173]

$$q(y|x) = \frac{1}{\sqrt{2\pi\gamma^2}} \exp\Big(-\frac{1}{2\gamma^2}\, \|y - x\|^2\Big), \quad \gamma > 0. \tag{4.34}$$

In other words, we assume that the random step from x to y is distributed as white noise $W = Y - X \sim \mathcal{N}(\mathbf{0}, \gamma^2 I)$. The value of γ controls the random step length and in turns the acceptance ratio A of the MH algorithm. It is troublesome to detect a reasonable value of γ: if it is too small, the new proposals are accepted frequently, but the chain explores the density too slowly. When γ is increased, we ensure a better coverage of the space, but A gets smaller meaning that more samples are rejected. An acceptance ratio around 30% is considered optimal in literature [173]. However, we chose to follow a different strategy: we

generate a small ensemble of samples using the proposal (4.34) with a certain value of γ; we calculate the empirical covariance matrix C of this sample; we continue the MH algorithm using the proposal distribution

$$q(y|x) \sim \mathcal{N}(y - x, C). \tag{4.35}$$

The motivation behind this is that the covariance matrix C carries information about the shape of the distribution, therefore the proposal covers the support of the density more effectively than the standard random sampler. With this approach, we are able to increase the acceptance ratio to at least 60% in all the tests we will discuss, thus avoiding the practical difficulty of tuning γ.

2. Another practical issue when sampling with MCMC algorithm is the dependence of the Markov chain from the initial state. Usually, it might take some samples before the chain starts representing the actual probability density. The initial stage of the chain, usually referred to as *burn-in* of the sample, has nothing to do with the target distribution and it is normal procedure in MCMC sampling to disregard the beginning of the sample to avoid that the burn-in affects the estimates that are subsequently calculated from the samples.

3. Since the sample is a realization of a Markov chain, complete independence of the sample points cannot be expected: every draw depends at least on the previous element in the chain. The *autocorrelation* of a signal is a useful to quantify the independence of the realizations [50]. Let $x_1, \ldots, x_N$ be samples (in our case, each sample is a two-dimensional vector of conductivities) from a Markov chain. The *lag k autocorrelation* of the $i - th$ component ($i = 1, 2$ in our case) can be defined as

$$\rho_i(k) = \frac{\sum_{j=1}^{N_s - k}(x_j - \bar{x})_i(x_{j+k} - \bar{x})_i}{\sum_{j=1}^{N_s}(x_j - \bar{x})_i^2} \tag{4.36}$$

where $\bar{x}$ is the sample average. The value k at which $\rho_i(k) \approx 0$ tells us the period after which the sample points can be considered insignificantly correlated for the $i - th$ component. It is reasonable to expect that the dependence of the draws decreases when k increases. The rate

of decay of the autocorrelation to zero is crucial for the efficiency of MCMC algorithms: if the decay is too slow, then many draws has to be disregarded to ensure independence. The rate of decay can be improved by properly tuning the step length γ of the proposal (4.34). In fact, the larger γ, the faster the Markov chain mixes and the faster the dependence decays in successive iterations. However, in this case, sampling from the target distribution would be more challenging as many samples points would be rejected. Using the proposal (4.35) is a great solution to this problem as well because the better coverage of the posterior space provided by the alternative proposal guarantees a reasonable mixing of the chain.

In practice, after burn-in removal, we compute the lag k autocorrelation for the components of $\boldsymbol{\sigma}$, σ_l and σ_t, then we pick k so that $\rho_{\sigma_l}(k)$ and $\rho_{\sigma_t}(k)$ are close to zero and eventually an independent set of samples is formed by taking only every $k - th$ sample points. Fig. 4.8(a) and Fig. 4.8(b) show an example of burn-in phase and lag k autocorrelation of the parameters σ_l and σ_t. For the parameter σ_t, it is evident that the chain depends on the initial state of the MH method, therefore the first 400 samples are disregarded. As for the Fig. 4.8(b), we note that as k gets larger, $\rho(k)$ decreases, as expected. In this case, we pick $k = 5$ since the autocorrelation is close to zero. It is not preferable to choose k too large since this would imply a huge waste of samples and so higher computational cost of the sampling algorithm.

4. The actual computations are performed in the log-domain, i.e., in the MH algorithm, the new proposal y moving from x is accepted if $\log u < \log p(y) - \log p(x)$. In this way, we avoid numerical problems with underflow or overflow in the computation of the ratio of $p(y)$ and $p(x)$.

5. Finally, the PPDF (4.28) does not have full support as $\boldsymbol{\sigma} \in \mathcal{C}_{ad}$, but the proposal distribution (4.35) does. Therefore, it is possible that a new move y from the sample x may not belong to $\mathcal{C}_{ad}$, so it should be immediately rejected without even computing $p(y)$. A solution might be to keep sampling y until we have $y \in \mathcal{C}_{ad}$, and then evaluate A to decide whether or not to accept it. As reasonable as this idea may at first seem, the MH algorithm needs to be adjusted to reflect this approach. In fact, by repeatedly sampling from the proposal until we obtain a feasible value, we are implicitly sampling from a different proposal distribution, which is still the proposal distribution $q(x|y)$, but truncated at zero
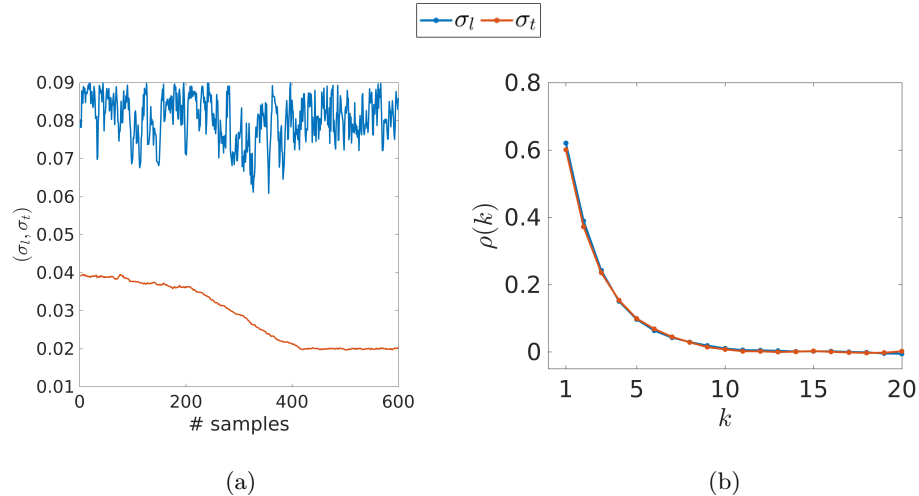
Figure 4.8: (a) Burn-in phase is visible especially for σ_t. To eliminate the impact of the initial state, we disregard the first 400 samples. (b) Lag k autocorrelation for the two conductivity parameters. When $\rho(k)$ is close to 0, we take every $k - th$ sample to form an independent ensemble of realizations.

outside $\mathcal{C}_{ad}$. This proposal distribution is totally reasonable so we can use it provided that we use the correct MH acceptance ratio. The truncated proposal has the same density as the normal proposal, but the integral of its probability density function does not equal 1 because of the truncated support. Therefore, we need to adjust it with a normalizing constant. Explicitly, we have that the truncated proposal is

$$\tilde{q}(y|x) = \frac{q(y|x)}{\Phi(x)}, \quad y \in \mathcal{C}_{ad} \tag{4.37}$$

where $q(y|x)$ is from (4.35) and $\Phi(x)$ is the cumulative distribution function (CDF) of a standard bivariate normal. In this way, the integral of the new proposal equals 1. Therefore, the correct MH acceptance ratio A is

$$A(x^{(*)}|x^{(i)}) = \min\left\{1, \frac{p(x^{(*)})q(x^{(i)}|x^{(*)})\Phi(x^{(*)})}{p(x^{(i)})q(x^{(*)}|x^{(i)}\Phi(x^{(i)})}\right\} = \min\left\{1, \frac{p(x^{(*)})\Phi(x^{(*)})}{p(x^{(i)})\Phi(x^{(i)})}\right\} \tag{4.38}$$

where we see that the normalizing constants do not cancel out.

4.4.4   Solution of the reduced bayesian MICP

We analyze the performance of MH algorithm on the 3D test case of canine tissue studied in Section 4.3 using the PGD basis obtained with $\text{tol}_e = 10^{-5}$. We consider the same synthetic measurements and conductivity values used in Table 4.7 so to compare deterministic and Bayesian estimates. The percentage of noise $p = 1, 5, 10\%$ corresponds to the standard deviation $\nu = 1, 5, 10$ mV, respectively. $N_s = 20000$ samples – after burn-in removal and subsampling – generated by MH algorithm are used to compute the estimates. This is a sufficient amount of samples to ensure the convergence of Monte Carlo integration. We emphasize again that the PGD approximation is remarkably convenient for estimating parameters in a Bayesian framework. In fact, generating the ensemble of samples took at most 3 hours in the following tests. This would be unachievable using FEM solution.

Fig. 4.9 shows the posterior densities varying the standard deviation ν of the noise and the conductivity values. This helps the visualization of the uncertainty related to the point estimates and the support of the posterior distribution in the parameter space. The confidence in the reliability of the point estimates depends on the width of the support of the posterior density along the σ_l and σ_t-directions. It is clear that if the support is wide, then we need to be more careful in evaluating the reliability of point estimates. We note from Fig. 4.9 that, regarding the parameter σ_t, the posterior density of the case $r = 2$ has a wider support than the other two ones, meaning that the point estimates for $r = 2$ feature more uncertainty. This is consistent with the results obtained in the Section 4.2.3 showing that the PGD approximation error for $r = 2$ is less accurate. Therefore, less precision affects our confidence in the reliability of the point estimates. As for σ_l, the support of the densities span a much wider interval. This agrees too with the previous results since we have noticed that the PGD solution in this test case is less sensitive to the parameter σ_l which causes more variability in the estimation. Furthermore, the support of the posteriors enlarges as the standard deviation ν increases, negatively affecting our confidence in the points estimates.

Point and spread estimates are presented in Table 4.9. For the sake of readability, we report the deterministic results $\boldsymbol{\sigma}_{det}$ shown in Table 4.7 as well. We expect $\boldsymbol{\sigma}_{MAP}$ and $\boldsymbol{\sigma}_{det}$

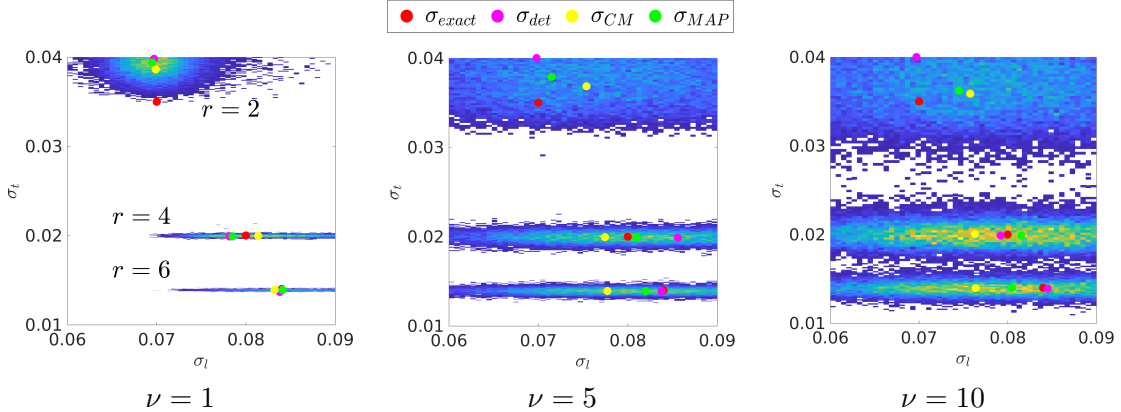Figure 4.9: Samples of MH algorithm varying noise standard deviation ν ([mV]) and conductivity values ($r = 2, 4$ and 6 corresponding to $\boldsymbol{\sigma} = (0.07, 0.035)$ cm^2/ms, $(0.08, 0.02)$ cm^2/ms and $(0.084, 0.014)$ cm^2/ms, respectively). Samples are colored in blue. In general, the higher the variance, the sparser the samples. σ_l features higher uncertainty, especially for $r = 2$, whereas, we can be more confident about the quality of the estimates of σ_t, in particular in the case $r = 4$ and 6.

to be comparable since they are solutions of similar optimization problems. The estimation are similar for $\nu = 1$ because the posterior densities are less sparse and so the peak of the distribution is easier to find. On the other hand, increasing the noise, the MAP and deterministic estimations of σ_l diverge whereas, for σ_t, they match in the cases $r = 4$ and 6. This is consistent with the fact that the variability featuring σ_l is much higher than σ_t for $r = 4$ and 6 and consequently there could be many local minima along the σ_l-direction in which the deterministic inversion could stall depending on the initial guess. For the same reason, the estimation of σ_t for $r = 2$ are not consistent. The MAP and CM estimates may not necessarily coincide because the PPDF (4.28) is not purely Gaussian, but a truncated Gaussian. Therefore, the density could have one tail heavier than the other resulting in a shifting of the mean and so a mismatch with the distribution peak. The difference between MAP and CM estimate is more visible for the parameter σ_l since it features higher uncertainty.

The key feature of Bayesian inversion is the quantification of the uncertainty, that can be performed by computing standard deviations as well as correlation of the estimates. From Table 4.9, we notice that the standard deviation of the samples of σ_l is always higher than σ_t, in particular for $r = 4$ and 6, in agreement with the fact that, in this specific test

case, the PGD approach is less sensitive to the value of σ_l. As for the correlation, which measures the degree to which the parameters are linearly related, it is always small enough to conclude that there is no linear relationship between the two unknown quantities σ_l and σ_t of the PGD solution.

Intervals of a given credibility with respect to single components of $\boldsymbol{\sigma}$ are also of interest. By looking at one component at the time, we can provide intervals $I_k(p)$, $k = l, t$, containing $p\%$ of the mass of the marginal density of σ_l or σ_t. Equal-tailed intervals $I_k(90)$ are reported in Table 4.10. The narrower the intervals, the more robust and reliable the estimates are. We note that, consistently with the results shown in Table 4.9, credible intervals related to σ_t are narrower than the ones corresponding to σ_l because of the lower standard deviations. Therefore, we rely more on the estimates of σ_t than the ones of σ_l. Notice that the intervals for σ_t in the case $\nu = 10$ – corresponding to highly noisy data – and $r = 4, 6$ are still reasonably tight meaning that the estimates are still reliable in that case.

Remark   As pointed out earlier, point and spread estimates may be computed via numerical quadrature rules. An important information to efficiently use this strategy regards a good a-priori knowledge of the support of the target distribution. This is not critical in the case $r = 2$ because the posteriors varying ν have wide supports in both σ_l and σ_t-directions. Therefore, using quadrature rules to compute point and spread estimates is the most convenient strategy in this case. However, this approach is unfeasible in the cases $r = 4$ and 6 because of the extremely tiny support along the σ_t-direction, in particular for $\nu = 1$ (see Fig. 4.9). Standard MATLAB®routines fail to compute the estimates in reasonable time. Thus, the MH algorithm is the preferred method.

4.5   Discussion

The high computational costs of standard variational data assimilation procedure analyzed in Chapter 3 motivates the investigation of accurate and efficient model reduction techniques. In the specific field of electrophysiology, consolidated model reduction techniques such as the POD may suffer from a non optimal selection of the snapshots. In this Chapter,

$r, \boldsymbol{\sigma}_{exact}$	ν	$\boldsymbol{\sigma}_{det}$	$\boldsymbol{\sigma}_{MAP}$	$\boldsymbol{\sigma}_{CM}$	$\mathrm{std}(\boldsymbol{\sigma}|U)$	$\mathrm{corr}(\sigma_l, \sigma_t)$
	1	(6.97,3.98)	(6.95,3.94)	(6.99,3.86)	(0.31,0.09)	-0.015
2,(7.00,3.50)	5	(6.98,4.00)	(7.15,3.79)	(7.45,3.68)	(0.81,0.20)	-0.011
	10	(6.97,4.00)	(7.45,3.62)	(7.58,3.59)	(0.81,0.26)	-0.013
	1	(7.82,1.99)	(7.85,1.99)	(8.14,2.00)	(0.45,0.01)	0.003
4,(8.00,2.00)	5	(8.56,1.99)	(8.10,1.99)	(7.75,2.00)	(0.75,0.06)	-0.018
	10	(7.92,1.99)	(8.15,1.99)	(7.63,1.97)	(0.80,0.12)	-0.030
	1	(8.38,1.37)	(8.41,1.39)	(8.32,1.39)	(0.41,0.007)	-0.015
6,(8.40,1.40)	5	(8.38,1.39)	(8.20,1.39)	(7.77,1.39)	(0.75,0.030)	-0.025
	10	(8.45,1.39)	(8.05,1.40)	(7.64,1.40)	(0.80,0.070)	-0.019

Table 4.9: Point and spread estimates varying noise variance ν and conductivity values. $\boldsymbol{\sigma}_{det}$ denotes the deterministic estimates reported in Table 4.7. Point estimates obtained with the Bayesian approach are $\boldsymbol{\sigma}_{MAP}$ and $\boldsymbol{\sigma}_{CM}$. We recall that σ_l and σ_t are the first and second component of the conductivity vector, respectively. There is a progressive loss of accuracy in the estimation of σ_l as the data gets noisier. σ_t is less precise for $r = 2$ because the PGD approximation features higher error in this case. Standard deviation increases with the noise, affecting our confidence in the quality of the estimation. Conductivity values and standard deviations are magnified by a factor of 100 and measured in cm^2/ms.

$r, \boldsymbol{\sigma}_{exact}$	ν	$I_l(90)$	$I_t(90)$
	1	(6.51,7.51)	(3.68,3.99)
2,(7.00,3.50)	5	(6.23,8.82)	(3.34,3.97)
	10	(6.22,8.83)	(3.14,3.95)
	1	(7.42,8.88)	(1.98,2.01)
4,(8.00,2.00)	5	(6.43,8.86)	(1.90,2.09)
	10	(6.27,8.85)	(1.82,2.21)
	1	(7.60,8.92)	(1.38,1.40)
6,(8.40,1.40)	5	(6.43,8.87)	(1.34,1.45)
	10	(6.27,8.85)	(1.28,1.52)

Table 4.10: Equal-tailed intervals $I_k(90)$, $k = l, t$ representing intervals in which 90% of the marginal densities of σ_l and σ_t falls. Estimates of σ_t are much more robust then the ones of σ_l because the credible intervals are narrower, in particular for $r = 4$ and 6. Conductivity values are magnified by a factor of 100 and measured in cm^2/ms.

for the first time we use a snapshot-free model order reduction such as the PGD, thus circumventing one of the drawbacks of the POD. All the results pinpoint that, in spite of an off-line stage that may be quite demanding in terms of CPU time, the PGD dramatically reduces the parameter identification to nearly real-time computations on common computational architectures. Moreover, the fast on-line evaluation of the PGD solution paves the way to the statistical interpretation of the MICP following Bayesian theory. In fact, the use of the reduced Monodomain model allows to rapidly explore the posterior distribution and, adopting the MH algorithm, it is possible to generate large ensembles of i.i.d. samples that can be used to quantify the reliability of the conductivity estimates. The PGD technique is a formidable tool to achieve fast sampling, otherwise unaffordable with high-fidelity models.

These preliminary results encourage further work for the extension of the methodology to the clinical practice. We list some of the possible developments: (1) The cost of the off-line phase can be dumped if it could be recycled on different geometries. This calls for the construction of a PGD library of off-line solutions on a reference geometry that could be eventually mapped to a real patient-specific morphology. While this may slow down the on-line phase, the overall benefit for a larger pool of patients and eventually the clinical applications is potentially high. (2) The extension to more complex and realistic ionic models than the RM model (and eventually the Bidomain model) needs to be pursued in view of clinical applications. However, this is a not trivial task, as the modeling of the ionic terms requires a specific development of the factorization of the increased linear functional $\mathcal{F}$. (3) As already pointed out in Chapter 3, the assumption of homogeneous tissue may be quite unrealistic. Therefore, research effort will be devoted to the formulation of the PGD technique including heterogeneity. This means that more conductivity parameters would be considered as independent variables, increasing the dimensions of the hypercube $\mathcal{S}$. Therefore, the ADS inner loop in Algorithm 1 may result in overwhelmingly heavy computations in high-dimensional cases. A reasonable trade-off may be considering the conductivity as a piecewise constant field varying over few macro-regions of the cardiac tissue. For instance, these regions might follow the segmentation of the myocardium proposed by the American Heart Association in [180], consisting of 17 portions on which conduction properties may significantly change. (4) The previous point is interesting also in view of the statistical

inversion. In fact, it would enable Uncertainty Quantification based on Bayesian theory for spatial dependent conductivity. However, more sophisticated sampling techniques need to be adopted in this case. In fact, the MH algorithm often results in high rejection rates in case of high dimensional distributions, thus the exploration of the posterior would be too slow impeding sufficient sampling with reasonable time frames.

Chapter 5

Ventricular Tachycardia Induction in Personalized Heart

This Thesis is intended to contribute to the improvement of treatments for cardiac arrhythmias using computational modeling. In this Chapter, we pursue this goal by providing a personalized electrophysiological heart model useful for planning support and guidance of catheter ablation therapy (see Chapter 1) for Ventricular Tachycardia (VT). VT is a type of arrhythmia caused by abnormal electrical activity in the lower chambers of the heart, the ventricles (see Section 2.1 for more details about the cardiac anatomy). Irregular electrical signals cause the heart to beat faster than normal, usually 100 or more beats a minute, out of sync with the upper chambers, the atria. The uncoordinated contraction of the cardiac muscle prevents the chambers from filling properly resulting in a lack of blood supply in the body. Brief or non-sustained VT may not have consequences, or, if it lasts for much longer, it may manifest with palpitations, dizziness or even loss of consciousness. On the other hand, sustained or more serious episodes of VT may lead to life-threatening conditions such as ventricular fibrillation occurring when the ventricles contract in a very rapid and uncoordinated manner. Ventricular fibrillation may cause sudden cardiac arrest and lead to death if not treated immediately.

VT is more likely to occur in patients with established heart disease such as coronary heart disease, which results from the obstruction of a coronary artery causing ischemia, i.e.,

the interruption of blood supply to the myocardium. This condition can cause irreversible tissue damage, known as myocardial infarction (MI). In patients who survive MI, the myocardium heals and dead cardiomyocytes are slowly replaced by collagen leading to the formation of a scar with a dense collagenous core surrounded by a thin layer of surviving myocardium, known as the infarct border zone (BZ). The BZ features a complex and altered electroanatomic structure [181, 182] with corridors of viable myocites scattered among the scarred tissue causing a discontinuous and anisotropic slow conduction. These channels, referred to as *conducting channels* [183], have been associated with higher arrhythmogenic risk since they promote the development of *re-entry* [184], a continuous circulating propagation in which an impulse re-enters and repetitively excites a region of the heart (see Fig. 5.1 for more details). Re-entrant circuits are well-known to be responsible of the majority of VTs encountered clinically [185–188]. Therefore, the elimination of conducting channels is critical to prevent inducibility of ventricular arrhythmias (VA). Conducting channels may be detected via contrast-enhanced cardiovascular magnetic resonance (CMR) imaging [189] and constitute the target for ablation [190].

However, the evaluation and the prediction of the outcome of ablation procedures with different target areas is quite challenging in clinical studies. Personalized computer models are a promising strategy to assess the efficacy of different ablation strategies. Recently, computational electrocardiology has been successfully used in clinical practice, for instance to predict VA risk in patients with chronic MI [12] and to study the effect of scar morphology on VA initiation [191]. Moreover, it is a valuable tool to predict VA inducibility and circuit morphology [192] and to investigate the effect of different representations of the BZ on VA [193]. This Chapter aims to reconstruct a personalized virtual heart and then studying VT inducibility with respect to different electrophysiological properties of the BZ. In particular, we investigate the stability of VT induction varying the conductivity of the BZ as well as the area originating the arrhythmia. VT induction is an important milestone in the investigation of ablation procedures *in silico*, in view of personalized therapy and proactive intervention. Moreover, this work is also meant to provide insights on electrical abnormalities promoting arrhythmias and better understand the mechanism of VT.

As usual, the personalization is done by retrieving patient-specific cardiac conductivi-

ties. However, here we consider a different formulation of the inverse conductivity problem (ICP). The reason is twofold: first, we privilege a fast and efficient estimation of an individualized heart model in a time frame comparable to the clinical ones. This can be done by following a *physics-based reduced-order modeling* approach focusing on graph-based EP models (introduced in Section 2.2.2) instead of the more expensive Monodomain or Bidomain equations. The use of simplified models forces us to modify the estimation problem. Second, transmembrane and extracellular potential data used for misfit evaluation in Chapter 3 and 4 are challenging to measure in vivo, whereas electrocardiogram (ECG) (refer to Section 2.1.3) is a practical, non-invasive and quick medical process conveying a large amount of information about the patient's conditions. Therefore, the optimization problem is reformulated so that the virtual heart reproduces relevant patient-specific ECG features.

The content of this Chapter is part of a project developed during a summer internship in 2018 at Siemens Corporation Research, Princeton, NJ, in the Image-Guided Therapy research group led by Tommaso Mansi. It will contribute to a future publication[3]. A detailed overview of the workflow generating a personalized anatomical and electrical cardiac model is given in Section 5.1, and ventricular tachycardia simulation is the topic of Section 5.2. We will conclude in Section 5.3 with a final discussion.

The software used during the project was already implemented by researchers in the group and object of several publications [21, 24, 25, 54, 194] (to mention a few). The contribution of the internship was bug fixing and optimizing software design (mainly of the code regarding Section 5.1.2) in the first place, then the work focused on performing the simulations presented in Section 5.2.

5.1 Patient-Specific Computational Model of the Heart

In this Section, we provide an overview of the pipeline (Fig. 5.2) generating the personalized heart model, from the clinical data to multi-scale, multi-physics prototype. Cardiac anatomy (Section 5.1.1) and electrophysiology (Section 5.1.2) are modeled based on imaging and 12-lead ECG data. We recall from Section 2.1.3 that ECG allows monitoring the

---

[3]The project concerned CRT (see Chapter 1) simulations as well, but unfortunately this part cannot be disclosed for intellectual property constraints yet.
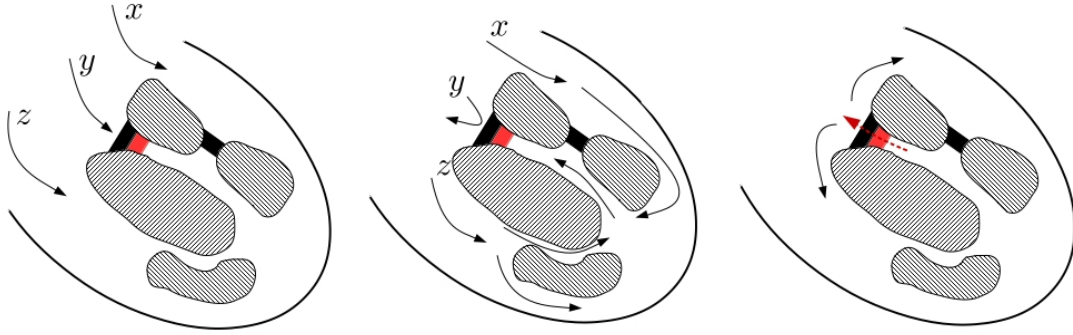
Figure 5.1: Example of scar-related re-entry. Left panel: Activation wavefronts approach the scarred area. Viable myocites form channels between areas of scar tissue, denoted by the gray islands. One single black block represents bidirectional blocks entirely stopping electrical conduction, and black and red blocks denote damaged but viable myocites where conduction is allowed only in one direction. Central panel: Wavefront x propagates inside the channel, wavefront y is blocked and reflected backwards, and wavefront z bifurcates because of the presence of the scar island with one wave propagating through the channel and merging with the wavefront x. Right panel: the wavefront propagating through the channel passes through the unidirectional block and re-excites the tissue triggering a re-entrant circuit.

electrical activity of the heart, with each lead representing the potential difference between different electrode groups. In particular, we focus on the lead I, computing the difference between left and right arms, and lead II, calculating the difference between left leg and right arm.

5.1.1 Cardiac anatomical model

A detailed model of the bi-ventricular myocardium is generated using the framework proposed in [21,53,54]. Heart morphology is automatically segmented using a machine-learning approach from cine Magnetic Resonance Images (MRI) (first panel in Fig. 5.2). In brief, the Marginal Space Learning framework and Probabilistic Boosting Trees [53] find the heart position, rotation and scale in the image following an algorithm trained from a large database of cine MRI. Myocardium contours are recognized through a boundary detector procedure learned from the database as well. Then, the algorithm fits a mean heart shape model whose contours are finally deformed according to the boundary detectors to match the myocardium boundaries. Once the model is detected, it is tracked over time using a symmetric image registration algorithm [195]. The whole process is supervised by an ex-
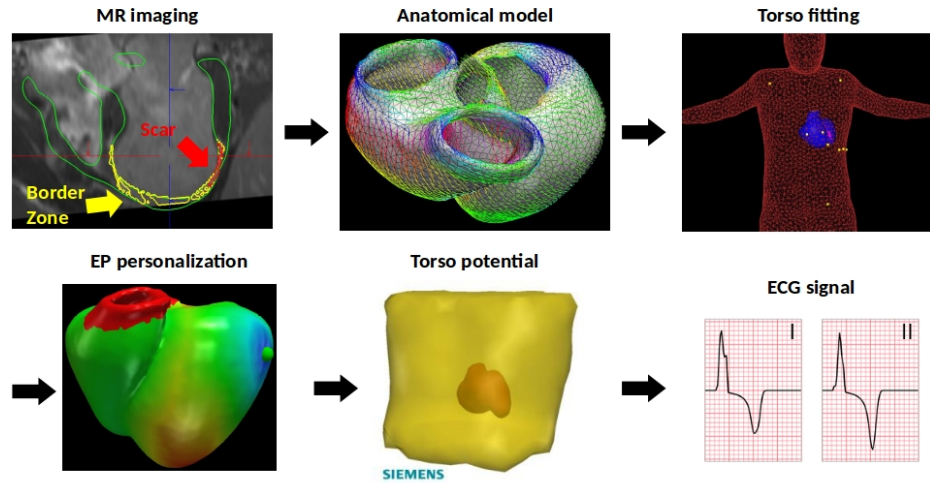
Figure 5.2: General workflow of the personalization procedure leading to patient-specific representation of the electrophysiological state of the heart. EP personalization step is explained in more details in Fig. 5.6. Data courtesy of Dr. Halperin, JHU.

pert that can intervene interactively if needed. Next, to form a closed surface mesh of the bi-ventricular myocardium, the segmented triangulations of the epicardium and endocardia are fused together. The final anatomical model includes five domains: (1) the left and (2) right ventricular septum, mimicking the His bundle (introduced in Section 2.1.3) and serves as initialization zone of the excitation wave; (3) the left and (4) right endocardia, with layers simulating the Purkinje system of fast electrical conductivity; the (5) myocardium featuring slower conductivity.

A model of myocardium fiber architecture is obtained following a rule-based strategy [196, 197]. In this study, left ventricle (LV) elevation angles vary linearly across the myocardium from -70° on the epicardium to 70° on the endocardium, whereas right ventricle (RV) elevation angles vary from -80° to 80°. Finally, a volumetric mesh defining the computational domain for solving the electrophysiology equations is generated (second panel in Fig. 5.2).

Then, a patient-specific torso model (third panel in Fig. 5.2) is obtained as follows [23]. First, the contours of the torso are outlined using cMRI images acquired in axial, sagittal and coronal views, and visualized together with the heart model. Second, a manual affine

registration of an atlas of torso geometry to the contours is performed. ECG leads are finally placed at their clinical locations on the personalized torso model. For the sake of simplicity, electrode positions are chosen to coincide with manually selected torso mesh vertex positions.

5.1.2   Electrophysiology personalization

Here, we first describe the computational tools used in this work for simulating electrophysiology (EP). Then, the personalization procedure is outlined.

Graph-based EP model   A graph-based EP model (a general description can be found in Section 2.2.2), termed GraphEP, is used to describe the *local activation times* (LATs) at each point of the patient-specific volumetric mesh. We recall that the LAT in the point $\mathbf{x}$ denotes the time at which the wavefront (also called depolarization wave) passes through the point $\mathbf{x}$. GraphEP works as follows [21,194]: the cardiac tissue is represented as a connected graph consisting of spatial nodes connected by edges (see Fig. 5.3(a)). A generalized weight w_{ij} is associated to the edge connecting to mesh points $\mathbf{p}_i$ and $\mathbf{p}_j$ and corresponds to the time needed to the action potential (AP) to travel from $\mathbf{p}_i$ to $\mathbf{p}_j$. w_{ij} takes into account the different tissue types where the points are located, the local anisotropy and the fiber orientation. The generalized weight is calculated as $w_{ij} = l_{ij}/c_{ij}$, where l_{ij} ([mm]) incorporates local anisotropy information depending on the fiber structure. It is computed as $l_{ij} = \sqrt{(\mathbf{e}_{ij}^T D \mathbf{e}_{ij})}$, $\mathbf{e}_{ij} = \mathbf{p}_i - \mathbf{p}_j$, D is the anisotropy tensor defined as $D = (1-r)\mathbf{f}_{ij}\mathbf{f}_{ij}^T + rI$, $\mathbf{f}_{ij}$ is the fiber direction along the edge and r the anisotropy ratio ($r = 0.3$). c_{ij} is the CV in mm/s along the edge approximated linearly from the CVs c_i and c_j. However, in this work, the CV is not defined point-wise, but we assume it only varies in three of the five anatomical regions described in the Section 5.1.1: two thin, 3mm-thick sub-endocardial layers located in the LV and RV (regions (3) and (4)), imitating fast conduction of the Purkinje system, denoted by c_{LV} and c_{RV} respectively, and the rest of the myocardium (region (5)) with a slower CV denoted by c_{myo} [23]. As previously mentioned, the activation of electrical signal occurs in the LV and RV septum, meaning that we set the LATs equal zero on these mesh regions. Using this approach, a full EP activation map described by the LATs at
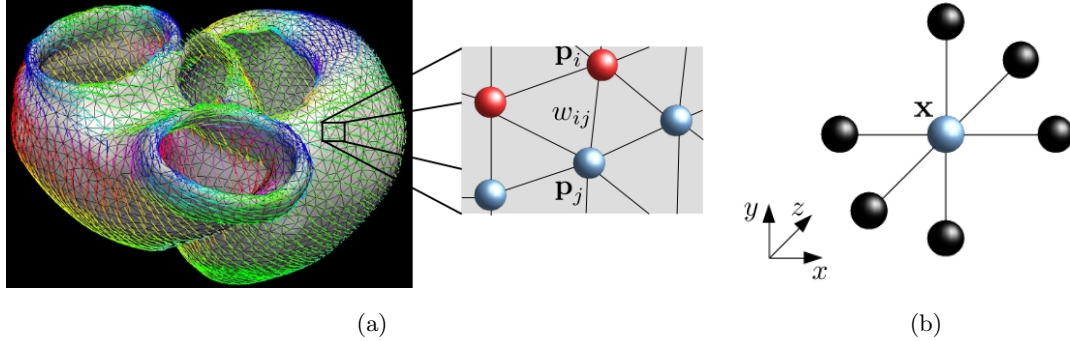
Figure 5.3: (a) In GraphEP model, the mesh is represented as a connected graph consisting in spatial nodes connected by edges. In the zoom, red nodes denotes points already activated, and blue nodes are still in resting state, thus the excitation wave propagates from red to blue points. For instance, the electrical wave travels from $\mathbf{p}_i$ to $\mathbf{p}_j$ through the edge with weight w_{ij}, which takes into account the local anisotropy, fiber orientation (represented by the colored field overlapped to the cardiac mesh) and conduction velocity. (b) 7-connectivity topology of the cubic grid used in LBM-EP. The blue node $\mathbf{x}$ is the central one and it is connected to 6 neighbors.

each point of the mesh is calculated using a Dijkstra shortest-path algorithm adapted to the EP case [54, 102]. Since GraphEP only describes local activation times instead of time dependent electrical propagation, computing the solution is very fast, thus it is well suited for real-time EP simulations.

Monodomain model solved with Lattice-Boltzmann method As mentioned in Section 2.2.2, GraphEP is not an appropriate choice to model cardiac arrhythmias because it disregards the state of repolarization of the AP and the refractoriness of cardiac cells which play a central role in arrhythmogenesis. While it has become possible to simulate wave re-entry phenomena with graph-based/Eikonal models [52], capturing other complex pathological conditions such as arrhythmias is more challenging. Here, the Monodomain model (2.25) coupled with Mitchell and Schaeffer (MS) model (2.8) is used to simulate electrical disorders such as VT. The MS model is popular in clinical applications because it captures pathological situations, such as arrhythmias and wave re-entry [11, 198], with low computational cost. Moreover, contrary to more complex ionic models, MS features parameters (see Section 2.1.2) with physiological meaning: τ_{close} regulates the duration of AP and ($\tau_{open}, \tau_{in}, \tau_{out}$) control the diastolic interval and the restitution curve. These parameters are kept to their standard values [68] in the whole computational domain, expect τ_{close} in

the BZ, since its altered electrical property is usually reflected in longer AP duration.

As we have seen throughout this Thesis, especially in Chapter 3, the numerical approximation of models in electrocardiology can be computationally too demanding and standard approaches such as finite element method are not suitable for real-time clinical setups and intervention guidance. Another limitation is the requirement of high-quality/high-resolution volume meshes, which can be difficult to obtain from patient-specific anatomies. In recent years, the Lattice-Boltzmann Method (LBM) [199, 200] has developed as a powerful technique for accurate simulation of a large class of partial-differential equations. In particular, it has been successfully applied to pattern-forming reaction-diffusion equations [201]. Some of the key strengths of this method are, i) local nature of the computational algorithm, which provides very high scalability on modern parallel computing architectures, ii) second-order accuracy in space, and iii) simplicity of implementation on a uniform Cartesian grid. Motivated by the recent breakthrough in LBM, a novel framework called LBM-EP has been developed for efficiently solving the Monodomain model at near real-time (≈ 3 s per heartbeat) and it is especially tailored for patient-specific simulations [198]. In short, the myocardium is mapped onto a Cartesian cubic grid with isotropic spacing and represented as a level-set. The grid has a 7-connectivity topology (6 connections and a central position, see Fig. 5.3(b)) . The fundamental variable of LBM-EP is the vector of distribution functions $\mathbf{f}(\mathbf{x}) = \{f_i(\mathbf{x})\}_{i=1,\dots,7}$, where $f_i(\mathbf{x})$ represents the probability of finding a particle traveling along the edge $\mathbf{e}_i$ of node $\mathbf{x}$. The computation of $\mathbf{f}(\mathbf{x})$ is composed of two consecutive steps: the *collision* phase, computing intermediate post-collision states f_i^*, and the *streaming* phase, propagating the distribution functions along their corresponding edges:

$$
\begin{aligned}
f_i^* &= f_i - A_{ij}(f_j - \omega_j u) + \delta t \omega_i (I_{ion}(u,v) + I_{app}), \\
f_i(\mathbf{x} + \mathbf{e}_i, t + \delta t) &= f_i^*(\mathbf{x}, t).
\end{aligned}
\tag{5.1}
$$

The collision matrix $A = (A_{ij})$, $i, j = 1, \dots, 7$ relaxes the distribution function f_i toward the local value of the potential u and takes into account the anisotropic fiber-related diffusion, represented by the conductivity values estimated through the personalization step. The weighting factors ω_i are utilized to emphasize the center position. v, the gating variable

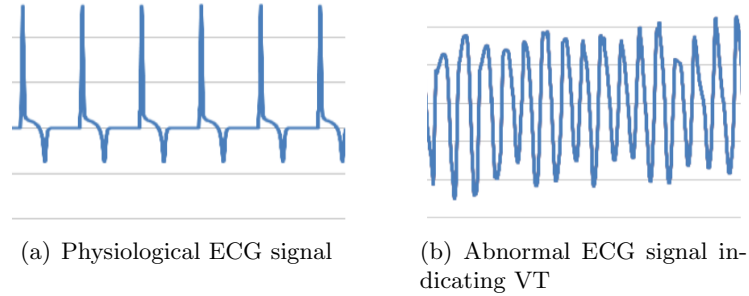(a) Physiological ECG signal   (b) Abnormal ECG signal in-
dicating VT

Figure 5.4: By looking at the ECG signal, electrical malfunction of the heart can be promptly detected.

of MS model (2.8), is updated at every node of the grid using a forward Euler scheme. Eventually, the transmembrane potential $u(\mathbf{x}, t)$ is defined as the sum of the distribution functions $u(\mathbf{x}, t) = \sum_i f_i(\mathbf{x}, t)$. We refer to [198] for further details.

Computation of torso potentials and ECG signals Once heart potentials are computed, they can be propagated through the body so to approximate the potential distribution on the torso and in turn produce a body surface ECG. The rationale is that the ECG signal has a central role in clinical practice to diagnose rhythm disorders, so it is an effective tool to check whether or not a VT has been induced on the cardiac muscle. Furthermore, it is a non-invasive and painless test with quick results. A comparison between normal ECG and ECG detecting VT is carried out in Fig. 5.4. To compute torso potentials, current approaches use both Finite Element (FEM) and Boundary Element (BEM) methods. While the former intrinsically takes into account anisotropy in the thoracic cavity [202–204], the latter assumes constant isotropic conductivity throughout the entire torso [7,205,206]. Since many of the different tissue types that together form the passive torso volume conductor are commonly modeled as isotropic, BEM is the preferred solution method. Moreover, it has been shown that decoupling the computation of cardiac electrophysiology and body surface potentials does not significantly modify ECG data [207].

Torso potential is modeled through a three-step procedure. First, it is necessary to estimate cardiac extracellular potentials u_e at the epicardium from u. To this end, the elliptic formulation [208] is used assuming a constant diffusion anisotropy ratio λ. Following

this approach, the extracellular potential u_e is expressed as

$$u_e(\mathbf{x}, t) = \frac{\lambda}{1 + \lambda} \frac{1}{|\Omega|} \int_\Omega (u(\mathbf{y}, t) - u(\mathbf{x}, t)) \, d\mathbf{y} \qquad (5.2)$$

where Ω denotes the entire myocardium domain. Second, tri-linear interpolation is used to map u_e from the Cartesian grid used for LBM-EP method back to the epicardial surface mesh. Finally, the extracellullar potential is projected from the epicardium to the torso via the BEM method. This method allows to compute a transfer matrix depending on the geometry and mapping the heart potentials to torso potentials. The computation is very fast since it only involves one matrix-vector multiplication. We refer to [23, 206] for a more comprehensive analysis of the procedure. Once the torso potentials are computed, 12-lead ECG signals are obtained by computing the potential difference between lead nodes.

EP personalization Using the computational tools introduced in the previous paragraphs, here we thoroughly describe the EP personalization step (fourth panel in Fig. 5.2). As anticipated in the introduction of the Chapter, estimation is performed by using cheaper computational models, such as GraphEP. The rationale is that the reduction of computational complexity enables a prompt estimation of a virtual patient-specific heart. The personalized EP model reproduces some significant ECG properties: in particular, we focus on two significant ECG features, the duration of the QRS complex (QRSd) and the electrical axis (EA) of the heart (see Fig. 5.5). QRSd represents the total time the electrical depolarization wave requires to propagate throughout the entire myocardium. If the QRSd is longer than 120 ms, it suggests disruption of the heart's conduction system that might trigger arrhythmia such as VT. On the other hand, EA is an angle measured in degrees reflecting the average direction of depolarization wavefront in the coronal plane (Fig. 5.5(b) shows the coordinate system). It is suited to detect imbalances between left and right ventricular wave conduction. Normal EA is from $-30°$ to $90°$, whereas abnormal values suggest a change in the physical shape and orientation of the heart or a defect in its conduction system that causes the ventricles to depolarize in an abnormal way. Both parameters can be easily measured from patients' ECG waves.

We refer to Fig. 5.6 for a visualization of the procedure. After initialization, the parameters are estimated via an alternated scheme. First, in step 1 of Fig. 5.6, myocardium CV c_{myo} is estimated by minimizing the mismatch between simulated and measured QRSd in the ECG signal in the lead I. Assuming one full heart cycle, the QRSd can be approximated directly from LATs as QRSd=$\max_{\mathbf{x}}$ LATs$(\mathbf{x}) - \min_{\mathbf{x}}$ LATs$(\mathbf{x})$. LV and RV sub-endocardial CVs, c_{LV} and c_{RV}, are fixed at this point. Next, in step 2 of Fig. 5.6, c_{LV} and c_{RV} are estimated to match the measured electrical axis angle EA. We use the estimate of c_{myo} computed at the previous step. Since EA can only be computed from ECG traces, we calculate ECG signals from LATs as follows. Given LATs and a user-defined AP duration (APD), controlled by τ_{close} of MS model, one can infer when a cell starts to depolarize (LAT) and how long it stays in this condition (APD). From this information, heart potentials can be reconstructed. Then, they are projected to the torso using BEM so to calculate torso potentials and in turn ECG signals. At this point, according to [23], EA is calculated from the ECG waves in the Einthoven leads I and II: EA=$\arctan[(2h_{II} - h_I)/(\sqrt{3}h_I)]$, where the h_i's are the sum of the R and S peak amplitudes (minimum and maximum) in the respective leads during the QRS complex (see Fig. 5.5(a)). The estimation is performed by a gradient-free optimization method, the NEWUOA algorithm [209]. These iterations end when a convergence test (step 3 in Fig. 5.6) is fulfilled. In details, the test checks whether the absolute values of the difference between consecutive updates of the CVs are below a certain threshold, i.e., $|c_i^{k+1} - c_i^k| <$ tol, where i refers to any of the three regions LV, RV and myocardium. If convergence is not reached, the iterations restart from step 1, otherwise the final estimates $\{c_{LV}, c_{RV}, c_{myo}\}$ are obtained.

Then, a transition from GraphEP to Monodomain model is needed to study VT. This is achieved by mapping the estimated CVs to conductivity values (step 4 in Fig. 5.6). The conversion is made through the empirical formula $\sigma_i = \alpha c_i^2$, where the factor α is manually tuned for each patient to still match the QRSd, c_i denotes the CVs in any of the three regions LV, RV and myocardium and σ_i the corresponding conductivity. Once the conductivities $\{\sigma_{LV}, \sigma_{RV}, \sigma_{myo}\}$ are obtained, VT induction studies can be performed. LBM-EP is used to efficiently simulate electrical propagation in the heart. Finally, torso potentials are computed via BEM method (fifth panel in Fig. 5.2) allowing the approximation of ECG
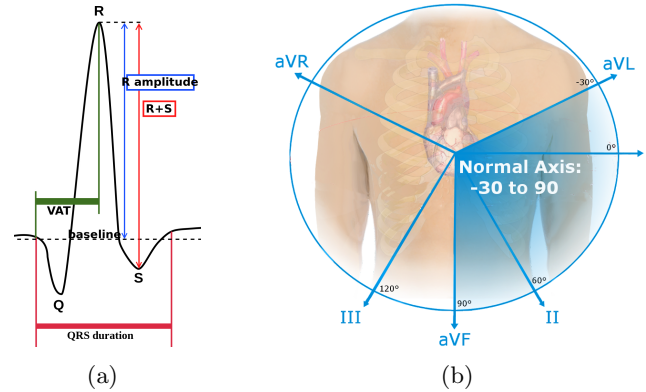
Figure 5.5: (a) As described in Section 2.1.3, QRS complex duration (QRSd) is the length of the QRS complex reflecting the depolarization of the ventricles. The sum of R and S peak amplitudes, R+S, is used to approximate the electrical axis of the heart. Image from Wikimedia Commons, source: Compendium for interpretation of ECG at Uppsala Institution for Clinical Physiology. Year 2010. (b) Electrical axis (EA) of the heart represents the direction of the excitation wave during ventricular contraction. Normal EA is between -30° and 90°, whereas abnormal values are a symptom of electrical malfunction. Image from Wikimedia Commons, Author: Npatchett.

signals (sixth panel in Fig. 5.2).

5.2 VT Induction

In view of clinical applications, we now focus on the simulation of ventricular tachycardia (VT) in personalized computational heart model. The induction of VT is essential to test different virtual ablation procedures, with a great predictive power to assess the effectiveness of the therapy beforehand and to support the decision making process. In particular, VT triggered by scar-related re-entry are investigated. As mentioned in the introduction of the Chapter, arrhythmogenic risk is higher in the border zone (BZ) of the scar because of the presence of slow conducting channels that may facilitate the creation of re-entrant circuits (Fig. 5.1). In this Section, virtual experiments are performed to analyze the sustainability of VT induction with respect to variations of CV in the BZ. The conductive properties of the BZ play a key role in arrhythmogenesis. In fact, re-entry waves generating VT may die out after a short period of time if conduction in the BZ is not slow enough. The numerical setup of the simulations is discussed in Section 5.2.1, and the results are showed in Section 5.2.2.
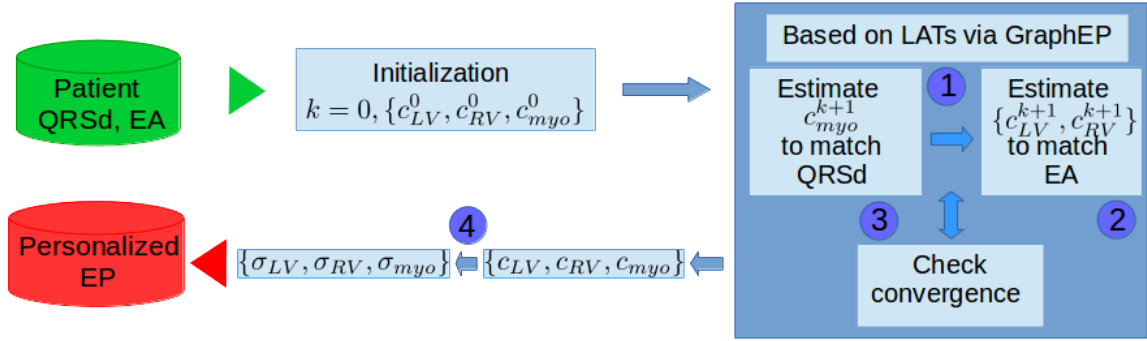
Figure 5.6: Detailed workflow of the personalization EP procedure. CVs in the LV, RV and myocardium are estimated so to match patient-specific ECG data, in particular QRSd and EA. Then, following an empirical formula, conductivity values for Monodomain simulations are computed. More details in the EP personalization paragraph.

5.2.1 Numerical setup

For this work, we refer to an experimental study in which in vivo experiments were conducted to induce VT in a pig heart and then different ablation therapies were tested to stop the arrhythmia. Portions of the myocardium were scarred using radio-frequency ablation before collecting the data so to facilitate electrical disorders. ECG signals were recorded at natural pacing before inducing VT: the measured QRSd was 78 ms (in the lead I) and EA was $0°$.

Before performing virtual VT experiments, the personalization step was performed. As described in Section 5.1.2, we focus on estimating the parameters $(c_{LV}, c_{RV}, c_{myo})$, with c_{LV} and c_{RV} denoting the conduction velocity (CV) in the fast Purkinje system in the LV and RV, and c_{myo} representing the slower propagation in the myocardium. This stage was carried out as follows:

- The pig heart morphology was segmented using high resolution MRI images such as the one in Fig. 5.7(a). The virtual heart consists of LV and RV endocardium, epicardium and septum as well as scar and BZ (Fig. 5.7(b)). This task is performed once.

- We assume no conduction in the scar region and reduced CV c_{BZ} in the BZ.

- For each value of c_{BZ} we want to investigate, we perform the EP personalization step to compute $(c_{LV}, c_{RV}, c_{myo})$ keeping c_{BZ} fixed. Of course, these estimates vary with

c_{BZ}.

- The parameter τ_{close} of MS model controlling AP duration is manually increased in the BZ to reflect electrical anomalies.

Once personalization is achieved, VT studies are performed. In order to induce VT, besides natural pacing coming from the sinoatrial node (as explained in Section 2.1.3), additional stimulation is applied nearby the BZ. The rationale is that, as explained in the Introduction of the Chapter, the BZ features slow conducting channels or particular shapes that may promote re-entrant circuits. Locating the artificial pacing in this area of the myocardium may trigger re-entry and thus VT. This stimulation has faster frequency than the natural heart beats since this facilitates electrical disruption. The pacing protocol is chosen so to match intra-operatory data. In particular, starting from t=0.5 s, the tissue is paced six times every 0.45 s, then the pacing period decreases in 0.05 s steps until reaching 0.2 s. One stimulus is applied at each decreasing step for a total of 11 stimuli. A visualization of the pacing protocol is displayed in Fig. 5.7(c). The pacing site depends on the morphology of the BZ.

5.2.2 Detecting VT with ECG signals

In this Section, preliminary results about VT simulations on the virtual heart are showed. The CVs $c_{BZ} = (0, 10, 50)$ mm/s in the BZ are analyzed. For each value of c_{BZ}, we personalize the heart model by estimating $(c_{LV}, c_{RV}, c_{myo})$ from ECG features: in all the cases tested, we obtained 200 mm/s $< c_{myo} <$ 400 mm/s and 2000 mm/s $< c_{LV}, c_{RV} <$ 4000 mm/s. On a standard desktop machine, the EP personalization step takes around one minute. Then, the estimated CVs are converted in conductivity values following the empirical procedure described in Section 5.1.2, allowing the use of LBM-EP to compute electrical propagation. The excitation wave is simulated for 40 s and its computation requires around 120 s. The natural heart rate is 80 beats per minute (BPM), which is physiological since normal heart rates are between 60 and 100 BPM. Besides natural pacing, stimuli for inducing VT are applied following the procedure described in Section 5.2.1. The pacing site is visualized in Fig. 5.9 by the yellow dot. We notice that the stimulation point
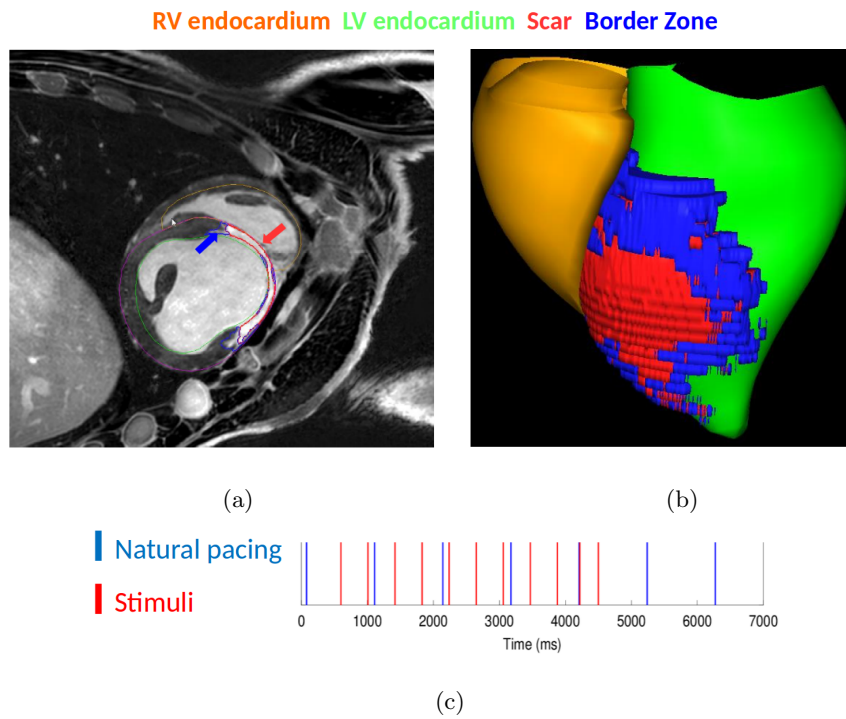
Figure 5.7: (a) Examples of high resolution MRI image used to segment the anatomical model. Scar and BZ portions are visible and highlighted in red and blue colors, respectively (b) Visualization of LV and RV endocardium, scar and BZ. (c) Pacing protocol for VT induction. Besides natural pacing from the sinoatrial node, stimuli are applied close to the BZ over a certain period of time so to trigger VT.

is situated in a particular area of the myocardium in which healthy tissue is surrounded by the BZ with low conductivity. As previously mentioned, electrical anomalies are usually recognized by examining ECG signals. Thus, after simulating excitation with LBM-EP, we compute ECG signals to monitor the electrical behavior of the heart.

Fig. 5.8(a) reports the simulated ECG signal in lead I varying c_{BZ} for BPM=80. The results show that sustained VT is induced only for $c_{BZ} = 10$ mm/s as the ECG wave does not show the normal physiological features meaning that electrical malfunction is occurring. In the other cases, disruption of the electrical conduction is visible at the beginning, but then the natural pacing of the heart is restored after few beats generating a standard ECG signal. Failing of VT induction for $c_{BZ} = 0$ mm/s may be a bit counterintuitive at first. However, this result is reasonable because, with no conduction, the BZ would behave like a simple scar, thus perturbation of the excitation caused by slow conduction in the BZ which promotes arrhythmias [184] would not occur. On the other hand, $c_{BZ} = 50$ mm/s generates a case of non-sustained VT, in which the malfunction is evident for a short period of time, but then proper electrical functioning is automatically restored. This means that the BZ does not interfere with the physiological propagation enough to cause persistent VT. Furthermore, we analyze the impact of the frequency of the natural stimulation on VT induction. Fig. 5.8(b) shows the results with faster natural pacing BPM=90. The ECG traces are similar to the ones obtained for BPM=80, thus it seems that the onset of VT does not depend on this parameter. Actually, for $c_{BZ} = 50$ mm/s, the disturbance disappears immediately after the stimulation in the BZ terminates, meaning that the higher heart rate helps ceasing any electrical disturbance.

Another aspect influencing VT induction is the position of the pacing stimulus. In the following experiment, we test a different stimulation point, visualized by the red dot in Fig. 5.9. The area was chosen because of its particular shape and the presence of little islands of BZ in healthy tissue which may perturb the normal electrical activity. Fig. 5.9 shows a comparison of the ECG waves obtained varying the pacing site (yellow and red dots) keeping $c_{BZ} = 10$ mm/s and BPM=80. The results confirm the fact that the initiation of VT strongly depends on the pacing location and in turn on the morphology of the BZ. In fact, we note that, while VT is induced in the case of pacing in the yellow point, stimulation
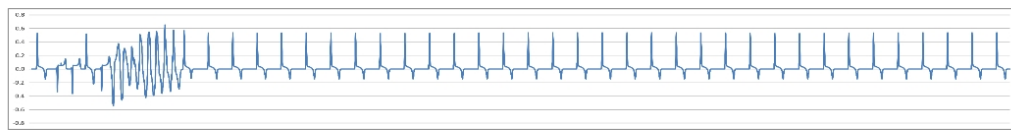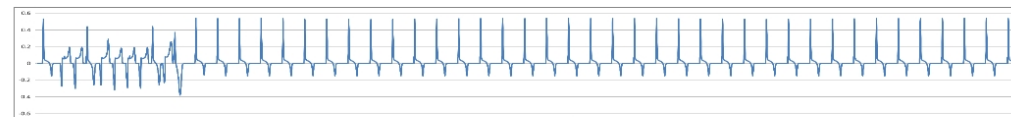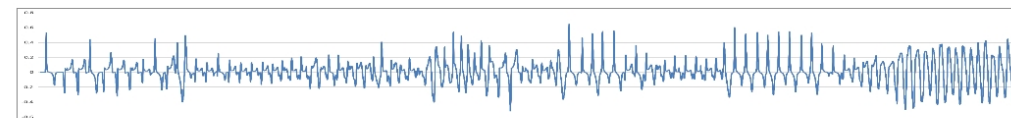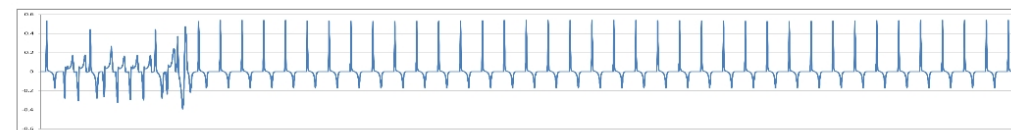
$c_{BZ} = 0$
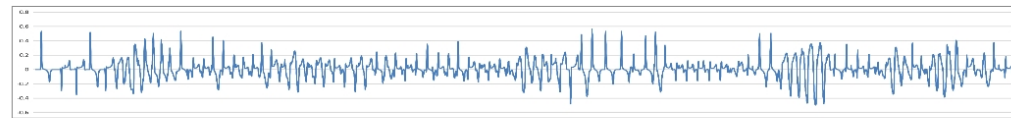
$c_{BZ} = 10$
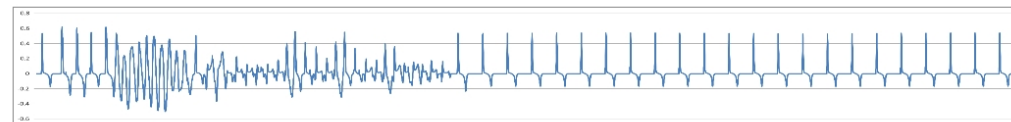
$c_{BZ} = 50$

(a) BPM $= 80$

$c_{BZ} = 0$

$c_{BZ} = 10$

$c_{BZ} = 50$

(b) BPM $= 90$

Figure 5.8: Computed ECG signals in lead I varying BZ conduction velocity c_{BZ} ([mm/s]) and pacing in the yellow dot displayed in Fig.5.9. BPM stands for beats per minute. The x-axis of the ECG signal is time, whereas the y-axis is the voltage measured in mV. VT is induced only in the case $c_{BZ} = 10$ mm/s regardless of the value of BPM. Arrhythmia does not initiate in the other cases: for $c_{BZ} = 0$ mm/s, BZ behaves like a normal scar so there is no slow conduction promoting electrical malfunction; on the other hand, for $c_{BZ} = 50$ mm/s, the BZ does not interfere enough to trigger VT.
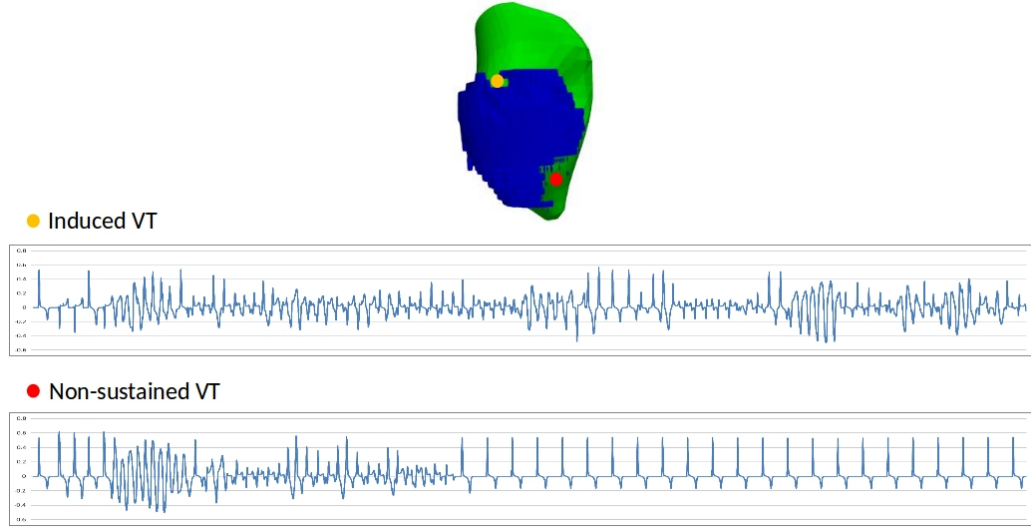

Figure 5.9: Results for different pacing location. The BZ is the blue region in the LV endocardium, visualized in green. The scar (red area in Fig. 5.7) is not present here. BPM=80 and $c_{BZ} = 10$ mm/s. We note that changing the pacing point influence the onset of VT as stimulating in the red point only provoke a non-sustained VT. This confirms that arrhythmogenesis depends on the anatomical properties of the scarred area, in particular on the morphology of the BZ.

in the red dot only triggers a non-sustained VT as the electrical disruption is visible in the ECG only in the first heartbeats, but then it vanishes in favor of normal pacing.

5.3   Discussion

This Chapter presents a preliminary study aiming to investigate the dynamics of VT and paves the way for virtual ablation procedures useful for support and therapy planning. A robust framework [21, 53, 54] is used to estimate a personalized model of heart function covering cardiac and torso anatomy and electrophysiology from cMRI images and 12-lead ECG data. We resort to GraphEP and LBM-EP methods which are especially tailored for efficient parameter estimation and simulations at near real-time. The virtual heart is used to study the influence of different conduction properties of the BZ as well as the dependence of the pacing site on the onset of VT. Results highlight that the CV in the BZ, which plays a key role in arrhythmogenesis, is required to be much slower (around 10 mm/s) than the myocardium and the Purkinje system (one and two orders of magnitude larger, respectively) so to originate sustained VT. Furthermore, the BZ morphology also has an impact on the

generation of arrhythmias.

Several assumptions were made in the model used in this study, which can be a limitation. First, the CV only changes in five regions of the domain. Including heterogeneity of the tissue might allow more accurate ECG computation since the heart muscle may present areas which are not scars but may feature different conduction properties. Work in this direction has been done in [194], in which estimation of point-wise CV was performed from local activation mappings of the myocardium. Then, the torso potentials and so the ECG signals were computed under the assumption of homogeneous tissue between the heart and the body surface, with one electrical conductivity [23]. While this simplification can have an impact on the shape of the ECG trace, numerical studies have shown that global parameters such as QRSd are minimally dependent on tissue heterogeneity and therefore justify our approach [207].

More work needs to be done in this frame, in particular the evaluation of more cases varying CVs in the BZ and stimulation sites as well as the study of the sensitivity with respect to the pacing protocol. Then, virtual ablation procedures need to be tested and validated against the postoperative ablation data retrieved from the pig experiment. Despite the contour-based registration, torso geometry was based on an atlas and does not entirely reflect patient-specific anatomy. Future work could thus improve the anatomical model by incorporating more imaging data from the heart to the body surface. In addition, the framework could be extended by using an electromechanical model of the heart [197] to cope with the influence of cardiac motion on the ECG. Finally, more complex biophysical Bidomain models and integration of atrial geometry could potentially increase the predictive power of the framework and are subject to future work. Reduced-order modeling could also be investigated to cope with the increase of computational complexity related to Bidomain simulations.

Chapter 6

Conclusion and Outlook

Advances in mathematical electrocardiology have made possible the use of numerical simulations in medical research and clinical practice. Computational modeling can potentially play a pivotal role in therapy planning, intervention guidance and device optimization. However, to make simulations clinically useful, an accurate and efficient parameter estimation is critical to customize models to patient-specific settings. We address this challenge focusing on data assimilation and reduced-order modeling techniques for the quantification of cardiac conductivities from medical data. The original contributions of this Thesis are the following:

1. In Chapter 3, we verify the accuracy and robustness of the variational data assimilation approach proposed in [26] using the Bidomain model with respect to noise and amount of information considering several in silico realistic settings in view of real validation.

2. After checking the effectiveness of the variational estimation of Monodomain conductivity as a surrogate of the Bidomain one, we extensively validate the methodology with optical mapping recordings of potential for the first time in this field. We show that we can successfully reproduce most of observed electrical dynamics providing reasonable estimates of conductivity fields that are consistent with the data.

3. In Chapter 4, we test the PGD technique [43] applied to the Monodomain model as a way to improve efficiency of forward and inverse simulations. After a careful calibration of the offline phase, we reduce the computational costs of the forward solve by two order of magnitudes. We then exploit the fast evaluation of the PGD solution to solve the Inverse

Conductivity Problem with very low computational effort.

4. We introduce for the first time the formulation of the inversion in a Bayesian framework [50] in view of quantifying the uncertainty of the estimates. This serves as the first application of such a technique to more accurate models such as the Monodomain one. We use the PGD approach for affordable sampling from the posterior distribution and efficiently obtain point and spread two-dimensional estimates in synthetic tests.

5. In Chapter 5, we reconstruct a personalized virtual heart model from medical images [21, 24] and ECG data to reproduce patient-specific electrophysiology. We focus on a simplified model to achieve this task in near real-time. Our contribution is the analysis of the induction of ventricular tachycardia with respect to different conduction properties in view of optimizing ablation therapy in silico.

Several directions for future work are worth exploring. The variational data assimilation procedure may be extended to include the estimation of other quantities beyond conductivities. The ionic-model parameters, dependent on the local natural heterogeneities of the cardiac tissue, as well as the fiber orientation, that in this Thesis we tuned empirically, may be estimated within a unified variational framework [111], even if this is currently too demanding from the computational point of view for a real application requiring the adoption of more involved physiological models. Moreover, we intend to include the modeling of electrical properties of the border zone (BZ) around a scar. Our methodology, combined with the analysis done in Chapter 5, might be helpful to further investigate and better understand the potential role of BZ in arrhythmogenesis [193, 210]. Moreover, the tuning of the parameters and the initial guess for the optimization algorithm is, at this stage, mostly empirical, even if we presented some approaches that improve the performances by a smart preprocessing of the arbitrary initial guess of the conductivities. Strategies for an automatic tuning of these parameters are an interesting practical follow-up.

Another important direction that would be worth investigating is to extend the proposed methodology to synchronous endocardial and epicardial recordings, e.g. the one provided in [119], such to estimate the intramural conductivity and ionic parameters, eventually, that is, at present, not measurable from state-of-the-art experimental techniques. Similarly, estimation and assimilation of conductivity along repetitive fast pacing stimulations are fore-

seen of great potential for complex spatio-temporal alternans predictions based on statistical correlation measures [211]. On the same direction, the methodology can be applied to the cellular scale by using fluorescence optical data of calcium imaging [212, 213] focusing on estimating QT syndrome related parameters [214]. In a multiphysics generalization of the present approach, it is also interesting to estimate temperature-dependent parameters, such as gating time constants [151, 215], or dispersive modeling approaches [154, 157, 216, 217] in which additional diffusivity parameters necessitate a rigorous experimental-based estimation. We also intend to combine the parameter estimation with the Hybridomain model, i.e., the adaptive modeling tool introduced in [94, 95] where the Bidomain model is turned on only when needed based on the indications of an *a posteriori* model estimator. The Hybrid Inverse Conductivity Problem (HICP) may provide a different, appropriate trade-off between reliability of the estimates and computational efficiency.

Another important follow-up of this Thesis is to apply the PGD technique to the case of spatial dependent conductivities and to other ionic models such as Fenton-Karma and Mitchell-Schaeffer. This would enable the application of the strategy to the inversion in experimental settings analogous to the ones discussed in Chapter 3. A comparison in terms of accuracy and the efficiency of the estimation would be interesting to carry out. Furthermore, we note that the offline phase can be quite expensive for low tolerance in the enrichment step. The computational complexity related to these cases may be reduced via parallelization of the code. We suggest the implementation in a shared memory system as opposed to a distributed one so to avoid queue wait times. This would allow the use of more accurate PGD solutions at limited costs. The application of PGD to the spatial dependent case would be beneficial to the Bayesian inversion enabling the quantification of the uncertainty in more realistic cases as well. This would require the investigation of more sophisticated MCMC methods as well as a careful prior modeling to guarantee reliability and computational efficiency. Finally, the LBM-EP method [198] used in Chapter 5 may be applied to the Monodomain Inverse Conductivity Problem (MICP) as an alternative to the finite element approximation to perform extremely fast estimation, also considering larger time frames which include multiple heart beats. However, the implementation would require special attention as a proper map to Cartesian grid is required as well as a level-set

representation of realistic geometries.

In conclusion, accurate and efficient customization of mathematical models of heart electrical disorders addressed in this work will be the key for their implementation into clinical practice. Quantitative adaption of such models to patient-specific data is required in order to test their realism and predictive power of therapy outcomes. In the long run, the use of personalized simulations in electrocardiology may greatly improve anti-arrhythmia treatments, such as CRT and catheter ablation. From preoperative data, several possible scenarios may be predicted and throughly analyzed to elaborate the best therapy plan for the patient, avoiding risky invasive tests. Patient-specific modeling may be extremely useful in biomedical research as well, in particular to optimize medical device design and development. Thorough in silico testing may provide profound, cost-efficient and painfree assessment of the effectiveness of pacemaker settings in the patient. The promising results presented in this Thesis give confidence that our parameter estimation and personalization techniques could be used in computational medicine to translate models to clinical care aiming to improve patient health.

Bibliography

[1] World Health Organization. Cardiovascular diseases. *Technical Report*, 2015.

[2] A. Auricchio, C. Stellbrink, S. Sack, M. Block, J. ürgen Vogt, P. Bakker, C. Huth, F. Schöndube, U. Wolfhard, D. Böcker, et al. Long-term clinical effect of hemodynamically optimized cardiac resynchronization therapy in patients with heart failure and ventricular conduction delay. *Journal of the American College of Cardiology*, 39(12):2026–2033, 2002.

[3] J. Cleland, J.-C. Daubert, E. Erdmann, N. Freemantle, D. Gras, L. Kappenberger, and L. Tavazzi. The effect of cardiac resynchronization on morbidity and mortality in heart failure. *New England Journal of Medicine*, 352(15):1539–1549, 2005.

[4] A. Auricchio and F. Prinzen. Non-responders to cardiac resynchronization therapy. *Circulation Journal*, 75(3):521–527, 2011.

[5] G. Hindricks, C. Piorkowski, H. Tanner, R. Kobza, J.-H. Gerds-Li, C. Carbucicchio, and H. Kottkamp. Perception of atrial fibrillation before and after radiofrequency catheter ablation: relevance of asymptomatic arrhythmia recurrence. *Circulation*, 112(3):307–313, 2005.

[6] H. Tanner, G. Hindricks, M. Volkmer, S. Furniss, V. Kühlkamp, D. Lacroix, C. De Chillou, J. Almendral, D. Caponi, K.-H. Kuck, et al. Catheter ablation of recurrent scar-related ventricular tachycardia using electroanatomical mapping and irrigated ablation technology: results of the prospective multicenter euro-vt-study. *Journal of cardiovascular electrophysiology*, 21(1):47–53, 2010.

[7] A. J. Pullan, M. L. Buist, and L. K. Cheng. *Mathematically Modelling the Electrical Activity of the Heart: From Cell to Body Surface and Back Again*. World Scientific, 2015.

[8] J. Sundnes, G. T. Lines, X. Cai, B. F. Nielsen, K.-A. Mardal, and A. Tveito. *Computing the electrical activity in the heart*, volume 1. Springer Science & Business Media, 2007.

[9] N. A. Trayanova. Whole-heart modeling: applications to cardiac electrophysiology and electromechanics. *Circulation research*, 108(1):113–128, 2011.

[10] R. H. Clayton and et. al. Models of cardiac tissue electrophysiology: progress, challenges and open questions. *Progress in Biophysics and Molecular Biology*, 104:22–48, 2011.

[11] J. Relan, P. Chinchapatnam, M. Sermesant, K. Rhode, M. Ginks, H. Delingette, C. A. Rinaldi, R. Razavi, and N. Ayache. Coupled personalization of cardiac electrophysiology models for prediction of ischaemic ventricular tachycardia. *Interface focus*, 1(3):396–407, 2011.

[12] H. J. Arevalo, F. Vadakkumpadan, E. Guallar, A. Jebb, P. Malamas, K. C. Wu, and N. A. Trayanova. Arrhythmia risk stratification of patients after myocardial infarction using personalized heart models. *Nature communications*, 7:11437, 2016.

[13] J. Almquist, M. Wallman, I. Jacobson, and M. Jirstrand. Modeling the effect of kv1. 5 block on the canine action potential. *Biophysical journal*, 99(9):2726–2736, 2010.

[14] M. Sermesant, R. Chabiniok, P. Chinchapatnam, T. Mansi, F. Billet, P. Moireau, J.-M. Peyrat, K. Wong, J. Relan, K. Rhode, et al. Patient-specific electromechanical models of the heart for the prediction of pacing acute effects in crt: a preliminary clinical validation. *Medical image analysis*, 16(1):201–215, 2012.

[15] C. Tobon-Gomez, N. Duchateau, R. Sebastian, S. Marchesseau, O. Camara, E. Donal, M. De Craene, A. Pashaei, J. Relan, M. Steghofer, et al. Understanding the mechanisms amenable to crt response: from pre-operative multimodal image data to

patient-specific computational models. *Medical & biological engineering & computing*, 51(11):1235–1250, 2013.

[16] H. Ashikaga, H. Arevalo, F. Vadakkumpadan, R. C. Blake III, J. D. Bayer, S. Nazarian, M. M. Zviman, H. Tandri, R. D. Berger, H. Calkins, et al. Feasibility of image-based simulation to estimate ablation target in human ventricular arrhythmia. *Heart Rhythm*, 10(8):1109–1116, 2013.

[17] J. D. Bayer, C. H. Roney, A. Pashaei, P. Jaïs, and E. J. Vigmond. Novel radiofrequency ablation strategies for terminating atrial fibrillation in the left atrium: a simulation study. *Frontiers in physiology*, 7:108, 2016.

[18] A. Petras, M. Leoni, J. M. Guerra, J. Jansson, and L. Gerardo-Giorda. Tissue drives lesion: computational evidence of interspecies variability in cardiac radiofrequency ablation. In *International Conference on Functional Imaging and Modeling of the Heart*, pages 139–146. Springer, 2019.

[19] P. M. Nielsen, I. J. Le Grice, B. H. Smaill, and P. J. Hunter. Mathematical model of geometry and fibrous structure of the heart. *American Journal of Physiology-Heart and Circulatory Physiology*, 260(4):H1365–H1378, 1991.

[20] J. Xi, P. Lamata, S. Niederer, S. Land, W. Shi, X. Zhuang, S. Ourselin, S. G. Duckett, A. K. Shetty, C. A. Rinaldi, et al. The estimation of patient-specific cardiac diastolic functions from clinical measurements. *Medical image analysis*, 17(2):133–146, 2013.

[21] E. Kayvanpour, T. Mansi, F. Sedaghat-Hamedani, A. Amr, D. Neumann, B. Georgescu, P. Seegerer, A. Kamen, J. Haas, K. S. Frese, et al. Towards personalized cardiology: multi-scale modeling of the failing heart. *PLoS One*, 10(7):e0134869, 2015.

[22] S. Marchesseau, H. Delingette, M. Sermesant, and N. Ayache. Fast parameter calibration of a cardiac electromechanical model from medical images based on the unscented transform. *Biomechanics and modeling in mechanobiology*, 12(4):815–831, 2013.

[23] O. Zettinig, T. Mansi, D. Neumann, B. Georgescu, S. Rapaka, P. Seegerer, E. Kayvanpour, F. Sedaghat-Hamedani, A. Amr, J. Haas, et al. Data-driven estimation of cardiac electrical diffusivity from 12-lead ecg signals. *Medical image analysis*, 18(8):1361–1376, 2014.

[24] P. Seegerer, T. Mansi, M.-P. Jolly, D. Neumann, B. Georgescu, A. Kamen, E. Kayvanpour, A. Amr, F. Sedaghat-Hamedani, J. Haas, et al. Estimation of regional electrical properties of the heart from 12-lead ecg and images. In *International Workshop on Statistical Atlases and Computational Models of the Heart*, pages 204–212. Springer, 2014.

[25] D. Neumann, T. Mansi, S. Grbic, I. Voigt, B. Georgescu, E. Kayvanpour, A. Amr, F. Sedaghat-Hamedani, J. Haas, H. Katus, et al. Automatic image-to-model framework for patient-specific electromechanical modeling of the heart. In *2014 IEEE 11th International Symposium on Biomedical Imaging (ISBI)*, pages 935–938. IEEE, 2014.

[26] H. Yang and A. Veneziani. Estimation of cardiac conductivities in ventricular tissue by a variational approach. *Inverse Problems*, 31(11):115001, 2015.

[27] M. J. Hoffman, N. S. LaVigne, S. T. Scorse, F. H. Fenton, and E. M. Cherry. Reconstructing three-dimensional reentrant cardiac electrical wave dynamics using data assimilation. *Chaos: An Interdisciplinary Journal of Nonlinear Science*, 26(1):013107, 2016.

[28] E. Cherry, D. Cairns, N. Holt, N. LaVigne, F. Fenton, and M. Hoffman. Data assimilation for cardiac electrical dynamics. In *Proceedings of the 5th International Conference on Computational and Mathematical Biomedical Engineering*, pages 423–426, 2017.

[29] G. Plank, R. Burton, P. Hales, M. Bishop, T. Mansoori, M. O. Bernabeu, A. Garny, A. J. Prassl, C. Bollensdorff, F. Mason, et al. Generation of histo-anatomically representative models of the individual heart: tools and application. *Philosophical Transactions of the Royal Society A: Mathematical, Physical and Engineering Sciences*, 367(1896):2257–2292, 2009.

[30] M. L. Neal and R. Kerckhoffs. Current progress in patient-specific modeling. *Briefings in bioinformatics*, 11(1):111–126, 2009.

[31] X. Cai and G. T. Lines. Full-scale simulation of cardiac electrophysiology on parallel computers. In *Numerical solution of partial differential equations on parallel computers*, pages 385–411. Springer, 2006.

[32] M. Vázquez, R. Arís, G. Houzeaux, R. Aubry, P. Villar, J. Garcia-Barnés, D. Gil, and F. Carreras. A massively parallel computational electrophysiology model of the heart. *International journal for numerical methods in biomedical engineering*, 27(12):1911–1929, 2011.

[33] D. Sato, Y. Xie, J. N. Weiss, Z. Qu, A. Garfinkel, and A. R. Sanderson. Acceleration of cardiac tissue simulation with graphic processing units. *Medical & biological engineering & computing*, 47(9):1011–1015, 2009.

[34] E. J. Vigmond, P. M. Boyle, L. J. Leon, and G. Plank. Near-real-time simulations of biolelectric activity in small mammalian hearts using graphical processing units. In *2009 Annual International Conference of the IEEE Engineering in Medicine and Biology Society*, pages 3290–3293. IEEE, 2009.

[35] A. Kaboudian, E. M Cherry, and F. H. Fenton. Real-time interactive simulations of large-scale systems on personal computers and cell phones: Toward patient-specific heart modeling and other applications. *Science advances*, 5(3):eaav6019, 2019.

[36] A. Kaboudian, E. M. Cherry, and F. H. Fenton. Large-scale interactive numerical experiments of chaos, solitons and fractals in real time via gpu in a web browser. *Chaos, Solitons & Fractals*, 121:6–29, 2019.

[37] M. Boulakia, E. Schenone, and J.-F. Gerbeau. Reduced-order modeling for cardiac electrophysiology. application to parameter identification. *International Journal for Numerical Methods in Biomedical Engineering*, 28(6-7):727–744, 2012.

[38] S. Marchesseau, H. Delingette, M. Sermesant, R. Cabrera-Lozoya, C. Tobon-Gomez, P. Moireau, R. M. Ventura, K. Lekadir, A. Hernandez, M. Garreau, et al. Personal-

ization of a cardiac electromechanical model using reduced order unscented kalman filtering from regional volumes. *Medical image analysis*, 17(7):816–829, 2013.

[39] J.-F. Gerbeau, D. Lombardi, and E. Schenone. Reduced order model in cardiac electrophysiology with approximated lax pairs. *Advances in Computational Mathematics*, 41(5):1103–1130, 2015.

[40] H. Yang, T. Passerini, T. Mansi, and D. Comaniciu. Data-driven model reduction for fast, high fidelity atrial electrophysiology computations. In *International Conference on Functional Imaging and Modeling of the Heart*, pages 466–474. Springer, 2015.

[41] H. Yang and A. Veneziani. Efficient estimation of cardiac conductivities via pod-deim model order reduction. *Applied Numerical Mathematics*, 115:180–199, 2017.

[42] P. R. Johnston. A sensitivity study of conductivity values in the passive bidomain equation. *Mathematical biosciences*, 232(2):142–150, 2011.

[43] F. Chinesta, R. Keunings, and A. Leygue. *The proper generalized decomposition for advanced numerical simulations: a primer.* Springer Science & Business Media, 2013.

[44] E. Pruliere, F. Chinesta, and A. Ammar. On the deterministic solution of multidimensional parametric models using the proper generalized decomposition. *Mathematics and Computers in Simulation*, 81(4):791–810, 2010.

[45] P.-E. Allier, L. Chamoin, and P. Ladevèze. Proper generalized decomposition computational methods on a benchmark problem: introducing a new strategy based on constitutive relation error minimization. *Advanced Modeling and Simulation in Engineering Sciences*, 2(1):17, 2015.

[46] A. Dumon, C. Allery, and A. Ammar. Proper general decomposition (pgd) for the resolution of navier–stokes equations. *Journal of Computational Physics*, 230(4):1387–1407, 2011.

[47] A. Falco and A. Nouy. A proper generalized decomposition for the solution of elliptic problems in abstract form by using a functional eckart–young approach. *Journal of Mathematical Analysis and Applications*, 376(2):469–480, 2011.

[48] M. Signorini, S. Zlotnik, and P. Díez. Proper generalized decomposition solution of the parameterized helmholtz problem: application to inverse geophysical problems. *International Journal for Numerical Methods in Engineering*, 109(8):1085–1102, 2017.

[49] A. Tarantola. *Inverse problem theory and methods for model parameter estimation*, volume 89. siam, 2005.

[50] J. Kaipio and E. Somersalo. *Statistical and computational inverse problems*, volume 160. Springer Science & Business Media, 2006.

[51] E. Konukoglu, J. Relan, U. Cilingir, B. H. Menze, P. Chinchapatnam, A. Jadidi, H. Cochet, M. Hocini, H. Delingette, P. Jaïs, et al. Efficient probabilistic model personalization integrating uncertainty on data and parameters: Application to eikonal-diffusion models in cardiac electrophysiology. *Progress in biophysics and molecular biology*, 107(1):134–146, 2011.

[52] E. Pernod, M. Sermesant, E. Konukoglu, J. Relan, H. Delingette, and N. Ayache. A multi-front eikonal model of cardiac electrophysiology for interactive simulation of radio-frequency ablation. *Computers & Graphics*, 35(2):431–440, 2011.

[53] Y. Zheng, A. Barbu, B. Georgescu, M. Scheuering, and D. Comaniciu. Four-chamber heart modeling and automatic segmentation for 3-d cardiac ct volumes using marginal space learning and steerable features. *IEEE transactions on medical imaging*, 27(11):1668–1681, 2008.

[54] D. Neumann, T. Mansi, L. Itu, B. Georgescu, E. Kayvanpour, F. Sedaghat-Hamedani, A. Amr, J. Haas, H. Katus, B. Meder, et al. A self-taught artificial agent for multi-physics computational model personalization. *Medical image analysis*, 34:52–64, 2016.

[55] S. Y. Ho, R. H. Anderson, and D. Sánchez-Quintana. Atrial structure and fibres: morphologic bases of atrial conduction. *Cardiovascular research*, 54(2):325–336, 2002.

[56] S. Y. Ho and D. Sánchez-Quintana. The importance of atrial structure and fibers. *Clinical Anatomy: The Official Journal of the American Association of Clinical Anatomists and the British Association of Clinical Anatomists*, 22(1):52–63, 2009.

[57] D. D. Streeter Jr, H. M. Spotnitz, D. P. Patel, J. Ross Jr, and E. H. Sonnenblick. Fiber orientation in the canine left ventricle during diastole and systole. *Circulation research*, 24(3):339–347, 1969.

[58] I. J LeGrice, P. J. Hunter, and B. H. Smaill. Laminar structure of the heart: a mathematical model. *American Journal of Physiology-Heart and Circulatory Physiology*, 272(5):H2466–H2476, 1997.

[59] C. Luo and Y. Rudy. A dynamic model of the cardiac ventricular action potential. i. simulations of ionic currents and concentration changes. *Circulation research*, 74(6):1071–1096, 1994.

[60] L. Sherwood. *Study Guide for Sherwood's Human Physiology: From Cells to Systems, 8th.* Cengage Learning, 2012.

[61] A. L. Hodgkin and A. F. Huxley. A quantitative description of membrane current and its application to conduction and excitation in nerve. *The Journal of physiology*, 117(4):500–544, 1952.

[62] G. W. Beeler and H. Reuter. Reconstruction of the action potential of ventricular myocardial fibres. *The Journal of physiology*, 268(1):177–210, 1977.

[63] M. Courtemanche, R. J. Ramirez, and S. Nattel. Ionic mechanisms underlying human atrial action potential properties: insights from a mathematical model. *American Journal of Physiology-Heart and Circulatory Physiology*, 275(1):H301–H321, 1998.

[64] K.H.W.J. Ten Tusscher, D. Noble, P.-J. Noble, and A. V. Panfilov. A model for human ventricular tissue. *American Journal of Physiology-Heart and Circulatory Physiology*, 286(4):H1573–H1589, 2004.

[65] F. H. Fenton and E. M. Cherry. Models of cardiac cell. *Scholarpedia*, 3:1868, 2008.

[66] J. Keener and J. Sneyd. *Mathematical Physiology*. Spinger–Verlag, 2009.

[67] J. M. Rogers and A. D. McCulloch. A collocation-galerkin finite element model of cardiac action potential propagation. *IEEE Transactions on Biomedical Engineering*, 41(8):743–757, 1994.

[68] C. C. Mitchell and D. G. Schaeffer. A two-current model for the dynamics of cardiac membrane. *Bulletin of Mathematical Biology*, 65(5):767–793, Sep 2003.

[69] F. H. Fenton and A. Karma. Vortex dynamics in three-dimensional continuous myocardium with fiber rotation: Filament instability and fibrillation. *Chaos*, 8:20–47, 1998.

[70] A. Bueno-Orovio, E. M. Cherry, and F. H. Fenton. Minimal model for human ventricular action potentials in tissue. *Journal of Theoretical Biology*, 7:544–560, 2008.

[71] D. I. Cairns, F. H. Fenton, and E. M. Cherry. Efficient parameterization of cardiac action potential models using a genetic algorithm. *Chaos: An Interdisciplinary Journal of Nonlinear Science*, 27:093922, 2017.

[72] R. FitzHugh. Impulses and physiological states in theoretical models of nerve membrane. *Biophysical journal*, 1(6):445–466, 1961.

[73] J. Nagumo, S. Arimoto, and S. Yoshizawa. An active pulse transmission line simulating nerve axon. *Proceedings of the IRE*, 50(10):2061–2070, 1962.

[74] P. Colli Franzone and L. F. Pavarino. A parallel solver for reaction–diffusion systems in computational electrocardiology. *Mathematical models and methods in applied sciences*, 14(06):883–911, 2004.

[75] A. Karma. Electrical alternans and spiral wave breakup in cardiac tissue. *Chaos: An Interdisciplinary Journal of Nonlinear Science*, 4:461–472, 1994.

[76] F. H. Fenton, E. M. Cherry, H. M. Hastings, and S. J. Evans. Multiple mechanisms of spiral wave breakup in a model of cardiac electrical activity. *Chaos: An Interdisciplinary Journal of Nonlinear Science*, 12(3):852–892, 2002.

[77] O. H. Schmitt. Biological information processing using the concept of interpenetrating domains. In *Information processing in the nervous system*, pages 325–331. Springer, 1969.

[78] W. T. Miller and D. B. Geselowitz. Simulation studies of the electrocardiogram. i. the normal heart. *Circulation Research*, 43(2):301–315, 1978.

[79] L. Tung. *A bi-domain model for describing ischemic myocardial d-c potentials.* PhD thesis, Massachusetts Institute of Technology, Cambridge, MA, USA, 1978. ndltd.org (oai:dspace.mit.edu:1721.1/16177).

[80] R. Plonsey and D. G. Fleming. Biomagnetic phenomena, 1969.

[81] E. M. Cherry and F. H. Fenton. Effects of boundaries and geometry on the spatial distribution of action potential duration in cardiac tissue. *Journal of Theoretical Biology*, 285:164–176, 2011.

[82] P. Colli Franzone and G. Savaré. Degenerate evolution systems modeling the cardiac electric field at micro-and macroscopic level. In *Evolution equations, semigroups and functional analysis*, pages 49–78. Springer, 2002.

[83] M. Veneroni. Reaction–diffusion systems for the macroscopic bidomain model of the cardiac electric field. *Nonlinear Analysis: Real World Applications*, 10(2):849–868, 2009.

[84] G. A. Holzapfel and R. W. Ogden. Constitutive modelling of passive myocardium: a structurally based framework for material characterization. *Philosophical Transactions of the Royal Society of London A: Mathematical, Physical and Engineering Sciences*, 367:3445–3475, 2009.

[85] E. W. Hsu and C. S. Henriquez. Myocardial fiber orientation mapping using reduced encoding diffusion tensor imaging. *Journal of Cardiovascular Magnetic Resonance*, 3(4):339–347, 2001.

[86] J. Peyrat, M. Sermesant, X. Pennec, H. Delingette, C. Xu, E. R. McVeigh, and N. Ayache. A computational framework for the statistical analysis of cardiac diffusion

tensors: application to a small database of canine hearts. *IEEE Transactions on Medical Imaging*, 26(11):1500–1514, 2007.

[87] L. Zhukov and A. H. Barr. Heart-muscle fiber reconstruction from diffusion tensor mri. In *IEEE Visualization, 2003. VIS 2003.*, pages 597–602. IEEE, 2003.

[88] M. Couade, M. Pernot, E. Messas, A. Bel, M. Ba, A. Hagege, M. Fink, and M. Tanter. In vivo quantitative mapping of myocardial stiffening and transmural anisotropy during the cardiac cycle. *IEEE transactions on medical imaging*, 30(2):295–305, 2010.

[89] L. F. Pavarino and S. Scacchi. Multilevel additive schwarz preconditioners for the bidomain reaction-diffusion system. *SIAM Journal on Scientific Computing*, 31(1):420–443, 2008.

[90] L. Gerardo-Giorda, L. Mirabella, F. Nobile, M. Perego, and A. Veneziani. A model-based block-triangular preconditioner for the bidomain system in electrocardiology. *Journal of Computational Physics*, 228(10):3625–3639, 2009.

[91] P. Colli Franzone, L. F. Pavarino, and B. Taccardi. Simulating patterns of excitation, repolarization and action potential duration with cardiac bidomain and monodomain models. *Mathematical biosciences*, 197(1):35–66, 2005.

[92] B. F. Nielsen, T. S. Ruud, G. T. Lines, and A. Tveito. Optimal monodomain approximations of the bidomain equations. *Applied Mathematics and Computation*, 184(2):276–290, 2007.

[93] J. Sundnes, B. F. Nielsen, K. A. Mardal, X. Cai, G. T. Lines, and A. Tveito. On the computational complexity of the bidomain and the monodomain models of electrophysiology. *Annals of biomedical engineering*, 34(7):1088–1097, 2006.

[94] L. Gerardo-Giorda, M. Perego, and A. Veneziani. Optimized schwarz coupling of bidomain and monodomain models in electrocardiology. *ESAIM: Mathematical Modelling and Numerical Analysis*, 45(2):309–334, 2011.

[95] L. Mirabella, F. Nobile, and A. Veneziani. An a posteriori error estimator for model adaptivity in electrocardiology. *Computer Methods in Applied Mechanics and Engineering*, 200(37-40):2727–2737, 2011.

[96] N. Trayanova. Defibrillation of the heart: insights into mechanisms from modelling studies. *Experimental physiology*, 91(2):323–337, 2006.

[97] F. H. Fenton and et. al. Termination of atrial fibrillation using pulsed low-energy far-field stimulation. *Circulation*, 120:467, 2009.

[98] S. Luther, F. H. Fenton, and et. al. Low-energy control of electrical turbulence in the heart. *Nature*, 475:235–239, 2011.

[99] J. P. Wikswo Jr, S. Lin, and R. A. Abbas. Virtual electrodes in cardiac tissue: a common mechanism for anodal and cathodal stimulation. *Biophysical journal*, 69(6):2195–2210, 1995.

[100] I. R. Efimov and et. al. Virtual electrode–induced phase singularity: A basic mechanism of defibrillation failure. *Circulation Research*, 82:918–925, 1998.

[101] P. Colli Franzone, L. Guerri, and S. Rovida. Wavefront propagation in an activation model of the anisotropic cardiac tissue: asymptotic analysis and numerical simulations. *Journal of mathematical biology*, 28(2):121–176, 1990.

[102] M. Wallman, N. Smith, and B. Rodriguez. Estimation of activation times in cardiac tissue using graph based methods. In *International Conference on Functional Imaging and Modeling of the Heart*, pages 71–79. Springer, 2011.

[103] M. Wallman, N. P. Smith, and B. Rodriguez. A comparative study of graph-based, eikonal, and monodomain simulations for the estimation of cardiac activation times. *IEEE Transactions on Biomedical Engineering*, 59(6):1739–1748, 2012.

[104] V. Jacquemet. An eikonal approach for the initiation of reentrant cardiac propagation in reaction–diffusion models. *IEEE Transactions on Biomedical Engineering*, 57(9):2090–2098, 2010.

[105] M. Sermesant, E. Konukoglu, H. Delingette, Y. Coudière, P. Chinchapatnam, K. S. Rhode, R. Razavi, and N. Ayache. An anisotropic multi-front fast marching method for real-time simulation of cardiac electrophysiology. In *International Conference on Functional Imaging and Modeling of the Heart*, pages 160–169. Springer, 2007.

[106] D. B. Geselowitz. An application of electrocardiographic lead theory to impedance plethysmography. *IEEE Transactions on biomedical Engineering*, 18(1):38–41, 1971.

[107] L. Clerc. Directional differences of impulse spread in trabecular muscle from mammalian heart. *The Journal of physiology*, 255(2):335–346, 1976.

[108] D. E. Roberts, L. T. Hersh, and A. M. Scher. Influence of cardiac fiber orientation on wavefront voltage, conduction velocity, and tissue resistivity in the dog. *Circulation research*, 44(5):701–712, 1979.

[109] D. E. Roberts and A. M. Scher. Effect of tissue anisotropy on extracellular potential fields in canine myocardium in situ. *Circulation Research*, 50(3):342–351, 1982.

[110] B. J. Roth. Electrical conductivity values used with the bidomain model of cardiac tissue. *IEEE Transactions on Biomedical Engineering*, 44(4):326–328, 1997.

[111] L. S. Graham and D. Kilpatrick. Estimation of the bidomain conductivity parameters of cardiac tissue from extracellular potential distributions initiated by point stimulation. *Annals of biomedical engineering*, 38(12):3630–3648, 2010.

[112] P. Le Guyader, F. Trelles, and P. Savard. Extracellular measurement of anisotropic bidomain myocardial conductivities. i. theoretical analysis. *Annals of Biomedical Engineering*, 29(10):862–877, 2001.

[113] J. G. Stinstra, B. Hopenfeld, and R. S. MacLeod. On the passive cardiac conductivity. *Annals of biomedical engineering*, 33(12):1743–1751, 2005.

[114] R. Sadleir and C. Henriquez. Estimation of cardiac bidomain parameters from extracellular measurement: two dimensional study. *Annals of biomedical engineering*, 34(8):1289–1303, 2006.

[115] L. S. Graham, D. Kilpatrick, F. Sainsbury, and A. C. Yong. The determination of the bidomain conductivity values of heart tissue. In *2008 Computers in Cardiology*, pages 193–196. IEEE, 2008.

[116] A. Barone, F. Fenton, and A. Veneziani. Numerical sensitivity analysis of a variational data assimilation procedure for cardiac conductivities. *Chaos: An Interdisciplinary Journal of Nonlinear Science*, 27:093930, 09 2017. https://doi.org/10.1063/1.5001454.

[117] A. Barone, A. Gizzi, F. Fenton, S. Filippi, and A. Veneziani. Experimental validation of a variational data assimilation procedure for estimating space-dependent cardiac conductivities. *Computer Methods in Applied Mechanics and Engineering*, 358:112615, 2020. https://doi.org/10.1016/j.cma.2019.112615.

[118] E. M. Cherry and F. H. Fenton. Visualization of spiral and scroll waves in simulated and experimental cardiac tissue. *New Journal of Physics*, 10(12):125016, 2008.

[119] A. Gizzi, E. M. Cherry, R. F. Jr. Gilmour, S. Luther, S. Filippi, and F. H. Fenton. Effects of pacing site and stimulation history on alternans dynamics and the development of complex spatiotemporal patterns in cardiac tissue. *Frontiers in Physiology*, 4:1–20, 2013.

[120] H. S. Oster, B. Taccardi, R. L. Lux, P. R. Ershler, and Y. Rudy. Noninvasive electrocardiographic imaging: reconstruction of epicardial potentials, electrograms, and isochrones and localization of single and multiple electrocardiac events. *Circulation*, 96(3):1012–1024, 1997.

[121] M. Cluitmans, P. Bonizzi, J. Karel, P. Volders, R. Peeters, and R. L. Westra. Inverse reconstruction of epicardial potentials improved by vectorcardiography and realistic potentials. In *Computing in Cardiology 2013*, pages 369–372. IEEE, 2013.

[122] J. Chen, M. M. Henneman, M. A. Trimble, J. J. Bax, S. Borges-Neto, A. E. Iskandrian, K. J. Nichols, and E. V. Garcia. Assessment of left ventricular mechanical dyssynchrony by phase analysis of ecg-gated spect myocardial perfusion imaging. *Journal of nuclear cardiology*, 15(1):127–136, 2008.

[123] F. Tröltzsch. *Optimal control of partial differential equations: theory, methods, and applications*, volume 112. American Mathematical Soc., 2010.

[124] M. D. Gunzburger. *Perspectives in flow control and optimization*, volume 5. Siam, 2003.

[125] A. Borzì and V. Schulz. *Computational optimization of systems governed by partial differential equations*, volume 8. SIAM, 2011.

[126] K. Kunisch and M. Wagner. Optimal control of the bidomain system (i): The monodomain approximation with the rogers-mcculloch model. *Nonlinear Analysis: Real World Applications*, 13(4):1525–1550, 2012.

[127] K. Kunisch and M. Wagner. Optimal control of the bidomain system (ii): Uniqueness and regularity theorems for weak solutions. *Annali di Matematica Pura ed Applicata*, 192(6):951–986, 2013.

[128] K. Kunisch and M. Wagner. Optimal control of the bidomain system (iii): Existence of minimizers and first-order optimality conditions. *ESAIM: Mathematical Modelling and Numerical Analysis*, 47(4):1077–1106, 2013.

[129] H. T. Banks. *A functional analysis framework for modeling, estimation and control in science and engineering*. Chapman and Hall/CRC, 2012.

[130] H. T. Banks and K. Kunisch. *Estimation techniques for distributed parameter systems*. Springer Science & Business Media, 2012.

[131] R. W. dos Santos, G. Plank, S. Bauer, and E. J. Vigmond. Parallel multigrid preconditioner for the cardiac bidomain model. *IEEE Transactions on Biomedical Engineering*, 51(11):1960–1968, 2004.

[132] M. Pennacchio and V. Simoncini. Algebraic multigrid preconditioners for the bidomain reaction–diffusion system. *Applied numerical mathematics*, 59(12):3033–3050, 2009.

[133] M. Perego and A. Veneziani. An efficient generalization of the rush-larsen method for solving electro-physiology membrane equations. *Electronic Transactions on Numerical Analysis*, 35:234–256, 2009.

[134] C. Pierre. Preconditioning the bidomain model with almost linear complexity. *Journal of Computational Physics*, 231(1):82–97, 2012.

[135] P. Bochev and R. B. Lehoucq. On the finite element solution of the pure neumann problem. *SIAM review*, 47(1):50–66, 2005.

[136] A. Quarteroni. *Numerical models for differential problems*, volume 2. Springer, 2009.

[137] Y. Saad. *Iterative methods for sparse linear systems*, volume 82. siam, 2003.

[138] J. Nocedal and S. Wright. *Numerical optimization.* Springer Science & Business Media, 2006.

[139] F. Hecht and O. Pironneau. freefem+. 2013.

[140] L. Bertagna, S. Deparis, L. Formaggia, D. Forti, and A. Veneziani. The lifev library: engineering mathematics beyond the proof of concept. *arXiv preprint arXiv:1710.06596*, 2017.

[141] T. Passerini, A. Quaini, U. Villa, A. Veneziani, and S. Canic. Validation of an open source framework for the simulation of blood flow in rigid and deformable vessels. *International journal for numerical methods in biomedical engineering*, 29(11):1192–1213, 2013.

[142] M. Heroux and et. al. An Overview of Trilinos. Technical Report SAND2003-2927, Sandia National Laboratories, 2003.

[143] E. Beretta, M. C. Cerutti, A. Manzoni, and D. Pierotti. An asymptotic formula for boundary potential perturbations in a semilinear elliptic equation related to cardiac electrophysiology. *Mathematical Models and Methods in Applied Sciences*, 26(04):645–670, 2016.

[144] E. Beretta, C. Cavaterra, M. C. Cerutti, A. Manzoni, and L. Ratti. An inverse problem for a semilinear parabolic equation arising from cardiac electrophysiology. *Inverse Problems*, 33(10):105008, 2017.

[145] E. Beretta, A. Manzoni, and L. Ratti. A reconstruction algorithm based on topological gradient for an inverse problem related to a semilinear elliptic boundary value problem. *Inverse Problems*, 33(3):035010, 2017.

[146] H. Lim, W. Cun, Y. Wang, R. A. Gray, and J. Glimm. The role of conductivity discontinuities in design of cardiac defibrillation. *Chaos*, 28:013106, 2018.

[147] S Pezzuto, J Hake, and J Sundnes. Space-discretization error analysis and stabilization schemes for conduction velocity in cardiac electrophysiology. *International journal for numerical methods in biomedical engineering*, 32(10):e02762, 2016.

[148] J. Jilberto and D. E. Hurtado. Semi-implicit non-conforming finite-element schemes for cardiac electrophysiology: a framework for mesh-coarsening heart simulations. *Frontiers in Physiology*, 9:1513, 2018.

[149] S. Brandstaeter, A. Gizzi, S. L. Fuchs, A. M. Gebauer, R. C. Aydin, and C. J. Cyron. Computational model of gastric motility with activestrain electromechanics. *ZAMM*, 98(12):2177–2197, 2018.

[150] D. E. Hurtado and D. Rojas. Non-conforming finite-element formulation for cardiac electrophysiology: an effective approach to reduce the computation time of heart simulations without compromising accuracy. *Computational Mechanics*, 61:485–497, 2018.

[151] F. H. Fenton, A. Gizzi, C. Cherubini, N. Pomella, and S. Filippi. Role of temperature on nonlinear cardiac dynamics. *Physical Review E*, 87:042709, 2013.

[152] A. Gizzi, A. Loppini, E. M. Cherry, C. Cherubini, F. H. Fenton, and S. Filippi. Multi-band decomposition analysis: Application to cardiac alternans as a function of temperature. *Physiological Measurements*, 38:833–847, 2017.

[153] D. D. Chen, R. A. Gray, I. Uzelac, C. Herndon, and F. H. Fenton. Mechanism for amplitude alternans in electrocardiograms and the initiation of spatiotemporal chaos. *Physical Review Letters*, 118:168101, 2017.

[154] A. Loppini, A. Gizzi, R. Ruiz-Baier, C. Cherubini, F. H. Fenton, and S. Filippi. Competing mechanisms of stress-assisted diffusivity and stretch-activated currents in cardiac electromechanics. *Frontiers in Physiology*, 9:1714, 2018.

[155] P. Colli Franzone, L. F. Pavarino, and S. Scacchi. *Mathematical cardiac electrophysiology*, volume 13. Springer, 2014.

[156] F. S. Costabal, F. A. Concha, D. E. Hurtado, and E. Kuhl. The importance of mechano-electrical feedback and inertia in cardiac electromechanics. *Computer Methods in Applied Mechanics and Engineering*, 320:352–368, 2017.

[157] D. E. Hurtado, S. Castro, and A. Gizzi. Computational modeling of non-linear diffusion in cardiac electrophysiology: A novel porous-medium approach. *Computer Methods in Applied Mechanics and Engineering*, 300:70–83, 2016.

[158] S. Niederer, L. Mitchell, N. Smith, and G. Plank. Simulating human cardiac electrophysiology on clinical time-scales. *Frontiers in physiology*, 2:14, 2011.

[159] E. Vigmond, F. Vadakkumpadan, V. Gurev, H. Arevalo, M. Deo, G. Plank, and N. Trayanova. Towards predictive modelling of the electrophysiology of the heart. *Experimental physiology*, 94(5):563–577, 2009.

[160] C. Nagaiah, K. Kunisch, and G. Plank. On boundary stimulation and optimal boundary control of the bidomain equations. *Mathematical biosciences*, 245(2):206–215, 2013.

[161] C. Nagaiah, K. Kunisch, and G. Plank. Optimal control approach to termination of reentry waves in cardiac electrophysiology. *Journal of Mathematical Biology*, 67(2):359–388, 2013.

[162] T. Yang, L. Yu, Q. Jin, L. Wu, and B. He. Localization of origins of premature ventricular contraction by means of convolutional neural network from 12-lead ecg. *IEEE Transactions on Biomedical Engineering*, 65(7):1662–1671, 2017.

[163] J. Wang, Y. Wang, M. Yang, S. Shao, Y. Tian, X. Shao, S. Fan, F. Zhang, W. Yang, W. Xin, et al. Mechanical contraction to guide crt left-ventricular lead placement instead of electrical activation in myocardial infarction with left ventricular dysfunction: An experimental study based on non-invasive gated myocardial perfusion imaging and invasive electroanatomic mapping. *Journal of Nuclear Cardiology*, pages 1–12, 2019.

[164] G. Rozza, D. B. P. Huynh, and A. T. Patera. Reduced basis approximation and a posteriori error estimation for affinely parametrized elliptic coercive partial differential equations. *Archives of Computational Methods in Engineering*, 15(3):1, 2007.

[165] J. S. Hesthaven, G. Rozza, B. Stamm, et al. *Certified reduced basis methods for parametrized partial differential equations*. Springer, 2016.

[166] A. Quarteroni, A. Manzoni, and F. Negri. *Reduced basis methods for partial differential equations: an introduction*, volume 92. Springer, 2015.

[167] D. Amsallem, M. J. Zahr, and C. Farhat. Nonlinear model order reduction based on local reduced-order bases. *International Journal for Numerical Methods in Engineering*, 92(10):891–916, 2012.

[168] S. Pagani, A. Manzoni, and A. Quarteroni. Numerical approximation of parametrized problems in cardiac electrophysiology by a local reduced basis method. *Computer Methods in Applied Mechanics and Engineering*, 340:530–558, 2018.

[169] F. S. Costabal, P. Perdikaris, E. Kuhl, and D. E. Hurtado. Multi-fidelity classification using gaussian processes: Accelerating the prediction of large-scale computational models. *Computer Methods in Applied Mechanics and Engineering*, 357:112602, 2019.

[170] A. Barone, M. G. Carlino, A. Gizzi, S. Perotto, and A. Veneziani. Efficient estimation of cardiac conductivities based on a proper generalized decomposition approach. *In preparation*.

[171] M. S. Spach. Anisotropy of cardiac tissue: a major determinant of conduction. *Journal of cardiovascular electrophysiology*, 10(6):887–890, 1999.

[172] M. S. Spach, J. F. Heidlage, R. C. Barr, and P. C. Dolber. Cell size and communication: role in structural and electrical development and remodeling of the heart. *Heart Rhythm*, 1(4):500–515, 2004.

[173] D. Calvetti and E. Somersalo. *An introduction to Bayesian scientific computing: ten lectures on subjective computing*, volume 2. Springer Science & Business Media, 2007.

[174] P. M. Lee. *Bayesian statistics*. Arnold Publication, 1997.

[175] P. Congdon. *Bayesian statistical modelling*, volume 704. John Wiley & Sons, 2007.

[176] J. O. Berger. *Statistical decision theory and Bayesian analysis*. Springer Science & Business Media, 2013.

[177] W. R. Gilks, S. Richardson, and D. Spiegelhalter. *Markov chain Monte Carlo in practice*. Chapman and Hall/CRC, 1995.

[178] C. Andrieu, N. De Freitas, A. Doucet, and M. I. Jordan. An introduction to mcmc for machine learning. *Machine learning*, 50(1-2):5–43, 2003.

[179] S. Geman and D. Geman. Stochastic relaxation, gibbs distributions, and the bayesian restoration of images. In *Readings in computer vision*, pages 564–584. Elsevier, 1987.

[180] American Heart Association Writing Group on Myocardial Segmentation and Registration for Cardiac Imaging. Standardized myocardial segmentation and nomenclature for tomographic imaging of the heart: a statement for healthcare professionals from the cardiac imaging committee of the council on clinical cardiology of the american heart association. *Circulation*, 105(4):539–542, 2002.

[181] P. I. Gardner, P. C. Ursell, J. J. Fenoglio Jr, and A. L. Wit. Electrophysiologic and anatomic basis for fractionated electrograms recorded from healed myocardial infarcts. *Circulation*, 72(3):596–611, 1985.

[182] P. C. Ursell, P. I. Gardner, A. Albala, J. J. Fenoglio Jr, and A. L. Wit. Structural and electrophysiological changes in the epicardial border zone of canine myocardial infarcts during infarct healing. *Circulation Research*, 56(3):436–451, 1985.

[183] J. Fernández-Armenta, A. Berruezo, D. Andreu, O. Camara, E. Silva, L. Serra, V. Barbarito, L. Carotenutto, R. Evertz, J. T. Ortiz-Pérez, et al. Three-dimensional architecture of scar and conducting channels based on high resolution ce-cmr: insights for ventricular tachycardia ablation. *Circulation: Arrhythmia and Electrophysiology*, 6(3):528–537, 2013.

[184] A. G. Kléber and Y. Rudy. Basic mechanisms of cardiac impulse propagation and associated arrhythmias. *Physiological reviews*, 84(2):431–488, 2004.

[185] N. El-Sherif, R. A. Smith, and K. Evans. Canine ventricular arrhythmias in the late myocardial infarction period. 8. epicardial mapping of reentrant circuits. *Circulation Research*, 49(1):255–265, 1981.

[186] M. E. Josephson. Sustained ventricular tachycardia in coronary artery disease–evidence for reentrant mechanism. *Cardiac electrophysiology and arrhythmias*, pages 409–418, 1985.

[187] J. M. De Bakker, F. J. Van Capelle, M. J. Janse, A. A. Wilde, R. Coronel, A. E. Becker, K. P. Dingemans, N. M. Van Hemel, and R. N. Hauer. Reentry as a cause of ventricular tachycardia in patients with chronic ischemic heart disease: electrophysiologic and anatomic correlation. *Circulation*, 77(3):589–606, 1988.

[188] J. M. De Bakker, F. J. Van Capelle, M. J. Janse, S. Tasseron, J. T. Vermeulen, N. de Jonge, and J. R. Lahpor. Slow conduction in the infarcted human heart.'zigzag'course of activation. *Circulation*, 88(3):915–926, 1993.

[189] L.-Y. Lin, M.-Y. M. Su, J.-J. Chen, L.-P. Lai, J.-J. Hwang, C.-D. Tseng, Y.-S. Chen, H.-Y. Yu, W.-Y. I. Tseng, and J.-L. Lin. Conductive channels identified with contrast-enhanced mr imaging predict ventricular tachycardia in systolic heart failure. *JACC: Cardiovascular Imaging*, 6(11):1152–1159, 2013.

[190] H. H. Hsia, D. Lin, W. H. Sauer, D. J. Callans, and F. E. Marchlinski. Anatomic characterization of endocardial substrate for hemodynamically stable reentrant ventricular tachycardia: identification of endocardial conducting channels. *Heart Rhythm*, 3(5):503–512, 2006.

[191] J. Ringenberg, M. Deo, V. Devabhaktuni, D. Filgueiras-Rama, G. Pizarro, B. Ibanez, O. Berenfeld, P. Boyers, and J. Gold. Automated segmentation and reconstruction of patient-specific cardiac anatomy and pathology from in vivo mri. *Measurement Science and Technology*, 23(12):125405, 2012.

[192] Z. Chen, M. Sohal, T. Voigt, E. Sammut, C. Tobon-Gomez, N. Child, T. Jackson, A. Shetty, J. Bostock, M. Cooklin, et al. Myocardial tissue characterization by cardiac magnetic resonance imaging using t1 mapping predicts ventricular arrhythmia in ischemic and non–ischemic cardiomyopathy patients with implantable cardioverter-defibrillators. *Heart Rhythm*, 12(4):792–801, 2015.

[193] C. M. Costa, G. Plank, C. A. Rinaldi, S. A Niederer, and M. J. Bishop. Modeling the electrophysiological properties of the infarct border zone. *Frontiers in Physiology*, 9(356), 2018.

[194] T. Pheiffer, D. Soto-Iglesias, Y. Nikulin, T. Passerini, J. Krebs, M. Sitges, A. Berruezo, O. Camara, and T. Mansi. Estimation of local conduction velocity from myocardium activation time: Application to cardiac resynchronization therapy. In *International Conference on Functional Imaging and Modeling of the Heart*, pages 239–248. Springer, 2017.

[195] C. Guetter, H. Xue, C. Chefd'Hotel, and J. Guehring. Efficient symmetric and inverse-consistent deformable registration through interleaved optimization. In *2011 IEEE international symposium on biomedical imaging: from nano to macro*, pages 590–593. IEEE, 2011.

[196] J. D. Bayer, R. C. Blake, G. Plank, and N. A. Trayanova. A novel rule-based algorithm for assigning myocardial fiber orientation to computational heart models. *Annals of biomedical engineering*, 40(10):2243–2254, 2012.

[197] O. Zettinig, T. Mansi, B. Georgescu, S. Rapaka, A. Kamen, J. Haas, K. S. Frese, F. Sedaghat-Hamedani, E. Kayvanpour, A. Amr, et al. From medical images to fast computational models of heart electromechanics: an integrated framework towards clinical use. In *International Conference on Functional Imaging and Modeling of the Heart*, pages 249–258. Springer, 2013.

[198] S. Rapaka, T. Mansi, B. Georgescu, M. Pop, G. A Wright, A. Kamen, and D. Comaniciu. Lbm-ep: Lattice-boltzmann method for fast cardiac electrophysiology simulation from 3d images. In *International Conference on Medical Image Computing and Computer-Assisted Intervention*, pages 33–40. Springer, 2012.

[199] S. Chen and G. D. Doolen. Lattice boltzmann method for fluid flows. *Annual review of fluid mechanics*, 30(1):329–364, 1998.

[200] S. Succi. *The Lattice Boltzmann Equation: For Complex States of Flowing Matter*. Oxford University Press, 2018.

[201] S. Ponce Dawson, S. Chen, and G. D. Doolen. Lattice boltzmann computations for reaction-diffusion equations. *The Journal of chemical physics*, 98(2):1514–1523, 1993.

[202] Z.S. Li, S.A. Zhu, and B. He. Solving the ecg forward problem by means of a meshless finite element method. *Physics in Medicine & Biology*, 52(13):N287, 2007.

[203] S. E. Geneser, R. M. Kirby, and R. S. MacLeod. Application of stochastic finite element methods to study the sensitivity of ecg forward modeling to organ conductivity. *IEEE Transactions on Biomedical Engineering*, 55(1):31–40, 2007.

[204] C. Liu, M. D. Eggen, C. M. Swingen, P. A. Iaizzo, and B. He. Noninvasive mapping of transmural potentials during activation in swine hearts from body surface electrocardiograms. *IEEE transactions on medical imaging*, 31(9):1777–1785, 2012.

[205] R. C. Barr, M. Ramsey, and M. S. Spach. Relating epicardial to body surface potential distributions by means of transfer coefficients based on geometry measurements. *IEEE Transactions on biomedical engineering*, (1):1–11, 1977.

[206] G. Shou, L. Xia, M. Jiang, Q. Wei, F. Liu, and S. Crozier. Solving the ecg forward problem by means of standard h-and h-hierarchical adaptive linear boundary element method: Comparison with two refinement schemes. *IEEE Transactions on Biomedical Engineering*, 56(5):1454, 2009.

[207] M. Boulakia, S. Cazeau, M. A. Fernández, J.-F. Gerbeau, and N. Zemzemi. Mathematical modeling of electrocardiograms: a numerical study. *Annals of biomedical engineering*, 38(3):1071–1097, 2010.

[208] M. Chhay, Y. Coudière, and R. Turpault. How to compute the extracellular potential in electrocardiology from an extended monodomain model. 2012.

[209] M. JD Powell. The newuoa software for unconstrained optimization without derivatives. In *Large-scale nonlinear optimization*, pages 255–297. Springer, 2006.

[210] F. O. Campos, Y. Shiferaw, R. W. dos Santos, G. Plank, and M. J. Bishop. Microscopic isthmuses and fibrosis within the border zone of infarcted hearts promote calcium-mediated ectopy and conduction block. *Frontiers in Physics*, 6(57), 2018.

[211] A. Loppini, A. Gizzi, C. Cherubini, E. M. Cherry, F. H. Fenton, and S. Filippi. Spatiotemporal correlation uncovers characteristic lengths in cardiac tissue. *Physical Review E*, 100(2):020201, 2019.

[212] J. Némec, J. Kim, and G Salama. *Optical Mapping: Its Impact on Understanding Arrhythmia Mechanisms*, chapter 8, pages 69–78. John Wiley & Sons, Ltd, 2012.

[213] M. Tanha, S. K. Chakraborty, B. Gabris, A.S. Waggoner, G. Salama, and D. Yaron. Computational and experimental characterization of a fluorescent dye for detection of potassium ion concentration. *Journal of Physical Chemistry A*, 118:9837–9843, 2014.

[214] T. Krogh-Madsen, A. F. Jacobson, F. A. Ortega, and D. J. Christini. Global optimization of ventricular myocyte model to multi-variable objective improves predictions of drug-induced torsades de pointes. *Frontiers in Physiology*, 8(1059), 2017.

[215] S. Filippi, A. Gizzi, C. Cherubini, S. Luther, and F. H. Fenton. Mechanistic insights into hypothermic ventricular fibrillation: the role of temperature and tissue size. *Europace*, 16:424–434, 2014.

[216] A. Gizzi, A. Loppini, R. Ruiz-Baier, A. Ippolito, A. Camassa, A. La Camera, E. Emmi, L. Di Perna, V. Garofalo, C. Cherubini, and S. Filippi. Nonlinear diffusion & thermo-electric coupling in a two-variable model of cardiac action potential. *Chaos: An Interdisciplinary Journal of Nonlinear Science*, 27:093919, 2017.

[217] C. Cherubini, S. Filippi, A. Gizzi, and R. Ruiz-Baier. A note on stress-driven anisotropic diffusion and its role in active deformable media. *Journal of Theoretical Biology*, 430:221–228, 2017.